

Allosteric regulation and targeting of Bruton's tyrosine kinase (Btk) in B-cell lymphoma

Présentée le 19 août 2020

à la Faculté des sciences de la vie
Unité de la Prof. Oricchio
Programme doctoral en approches moléculaires du vivant

pour l'obtention du grade de Docteur ès Sciences

par

Daniel PEREIRA DUARTE

Acceptée sur proposition du jury

Prof. C. Briskin, présidente du jury
Prof. E. Oricchio, Prof. O. Hantschel, directeurs de thèse
Dr M. Thome Miazza, rapporteuse
Dr S. Knapp, rapporteur
Dr B. Correia, rapporteur

“Remember to look up at the stars and not down at your feet
... and however difficult life may seem, there is always something
you can do and succeed at.”

– *Stephen Hawking*



ACKNOWLEDGEMENTS

This project could not have been executed without the support of incredible people.

I would like to thank Oliver Hantschel for his valuable support, constant motivation, and guidance provided through these few years. I would like to also express my appreciation for his positive attitude when facing several challenges and his efforts to ensure the successful conclusion of my degree at EPFL.

I would like to thank Elisa Oricchio for her flexibility and for also providing the essential tools at the end of my Ph.D. Many thanks also to Nathalia Katanayeva for the technical support during the past few months.

I would like to thank my colleagues for their support. Allan, thank you very much for teaching me most of the techniques applied herein. Sandrine, your constant contributions were essential and I truly appreciate your patience and time when sharing your technical expertise. It was also great to meet Sara and speak some charming Portuguese while away from home. I must also thank Sina for the cheerful discussions and for always being available to help. It was also a pleasure to work with my Ph.D. colleagues Nadine and Grégory, thank you both for being always smiley and available whenever needed. Thanks Tim K. and all other lab members for sharing your expertise. Finally, Christine thank you for the administrative support through these years.

I also counted with some brilliant experts who provided the technical support needed through this project. Thank you, Florence Pojer and Aline Reynaud, for helping me out during the exhaustive crystallization protocols. I am thankful to Prof. Dimitri Svergun and Alejandro Panjkovich from the EMBL Hamburg for their technical advice. I must also thank Giuseppina La Sala for her time and exceptional contribution to the history described herein. It was also great to share enjoyable moments at the synchrotron with Maria M. Finally, I thank all professors who have provided important insights to improve this manuscript, including Prof. Mateo Dal Peraro, Prof. Stefan Knapp, Prof. Margot Thomé

Miazza, Prof. Etienne Meylan, and Prof. Bruno Correia. Thank you also to our collaborator Prof. Hak-Sung Kim.

It is priceless to count with my dearests' friends who supported me along these years, even the ones physically far away. ¡Gracias Fabiana! It is incredible that we still laugh about our jokes from more than 10 years ago. It is also nice to count on Betânia and Raquel in our very insightful conversations. Gavin, it was nice to meet you and thanks for your support.

Je tiens à remercier aussi Jean-Baptiste qui a toujours été là pour moi. Merci pour ton soutien quotidien et tes encouragements pendant ces années-là. Je souhaite également remercier Myriam et Dominique pour les bons moments partagés avec tout le monde. Vous êtes devenus ma deuxième famille !

Finally and most importantly, I would like to thank my family. Mãe, pai e Raquel, vocês sempre fizeram todo o possível pela minha felicidade desde meu primeiro momento nesse mundo. Sem vocês eu jamais teria chegado tão longe. Muito obrigado a todos vocês!

Lausanne, 22nd March 2020.

– *Daniel Duarte*

PUBLICATIONS AND CONFERENCES

Publications

Daniel P. Duarte, Allan J. Lamontanara, Giuseppina La Sala, Sukyo Jeong, Yoo-Kyoung Sohn, Alejandro Panjkovich, Sandrine Georgeon, Tim Kükenshöner, Maria J. Marcaida, Florence Pojer, Marco De Vivo, Dmitri Svergun, Hak-Sung Kim, Matteo Dal Peraro, and Oliver Hantschel. **Btk SH2-kinase interface is critical for allosteric kinase activation and its targeting inhibits B-cell neoplasms.** *Nat. Comm.* 11, 2319 (2020). doi.org/10.1038/s41467-020-16128-5

Conferences

- EMBO Solution Scattering for biological macromolecules. Hamburg, Germany (17-24th October 2016). Short talk: “Allosteric regulation of tyrosine kinases in cancer”.
- ISREC retreat, Lausanne, Switzerland (20th June, 2017). Poster “Tyrosine kinases in haematological malignancies: mechanism of regulation and signaling networks.”
- 6th SCCL Faculty & Staff Retreat, Lausanne, Switzerland (14-15th November 2017). Poster “Allosteric regulation of non-receptor tyrosine kinases (NRTKs) - A close view on Bruton’s tyrosine kinase (Btk).”
- Hercules School: Biomolecular Structure and Dynamics, Grenoble, France (January – February 2018). Poster “Regulation and inhibition of Bruton’s tyrosine kinase (Btk).” Best poster award.
- FASEB Protein Kinases and Protein Phosphorylation Conference: Mechanisms to Therapeutics, Palm Springs, USA (7-12th July 2019). Short talk and poster “Allosteric regulation and inhibition of Bruton’s tyrosine kinase (Btk) via its SH2 domain.”

ABSTRACT

Bruton's tyrosine kinase (Btk) is a key component of BCR signaling required for B-cell maturation and activation. Loss-of-function mutations throughout the Btk protein cause human X-linked agammaglobulinemia (XLA), a heritable genetic disorder characterized by the absence of mature B-cells and lack of adaptive immune response. In contrast, Btk signaling sustains the growth of several B-cell neoplasms, which may be treated with small-molecule tyrosine kinase inhibitors (TKIs) targeting the ATP-site of the kinase. No alternative targeted therapy is available for patients who acquire resistance to current Btk inhibitors. Whereas a number of intramolecular interactions amongst the PH, SH3, SH2, and kinase domain (KD) are well resolved and stabilize a compact autoinhibited conformation, the molecular mechanisms governing Btk activation are not fully understood.

Using a combination of *in silico*, structural, cellular, and molecular approaches, we discovered an allosteric interface between the SH2 and the N-lobe of the KD that is critical for kinase activation *in vitro* and cells. In contrast to the low Btk activity of the KD alone, the presence of the SH2 domain is sufficient to increase Btk phosphorylation at Y551 and multiple other sites. This provides the structural mechanism by which a subset of XLA mutations mapped to the SH2 domain near the interface region strongly perturbs Btk activation, even though the SH2 canonical function is preserved. Furthermore, we demonstrated that the active Btk SH2-kinase adopts an elongated conformation with a dynamic contact interface structurally distinct than to the ones observed for other tyrosine kinases, such as Abl, Fes, and Csk.

As allosteric interactions provide unique targeting opportunities far from the ATP-site, we developed an engineered rebody protein binding to the human Btk SH2 domain. The crystal structure of the SH2-rebody complex combined with other structural approaches demonstrated that the rebody disrupts the SH2-kinase interaction. The rebody prevented activation of wild-type and TKI-resistant Btk *in vitro* and cells seen by a significant decrease in Btk phosphorylation. In parallel, sole allosteric targeting

inhibited Btk-dependent signaling and reduced proliferation of malignant B-cells dependent on the BCR signaling.

Therefore, the SH2-kinase interface is critical for Btk activation and is the first targetable site able to trigger allosteric inhibition. As Btk targeted therapy has a great impact on several conditions, including B-cell malignancies and autoimmune diseases, this study provides a rationale to support the development of alternative Btk inhibitors. This approach for targeted inhibition could particularly benefit patients with current therapy-resistant Btk variants.

Keywords: Bruton's tyrosine kinase, Btk, SH2 domain, allosteric activation, B-cell malignancies, allosteric inhibition, engineered rebody.

RÉSUMÉ

La tyrosine kinase de Bruton (Btk), composant indispensable de la signalisation BCR, est requise pour la maturation et l'activation des cellules B. Des mutations par perte de fonction dans la protéine Btk provoquent une agammaglobulinémie liée au sexe (XLA), maladie génétique héréditaire caractérisée par l'absence de lymphocytes B matures et un manque d'immunité à médiation humorale. En revanche, la signalisation Btk soutient la croissance de plusieurs néoplasmes à cellules B qui peuvent être traités avec des inhibiteurs de tyrosine kinase (TKIs) ciblant le site de liaison à l'ATP de la kinase. Aucune thérapie ciblée alternative n'est disponible pour les patients qui souffrent de résistances aux médicaments existants pour l'inhibition de Btk. Un certain nombre d'interactions moléculaires entre les domaines PH, SH3, SH2 et catalytique (KD) sont stabilisées dans une conformation compacte entraînant l'auto-inhibition de Btk. En revanche, les mécanismes moléculaires régissant son activation grâce à ses domaines non-catalytiques ne sont pas entièrement compris.

En utilisant une combinaison d'approches informatiques, structurales, cellulaires et moléculaires, nous avons découvert une interface allostérique entre le domaine SH2 et le lobe N-terminal du KD qui fonctionne comme régulateur allostérique de l'activité kinase. Cette interaction est critique pour l'activation de la kinase. Contrairement à la faible activité du KD isolé, la présence du domaine SH2 est suffisante pour augmenter la phosphorylation de Btk au niveau de Y551 et de plusieurs autres sites. Cela fournit le mécanisme moléculaire par lequel un sous-ensemble de mutations XLA au domaine SH2 à l'interface perturbent fortement l'activation de Btk tout en conservant la fonction canonique de SH2. Nous avons aussi démontré que l'unité Btk SH2-kinase activée adopte une conformation allongée avec une interface de contact dynamique et structuellement distincte de celles observées pour d'autres tyrosine kinases, telles que Abl, Fes et Csk.

Comme les interactions allostériques offrent des opportunités de ciblage uniques, nous avons développé une protéine repebody artificielle se liant au domaine SH2 de Btk. La structure cristallographique du complexe SH2-repebody combinée avec d'autres approches structurales a démontré que le repebody perturbe l'interaction SH2-kinase. Le

repebody a empêché l'activation de Btk de type sauvage et résistante aux TKI disponibles, ce qui s'est traduit par une diminution significative de la phosphorylation de Btk. En parallèle, la seule utilisation du ciblage allostérique a été suffisante pour inhiber la signalisation Btk-dépendante et a permis de réduire la prolifération des cellules B malignes.

Enfin, nous avons montré avec succès que l'interface SH2-kinase est critique pour l'activation de Btk et est le premier site capable de déclencher une inhibition allostérique. Étant donné que la thérapie ciblant Btk a un fort impact sur plusieurs maladies, comme les hémopathies malignes à cellules B et des maladies auto immunes, cette étude encourage le développement d'inhibiteurs alternatifs de Btk. L'inhibition allostérique pourrait particulièrement bénéficier aux patients présentant des résistances de Btk aux thérapies existantes.

Mots-clés : tyrosine kinase de Bruton, Btk, domaine SH2, activation allostérique, tumeurs malignes des cellules B, inhibition allostérique, repebody artificiel.

CONTENTS

ACKNOWLEDGEMENTS	5
PUBLICATIONS AND CONFERENCES	7
Publications	7
Conferences	7
ABSTRACT	9
RÉSUMÉ	11
CONTENTS	13
LIST OF FIGURES	17
LIST OF TABLES	19
ABBREVIATIONS	21
1 INTRODUCTION	25
1.1 Tyrosine kinases and their regulatory elements	25
1.1.1 The catalytic domain	25
1.1.2 Non-catalytic domains	27
1.1.3 Targeting tyrosine kinases in cancer	29
1.2 B-cell malignancies	32
1.2.1 BCR signaling in B-cell malignancies	33
1.2.2 Current approaches to treat B-cell malignancies	35
1.2.3 B-cells are implicated in autoimmune diseases	36
1.3 Impairment of normal B-cell development: a critical role for Btk	36
1.3.1 Btk is an important target in multiple human diseases	38
1.3.2 Drug resistance: a drawback of Btk targeted inhibition	41
1.4 Btk activation	42
1.5 Btk regulation and structural highlights	43
1.5.1 Allosteric regulation of Btk	45
2 AIMS	49
3 RESULTS	51
3.1 Allosteric activation of Btk	51
3.1.1 Production and functional characterization of recombinant Btk proteins	51
3.1.2 Uncovering the conformation of the active Btk SH2-KD using MD simulations and SAXS.	57

3.1.3 Mapping of the Btk SH2-KD interaction revealed an interface critical for kinase activation	61
3.1.4 Mutation on the Btk SH2-KD interface affects the conformation of the active unit	66
3.2 Targeting the Btk SH2-KD interface	69
3.2.1 Production and functional characterization of repebodies.	69
3.2.2 The rF10-SH2 crystal structure	71
3.2.3 Binding to rF10 abrogates the Btk SH2-KD interface.	72
3.2.4 rF10 functions as an antagonist of Btk activity	76
3.2.5 Targeting the Btk SH2-KD interface decreases the viability and inhibits signaling of lymphoma cells	79
3.2.6 Therapy-resistant Btk is targeted and inhibited by rF10	82
4 DISCUSSION	85
4.1 Allosteric activation of Btk	85
4.2 Allosteric inhibition of Btk	87
5 MATERIAL AND METHODS	91
5.1 Cell lines and culture conditions	91
5.2 Protein expression and purification	91
5.3 Mass spectrometry	92
5.4 Multi-angle light scattering analysis (SEC-MALS)	92
5.5 Site-directed mutagenesis	93
5.6 Circular dichroism (CD)	93
5.7 Kinase autophosphorylation assay	94
5.8 HEK293 transfection	94
5.9 Cell lysis and immunoblotting	94
5.10 Antibodies	95
5.11 Immunoprecipitation	95
5.12 B-cell transduction and BCR stimulation	96
5.13 Cell viability assays	96
5.14 Apoptosis staining	97
5.15 Development of repebodies	97
5.16 Molecular dynamics (MD) simulations	97
5.17 Small-angle X-ray scattering (SAXS)	98
5.18 Crystallization, data collection, and structure determination	99
5.19 Isothermal titration calorimetry (ITC)	99
5.20 Fluorescent polarization (FP) binding assays	100
5.21 <i>In vitro</i> kinase assay	100
5.22 Mapping of Btk autophosphorylation sites	100

5.23 Quantification and statistical analysis	101
5.24 Data availability	101
6 REFERENCES	103
7 CURRICULUM VITAE	117
8 ANNEX	119

LIST OF FIGURES

Figure 1 – Schematic view of CTKs families and their members. _____	26
Figure 2 – Main structural elements controlling catalytic activity in the tyrosine kinase domain. _____	27
Figure 3 – Multiple intramolecular interactions maintain Src-module-containing kinases in the autoinhibited state. _____	29
Figure 4 – The SH2-KD interface of active Abl is mediated by the SH2 I164 residue. ____	29
Figure 5 – Main stages of the development and malignancies affecting B-cells. ____	33
Figure 6 – Schematic overview of the BCR signaling in B-cells. _____	34
Figure 7 – Current model of Btk activation in B-cells. _____	43
Figure 8 – Full-length Btk model in its autoinhibited and extended conformations. ____	47
Figure 9 – Production of recombinant Btk proteins in insect cells. _____	52
Figure 10 – Recombinant Btk proteins are functional and revealed a critical role of the SH2 domain in activating the kinase. _____	54
Figure 11 – <i>In vitro</i> kinetics of Btk Y223 vs. Y551 phosphorylation. _____	55
Figure 12 – The SH2 domain is sufficient to increase Btk activation in cells. _____	56
Figure 13 – MD simulations suggest alternative conformations for the Btk SH2-KD protein. _____	58
Figure 14 – Comparative SAXS analysis of recombinant WT Btk proteins. _____	59
Figure 15 – Flexibility analysis of recombinant Btk proteins using SAXS. _____	62
Figure 16 – A subset of XLA in the SH2 domain does not significantly affect domain stability and canonical function. _____	63
Figure 17 – XLA mutations in the SH2 domain impair Btk activity. _____	65
Figure 18 – An XLA mutation facing the predicted Btk SH2-KD interface negatively impact kinase activity. _____	67
Figure 19 – A mutation in the SH2-KD interface forces Btk towards a more compact conformation. _____	68
Figure 20 – Mutation L405E in the N-lobe of Btk increases kinase activation. _____	68
Figure 21 – rF10 repebody binds to Btk SH2 domain with great affinity. _____	70
Figure 22 – rF10 repebody does not bind to SH2 domains of related kinases. _____	71

Figure 23 – rF10 repebody does not affect Btk SH2 pY-binding. _____	71
Figure 24 – The high-resolution structure of rF10-SH2 complex. _____	73
Figure 25 – Binding to rF10 may abrogate the Btk SH2-KD interaction. _____	74
Figure 26 – rF10 repebody inhibits Btk activation <i>in vitro</i> . _____	77
Figure 27 – rF10 repebody inhibits Btk phosphorylation in the cellular context. _____	78
Figure 28 – Allosteric inhibition of Btk decreases DLBCL cell proliferation. _____	80
Figure 29 – Allosteric inhibition of Btk in DLBCL cells. _____	81
Figure 30 – Combination of rF10 and ibrutinib in HBL-1 cells. _____	82
Figure 31 – Targeting the SH2-KD interface in the therapy-resistant Btk C481S. _____	83
Figure 32 – Sequence alignment of SH2 domains from human Btk and related kinases. _____	87
Figure 33 – Proposed model for the allosteric activation and inhibition of Btk via its SH2 domain. _____	89

LIST OF TABLES

Table 1 – Btk inhibitors approved and under clinical development.	39
Table 2 – Selected Btk high-resolution molecular structures available.	45
Table 3 – <i>In vitro</i> autophosphorylation sites on the Btk SH2-KD protein.	55
Table 4 – SAXS parameters of human Btk WT and mutants.	60
Table 5 – X-ray parameters of the rF10-SH2 crystal structure (6HTF).	72
Table 6 – SAXS parameters of rF10-Btk complexes.	75
Table 7 – Oligonucleotides used for site-directed mutagenesis.	93
Table 8 – List of antibodies.	95

ABBREVIATIONS

ABC DLBCL – activated B-cell subtype of diffuse large B-cell lymphoma
ABL – Abelson tyrosine kinase
AGC – protein kinase A, G, and C family of kinases
ALL – acute lymphoblastic leukemia
ATP – adenosine triphosphate
BCR – B-cell receptor
BCR-ABL – breakpoint cluster Abl kinase fusion oncogene
BLNK – B-cell linker protein
Btk – Bruton's tyrosine kinase
CAR-T – chimeric antigen receptor T cells
CD – circular dichroism
CD20 – cluster of differentiation 20
CD79 – cluster of differentiation 79
CLL – chronic lymphocytic leukemia
Csk – C-terminal Src kinase
CTK – cytoplasmic tyrosine kinase
DAG – diacylglycerol
DLBCL – diffuse large B-cell lymphoma
EGFR – epidermal growth factor receptor
EOM – ensemble of optimization method
FcR – Fc receptor
FDA – U.S. Food and Drug Administration
Fes – feline sarcoma tyrosine kinase
FL – follicular lymphoma
FP – fluorescent polarization
GC – germinal center
GCL DLBCL – germinal center B-cell subtype of diffuse large B-cell lymphoma
GvHD – graft versus host disease
HDX-MS – hydrogen-deuterium exchange mass spectrometry

IL – interleukin
IP₃ – inositol triphosphate
IP₆ – inositol hexakisphosphate
ITAM – immunoreceptor tyrosine-based activation motif
ITC – isothermal titration calorimetry
Itk – inducible T cell kinase
KD – kinase domain
LRR – leucine-rich repeat
MALS – multi-angle light scattering
MCL – mantle cell lymphoma
MD – molecular dynamics
MLL – mixed-lineage leukemia protein
MS – mass spectrometry
NHL – non-Hodgkin's lymphoma
NMR – nuclear magnetic resonance
NSAIDs – non-steroidal anti-inflammatory drugs
OS – overall survival
PDB – protein data bank
PFS – progression-free survival
PI3K – phosphoinositide 3-kinase
PID – protein interaction domain
PIF – PDK1-interacting fragment
PIP₃ – phosphatidylinositol-3,4,5-triphosphate
PLCγ2 – phospholipase C gamma 2
PPR – proline-rich repeat
PROTAC – proteolysis-targeting chimera
RA – rheumatic arthritis
R-CHOP – rituximab, cyclophosphamide, doxorubicin, vincristine, and prednisone
RTK – receptor tyrosine kinase
SASDB – small-angle scattering biological data bank
SAXS – small-angle X-ray scattering
SD – standard deviation
SEC – size exclusion chromatography
SH2 – src homology domain 2
SH3 – src homology domain 3

Src – sarcoma tyrosine kinase
 TCEP – tris(2-carboxyethyl)phosphine
 Tec – Tec protein tyrosine kinase
 TKI – tyrosine kinase inhibitor
 TNF – tumor necrotic factor
 TSA – thermal shift assay
 XLA – X-linked agammaglobulinemia
 WT – wild-type
 WV – Waldenstrom’s macroglobulinemia

1 INTRODUCTION

1.1 Tyrosine kinases and their regulatory elements

Post-translational modifications of proteins are key regulatory mechanisms governing all aspects of cellular biology. Phosphorylation of serine, threonine, and tyrosine residues have a central role in multiple signaling pathways regulating cell development, proliferation, motility, and metabolism¹.

The human genome encodes 518 putative kinases of which 90 exclusively phosphorylate tyrosine residues. Tyrosine kinases are grouped in two major classes: receptor tyrosine kinases (RTKs) and cytoplasmic tyrosine kinases (CTKs), which are classified into several families based on structural similarities². RTKs are membrane proteins and contain an extracellular ligand-binding domain connected to the intracellular kinase domain via one transmembrane segment, whereas CTKs are intracellular multidomain proteins commonly found associated with the inner leaflet of the plasma membrane. The architecture of CTKs (Fig. 1) varies by the presence of different non-catalytic and ligand-binding domains in addition to the main catalytic core.

1.1.1 The catalytic domain

Tyrosine kinases share a well-conserved catalytic domain (or kinase domain, KD) containing crucial regulatory elements that strictly control kinase activity under physiological conditions. The KD assumes a common fold consisting of a bilobal structure connected by a short hinge region shaping a deep cleft where ATP, Mg^{2+} cations, and substrate interact. The interplay amongst different structural elements distributed in these N- and C-terminal lobes participate in the catalysis and carry out the transfer of the gamma phosphate group of ATP onto the substrate peptide³.

Since the first kinase structure was solved⁴, multiple crystal structures have helped to elucidate the molecular basis of kinase activation. These structures revealed that at least three flexible elements from the active site are important for phosphoryl transfer reaction

during the catalytic cycle: the C-helix, activation loop, and catalytic loop⁵ (Fig. 2, residue number refers to Src). The C-helix located in the N-lobe essentially adopts a range of positions that directly impact the catalytic mechanism. In the active state, the C-helix adopts an “in” conformation that induces a salt bridge between its conserved glutamate (E310) and an adjacent N-lobe lysine (K295), reorienting a highly mobile glycine-rich loop (or P-loop) that interacts with the ATP alpha and beta phosphates. In the C-lobe, activation loop phosphorylation (Y416) stabilizes and provides a platform for binding and positioning of the hydroxyl group from the tyrosine of the substrate. Flanked to the activation loop, the Asp residue (D404) from a DFG motif recognizes the ATP-bound Mg^{2+} ion, whereas its phenylalanine makes further hydrophobic contact with the C-helix and the nearby catalytic loop when the DFG motif is positioned in the DFG-in conformation. The HRD motif within the catalytic loop contains the aspartate (D386) that provides a precise spatial arrangement of the catalytic residues required for the reaction mechanism^{3,6}. Altogether, these key components are stabilized by a network of hydrophobic residues forming the regulatory and catalytic spines anchored in a central F-helix buried in the C-lobe.

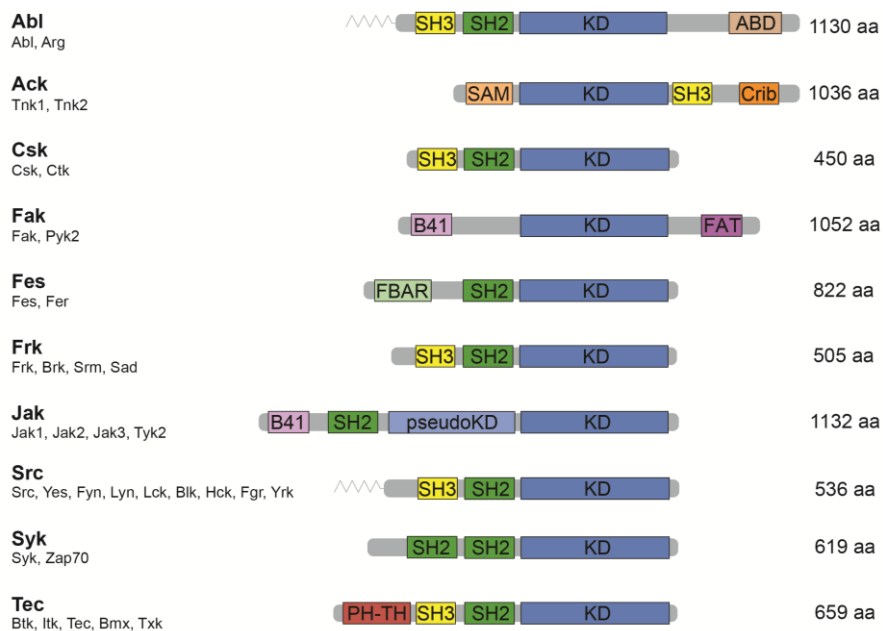


Figure 1 – Schematic view of CTKs families and their members.

The protein length refers to the first family member as a reference. SH2/3: Src homology 2/3 domains, KD: kinase domain, ABD: actin-binding domain, SAM: sterile alpha motif, Crib: Cdc42- and Rac-interactive binding domain, B41: band 41, FAT: Frap-Atm-Trapp domain, PH-TH: pleckstrin and Btk homology domains.

In the majority of kinases, the activation loop undergoes large conformational changes and is stabilized by phosphorylation of one or more residues, depending on the kinase, to stabilize its active conformation and allows substrate binding and catalysis. In contrast, when in the inactive state, the unphosphorylated activation loop folds into an autoinhibitory conformation where it may act as pseudo-substrate to inhibit substrate binding⁷. Therefore, activation loop phosphorylation is commonly used as a hallmark of the active state of kinases^{3,5}.

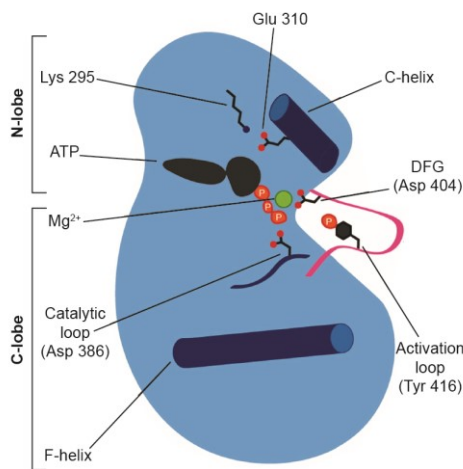


Figure 2 – Main structural elements controlling catalytic activity in the tyrosine kinase domain.

Residue number refers to chicken c-Src. Figure adapted from⁸.

1.1.2 Non-catalytic domains

In addition to the highly dynamic structures commanding catalytic activity within the KD, kinases commonly display several non-catalytic domains. These structures play important regulatory roles in stabilizing the inactive or inducing an active conformation of the KD by mediating important molecular interactions. Protein-lipid and protein-protein interaction domains (PIDs) can be targeted by specific ligands or modulated by posttranslational modifications, and participate in substrate interaction, kinase localization, and intramolecular allosteric interactions with the main catalytic core⁹.

A PID of major importance in cell signaling is the Src-homology 2 (SH2) domain, originally characterized in the Src kinase and later identified in multiple other kinases, adaptors, and scaffold proteins. SH2 domains are approximately 100 residues in size and show striking structural conservation – over 300 structures deposited into the protein databank display a core made of three β -sheets surrounded by two α -helices¹⁰. SH2 domains contain a central motif that interacts with specific peptide sequences containing phosphotyrosine (pY +3

residues) with variable affinity⁹. Another important PID is the Src-homology 3 (SH3) domain, which is smaller in size and has typically around 60 amino acids. It contains two surface grooves that accommodate proline-rich peptides (motif PxxP)¹¹. Both SH2 and SH3 domains enormously increase substrate specificity and play a role in multiple signaling pathways^{9,10}.

In addition to their canonical roles, PIDs also mediate important allosteric interactions with the KD core, directly impacting its catalytic activity. For instance, the interaction of Src SH3 and SH2 domains with the C-lobe negatively regulates kinase activity by stabilizing its inactive state and hindering substrate phosphorylation (Fig. 3A)^{12,13}. This autoinhibited conformation is maintained by two important interactions: (1) the phosphorylated Y527 on the C-terminal portion of KD interacting with the SH2 pY-binding pocket, and (2) the additional interaction of the SH2-KD linker with the SH3 domain, creating a compact arrangement locking the SH3-SH2 domains on the “back” of the KD. This conserved SH3-SH2-KD autoinhibitory configuration, known as Src-like module, is also found in other CTK families such as Abl, Tec, and Csk kinases (Fig. 3B and C)⁸. Furthermore, certain kinases evolved unique intramolecular interactions important for their regulation. This is the case of Abl kinase where its N-terminal myristoyl modification docks into an allosteric pocket of the C-lobe and helps to stabilize its autoinhibited conformation (Fig. 3B)^{14,15}.

In contrast to autoinhibitory allosteric interactions, PIDs can contribute to enhancing kinase activation. Crystal structures of active Abl and Fes kinases (PDB: 4XEY and 3BKB, respectively) show the formation of an interface between the SH2 domain and N-lobe, creating an open elongated complex accompanied by an increase in catalytic activity^{16,17}. In Abl, this large interdomain interface is mediated by the contact of SH2 residue I164 (Fig. 4), which promotes a shift of the activation loop towards an open conformation^{18,19}. While the I164E mutation abrogates this interaction and decreases Abl activity and leukemogenesis *in vivo*, the T231R mutation strengthens this elongated SH2-KD conformation and is accompanied by a moderate enhancement of kinase activation^{20,21}. Thus, the interplay between KD and PIDs can impact the state of KD and significantly affect kinase activity.

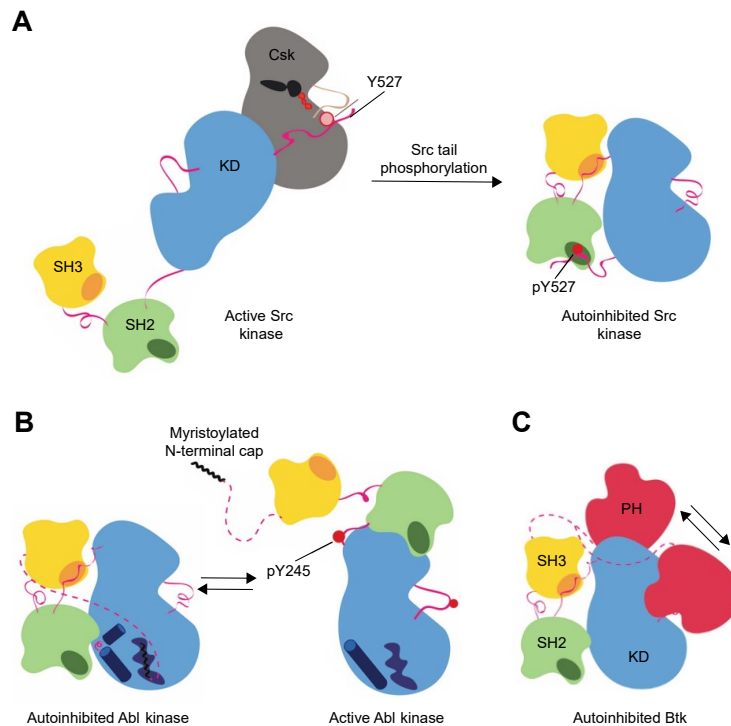


Figure 3 – Multiple intramolecular interactions maintain Src-module-containing kinases in the autoinhibited state.

A: Phosphorylation of Src Y527-tail by Csk induces interaction with its SH2 pY-binding pocket and induce a close conformation.

B: Autoinhibited Abl is released of its closed conformation by unlatching its N-terminal myristate and Y245 phosphorylation within the SH2-KD linker.

C: The PH domain further stabilizes Btk autoinhibition by interacting with the front of the KD, discussed in details later. Figure adapted from⁸.

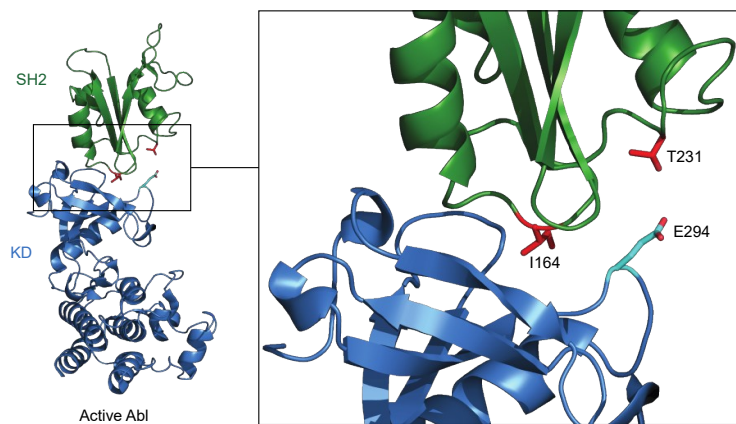


Figure 4 – The SH2-KD interface of active Abl is mediated by the SH2 I164 residue.

Cartoon representation of active Abl (1OPL) showing the SH2 domain (green) sitting on top of the KD (blue). The position of the residues facing the SH2-KD interaction (red) and the KD residue E294 are highlighted.

1.1.3 Targeting tyrosine kinases in cancer

Aberrant activation of protein tyrosine kinases, commonly due to point mutations, deletions, duplications, chromosomal fusions or overexpression, drives cell transformation and multiple malignancies. Alternatively, cancer cells can also hijack certain oncogenic proteins to support growth and survival even when these proteins are not mutated. The development of a repertoire of small-molecule inhibitors targeting critical tyrosine kinases has revolutionized cancer treatments – as of March 2020, 66 inhibitors have been approved by the U.S. Food and Drug Administration (FDA) for clinical use. Targeted therapies have considerably reduced side effects compared to traditional chemotherapy, lead to remarkable and sustainable tumor remissions, and increase overall survival of patients suffering from hematological and solid tumors²².

A particularly successful group of tyrosine kinase inhibitors (TKIs) has been developed against the BCR-ABL fusion gene, a well-characterized aberrant chromosomal translocation that produces a constitutively active form of Abl kinase and drives the development of chronic myeloid leukemia (CML) and a subset of B-cell acute lymphocytic leukemia (B-ALL)²³. Imatinib (Gleevec) was the first TKI approved for the treatment of CML and achieves durable remissions in the majority of patients²⁴. A common drawback seen in patients treated with imatinib is the emergence of Bcr-Abl point mutations that decreases protein affinity to the drug and promotes CML relapse²⁵. Second and third generations of ATP-site inhibitors such as dasatinib, nilotinib, bosutinib, and ponatinib were developed as alternative agents to target these Bcr-Abl variants, although novel mutations and resistance mechanisms also evolve in patients treated with these drugs²³. Hence the need for an arsenal containing multiple drugs reaching common targets.

Due to the structural constraints of the ATP-site of kinases, the design of specific small-molecules binding to this region is extremely difficult. Although off-targets do not always lead to adverse effects in patients, they commonly trigger undesirable side effects that require treatment discontinuation as seen for instance in 21% of patients receiving nilotinib²⁶. Life-threatening adverse events observed in patients under prolonged regimens on TKIs include atrial fibrillation, hypertension, and bleeding, which commonly require hospitalization and impact their quality of life.

An attractive strategy to improve targeted therapies is the combination of multiple drugs hitting the same target or targeting complementary pathways to allow a more effective

response, decrease the emergence of resistant mutations, and minimize side effects. In the context of Bcr-Abl, the development of asciminib, the first allosteric inhibitor binding to the Abl myristate pocket to achieve clinical development, has been shown to inhibit Bcr-Abl kinase and lead to tumor regression²⁷. Although asciminib alone shows significant anti-tumoral effect in CML patients without apparent side effects²⁸, it is less effective against more aggressive variants of Bcr-Abl which harbor multiple mutations. Elegant studies have suggested that combination of allosteric with ATP-site inhibitors (e.g. nilotinib or ponatinib) is a promising strategy to target highly resistant Bcr-Abl variants such as T315I or compound mutations^{29,30}. In this context, binding of asciminib forces an autoinhibited conformation of the KD that facilitates binding to ponatinib at clinically achievable concentrations to restore the efficacy of these drugs³⁰. Therefore, identification of allosteric sites is one promising approach towards the development of the next generation of kinase inhibitors and rational combinations to suppress emerging of novel resistant variants.

Multiple approaches are available to investigate protein-protein interactions, validate clinical targets, and develop novel therapies. Engineered protein binders such as monobodies³¹ and repebodies³² are powerful and versatile tools that can be designed to bind specific sites that would be otherwise undruggable. Monobodies are synthetic antibody-mimetic proteins generated by diversifying certain residues from a fibronectin type III (FN3) scaffold and selected to bind specific targets. The use of monobodies to target protein-protein interactions has been demonstrated against a variety of targets including SH2 domains of Abl and Src kinases, as well as Ras³³⁻³⁵. Abl SH2-binding monobodies abrogating the critical SH2-KD interaction in Bcr-Abl decrease kinase activity and viability of leukemic cells²¹, while genetically encoded monobodies targeting the MLL complex *in vivo* conferred survival benefit in a mouse model for leukemia³⁶. In parallel, repebodies composed of an alternative synthetic scaffold containing modifiable leucine-rich repeat (LRR) modules have been engineered to target epidermal growth factor receptor (EGFR) and detect EGFR-expressing malignant tumors by positron emission tomography (PET-Scan)³⁷. Thus, engineered proteins are an attractive approach towards the discovery of critical protein-protein interactions and accelerate translation to the development of targeting strategies.

1.2 B-cell malignancies

B-cells play a critical role in the immune system by generating and secreting antibodies. Pre-B-cells undergo an extensive genetic reprogramming acting in the variable, joining, and diversity (V(D)J recombination) segments of heavy and light chains – this process generates a large repertoire of immunoglobulins that are expressed as part of the B-cell receptor (BCR)³⁸. Transitional B-cells expressing functional BCRs from the bone marrow migrate to lymphoid organs and further differentiate into various B-cell subsets (follicular, marginal zone, and germinal center B-cells). Upon antigen engagement by BCRs, B-cells promote antigen presentation to T cells via major histocompatibility complex II (MHC-II), followed by additional rounds of class-switch recombination and affinity maturation through somatic hypermutation to generate high-affinity antibodies and increase proliferation. While these early-stage activated plasma cells can secrete lower affinity IgM BCRs, activated B-cells entering germinal centers (GCs) give rise to long-lived plasma cells and memory B-cells capable of producing higher-affinity IgG BCRs^{39,40}.

Transformed B-cells at different stages of development give rise to leukemias, lymphomas, or myelomas (Fig. 5). The complex reprogramming that naturally drives the development of BCRs in pre-B-cells can potentially lead to aberrant genetic events such as BCR-ABL1 translocations and point mutations affecting several oncogenes (e.g. RAS). Although these transforming events are found silent in most people, they can drive B-ALL, which accounts for the majority of leukemias derived from B-cells in the bone marrow⁴¹. Genetic rearrangements particularly happening in the activated GCs can also lead to the development of indolent or more aggressive non-Hodgkin's lymphomas (NHL) such as follicular lymphoma, Burkitt's lymphoma, and diffuse large B-cell lymphoma (DLBCL). Genetic translocations that trigger constitutive expression of BCL-2 and MYC are common drivers of follicular lymphoma and Burkitt's lymphoma, respectively. B-cell malignancies comprise approximately 85% of NHLs, of which 40% are DLBCL followed by follicular lymphoma in 16% of cases. Although occurring at any age, the risk of developing NHL increases throughout life, with a median age at diagnosis around 78 years of age^{40,42}.

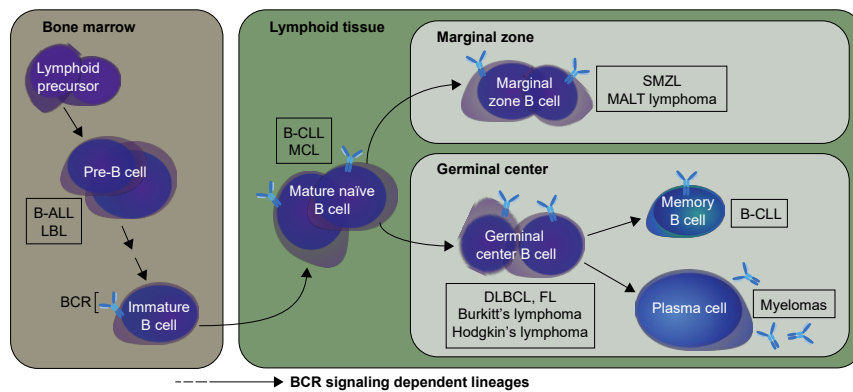


Figure 5 – Main stages of the development and malignancies affecting B-cells.

The initial stages of development in the bone marrow give rise to immature B-cells that migrate to lymphoid tissues to differentiate into mature B-cells, plasma cells, or memory B-cells. ALL: acute lymphoblastic leukemia, LBL: lymphoblastic lymphoma, CLL: chronic lymphocytic leukemia, MCL: mantle cell lymphoma, DLBCL: diffuse large B-cell lymphoma, FL: follicular lymphoma, SMZL: small marginal zone lymphoma, MALT: mucosa-associated lymphoid tissue, BCR: B-cell receptor.

1.2.1 BCR signaling in B-cell malignancies

BCR signaling is essential for B-cell development, differentiation, and activation during the humoral immune response. As illustrated in Figure 6, BCRs are expressed on the cell surface and composed of one immunoglobulin (i.e. IgM or IgG) associated with a transmembrane complex Ig α /Ig β heterodimer (CD79 α / β). Antigen engagement by the BCR promotes tyrosine phosphorylation of immunoreceptor tyrosine-based activation motifs (ITAMs) in the intracellular tails of CD79 α / β by different proposed mechanisms, including receptor aggregation and direct phosphorylation by Lyn, a member of the Src family^{43,44}. Phosphorylation of ITAMs further recruits Syk to activate the BCR signalosome, a multiprotein complex composed by scaffold proteins CD19 and B-cell linker protein (BLNK), and the enzymes Btk, phospholipase gamma 2 (PLC γ 2) and phosphoinositide 3-kinase (PI3K). Following engagement of Btk to the plasma membrane and its activation by Lyn/Syk, Btk phosphorylates PLC γ 2 Y753 and Y1417 sites leading to the generation of second messengers (i.e. IP $_3$ and DAG) and cellular calcium influx⁴⁵. These events trigger B-cell reprogramming mediated PKC β , transcription factors (e.g. NFAT), and phosphorylation events that mediate MAPK, JNK, and NF- κ B pathways. All these signals have important regulatory roles in B-cell activation, maturation, and survival⁴⁰. In contrast, key factors suppressing this antigen-induced response include CD22 and SH2 domain-containing tyrosine phosphatase-1 (SHP-1)⁴⁶. This dynamic and complex equilibrium

between the positive and negative regulatory circuits determines the magnitude and duration of BCR signal and subsequent B-cell differentiation.

Besides the heterologous nature of B-cell malignancies, BCR is critical for the development and progression of certain B-cell neoplasia as it can exert a tonic effect (antigen-independent) or antigen-dependent signaling^{47,48}. Whereas loss of CD79 α/β can be lethal for certain B-cell lymphomas⁴⁹, constitutive activation of CD79 α/β results in enhanced BCR signaling. For example, activated B-cell (ABC) DLBCL, the most aggressive type of NHL, is commonly associated with tonic BCR signaling due to gain-of-function mutations on ITAM tyrosines that sustain tumor growth⁵⁰⁻⁵². In contrast, CD79 mutations are rare in CLL⁵³, where the relative contribution of BCR to the disease initiation is still debated. In CLL, tonic BCR signaling has been identified by an increase in phosphorylation of Lyn⁵⁴, Syk⁵⁵, Erk⁵⁶, and NF- κ B⁵⁷, and possibly associated with Myc overexpression⁵⁸. Nevertheless, reactive BCR caused by self-antigens within the tumor microenvironment may also play a role to activate B-cells and sustain CLL⁵⁹. It is worth noting that sustained BCR signaling can also be the product of a failure in negative feedback, such as impairment of Lyn⁶⁰. Thus, the status of BCR signaling has a central role in the initiation and progression of multiple B-cell malignancies.

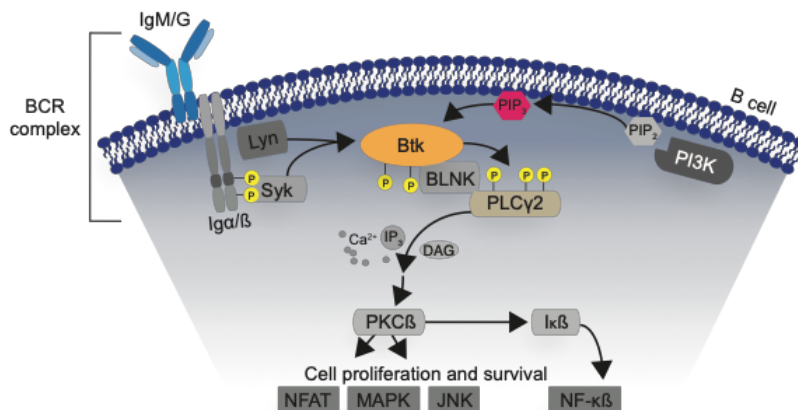


Figure 6 – Schematic overview of the BCR signaling in B-cells.

Antigen engagement promotes BCR activation by phosphorylation of ITAM from Ig α/β by different mechanisms (see text), activation of Lyn/Syk, and recruitment of BCR signalosome which includes BLNK, PI3K, Btk, and PLC γ 2. BCR signaling results in the generation of second messengers IP $_3$ and DAG, calcium influx, and a complex genetic reprogramming via multiple pathways.

1.2.2 Current approaches to treat B-cell malignancies

Several therapies are available to treat B-cell malignancies. A combination of chemotherapy, radiotherapy, immunotherapy, stem-cell transplantation, and/or targeted inhibition can be applied depending on the stage, clinical behavior, and response to previous treatments.

Multidrug regimens composed of small-molecules and biologic drugs (i.e. antibodies) are currently employed as first and second-line therapies against B-cell-derived tumors. For more than a decade, these combinations result in a very positive response in different NHLs as seen, for example, with the combination of monoclonal anti-CD20 (e.g. rituximab) and cyclophosphamide, doxorubicin, vincristine, and prednisolone (R-CHOP). This potent association is currently the gold standard for the treatment of NHLs and results in 5-year survival of 80% for patients with DLBCL and other tumors⁶¹.

Given the heterogeneous response of B-cell malignancies to current therapies, investigators have searched for alternative approaches that could overcome or delay tumor relapse. Targeted therapies have become a breakthrough for patients with NHLs and other malignancies. Diverse ATP-site inhibitors have been developed against critical kinases involved in BCR signaling, notably fostamatinib⁶², ibrutinib (discussed below), and idelalisib⁶³, as well as targeting alternative pathways playing a role on B-cell survival, such as Bcl-2⁶⁴ and the proteasome^{65,66}. A number of ongoing clinical trials will support the clinical development of rational combinations with superior efficacy compared to the traditionally applied regimens.

Finally, cell-based therapies consisting of engineering chimeric antigen receptors on T cells (CAR-T) that recognize specific antigens to effectively destroy cancer cells have recently changed the treatment landscape for NHLs⁶⁷. CAR-T therapies have been developed against a variety of surface targets and demonstrate impressive efficacy in aggressive diseases unresponsive to previous treatments. For example, targeting CD19 using CAR-T leads to a positive response in 86% of refractory DLBCL patients⁶⁸, as well as 93% of patients with ALL⁶⁹, some showing long-term remissions. These results supported the recent FDA approval of two anti-CD19 CAR-T products for relapsed/refractory disease: tisagenlecleucel and axicabtagene ciloleucel. Drawbacks of this approach include the lack of control on T cell activation and adverse effects promoted by cytokine release⁷⁰. Ongoing

studies aim to engineer a mechanism for precise control of receptor activation, as well as to apply CARs in other immune cell types⁷¹.

1.2.3 B-cells are implicated in autoimmune diseases

During B-cell development, pre-B-cells acquire a large repertoire of BCRs capable of also recognizing ubiquitous self-antigens. A robust mechanism of negative selection is placed to eliminate autoreactive BCRs, which can account for up to 75% of newly formed B-cells⁷². Impairment of this tolerance mechanism promotes abnormal B-cell activation and inflammatory response.

Autoimmune diseases, such as rheumatoid arthritis (RA)⁷³ and systemic lupus erythematosus⁷⁴, commonly affect multiple organs and are driven by a T cell and/or autoantibody-mediated dysfunction in the immune system. RA is a chronic inflammatory disease that affects approximately 1 % of the population and is commonly associated with progressive disabilities and systemic complications⁷⁵. Although the pathogenesis of RA remains unclear, autoantibodies against multiple cartilage components, stress proteins, and citrullinated proteins are commonly detected in the serum of patients and include for example antibodies against types I and II collagen and fibrin⁷⁶. Thus, it is evident that immunopathologies are at least partially mediated by B-cells.

Although incurable, adequate clinical management of patients with autoimmune diseases can slow disease progression and improve life quality. Disease-modifying anti-rheumatic drugs include anti-inflammatory and analgesics drugs (e.g. glucocorticoids and NSAIDs such as celecoxib), anti-tumor necrotic factor (TNF) biologics and target therapy against B-cells (e.g. rituximab). The anti-CD20 antibody rituximab is approved for RA patients not responding adequately to anti-TNF drugs and promotes sustainable remissions of symptoms achieved by repeated courses of treatment⁷⁷. Several ongoing trials using small-molecules targeting Jak, PI3K, and Btk⁷⁸ will soon provide further evidence on the benefits of kinase inhibition in the context of autoimmune disorders.

1.3 Impairment of normal B-cell development: a critical role for Btk

Primary immunodeficiencies are a heterogeneous group of disorders characterized by hypo- or agammaglobulinemia that typically arrives at early stages as the

maturation of pre-B-cells requires a functional BCR signaling. Genetic alterations on BCR components such as CD79 α , μ light chain, BLNK, Btk, and others⁷⁹ are critical for disease initiation and lead to impaired adaptive immune responses that require long-life treatment with IgG infusions combined with the aggressive use of antibiotics.

Approximately 90% of patients with an early-onset agammaglobulinemia show defects in BTK⁸⁰, a gene consisting of 19 exons located at band q21.3 on the X chromosome, hence named X-linked agammaglobulinemia (XLA) in humans. The XLA syndrome was initially described by Colonel Ogden Bruton in 1952, although the link to BTK alterations was only discovered in 1993⁸¹. Mice lacking Btk activity develop murine X-linked immunodeficiency (xid), a phenotype similar to human XLA, but less severe⁸².

Btk is a CTK composed of 659 amino acids and multiple domains: the N-terminal pleckstrin homology (PH) and a proline-rich Tec homology (TH) domains, followed by an SH3 and SH2 flanked to its catalytic domain. More than 600 loss-of-function missense mutations have been identified throughout the protein but on the SH3 domain⁸². Mutations in the PH domain cause severe forms of XLA mainly by disruption of its canonical lipid-binding site (e.g. R38C/H mutation) or affecting domain folding and stability (e.g. V64F and V133D). These mutations impair membrane translocation of Btk that is required for kinase activation^{83,84}.

Although no point mutation on SH3 is known to cause XLA, the deletion of 14aa constituting the C-terminal portion of the domain (260-273) has been identified as the cause of XLA in one family⁸⁵. In contrast, dozens of XLA-missense mutations have been identified and throughout the Btk SH2 domain. Of these, only very few mutations have been well characterized at the molecular level. Those are linked to decreased pY-binding or that affect protein stability. Amino acid substitutions within the FVDR motif (e.g. R307G) impair pY-binding without an effect on domain folding⁸⁶, and negatively impact PLC γ 2 activation upon BCR stimulation⁸⁷. While certain SH2 mutants are correlated with a decrease in protein stability in XLA patients, others abrogate Btk activation without a clear molecular explanation (e.g. K374N and H364D)^{88,89}.

Approximately half of missense XLA mutations are located in the catalytic core, most frequently in the N-lobe where they typically disturb ATP or substrate binding⁸². X-ray structures of the KD suggest that substitution of highly conserved G414 located right on top of the ATP-site to a residue with a larger side chain (e.g G414R) dramatically limits the

space necessary to accommodate the ATP, while the mutation W563L impacts peptide substrate binding^{90,91}. Moreover, C-lobe mutations likely affect the regulatory spine, substitute residues critical for kinase activation (e.g. Y551), as well as possible impact domain stability⁹⁰.

Btk mutations play a complex role in XLA pathogenesis – they can impact the catalytic activity but also kinase-independent functions of Btk. It has been reported that a few mutations on the SH2 domain (e.g. L369F and R372G) can abolish Btk-mediated calcium response in cells without significantly affecting kinase phosphorylation⁹². However, how Btk function as a scaffold protein during B-cell development remains yet unclear⁹³.

1.3.1 Btk is an important target in multiple human diseases

Integration of genetic and functional approaches has recently revealed common molecular traits underneath B-cell malignancies phenotypically heterogeneous. For example, ABC DLBCL and a second subtype originated in the germinal center (GCB DLBCL) respond differently to chemotherapy and target agents. The genetic approach identified a pool of mutations in certain subtypes that explained the disease response to the therapies, such as the co-existence of gain-of-function mutations on CD79 β and MYD88 that promote chronic activation of BCR^{52,94}. Interestingly, synthetic lethality screening uncovered a cooperative pathway between BCR and MYD88 to sustain the oncogenic activation of NF- κ B that sustains tumor growth^{95,96}. These studies uncovered new genetic subtypes and provided a rational basis for precision-medicine strategies for targeted therapy.

Due to its essential role in BCR signaling and B-cell viability, the Btk kinase is an attractive target for therapeutic intervention particularly in cancer and autoimmune disorders. In addition to its essential role in BCR signaling^{97,98}, Btk is also a key mediator for pro-inflammatory cytokines production such as TNF α and IL-6 in response to the Fc receptor (FcR) signaling in macrophages⁹⁹, neutrophils and mast cells. This latter observation suggests that Btk inhibition could decrease inflammatory manifestations in RA, systemic lupus erythematosus, and multiple sclerosis¹⁰⁰. Furthermore, the apparent role of Btk in modulating tumor-induced immune tolerance by acting over tumor-infiltrating cells and the release of immunosuppressive cytokines imply that Btk inhibition could also have clinical benefit in solid tumors¹⁰¹.

Although a few pan-kinase inhibitors were found to bind and inhibit Btk, such as LFM-A13^{102,103} and dasatinib¹⁰⁴, they lacked the desired selectivity required for Btk targeted therapies. Novel generation more Btk-selective small-molecule inhibitors, including several currently under clinical development, have achieved an acceptable selectivity and promising clinical benefits particularly in B-cell malignancies and autoimmune diseases (Table 1). Currently, Btk inhibition is achieved by ATP-competitive small-molecule inhibitors that bind the kinase reversibly or irreversibly depending on the inhibitor type. All three approved Btk inhibitors covalently bind to an exposed cysteine (C481) within the active site nearby the ATP-binding pocket, and achieve irreversible inhibition allied to a satisfactory kinome selectivity, as only 10 other kinases contain cysteine at a homologous position¹⁰⁵.

Table 1 – Btk inhibitors approved and under clinical development.

Small-molecule	Class	Status	Condition	Reference
Dasatinib*	Reversible	First approval in 2006	CML, ALL	106
Ibrutinib	Irreversible	First approval in 2013	MCL, CLL, MZL, WM, GvHD	107
Acalabrutinib	Irreversible	First approval in 2017	MCL, CLL	108
Zanubrutinib	Irreversible	Approved in 2019	MCL	109
Tirabrutinib	Irreversible	CT II	WM	110
Fenebrutinib	Reversible	CT II	RA	111
Vecabrutinib	Reversible	CT II	CLL, NHL	112
ARQ-531	Reversible	CT I	CLL	113
LOXO-305	Reversible	CT I	CLL, MCL, WM	114

* Dasatinib has only been used in pre-clinical models as a Btk inhibitor.

The first-in-class irreversible Btk inhibitor was ibrutinib (PCI-32765, Imbruvica, Janssen)^{107,115}, currently the first-line oral drug for mantle cell lymphoma (MCL), chronic lymphocytic leukemia (CLL), graft versus host disease (GvHD), and Waldenstrom's macroglobulinemia (WM). Ibrutinib has shown an impressive response in the majority of CLL patients and tolerable side effects in comparison with the previous chlorambucil-based regimens (RESONATE-2 study reports a PFS of 70% after 5 years compared to 12% from the chlorambucil arm¹¹⁶). Btk inhibition has also shown consistent benefits in CLL patients when compared to anti-CD20 treatments such as ofatumumab¹¹⁷. Ongoing clinical trials aim to assess the clinical benefit of ibrutinib particularly in CLL patients with del(17p13.1) associated with poorer prognosis¹¹⁸ and other genetic subgroups.

Although generally well-tolerated, follow-up studies reported an increase in life-threatening events associated with the continuous use of ibrutinib. Atrial fibrillation has been detected in a significant percentage of patients (6 to 16%) and imposes unique challenges on clinical management due to the inherent risk of bleeding¹¹⁹⁻¹²¹. Broad-spectrum kinome profiling of ibrutinib identified few homologous active-site-cysteine-containing kinases, including Itk, Tec, Hck, and EGFR^{122,123}, as well as transient inhibition of other kinases. These off-targets are believed to contribute to ibrutinib toxicity as they play a role in platelet activation (Src members¹²⁴), platelet aggregation^{125,126}, and Btk/Tec mediating cardiac stress via PI3K signaling¹²⁷. The validation of Btk as a critical target to B-cell malignancies encourages the development of alternative yet more selective Btk inhibitors.

The second-generation drug acalabrutinib (ACP-196, Calquence, AstraZeneca) was designed to be a potent Btk-selective irreversible inhibitor with minimized off-target activity compared to ibrutinib¹²⁸. Acalabrutinib shows indeed an improved selective spectrum with virtually no inhibition of Tec, Itk, EGFR and Src family of kinases^{108,129}. The drug was FDA-approved in 2017 as a second-line treatment for relapsed MCL and in 2019 as monotherapy for CLL. A remarkable ORR of 95% in the acalabrutinib arm in relapsed CLL patients was accompanied by the absence of cardiac toxicity and major bleeding events^{130,131}. Ongoing clinical studies support an improved safety profile of acalabrutinib compared to ibrutinib and 100% activity in CLL patients with del(17p13.1) background¹³⁰, which will probably become the best-in-class treatment for B-cell malignancies.

In November 2019, the new oral Btk inhibitor zanubrutinib (BGB-3111, Brukinsa, BeiGene) received accelerated approval for MCL patients who received at least one prior therapy. Similar to ibrutinib and acalabrutinib, zanubrutinib irreversibly inhibits Btk^{109,132}. Two single-arm clinical trials of zanubrutinib demonstrated an excellent efficacy with an ORR of 84% with a median response of 18.5-19.5 months before MCL progresses¹³³. Zanubrutinib has an improved selectivity towards Btk showing minimal off-target activity on Tec, Itk, Lck, EGFR, and other kinases *in vitro*¹³⁴ which translates to a promising safety profile – although it did not reach superiority on its primary endpoint compared to ibrutinib in WM (ASPEN trial, NCT03053440), only 2% occurrence of atrial fibrillation was observed in the zanubrutinib arm compared to 15.3% in patients receiving ibrutinib. Zanubrutinib alone and associated with anti-CD20 therapy are currently being evaluated for other B-cell malignancies, including WM, both treatment-naïve and refractory MCL and CLL, and DLBCL.

No Btk-targeted therapy has yet been approved for autoimmune diseases. Btk inhibition is particularly attractive in RA as B-cells play a dual-role in mediating inflammation via a decrease of humoral response and cytokines production^{99,135}. However, covalently bound drugs impose certain safety concerns that are acceptable for terminal illness but not for chronic conditions. Interestingly, ibrutinib demonstrated efficacy in an RA murine model¹³⁶ but later patient trials reported the emergence of arthralgia at the early phase of treatment. The etiology behind this paradoxical observation is unknown but possibly linked to ibrutinib off-targets as the frequency of arthralgia is reduced in patients receiving acalabrutinib¹³⁰. The clinical management using anti-inflammatory agents is not advised due to the risk of bleeding events, and thus none of the approved Btk inhibitors has been considered safe for autoimmune conditions.

Reversible inhibition of Btk emerged as an alternative strategy particularly attractive to autoimmune disorders. The compound CGI1746 is a highly selective potent Btk inhibitor that, in contrast to other previously described molecules, reversibly binds to the ATP-site and stabilizes the inactive kinase conformation. CGI1746 efficiently inhibits the inflammatory response in arthritis⁹⁹ – improvement of PK properties led to the development of fenebrutinib (GDC-0853¹¹¹), the only reversible Btk inhibitor that reached an ongoing phase II for RA (NCT02983227). If succeeded, this molecule will be the first candidate from this series to reach the market.

1.3.2 Drug resistance: a drawback of Btk targeted inhibition

Btk inhibition revolutionized the treatment of B-cell malignancies. However, as frequently observed with other kinase inhibitors, drug resistance has been reported in a subset of patients under prolonged treatment with ibrutinib. This resistance mechanism correlates with more aggressive disease and involves Richter transformation at the early stage of the treatment (<18 months), acquisition of Btk C481S/T alone or with PLCγ2 mutations in multiple hotspots at the late stage of CLL progression (>15 months)^{137,138} and activation of alternative survival pathways. Mutation of Btk C481, commonly to serine or threonine, decreases drug affinity to ibrutinib and thus diminishes its efficacy at clinically achievable concentrations¹³⁹.

Alternative therapeutic approaches offered for relapsed patients are very limited and include stem cell transplantation or enrolment in clinical trials. Although no approved drug is able to circumvent ibrutinib-resistant Btk variants, new non-covalent inhibitors such as

vecabrutinib (SNS-062) have been designed to target the H3 pocket near the active site and to reversibly inhibit both wild-type (WT) and C481-mutated Btk¹⁴⁰. Vecabrutinib is currently under clinical development for CLL/NHL patients (NCT03037645), while other reversible Btk inhibitors such as fenebrutinib are promising candidates for patients harboring this resistant variant¹¹¹.

It is worth noting that all small-molecule drugs targeting Btk are ATP-competitive, including all reported inhibitors under development. The fact that mutations on the active site can affect the affinity to these drugs reveals a vulnerability in the current targeting approach. Thus, there is an unmet need for alternative molecules targeting distinct (i.e. allosteric) sites of the kinase that could positively impact the treatment of B-cell malignancies.

1.4 Btk activation

Following BCR engagement by antigen and receptor activation, Btk is recruited to the plasma membrane by PI3K, where it binds to phosphatidylinositol-3,4,5-triphosphate (PIP₃) via its PH domain¹⁴¹. Btk is subsequently phosphorylated at Y551 within the activation loop by Lck or Syk disposed near the activated BCR receptor^{142,143}. It is suggested that PH-mediated Btk dimerization (named Saraste dimer) also contributes to kinase activation via trans-autophosphorylation on its activation loop^{84,144} (Fig. 7). The presence of pY551 further increases kinase activity and promotes autophosphorylation on the Y223 within its SH3 domain. The importance of the pY223 remains debatable as it affects SH3 selectivity^{93,147,148} but shows no apparent influence on Btk catalytic activity¹⁴⁵ as also observed in other members of Tec family members (e.g. Itk¹⁴⁶). Several other autophosphorylation sites (e.g. Y375) have been mapped throughout the protein although the role of the great majority has not been established^{92,149}. In cooperation with BLNK¹⁵⁰, activated Btk propagates the BCR signal to its direct substrate PLCγ2 Y753/Y759 and Y1217 for further continuation of the signaling cascade^{151,152}.

In addition to its role in promoting substrate phosphorylation, Btk seems to also play kinase-independent roles as a scaffold protein in other signaling pathways including chemokine receptor, FcR signaling, and Toll-like receptors pathway¹⁵³. Although the molecular mechanism on how it participates as a scaffold on BCR and other signaling pathways is being investigated, non-catalytic domains of Btk likely play a critical role in this process.

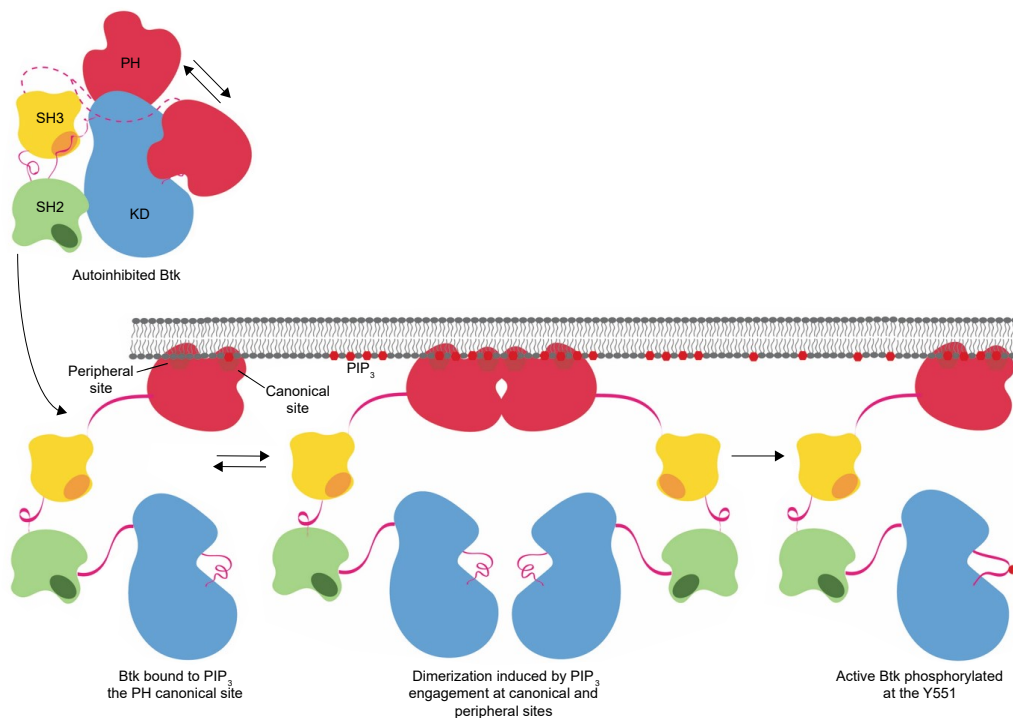


Figure 7 – Current model of Btk activation in B-cells.

Autoinhibited Btk is activated by binding to PIP₃ via the PH domain and translocation to the plasma membrane. PH-dependent dimerization triggered via inositol interaction (PIP₃ or IP₆) further activates the kinase via transautophosphorylation of the activation loop (Y551). Figure adapted from⁸.

1.5 Btk regulation and structural highlights

Although Btk shares structural similarities with Src and Abl families, some aspects of its intramolecular regulation are substantially different from these tyrosine kinases. No high-resolution structure of full-length Btk protein has yet been determined, which limits our current understanding on the interconnectivity of the different domains to regulate kinase activity. However, NMR and X-ray crystallographic structures are available for individual domains, as well as two multi-domains constructs (Table 2).

The crystal structures of Btk PH domain revealed a canonical inositol-binding site essential for the translocation of Btk to the plasma membrane upon PIP₃ binding. The flanking TH region comprises only a sequence of about 26 amino acids and contains several proline residues, thus commonly designated proline-rich repeats (PPR). While loss-of-function mutations that abrogate PIP₃ binding have been identified in XLA patients^{83,154,161}, the

synthetic mutation E41K increases affinity to lipid ligands, triggers constitutive activation, enhances tyrosine phosphorylation and transforms NIH3T3 fibroblasts¹⁶². In addition to its canonical role, the crystal structure of the PH-TH has also evoked a possible homodimerization surface⁸⁴, a feature not observed with other PH-containing proteins¹⁵⁵. Molecular simulation and biochemical studies have revealed an unexpected second site that binds IP₆ to induce PH homodimerization and potentially creates a positive feedback loop that activates the kinase via transautophosphorylation^{144,163}.

The structure of Btk SH3 domain has been solved by NMR spectroscopy and revealed a well-defined β -barrel structured containing a central groove that binds polyproline peptides (PXXP motif)¹⁵⁷. The Y223 residue near the ligand-binding surface undergoes autophosphorylation upon Btk activation¹⁴⁵ and affects SH3-interacting proteins such as WASP and Syk¹⁴⁷. Phosphorylation on Y223 is historically used as a molecular marker to access Btk activity. The apparent absence of SH3 mutations in XLA patients supports the experimental observation that Y223F mutation potentiates fibroblasts transformation and suggests that SH3 may play a negative regulatory role in Btk regulation¹⁴⁵.

The only NMR structure of Btk SH2 (2GE9) revealed a small-globular domain structurally well conserved compared to that of Src kinases, with a central β -sheet contain its phosphotyrosine-binding motif (FIVRD)¹⁵⁸. Btk SH2 directly interacts with BLNK scaffold protein from the BCR signalosome which plays an essential role in the spatial proximity required to activate PLC γ 2¹⁶⁴.

Finally, the first unphosphorylated structure of apo Btk KD (1K2P) revealed that its activation loop does not directly occlude the active site but adopts a non-inhibitory conformation similar to that of the active state of Src member Lck⁹⁰. Several other Btk structures bound of mutated form and bound to inhibitors including dasatinib and B43, revealed different activation loop and DFG positions that represent unique inactive states of the kinase^{165,166}. In contrast to Src kinases, the default inactive state of Btk KD is maintained by one isoleucine in the N-lobe that increases catalytic activity by shifting to a C-helix “in” position if mutated to I432L¹⁶⁶. Activation of the kinase requires activation loop phosphorylation at Y551 that then disrupts the E445/R544/Y551 interaction maintaining the C-helix in its “out” conformation, and induces the K430/E445 salt bridge that relocates the C-helix towards its active state⁹⁰.

Table 2 – Selected Btk high-resolution molecular structures available.

Domain (residues)	PBD	Description	Reference
PH-TH (3-170)	1B55, 1BTK	X-ray, WT and E41K mutant in complex with inositol	84, 154
PH-TH (2-170)	2Z0P	X-ray, bound to phosphatidylinositol	155
SH3 (212-275)	1AWW, 1AWX	NMR	156
SH3 (198-273)	1QLY	NMR, bound to proline-rich peptide	157
SH2 (270-387)	2GE9	NMR	158
SH2 (276-379)	6HTF	X-ray, bound to the rF10 repebody	This study
KD Y551E (396-659)	3K54	X-ray, active Btk bound to dasatinib	159
KD (396-659)	3GEN	X-ray, unphosphorylated Btk bound to B43 inhibitor	159
KD (382-659)	5P9J	X-ray, bound to ibrutinib	160
KD (393-659)	6J6M	X-ray, bound to zanubrutinib	109
KD (397-659)	1K2P	X-ray, unphosphorylated apo form	90
PH-TH-KD (4-168 and 384-658)	4Y93	X-ray, PH-TH tethered to KD, activation loop from Itk	144
SH3-SH2-KD (214-659)	4XI2	X-ray, domain-swapped murine Btk	144

1.5.1 Allosteric regulation of Btk

The first Btk multidomain structure reported in a study led by John Kuriyan revealed an autoinhibited SH3-SH2-KD core (PDB 4XI2) that adopts a similar conformation to Abl and Src kinases¹⁴⁴. A second multidomain X-ray structure containing the PH-TH domain directly tethered to the KD (PDB 4Y93) captured a preferential state where the PH stabilizes the C-helix in an inactive position¹⁴⁴. Although this interdomain interface may not represent its primary autoinhibitory contact in the context of the full-length protein, it provided a hint on the plausible interaction between the two domains. Together, these structures highlighted the molecular interactions within the SH3-SH2-KD module, presumed that its PH-TH domain further stabilizes the autoinhibited state, and were key to drawing the first autoinhibit model of full-length Btk (Fig. 8A).

More recently, two additional intramolecular contacts critical for Btk autoinhibition in the full-length context have been reported by the Andreotti group. Using a combination of NMR and HDX-MS, they demonstrated that the D656 located at the C-terminal extremity of the KD directly interacts with the SH2 pY-binding pocket and acts as a latch to further stabilize the Btk autoinhibited core¹⁶⁷, mimicking the Y527 found in c-Src (Fig. 3B)^{12,13}. Furthermore, they presented additional evidence that the PH-TH domain is a crucial component to

stabilize autoinhibited Btk by facing the activation loop surface and occluding the substrate-docking site. Although the PH-KD seems rather a dynamic interaction in their experimental setting compared to the previous static PH-TH-KD crystal structure, localized NMR spectra changes suggest that this interaction indeed promotes important allosteric shifts in regions critical for catalysis^{167,168}. This data provided additional understanding on Btk autoinhibition and particularly its unique regulatory mechanisms dependent on the PH-TH domain.

In contrast to its autoinhibitory apparatus, Btk adopts an extended arrangement upon binding to lipidic ligands or activation-mimicking mutations (e.g. Y42A/D63A). Its open conformation captured by SAXS and increased deuterium exchange throughout the protein seen by HDX-MS suggests that, upon activation, interdomain interactions become significantly loose and flexible^{167,169}. Notably, this is accompanied by the solvent-exposition of the activation segment due to the unlatch of PH-TH unit, which may contribute to the PH-mediated dimerization to further increase kinase activation^{167,168}. Importantly, its unique PPR region within the TH has been shown to compete with SH2-KD linker to the SH3, forcing Btk in a dynamic equilibrium between multiple conformation states, although predominantly autoinhibited in solution¹⁶⁷. These findings illustrated the complexity of the gradual kinase activation which plays a role in Btk and Tec family as opposed to a binary active/inactive shift as seen on other kinases.

Whereas the KD of Src kinases are by default in an active state and are negatively regulated by their non-catalytic domains (i.e. SH2 and SH3)¹³, few studies indicated a significantly lower catalytic activity of KD from Tec members which are in turn positively regulated by the presence of non-catalytic domains¹⁷⁰⁻¹⁷². Although the mechanism behind this dependence is not fully characterized, mutagenesis studies demonstrated that the conserved tryptophan residue within the WEI motif in SH2-KD linker (W395, Fig. 8B) caps the R-spine and forces Btk towards its active state, whereas the alanine side chain from the W395A mutant bends the C-helix to an “out” conformation^{92,173}; this is in contrast with the analogous mutation W260A in Src that positively regulates kinase and the SH2-dependent activation of Abl, which does not require direct participation of its SH2-KD linker^{15,17}. Therefore, the SH2-KD linker has distinct roles depending on the kinase and supports the hypothesis that non-catalytic domains somewhat participate in the Btk activation.

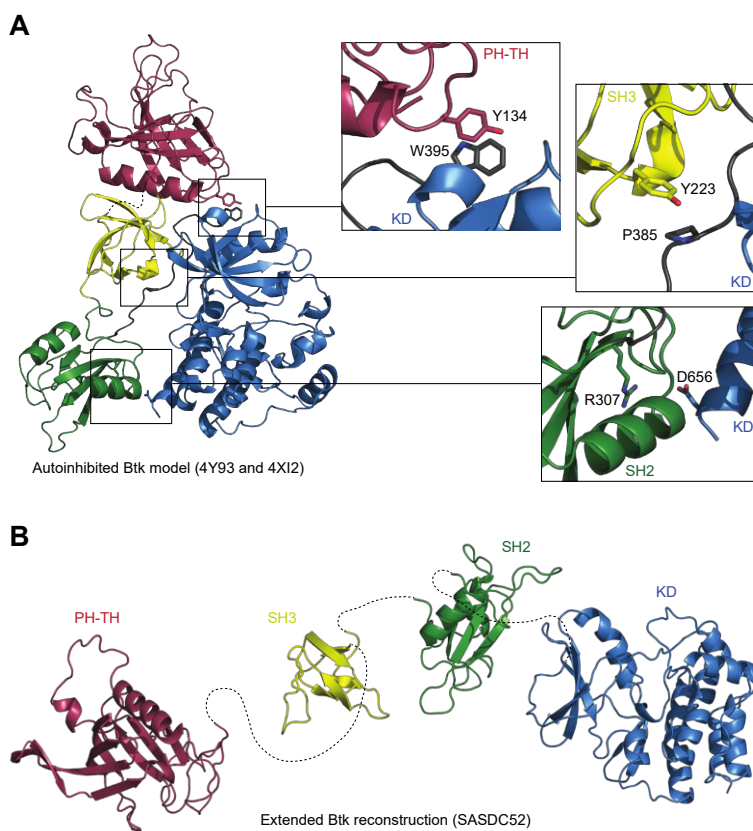


Figure 8 – Full-length Btk model in its autoinhibited and extended conformations.

A: Molecular model of autoinhibited Btk was generated by merging the PH-TH-KD and SH3-SH2-KD crystal structures (PDB 4Y93 and 4XI2, respectively¹⁴⁴). Three important intramolecular contacts and key residues are depicted in the detail on the right.

B: Release of these intramolecular constraints leads to an elongated Btk conformation with loose interdomain contacts as captured by SAXS (SASDC52¹⁶⁹).

2 AIMS

Btk is a major drug target for multiple B-cell malignancies and other B-cell-mediated diseases. Strikingly, the mechanism of action of the three Btk target therapies clinically available is identical - all covalently bind to the C481 within the ATP-site. The identification of resistant mutations that make patients refractory to these drugs leaves no alternative for Btk inhibition and demonstrates the urgent need for novel ways to achieve Btk inhibition via alternative mechanisms.

The intramolecular events that trigger Btk activation are far from being completely understood, particularly because no high-resolution multi-domain structures are available for the active Btk. Although the PH-dependent dimerization is important to kinase activation when interacting with the plasma membrane, this site has not yet been therapeutically explored. The contribution of other Btk domains to the kinase activation in the full-length context remains elusive.

Although few studies have provided a hint that the SH2-linker plays a positive role in Tec kinases activation¹⁷¹, and the SH2-linker seems partially exposed in the active conformation as seen by a subtle increase in the deuterium uptake in this region¹⁶⁷, they did not address the actual effect of the SH2 to trigger kinase activation. Moreover, the evidence that several XLA mutations in the SH2 domain are located away from its phosphotyrosine binding motif suggests that SH2 could also play a non-canonical role yet to be determined.

This work aims to characterize the role of the SH2 domain to the kinase activation, and, more importantly, develop a novel approach that could lead to allosterically inhibition of Btk. We hope to provide key evidence for the rational development of a new class of Btk inhibitors targeting an alternative site.

The major objectives of my thesis are the following:

- What is the actual contribution of the SH2 domain to the activation of Btk? Firstly, it is important to obtain highly-quality and active recombinant Btk proteins to recapitulate the contribution of non-catalytic domains to the kinase activation in a measurable approach.
- Can point mutations on the SH2 domain (e.g. XLA mutations) provide a rationale to understand the molecular contribution of SH2 to Btk activity? Explore a range of patient-derived and synthetic mutations as a tool to validate the hypothesis of the SH2-dependent activation of Btk. This can also offer the first molecular explanation of how certain mutations impact the functionality of Btk to trigger XLA in patients.
- Exploit critical Btk intramolecular interactions as an alternative targeting strategy to inhibit kinase activity. Depending on the nature of the interaction, the feasibility of small-molecule inhibitors can be extremely challenging. High-affinity protein binders offer an attractive and reliable approach to understand the structural impact of protein-protein interactions and to identify allosteric regions important for kinase function.
- Can Btk allosteric targeted inhibition have a therapeutic impact in the context of B-cell malignancies? Investigate whether allosteric inhibition can be employed as an alternative approach to target Btk kinase, and measure its effects on cell viability and BCR signaling in B-cell lymphomas.

3 RESULTS

Although recent studies have provided structural information on the autoinhibited Btk, little is known about the precise conformation controlling the activation of the kinase in the full-length context. While it has been known that the PH-dependent translocation to the plasma membrane is required for Btk activation (Fig. 7)^{144,168,174}, it remains unclear how the interplay with other domains participate in this activating mechanism.

3.1 Allosteric activation of Btk

3.1.1 Production and functional characterization of recombinant Btk proteins

In order to investigate the contributions of PIDs for Btk activation in a comparative approach, we first generated a series of human Btk constructs with serial domain truncations (Fig. 9A). In an initial attempt to obtain recombinant proteins, we set-up a system for baculovirus-mediated expression in *Spodoptera frugiperda* Sf9 cells, which provide a platform for relatively easy culture and fast production of the amounts of proteins at the required scale^{175,176}. However, the expression of Btk proteins in the cytoplasm of insect cells promoted pre-autophosphorylation particularly of the SH2-KD construct and that was insensitive to phosphatase treatments after protein purification (not shown).

To overcome this complication, we generated baculoviruses to allow co-expression of Btk constructs with *Yersinia pestis* outer phosphatase (YopH) which has high non-specific tyrosine phosphatase activity¹⁷⁷. A flag-tag added to YopH was used to assess its expression and confirmed excellent levels of the phosphatase in the insect cells (Fig. 9B). The proteins of interest were purified using a combination of nickel-affinity and size exclusion chromatography (SEC), followed by the removal of purification his-tag by TEV protease (Fig. 9C). It is worth noting that only homogenous proteins from monomeric peaks were employed in our experiments (Fig. 9D), which were confirmed to be unphosphorylated

3. RESULTS

by MS (Fig. 9E), and resulted in highly pure proteins with absence of phosphatase or other contaminants (Fig. 9F).

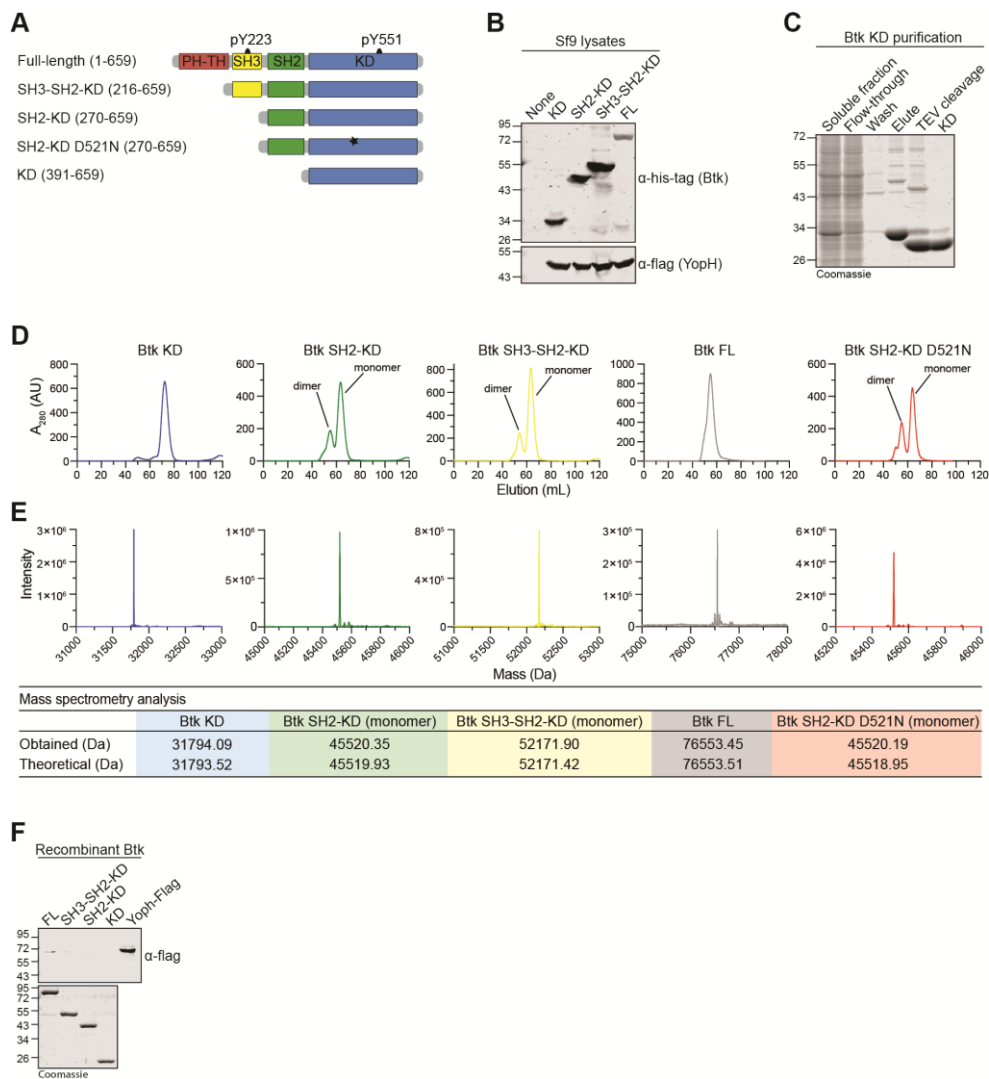


Figure 9 – Production of recombinant Btk proteins in insect cells.
A: Schematic overview of the recombinant Btk constructs used in our experiments. Domain boundaries and the two important phosphorylation sites (pY223 and pY551) are indicated. The D521N mutant was used as kinase-dead control.
B: Immunoblotting of the soluble fraction from insect cell expressing the dual-construct containing a flag-tagged YopH with each respective his-tagged Btk sequence.
C: Coomassie staining of the purification protocol from a representative Btk construct. All proteins were purified using an identical methodology.
D: SEC profile of recombinant Btk proteins.
E: MS spectra showed >95% of protein matching its native unphosphorylated state.
F: Coomassie staining of the recombinantly purified Btk proteins (top) and immunoblotting to detect flagged-YopH (bottom).

We then performed the functional characterization of recombinant Btk proteins, which can be readily assessed by their autophosphorylation capacity within the activation loop (Y551), SH3 domain (Y223), as well as other global autophosphorylation sites throughout the protein. Time course autophosphorylation *in vitro* assays in the presence of Mg^{2+} and ATP indicated that Btk KD alone has little activity (Fig. 10A-D), which is in agreement with previous studies reporting the very low catalytic activity of Tec kinases when compared to Src KD^{89,171}. In contrast, our assays revealed that the presence of SH2 domain (SH2-KD) increase Btk pY551 to approximately 3-fold compared to the KD alone. Btk proteins containing the SH3 and PH domains showed only a moderate pY551 phosphorylation capacity corroborating their inhibitory contribution in stabilizing Btk autoinhibition (Fig. 10A-D)^{144,167}. Assessment of total pY phosphorylation further demonstrated the significant positive effect of SH2 in kinase activity with a surprisingly near 20-fold increase in phosphorylation compared to the KD alone (Fig. 10E-G). This data indicates that purified proteins are functional *in vitro* and provide a reliable method to quantify the contribution of different domains to kinase activation. Importantly, this experiment revealed that the SH2-KD is the most catalytically active construct, and provides a first glimpse of the yet unknown mechanism of Btk activation dependent on its SH2 domain.

Autophosphorylation on multiple tyrosine residues can be employed to assess the catalytic activity of kinases. In Btk, phosphorylation on the activation loop is a hallmark of kinase activation, as well as its autophosphorylation Y223 residue within the SH3 domain. The substantial increase in total pY-phosphorylation seen in the SH2-KD construct corresponds to multiple tyrosine residues that we mapped using MS analysis of autophosphorylated recombinant protein (Table 3).

In an attempt to understand the kinetics of Y223 and Y551 phosphorylation *in vitro*, we assessed phosphorylation on these two sites overtime using an identical autophosphorylation assay for the constructs containing the SH3 domains (i.e SH3-SH2-KD and FL, Fig. 11A). Using this assay, we could also show that phosphorylation on Y223 preceded Y551 phosphorylation *in vitro* (Fig. 11B). This observation agrees with a previous model where autophosphorylation on Y223 happens in cis¹⁴⁵ that would in turn contribute to full kinase activation to further transphosphorylate other Btk molecules at the Y551 site.

3. RESULTS

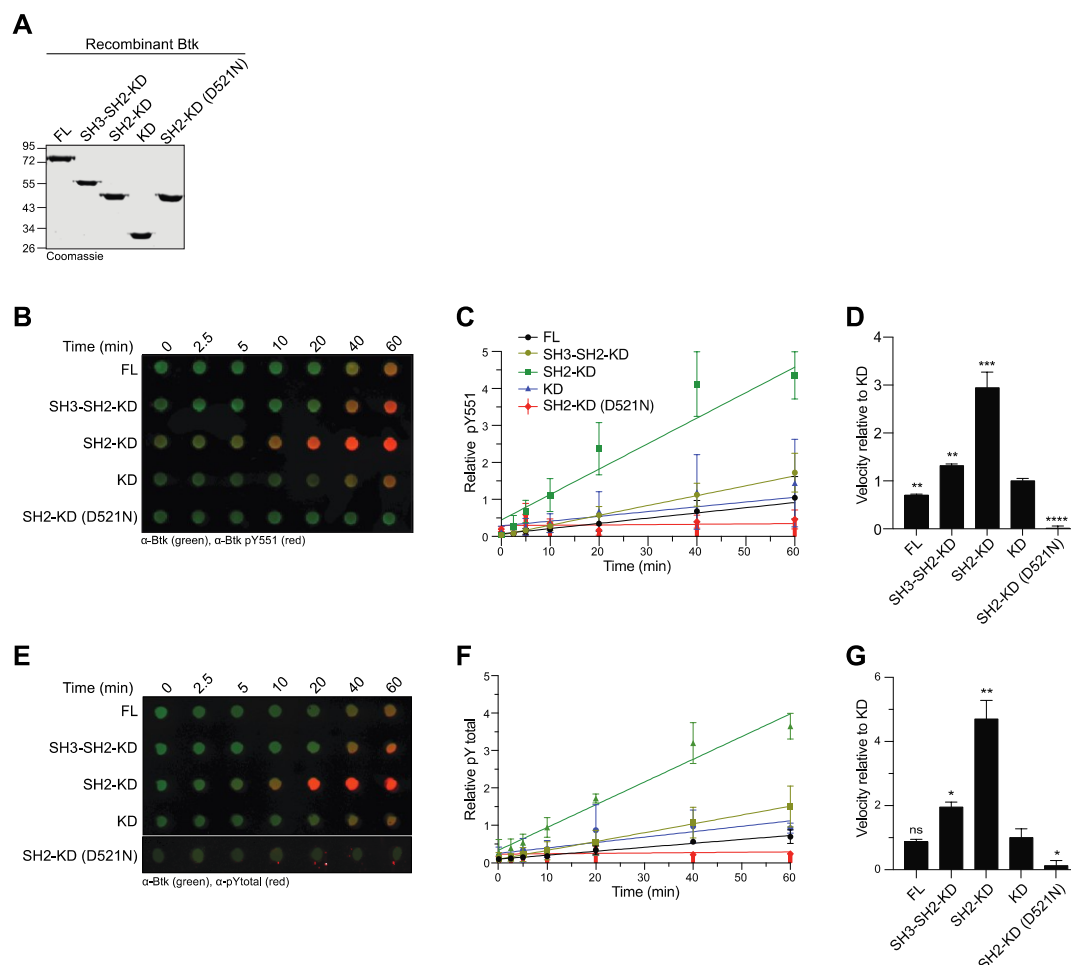


Figure 10 – Recombinant Btk proteins are functional and revealed a critical role of the SH2 domain in activating the kinase.

A: Coomassie representation of Btk autophosphorylation reactions.

B: Autophosphorylation assay was performed by incubating 1 μ M of recombinant Btk proteins with 1 mM ATP and 20 mM Mg^{2+} at room temperature. The levels of pY551 (red channel) and total Btk (green channel) were assessed via immunoblotting using a dot blot apparatus.

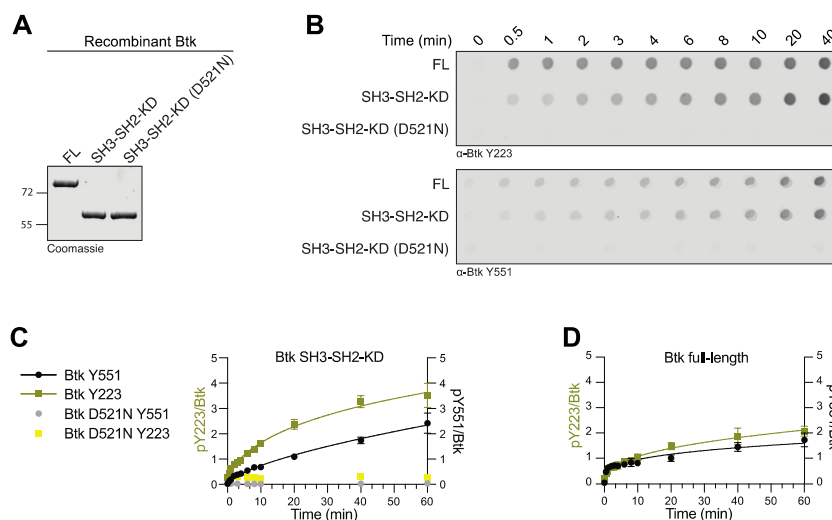
C: Quantitative analysis of Btk autophosphorylation kinetics from dot-blot experiments shown in B. The ratio of pY551 and total Btk protein is plotted over time. The mean \pm SD of at least three independent experiments are shown with calculated linear fits.

D: Relative pY551 autophosphorylation velocities relative to the Btk KD are shown. Data are means \pm SD of at least three independent experiments.

E-G: Autophosphorylation effect on total pY phosphorylation was performed as described above. P-values were calculated using an unpaired *t*-test.

Table 3 – *In vitro* autophosphorylation sites on the Btk SH2-KD protein.

Site	Peptide sequence	Location	Peptide count
Y279	SDSIEM \underline{Y} EWYSK	SH2	56
Y282	SDSIEM \underline{Y} EWYSK	SH2	56
Y315	AGKY \underline{T} VSVFAK	SH2	60
Y334	STGDPQGVIRHY \underline{V} VCSTPQSQYYLAEK	SH2	46
Y344	STGDPQGVIRHY \underline{V} VCSTPQSQYYLAEK	SH2	46
Y345	STGDPQGVIRHY \underline{V} VCSTPQSQYYLAEK	SH2	46
Y361	HLFSTIPELIN \underline{Y} HQHNSAGLISRLK	SH2	4
Y375	\underline{Y} PVSQQNK	SH2-KD linker	3
Y392	NAPSTAGLG \underline{Y} GSWEIDPK	SH2-KD linker	10
Y425	WRGQ \underline{Y} DVAIK	KD	10
Y461	LVQL \underline{Y} GVCTK	KD	2
Y511	DVCEAME \underline{Y} LESK	KD	4
Y545	VSDFGLSR \underline{Y} VLDDEYTSSVGSK	KD	37
Y551	VSDFGLSR \underline{Y} VLDDEYTSSVGSK	KD	37
Y571	FPVRWSPPEVLM \underline{Y} SK	KD	15
Y627	V \underline{Y} TIMYSCWHEK	KD	6
Y631	V \underline{Y} TIMYSCWHEK	KD	6
Total peptide count			444

**Figure 11 – *In vitro* kinetics of Btk Y223 vs. Y551 phosphorylation.**

A: Coomassie representation of Btk autophosphorylation reactions.

B: Autophosphorylation assay was performed as described above and levels of pY223 and pY551 assessed via immunoblotting.

C and D: Btk autophosphorylation kinetics showing Y223 or Y551 levels normalized to total Btk signal and plotted over time. The mean \pm SD of two technical replicates are shown with calculated non-linear fits.

To recapitulate the effect of PIDs into Btk activation in the physiologic context, myc-tagged Btk constructs were transiently expressed in HEK293 cells and Y551 and global pY phosphorylation verified using immunoblot (Fig. 12A). Again, KD alone showed undetectable phosphorylation compared to the Btk constructs containing SH2 and SH3-SH2 domains (Fig. 12B and C). The SH3-SH2-KD construct showed activity similar to the SH2-KD in cells, which is explained by its interaction with intracellular partners that opens-up the autoinhibited configuration when the PH domain is absent.

Finally, the full-length construct is slightly more active than KD alone in agreement with a reported study comparing full-length and KD phosphorylation¹⁷⁸, although it is evident that the presence of the PH domain further stabilizes the autoinhibited conformation also in cells (Fig. 12B and C). Together, this data provided evidence that the SH2 is critical and significantly increases kinase activation both *in vitro* and in the cellular context, and argues towards an allosteric effect of SH2 in analogy as seen with Abl and Fes kinases^{16,17}.

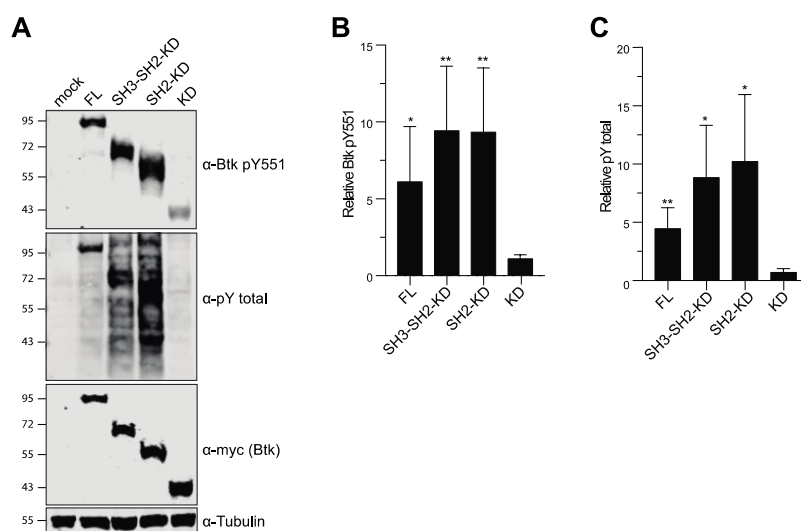


Figure 12 – The SH2 domain is sufficient to increase Btk activation in cells.

A: HEK293 cells were transiently transfected with the indicated Btk constructs containing an N-terminal 6x-Myc tag. Immunoblotting of total cell lysates was performed to assess Btk expression and activation.

B: Quantification of pY551 normalized to total Btk (Myc-Btk) from the immunoblot shown in A and relative to the KD.

C: Quantification of pY total was performed as described in B. Data shown are the mean \pm SD of three biological replicates. P-values were calculated using an unpaired *t*-test.

3.1.2 Uncovering the conformation of the active Btk SH2-KD using MD simulations and SAXS.

The linker connecting the Btk SH2 and KD consists of 22 residues and includes a proline (P385) which interacts with the SH3 to further stabilize the autoinhibited structure (Fig. 8A). Introduction of an SH3-binding peptide or P385A/T387A mutations in this linker region increases Btk activation consistent with the release of its closed conformation^{144,167}. However, the conformation of active Btk and contribution of the SH2-KD linker to this activating mechanism is unknown. In contrast to Fes, Abl, and Csk kinases where the SH2-KD units resembling active conformations could be crystallized and had revealed diverse intramolecular interfaces with the N-lobe^{16,17,179}, our attempts to crystalize Btk on its active form failed.

We next turned our focus to investigate the structural basis for this SH2-dependent allosteric activation of Btk using enhanced sampling molecular dynamic (MD) simulations. Scaled MD is an enhanced sampling MD simulation scheme that allows the sampling of μ s-ms time-scale events, such as domain-domain binding¹⁸⁰. This time frame is prohibitive using classical methods, such as equilibrium MD simulations. Using this approach to probe for domain-domain interactions in collaboration with Dal Peraro Lab (EPFL), we ran multiple replicas of scaled MD simulations for a total of $\sim 4 \mu$ s long trajectories and collected multiple binding events that provide molecular models of the Btk SH2-KD unit. Our MD data demonstrated that the SH2 may interact with the KD at different positions, notably at the back, top, and front of the KD N-lobe (Fig. 13A). The most representative clusters were located in the back of the KD, followed by a more elongated conformation with the SH2 placed on top of the N-lobe. A detailed view of the predicted SH2-KD interface suggested that different residues from the C-terminal portion of the SH2 possibly interact with the N-lobe region in this elongated conformation (Fig. 13B).

To provide an unbiased and independent experimental validation of the MD model for the active Btk SH2-KD unit, we carried out an extensive comparative analysis of multiple recombinant Btk proteins using small-angle X-ray scattering (SAXS). This method allows one to directly reconstruct low-resolution particle shapes *ab initio* and study conformational dynamics of multidomain proteins and complexes in solution¹⁸¹. Importantly, X-ray scattering of proteins in solution is very sensitive to the oligomeric state of the sample, which requires at least >95% protein in the monomeric form in the molecular size range of most kinases. To ensure that the quality of recombinant proteins was sufficient for SAXS

measurements, we performed SEC-multi-angle light scattering (MALS) of representative multidomain Btk proteins to attest the stability of its monomeric state in solution (Fig. 14A). SAXS data from Btk protein preparations confirmed the absence of protein aggregation and allowed a reliable estimation of molecular dimensions (Fig. 14B and C, Table 4). *Ab initio* shape reconstructions from SAXS show a clear globular structure with excellent agreement with the available KD and closed autoinhibited SH3-SH2-KD crystal structures and low protein flexibility as seen in the bell-shaped curves in the normalized Kratky plot (Fig. 14D).

In contrast, the SAXS data of the SH2-KD construct suggests a more elongated conformation with increased R_g and maximal particle dimension (D_{max}) in comparison to the KD and SH3-SH2-KD proteins (Fig. 14C). In addition to the increased particle dimension, the Kratky plot suggests that SH2-KD is more flexible compared to the globular KD and SH3-SH2-KD proteins (Fig. 14D, bottom). Importantly, the generated SH2-KD *ab initio* envelopes can be superimposed very well with the elongated MD models (e.g. C15, $\chi^2=1.50$) in which the SH2 domain is interacting with the N-lobe of the KD (Fig. 14D, top and 12E).

Finally, the full-length protein has been previously reported to adopt an equilibrium of conformations with a predominant compact and autoinhibited state in solution¹⁶⁷, whereas our SAXS data from the full-length protein captured a preferentially opened extended state (Fig. 14D) compatible with a previous report¹⁶⁹.

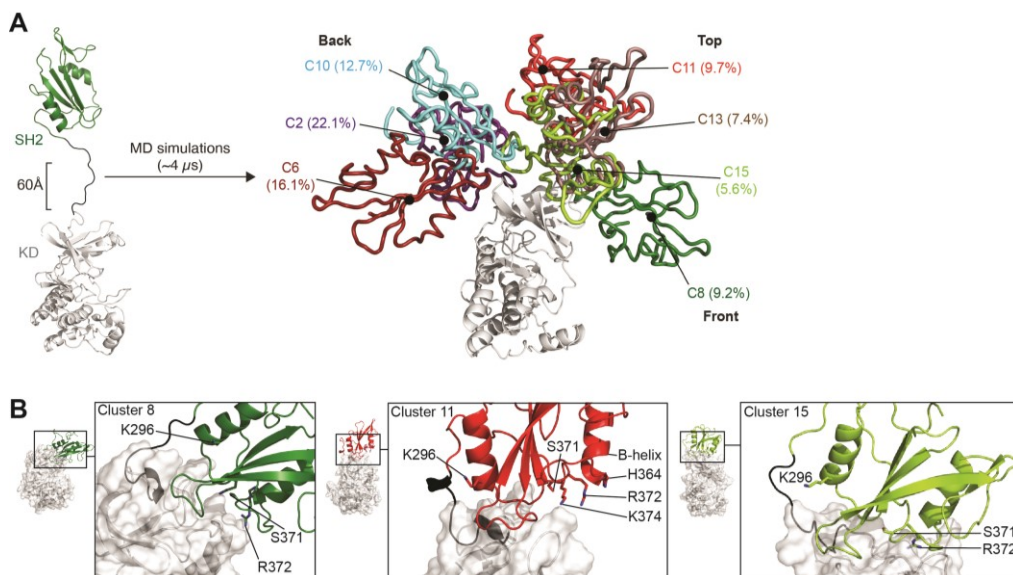


Figure 13 – Caption on the next page.

◀ Figure 13 – MD simulations suggest alternative conformations for the Btk SH2-KD protein.

A: Scaled MD simulations were carried out using Btk SH2 and KD crystal structures (PDB 6HTF and 1K2P, respectively) linked by the manual addition of the SH2 linker (left). The most populated clusters of the SH2 positions (several colors) relative to the KD (white) are shown with the cluster population with respect to the entire simulation time.

B: Detailed view of the SH2-KD interface from clusters 8, 11, and 15. A few SH2 residues nearby this interface are indicated as sticks.

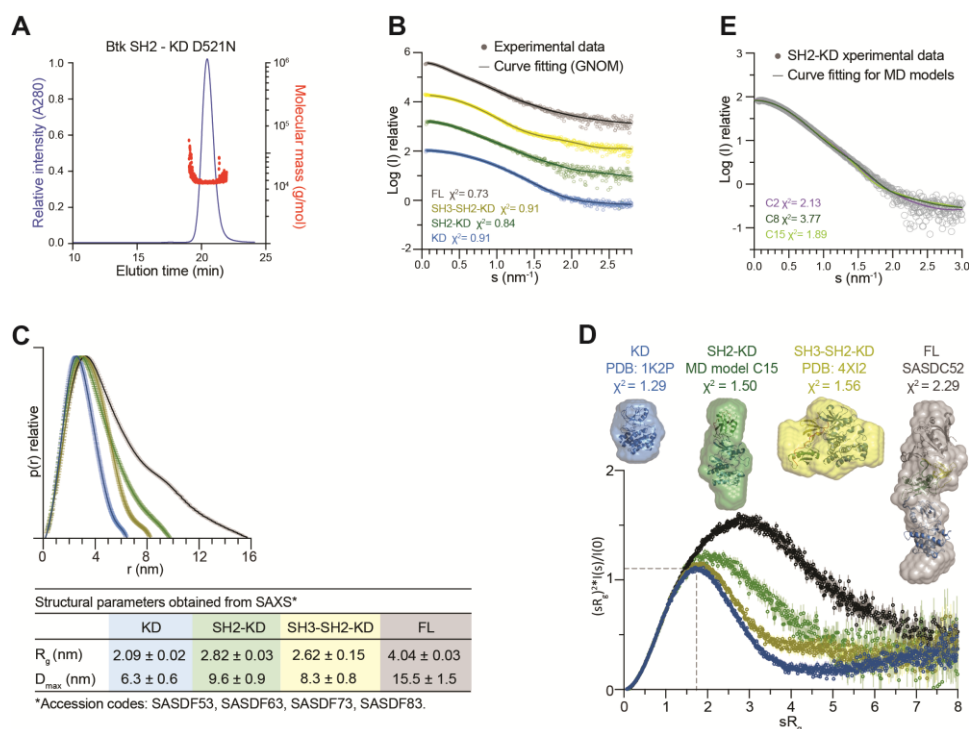


Figure 14 – Comparative SAXS analysis of recombinant WT Btk proteins.

A: Representative SEC-MALS analysis of purified Btk SH2-KD D521N (monomer=45.5 kDa) to confirm its homogenous state in solution.

B: Experimental SAXS data (dots) and GNOM fitting (line) for Btk proteins. Reported χ^2 represents the curve fitting against the experimental data. See Table 4 for details.

C: Maximal particle dimension (D_{max}) of Btk proteins and summary of structural parameters (R_g and $D_{max} \pm$ error) obtained from SAXS. The table summarizes the particle dimensions for the indicated constructs.

D: Dimensionless Kratky plot of Btk proteins. The grey dashed line represents a theoretical peak assuming an ideal Guinier region for a globular particle. *Ab initio* envelope reconstructions obtained from SAXS (surface representation) were superimposed on the crystal structures for Btk KD and SH3-SH2-KD (PDB 1K2P and 4XI2, respectively) are shown on top. For the SH2-KD protein, the structure of an elongated MD model with the best agreement with the experimental SAXS data is shown. FL protein shows an extended conformation as observed in a previously SAXS reconstruction (SASDC52).

E: Fitting of representative MD models against the SAXS data from the SH2-KD protein.

3. RESULTS

Table 4 – SAXS parameters of human Btk WT and mutants.

Data collection parameters							
Instrument	MD29 beamline, ESRF Grenoble - France						
Wavelength (Å)	0.9919						
q-range (nm ⁻¹)	0.03563 - 5						
Exposure time (sec)	5 (10 frames x 0.5 sec) or 1 (1 frame per sec for SEC-SAXS)						
Temperature (K)	290						
Protein	KD	SH2-KD	SH3-SH2-KD	Full-length	SH2-KD K296E	SH2-KD S371P	SH2-KD D521N
Measurement	batch	SEC-SAXS	batch	batch	SEC-SAXS	SEC-SAXS	batch
Concentration range (mg.ml ⁻¹)	0.9 – 4.2	100µl at 20.4	0.9 – 9.2	0.4 – 5.5	100µl at 30	100µl at 10.8	0.6 – 1.9
SASBDB identifier	SASDF53	SASDF63	SASDF73	SASDF83	N/A	N/A	N/A
Structural parameters							
R _g (nm) Guinier	2.09±0.02	2.832±0.3	2.62±0.15	4.04±0.03	2.92±0.04	2.64±0.23	2.83±0.07
I(0)* (cm ⁻¹) Guinier	24.86±0.036	85.5±0.12	44.28±0.056	60.24±0.16	171.59±0.15	8.66±0.075	20.71±0.044
R _g (nm) from P(r)	2.096±0.0003	2.88±0.0005	2.62±0.0006	4.34±0.0014	2.95±0.0003	2.70±0.03	2.9±0.05
D _{max} (nm)	6.75±0.67	9.6±0.95	8.3±0.83	15.5±1.2	10±1.0	8.5±0.86	10.3±1.2
Porod vol. (nm ³)	52.4	65.9	72.44	114.07	66.47	62.53	60.82
Dry vol. from sequence (nm ³)**	38.468	55.077	63.126	92.784	55.059	55.89	55.076
Molecular mass determination (kDa)							
Porod (V _p /~1.6)	24.9	47.6	40.9	76.1	48.5	39.1	42.7
SAXS MoW2	28.9	49.7	35.7	65.2	50.9	44.6	46.4
Bayesian inference	28.9	46.6	41.9	67.1	46.6	42.8	40.2
I(0) using V _c invariant	28.2	43.5	43.4	65.6	43.7	40.2	42.7
Theoretical***	31.8	45.5	52.2	76.5	45.5	45.5	45.5
Residues	274	396	452	664	396	396	396
Software list							
Primary data reduction	Automated pipeline at beamline						
Data processing	PRIMUS (ATSAS v.2.8.0)						
Ab initio analysis	DAMMIN and GASBOR						
Fitting	CRY SOL						
Model refinement	SREFLEX						
Flexibility analysis	EOM 2.0						
Model superimpositions	SASPy plugin for Pymol						
3D graphics images	Pymol (v.1.8.2.1)						

*I(0) for SEC-SAXS is not normalized to protein concentration. The structural parameters analyzed are independent of this value.

**<http://biotools.nubic.northwestern.edu/proteincalc.html>

***<http://web.expasy.org/>

SAXS provides an averaged scattering profile for the measured protein, which can be decomposed into an ensemble of conformations that agree with the experimental curve¹⁸². This is an interesting approach particularly for multidomain proteins with features of flexibility observed by an elongated Kratky tail as seen for the SH2-KD and full-length Btk (Fig. 14D). We next carried out a semi-quantitative flexibility analysis using the ensemble of optimization method (EOM 2.0)^{183,184} for the multidomain Btk constructs. EOM generates a large number of theoretical conformations (>10,000) using the KD and SH2 domain structures taking the native linker into account, compute the SAXS curves for all models, and selects a mixture of conformers that best agrees with the experimental SAXS data. Analysis of Btk SH2-KD revealed different conformers SH2-KD co-existing in solution (Fig. 15A) which partially includes extended conformations with the SH2 placed on top of the kinase (Fig. 15B). The extended conformation of the SH2-KD protein is independent of kinase activity, as also seen with a kinase-inactive mutant D521N (Fig. 15A) and consistently revealed by batch and also size exclusion chromatography coupled to SAXS (SEC-SAXS) measurements (data not shown).

We assessed the flexibility of SH3-SH2-KD and full-length proteins using an identical approach as a way to probe the reliability of this *in silico* method. Interestingly, EOM 2.0 analysis for Btk SH3-SH2-KD (Fig. 15C) and full-length (Fig. 15D) WT proteins is consistent with the models showing, respectively, a compact and a mixture of compact and elongated conformations in solution. Overall, our comparative SAXS analysis provided new insights in the conformation of Btk proteins in solution and, combined with the independent use of MD, supports an extended model for the SH2-KD where the SH2 is placed on top and predominantly interacts with the N-lobe of the KD.

3.1.3 Mapping of the Btk SH2-KD interaction revealed an interface critical for kinase activation

The SH2 position of the extended conformations generated by our MD simulations revealed a potential SH2-KD interface that could play a role in the SH2-dependent allosteric activation of the kinase. Interestingly, several mutated residues causing XLA in patients form a hotspot on the SH2 surface possibly interacting with the N-lobe (Fig. 16A and Fig. 13B). Five representative XLA mutations in this area (K296E, H364D, S371P, R372G, and K374N) and one control XLA mutation (R307G) in the pY binding pocket were selected to initially assess their effect on the domain stability and canonical function. Recombinant isolated SH2 domains containing a his-GST purification tag were expressed

in *E. coli* and purified using nickel affinity, followed by tag removal using TEV protease and size exclusion chromatography (Fig. 16B), resulting in highly pure and homogeneous native Btk SH2 domains (Fig. 16C-D).

Far-UV circular dichroism (CD) spectra and thermal shift analysis demonstrated that the XLA mutations did not impact significantly the Btk SH2 domain folding (Fig. 16E) and only mildly decreased melting temperature compared to the WT protein (Fig. 16F). These mutations also do not affect pY-binding in a fluorescence-polarization (FP) binding assay with a labeled pY-peptide. All XLA mutants bound the pY-peptide with similar affinities as the WT Btk SH2 domain, whereas the R307G control mutation in the pY binding pocket strongly impaired binding (Fig. 16G). Thus, the selected XLA mutations do not act by perturbing folding, stability, or pY-binding of the Btk SH2 domain.

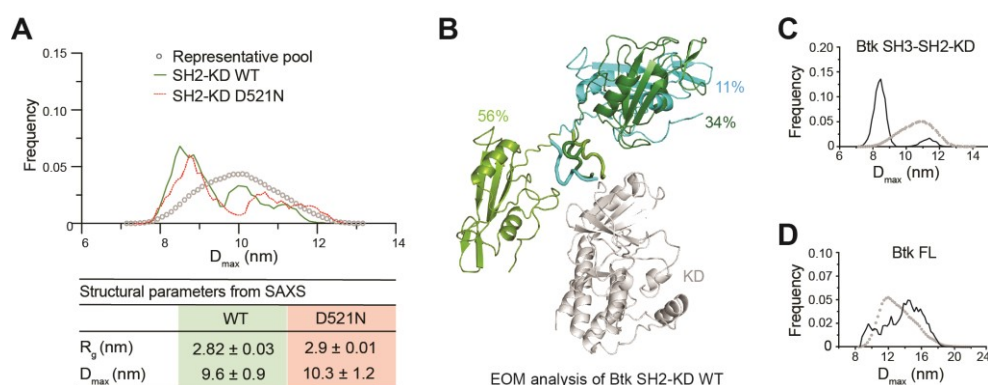


Figure 15 – Flexibility analysis of recombinant Btk proteins using SAXS.

A: EOM analysis of SH2-KD WT and D521N mutant showing a combination of different conformations contributing to the experimental SAXS scattering. On top, the maximal particle dimension (D_{max}) of selected conformers for each protein (lines) from a representative pool of theoretical conformations (dotted line). The table shows a summary of structural parameters obtained for WT and kinase-dead proteins.

B: Cartoon representation of the ensemble of the most populated SH2-KD conformations selected by EOM. The KD is represented in white, and selected SH2 conformers are colored. SH2-linker distance estimated by the algorithm is represented as ribbon.

C and D: EOM analysis of SH3-SH2-KD and full-length WT proteins.

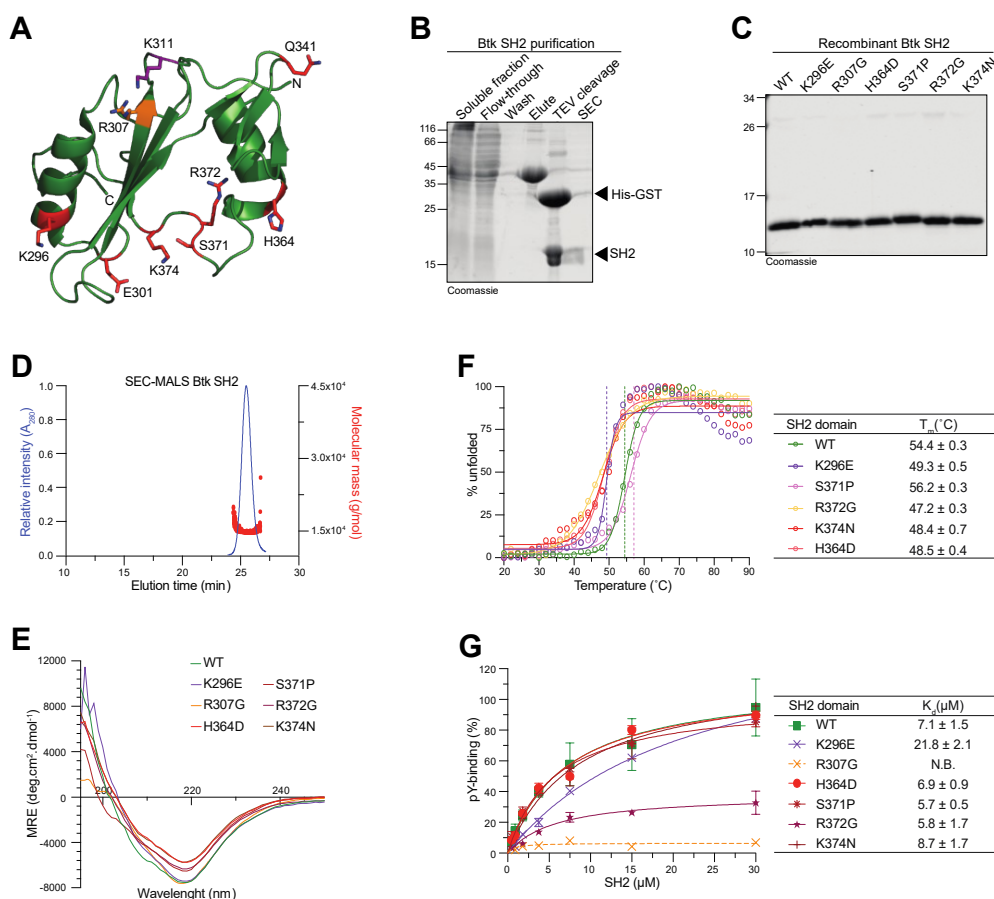


Figure 16 – A subset of XLA in the SH2 domain does not significantly affect domain stability and canonical function.

A: XLA-patient mutations (red) mapped onto the human Btk SH2 structure (PDB 2GE9). The residue R307 (orange) is part of the pY-binding motif (FIVRD). The residue K311 (magenta) is a non-XLA control mutation introduced for control facing the opposite surface. N- and C-terminal are indicated for reference.

B: Representative Coomassie staining of purification steps for recombinant Btk SH2 WT from *E. coli*. All Btk SH2 mutants were purified using an identical protocol.

C: Coomassie staining of recombinant WT and mutant isolated SH2 domains.

D: Representative SEC-MALS analysis of purified Btk SH2 domain WT (monomer=13.2 kDa). All SH2 domains were analyzed by SEC-MALS and found in the homogenous state in solution.

E: Averaged far-UV circular dichroism (CD) spectra of recombinant SH2 domains. Mean residue ellipticity (MRE) for each protein was calculated from three independent measurements.

F: Thermal shift assay (TSA) of recombinant Btk SH2 domains. Melting temperature (T_m) was calculated from two independent measurements.

G: Binding of a fluorescently labeled pY-peptide (ADNDpYIIPDP) to recombinant Btk SH2 domains. Indicated K_d values were obtained from at least two technical replicates. The errors indicated are the standard deviations from the curve fitting of the 1:1 binding model. Non-binding (N.B.)

In order to assess the effect of XLA mutations in the cellular context, they were introduced in the Btk SH2-kinase domain (SH2-KD) construct and expressed in HEK293 cells. Expression of WT SH2-KD resulted in robust activation loop phosphorylation (pY551) which contrasted to a strong decrease seen in mutated constructs (Fig. 17A). To evaluate the effect of these mutations on phosphorylation of Y223 within the Btk SH3 domain, which is a common readout for Btk activity, they were then introduced into the larger Btk construct spanning the SH3, SH2 and kinase domains (SH3-SH2-KD). The deleterious effect of an even larger set of XLA mutations in the Btk SH2 domain (Fig. 17 B) could be corroborated in the SH3-SH2-KD construct with a strong impairment of both pY551 (Fig. 17B), pY223 (Fig. 17C), and total pY (Fig. 17D). Importantly, a control non-XLA mutation (K311E) on the opposite side of the SH2 domain (Fig. 16 A) did not affect Btk phosphorylation. Finally, in the full-length context, the effect of XLA mutations was negligible as this construct is autoinhibited (Fig. 17E).

To further probe the validity of the proposed SH2-KD active model, we took advantage of XLA mutations at different positions on the SH2 surface. Based on our SH2-KD model, S371 is part of the interface with the N-lobe, while K296 is solvent-exposed and does not directly participate in this interdomain interaction (Fig. 13B). These recombinant Btk SH2-KD mutants were expressed and purified from insect cells and also resulted in highly pure unphosphorylated protein (Fig. 18A and B). Autophosphorylation *in vitro* assays showed a decrease in S371P autophosphorylation kinetic on Y551 compared to the WT protein (Fig. 18C-E). Interestingly, the K296E mutant protein showed a mild increase in Y551 autophosphorylation compared to WT, implying that this mutation may disfavor a more inactive conformation of the SH2-KD protein (Fig. 18C-E). In addition, total pY phosphorylation of the S371P protein was also impaired and further supports the lower autophosphorylation capacity observed for this construct (Fig. 18F-H).

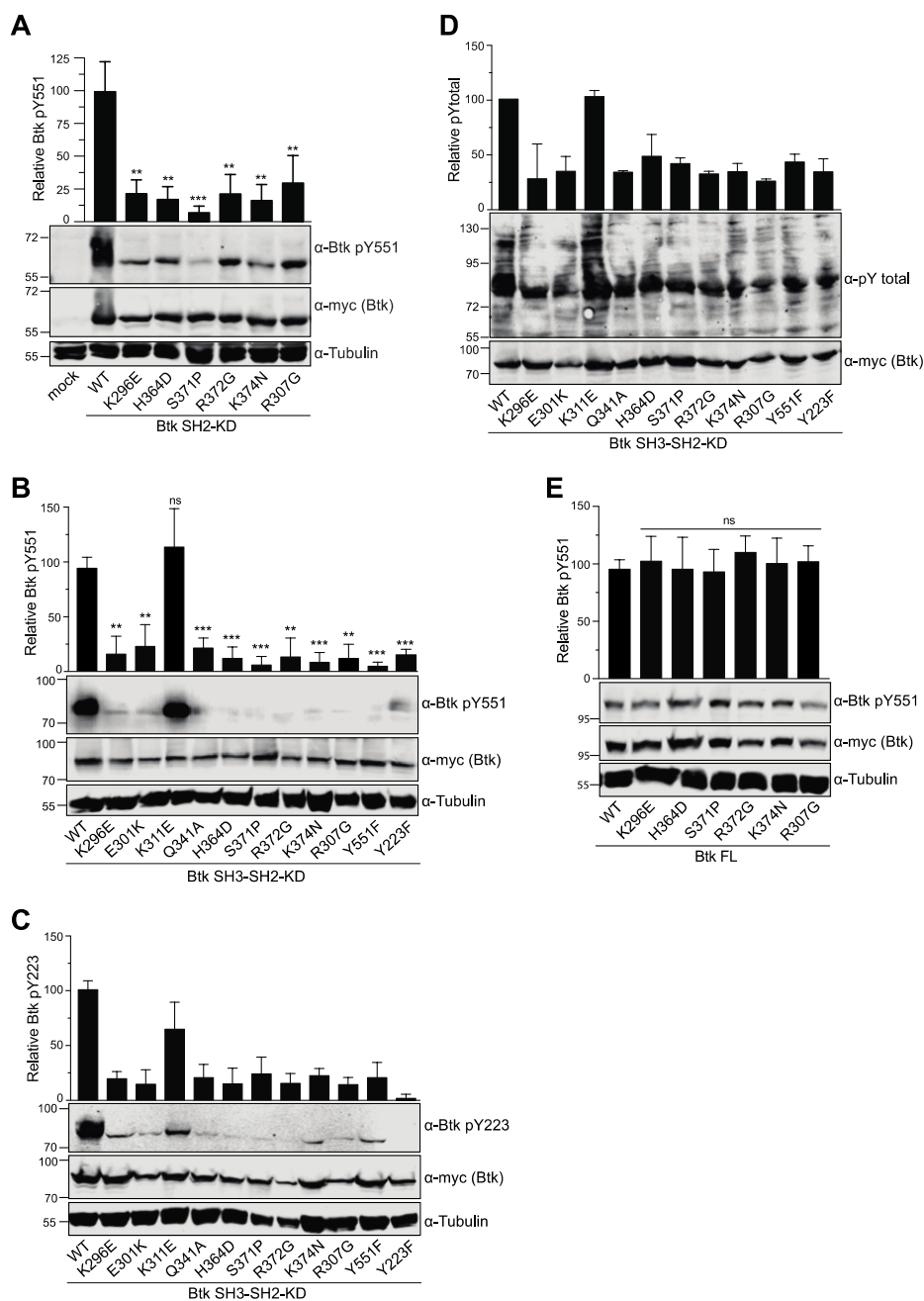


Figure 17 – XLA mutations in the SH2 domain impair Btk activity.

A-E: HEK293 cells were transiently transfected with Btk constructs, phosphorylation on sites Y551, pY223 or pY total assessed by immunoblotting, and relative phosphorylation normalized to total Btk (myc-Btk) expression. Tubulin was used as loading control. Data shown in A, B and E are the mean \pm SD of three biological replicates, while data shown in C, D are the mean \pm SD of two technical replicates. P-values were calculated against the WT using an unpaired *t*-test.

3.1.4 Mutation on the Btk SH2-KD interface affects the conformation of the active unit

To provide additional insights on how these mutations affect SH2-KD conformation, we carried out SAXS measurements of the recombinant proteins, and assessed protein flexibility using the EOM to be compared to the Btk SH2-KD WT (Fig. 19A). Whereas the kinase-dead D521N and K296E SH2-KD proteins indicate similar overall molecular dimensions (R_g and D_{max}) and flexibility as for the WT protein, the S371P mutant showed a shift towards more compact conformation, with a decrease in R_g and D_{max} , (Fig. 19B and C). Importantly, measurements of the SH2-KD S371P protein using the purified protein in batch mode as well as SEC-SAXS showed similar features (data not shown). The compact conformation adopted by the SH2-KD S371P is consistent with the decrease in autophosphorylation *in vitro* (Fig. 18D).

As an extra effort to further challenge our findings, we engineered non-XLA point mutations in the N-lobe that were structurally predicted to disrupt the allosteric SH2-KD interface and tested their effect on Btk activation in HEK293 cells. In general, these mutations had a mildly negative impact on Btk phosphorylation (Fig. 20A-C). Interestingly, the L405E mutation in the N-lobe resulted in a strong over-activation of SH2-KD in cells (Fig. 20C). This gain-of-function phenotype is compatible with an additional salt bridge with positively charged residues in the SH2 domain that may cause stabilization of the SH2-KD interface (Fig. 20D). Therefore, our model of the active Btk SH2-KD unit suggests that interaction between the SH2 and the N-lobe creates an interface that has a critical impact on Btk activation. Noteworthy, the Btk SH2-KD interaction seems less sturdy as in Abl and Fes, where a more stable interaction was captured in the crystalized structures of active Abl and Fes kinases^{16,17}

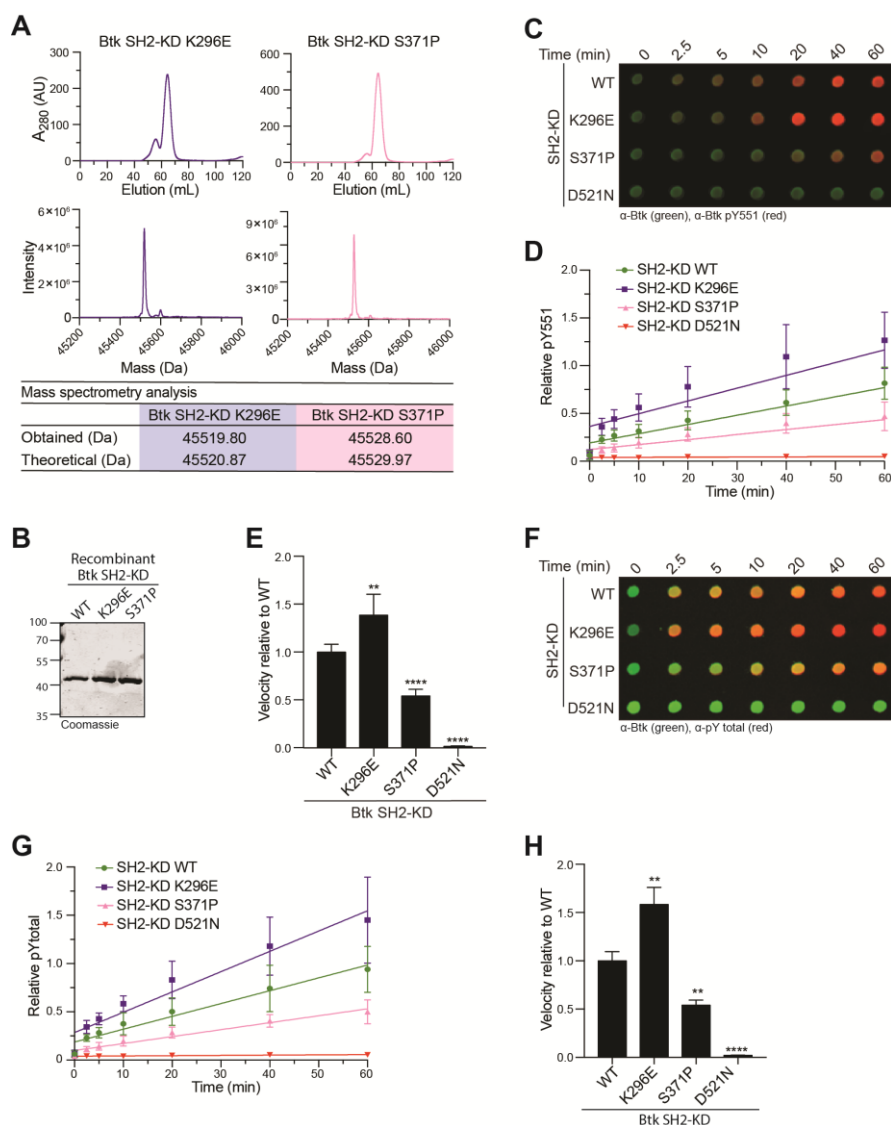


Figure 18 – An XLA mutation facing the predicted Btk SH2-KD interface negatively impact kinase activity.

A: SEC of recombinant mutant Btk purified from Sf9 cells (top). All samples were subjected to MS analysis for confirmation of protein identity and unphosphorylated state (>95% for all samples).

B: Coomassie staining of recombinant untagged SH2-KD proteins purified from Sf9 cells.

C: Autophosphorylation assay performed as described and levels of pY551 (red channel) and total Btk (green channel) assessed using immunoblotting in a dot blot apparatus.

D: Quantitative analysis of Btk autophosphorylation kinetics from dot-blot experiments shown in C. The ratio of pY551 and total Btk protein is plotted over time. Means \pm SD of three independent experiments are shown. The slopes (relative velocities) of linear fits were calculated.

E: Autophosphorylation velocities relative to the Btk KD. Data show the mean \pm SD of three independent experiments. P values relative to WT were calculated using an unpaired *t*-test.

F-H: Autophosphorylation assay showing the analysis of total pY phosphorylation.

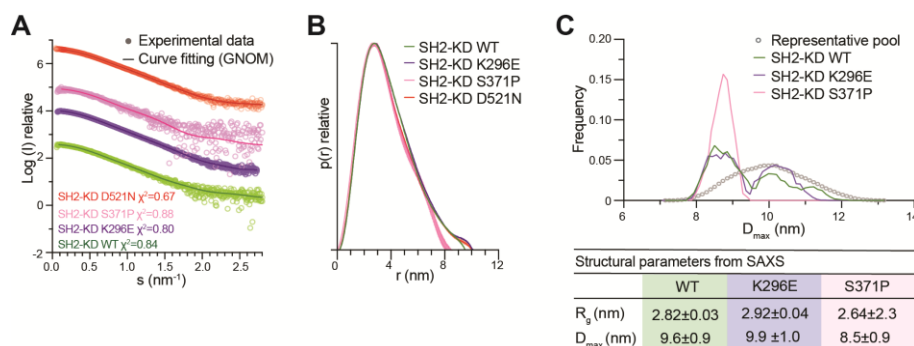


Figure 19 – A mutation in the SH2-KD interface forces Btk towards a more compact conformation.

A: Experimental SEC-SAXS data of mutant Btk proteins. See Table 4 for details.

B: Maximal particle dimension (D_{max}) of mutant Btk proteins.

C: EOM analysis of SH2-KD mutants compared to WT protein.

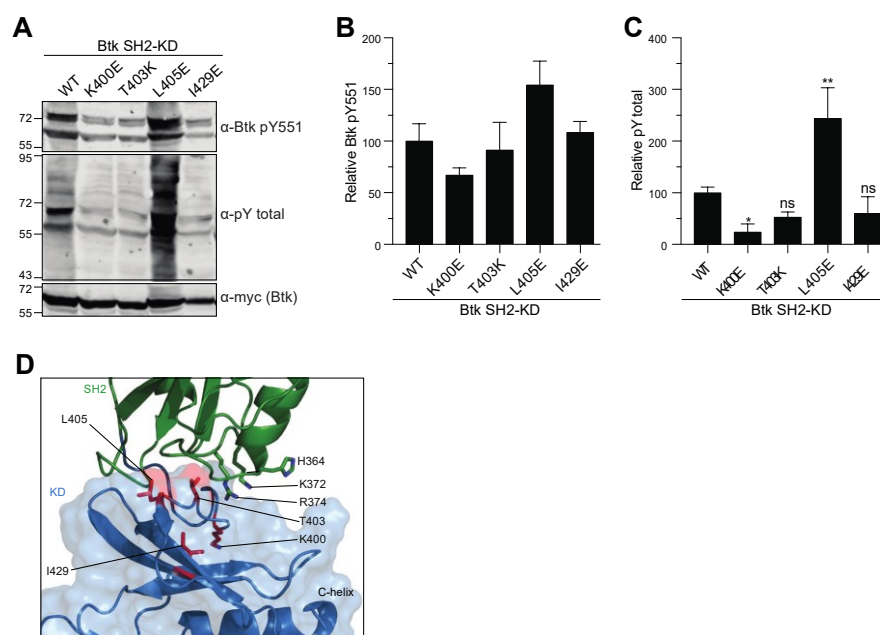


Figure 20 – Mutation L405E in the N-lobe of Btk increases kinase activation.

A-C: HEK293 cells were transiently transfected with Btk constructs, phosphorylation on sites Y551 or pY total assessed by immunoblotting, and relative phosphorylation normalized to total Btk (myc-Btk) expression. Data are the mean \pm SD of two ($n=2$) and three technical ($n=3$) replicates, respectively. P-values relative to Btk WT were calculated using an unpaired t -test.

D: N-lobe residues mutated are shown as red sticks in a representative Btk SH2-KD structure obtained in the MD simulation (model C15).

3.2 Targeting the Btk SH2-KD interface

Allosteric interactions provide unique targeting opportunities in kinases and other proteins and may offer an attractive strategy for specific inhibition. The design of small-molecule inhibitors targeting protein-protein interactions is challenging. High-affinity protein binders can be designed against a wide variety of protein surfaces and are a feasible approach to investigate critical allosteric sites and validate as targets in multiple disease contexts.

In order to demonstrate the importance of the proposed allosteric interaction of the Btk SH2 domain with the kinase domain in regulating Btk activity, we developed a repebody binder protein able to bind human Btk SH2 domain in collaboration with Hak-Sung Kim group (KAIST). This engineered protein was selected from a pool of repebody scaffold with randomized LRRs, and affinity further increased using multiple cycles of affinity maturation. We received the repebody sequences and carried out its full structural and functional characterization using Btk proteins.

3.2.1 Production and functional characterization of repebodies.

The SH2-binding repebody (rF10) and a non-binding repebody scaffold (rNB) used as control were purified from *E.coli* (Fig. 21A and B) and resulted in stable high concentrations of recombinant proteins. Isothermal titration calorimetry (ITC) with rF10 and isolated Btk SH2 domain indicated an affinity of ~15 nM with a binding stoichiometry of 1:1 (Fig. 21C). Similar low nanomolar affinities were detected in all Btk constructs containing the SH2 domain SH2-KD, SH3-SH2-KD, and full-length Btk (Fig. 21D). Consistent with a high-affinity interaction, a stable 1:1 rF10-SH2 complex could be recovered by size-exclusion chromatography either in complex with the Btk SH2 domain alone (Fig. 21E), as well as the SH2-KD and full-length Btk proteins (data not shown). Importantly, to probe the specificity of rF10 repebody, the affinity of rF10 to SH2 domains from Lck and Abl kinases were verified using ITC, and demonstrated a >500-fold selectivity for the Btk SH2 domain (Fig. 22).

As other engineered SH2 binders, in particular monobodies^{33,34}, predominantly target the pY peptide binding site, we tested whether the rF10 repebody interferes with pY-peptide binding using an FP binding assay. Even in the presence of a 20-fold molar excess of rF10, no competition with pY-peptide binding was observed (Fig. 23). The observed increased

FP signal with increasing rF10 concentrations is consistent with the formation of a ternary complex (SH2-pY-peptide-rF10). Together, our data indicate that the rF10 binds to Btk SH2 with great affinity and does not interfere with the pY-binding, indicating that rF10 has a different binding epitope on the SH2 domain.

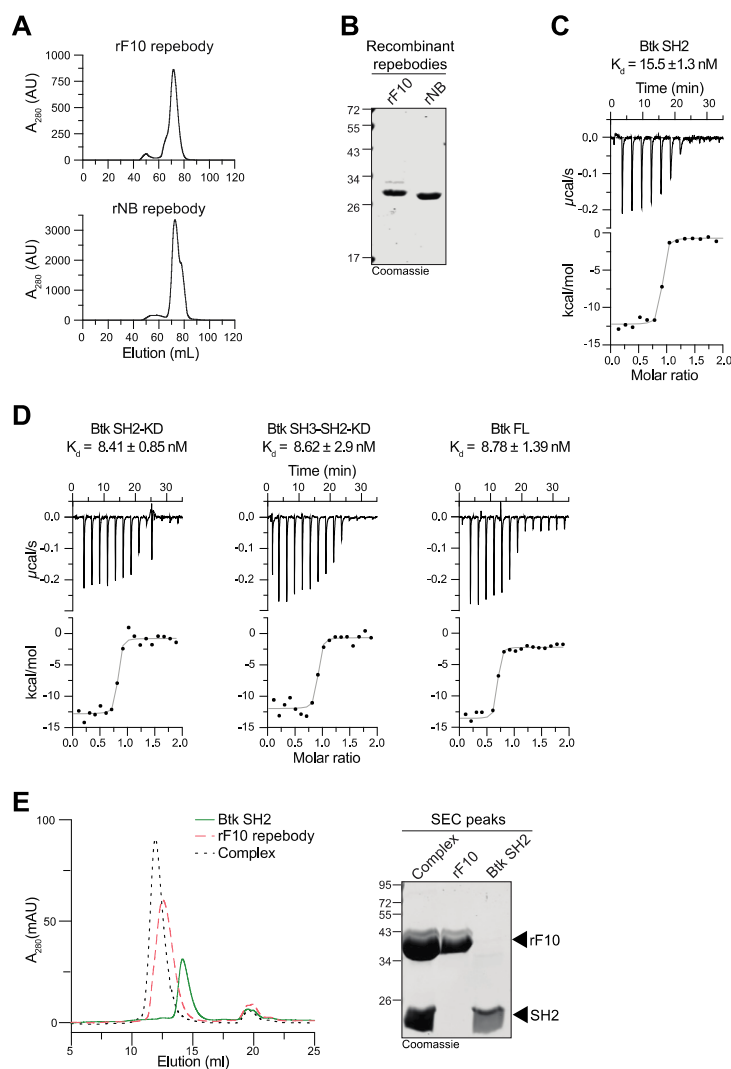


Figure 21 – rF10 repebody binds to Btk SH2 domain with great affinity.

A: SEC profile of purified rF10 and rNB control repebodies.

B: Coomassie staining of repebodies purified from *E. coli*.

C: Representative ITC experiment of rF10 and isolated Btk SH2 domain. The reported K_d is the mean \pm SD of three independent measurements.

D: Representative ITC experiment with indicated Btk constructs. The reported K_d is the mean \pm SD of two independent measurements.

E: Analytical SEC profile from Btk SH2 and rF10 alone superimposed with profile from the SH2-rF10 complex (left). Coomassie staining of representative peaks is shown on the right.

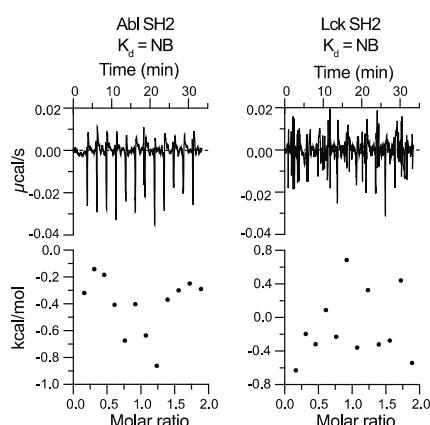


Figure 22 – rF10 repebody does not bind to SH2 domains of related kinases.

Representative ITC experiments using rF10 and indicated SH2 domains.

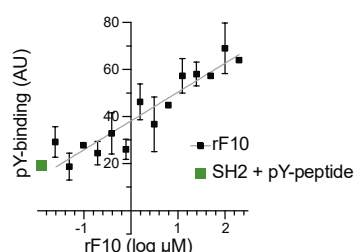


Figure 23 – rF10 repebody does not affect Btk SH2 pY-binding.

Binding-competition assay using a fluorescently labeled pY-peptide and recombinant Btk SH2 domain in the presence of various concentrations of rF10 repebody. Data are the mean \pm SD from three technical replicates.

3.2.2 The rF10-SH2 crystal structure

In order to identify the SH2 domain epitope where rF10 binds, we next solved the crystal structure of the Btk SH2-rF10 complex at 2.1 Å resolution (Table 5), which is the first crystal structure of the isolated human Btk SH2 domain (PDB 6HTF). The overall SH2 domain conformation is very similar to the previously published NMR structure of human Btk SH2 domain (PDB 2GE9), indicating that rF10 binding does not result in major conformational changes. Consistent with the ITC and pY binding assays, the rF10-SH2 crystal structure indicates that rF10 binds to the SH2 domain in a 1:1 interaction and the interaction does not involve the pY-binding groove (Fig. 24A and B). The residues within multiple LRR loops from the rF10 create a three-dimensional structure that interacts with the SH2 domain (Fig. 24A). rF10 binds to multiple residues from the SH2 domain BC loop (K322, S323, G325, and P327) and the C-terminus of the α -helix B (S366 and K374), and it buries a surface area of 2274 Å² (Fig. 24B). To further corroborate the rF10 interaction site, a recombinant SH2 containing the XLA mutation K374N in the interface between the SH2-rF10 showed a \sim 10-fold decreased affinity (Fig. 24C) compared to the WT SH2 domain.

Table 5 – X-ray parameters of the rF10-SH2 crystal structure (6HTF).

Data collection	
Space group	P 21 21 2
Cell dimensions	
<i>a</i> , <i>b</i> , <i>c</i> (Å)	145.53, 32.95, 80.63
α , β , γ (°)	90, 90, 90
Resolution (Å)	50 (2.1)*
<i>R</i> _{meas}	10.2 (81.1)
<i>I</i> / σ <i>I</i>	12.99 (1.95)
Completeness (%)	93.93 (84.43)
Redundancy	3.89 (3.90)
Refinement	
Resolution (Å)	2.1
No. reflections	22064
<i>R</i> _{work} / <i>R</i> _{free}	0.213 / 0.252
No. atoms	3041
Protein	2915
Water	126
Protein residues	362
<i>B</i> -factors	
Protein	40.75
Water	36.85
R.m.s. deviations	
Bond lengths (Å)	0.023
Bond angles (°)	1.44
Ramachandran analysis	
Favored regions	95.53%
Allowed regions	4.47%
Outliers	0

*Values in parentheses are for the highest-resolution shell.

3.2.3 Binding to rF10 abrogates the Btk SH2-KD interface.

Our next attempt was to verify whether binding to repebody abrogates the SH2-KD interaction which is critical for kinase activation. Superimposition of the Btk SH2-rF10 structure with a representative model of the active SH2-KD unit (MD model C15) revealed dramatic steric clashes of the KD and rF10 (Fig. 25A). The coincidental strong overlap of the rF10 binding epitope with the proposed Btk SH2-kinase interface led us to hypothesize that rF10 may abrogate the SH2-KD interaction and thereby act as an allosteric Btk

antagonist. To probe this hypothesis, we first performed a SAXS analysis of rF10 alone and in complex with several Btk constructs (Fig. 25B, Table 6). In line with our hypothesis, SAXS-based reconstructions of rF10-Btk complexes indicate that the conformation of SH2-KD is altered and the interdomain interface is disrupted. This observation encouraged us to further investigate the functional effects of the rF10 repebody on Btk activity and signaling *in vitro* and cells.

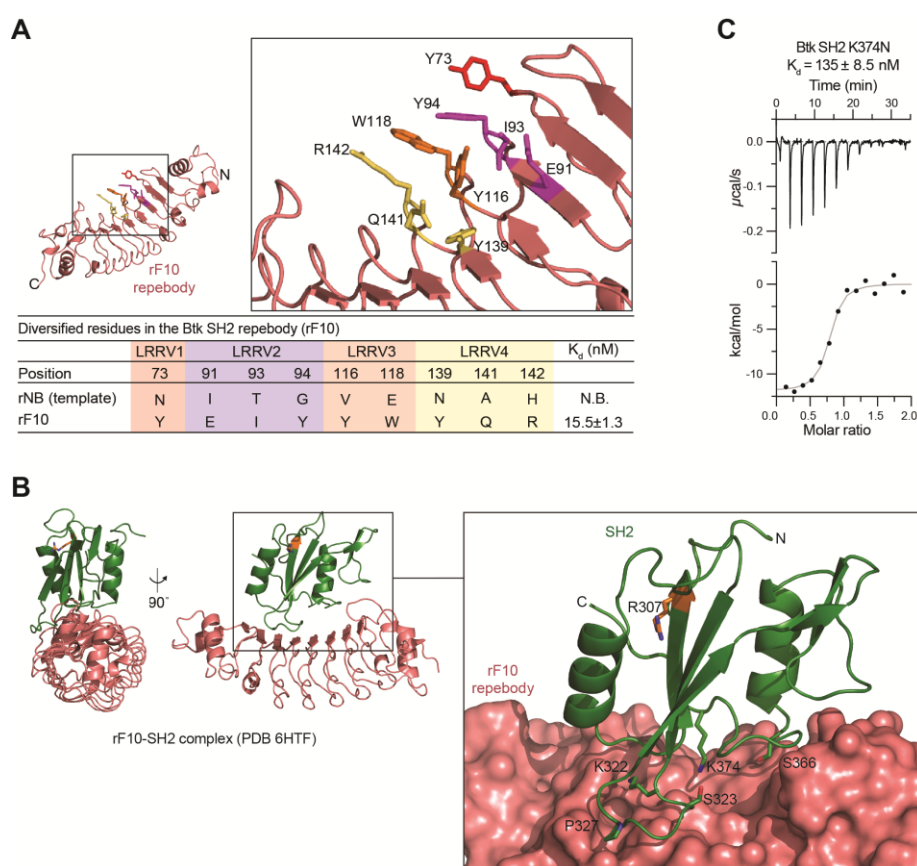


Figure 24 – The high-resolution structure of rF10-SH2 complex.

A: rF10 residues (sticks) mediating the interaction with the human SH2 domain. The table indicates the sequence and binding affinity. Non-binding (N.B.).

B: Cartoon representation of the crystal structure (PDB 6HTF) showing the rF10 (salmon) and SH2 (green). Detailed view of side chains from SH2 residues interacting with the rF10 (surface representation). The R307 residue from the pY-binding is shown in orange.

C: Representative ITC measurement of rF10 repebody to Btk SH2 K374N. The K_d value was calculated from two independent measurements.

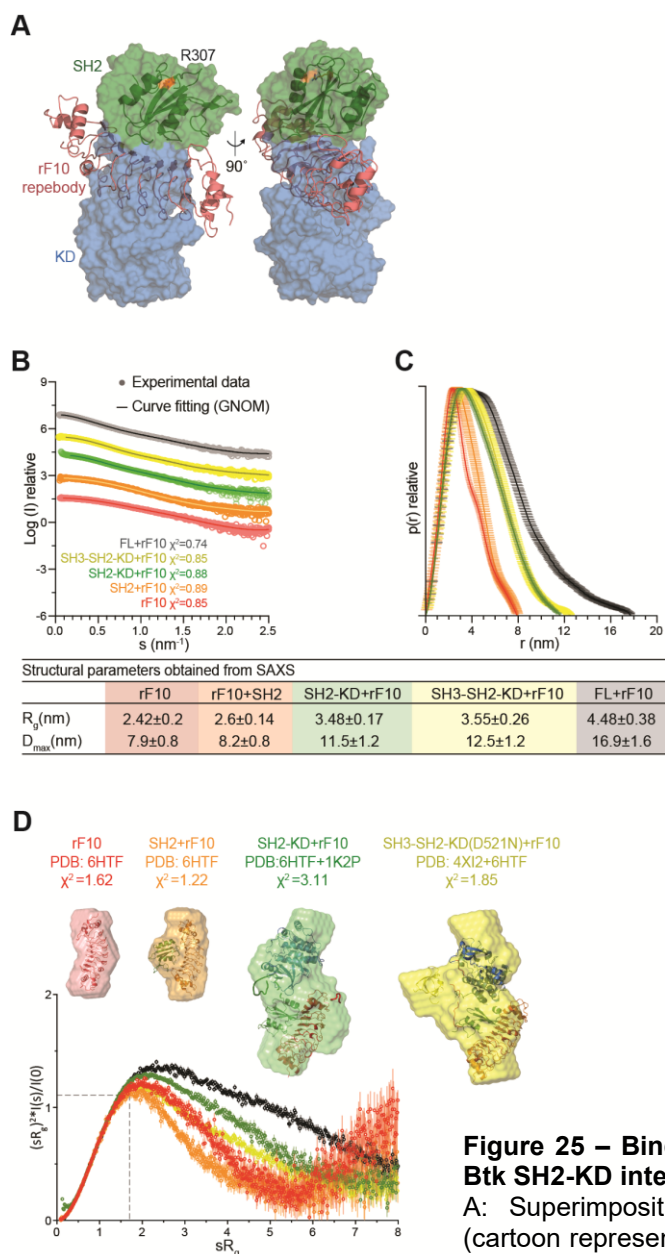


Figure 25 – Binding to rF10 may abrogate the Btk SH2-KD interaction.

A: Superimposition of the rF10-SH2 structure (cartoon representation, SH2 in green and rF10 in salmon) with the active Btk SH2-KD model (surface representation, SH2 in green and KD in blue).

B: Experimental SEC-SAXS data for rF10 alone and rF10-Btk complexes. The indicated χ^2 represents the GNOM fitting (line) against the experimental data (dots) for each respective sample. See Supplementary Table 4 for details.

C: Maximal particle dimension (D_{max}) of rF10 alone and rF10-Btk complexes. The table on the bottom summarizes the particle dimensions (R_g and $D_{max} \pm$ error) for the indicated constructs.

D: Dimensionless Kratky plot of rF10 alone and rF10-Btk complexes. Ab initio reconstructions obtained from SAXS (surface representation) were superimposed to the indicated crystal/MD structures. For the rF10-SH2-KD and rF10-SH3-SH2-KD complexes, rigid body modeling using SASREF was applied to obtain the final models displayed.

Table 6 – SAXS parameters of rF10-Btk complexes.

Data collection parameters					
Instrument	MD29 beamline, ESRF Grenoble - France				
Wavelength (Å)	0.9919				
q-range (nm ⁻¹)	0.03563 - 5				
Exposure time (sec)	5 (10 frames x 0.5 sec) or 1 (1 frame per sec for SEC-SAXS)				
Temperature (K)	290				
Protein	rF10 alone	SH2-rF10	SH2-KD-rF10	SH3-SH2-KD-rF10	Full-length-rF10
Measurement	SEC-SAXS	batch	SEC-SAXS	batch	batch
Concentration range (mg.ml ⁻¹)	100 µl at 14	0.6 – 2.7	100µl at 20	0.4 – 3.6	0.4 – 2.9
SASBDB identifier	N/A	N/A	N/A	N/A	N/A
Structural parameters					
R _g (nm) Guinier	2.42±0.2	2.6±0.3	3.46±0.12	3.55±0.26	4.48±0.38
I(0)* (cm ⁻¹) Guinier	37.12±0.06	35.7±0.18	87.82±0.24	61.09±0.19	79.46±0.23
R _g (nm) from P(r)	2.47±0.006	2.6±0.01	3.52±0.007	3.6±0.01	4.69±0.02
D _{max} (nm)	7.9±0.8	8.2±0.8	11.5±1.2	12.5±1.2	16.9±1.7
Porod vol. (nm ³)	50.85	67.4	100.6	116.46	156.04
Dry vol. from sequence (nm ³)**	37.581	53.569	92.638	100.685	130.345
Molecular mass determination (kDa)					
From Porod volume (V _p /~1.6)	24.8	37.9	70.4	81.2	100.8
SAXS MoW2	27.1	41.9	79.5	86.2	116.2
Bayesian inference	28.2	37.7	67.1	74.3	94.2
I(0) using V _c invariant	27.6	39.3	63.5	74.6	89.4
From sequence***	31.1	44.3	76.6	83.2	107.7
Residues	274	391	670	726	938
Software list					
Primary data reduction	Automated pipeline at beamline				
Data processing	PRIMUS (ATSAS v.2.8.0)				
Ab initio analysis	DAMMIN and GASBOR				
Fitting	CRY SOL				
Model refinement	SREFLEX				
Flexibility analysis	EOM 2.0				
Model superimpositions	SASpy plugin for Pymol				
3D graphics images	Pymol (v.1.8.2.1)				

*I(0) for SEC-SAXS is not normalized to protein concentration. The structural parameters analyzed are independent of this value.

**<http://biotools.nubic.northwestern.edu/proteincalc.html>

***<http://web.expasy.org/>

3.2.4 rF10 functions as an antagonist of Btk activity

We next performed *in vitro* autophosphorylation assays using different recombinant Btk constructs in the presence of a 2-fold molar excess of rF10 or the rNB control (Fig. 26A). rF10 showed a strong inhibitory effect on pY551 autophosphorylation of all tested Btk constructs containing the SH2 domain (Fig. 26B-D). Interestingly, even though the constructs SH3-SH2-KD and full-length Btk adopt an autoinhibited conformation with low autophosphorylation activity (Fig. 10D), rF10 strongly decreased their remaining activity (Fig. 26D). Consistent with this data also total pY phosphorylation of Btk was decreased in the presence of rF10 (Fig. 26E-G). Finally, to determine the effect of allosteric inhibition of Btk by rF10 on kinase activity, we performed *in vitro* kinase assays with a substrate peptide encompassing Y753 of PLC γ 2, a canonical Btk substrate. In the presence of rF10, but not rNB, kinase activity of full-length Btk was strongly inhibited (Fig. 26H).

To test the ability of rF10 to act an allosteric Btk inhibitor in cells, we first tested whether rF10 interacted with different Btk constructs in mammalian cells. Pull-down assays using cell lysates from HEK293 co-expressing Btk and reprobodies proteins showed interactions of rF10 with all Btk constructs containing the SH2 domain (Fig. 27A). As expected, Btk proteins co-expressed with control rNB showed no interaction.

We next sought to test the effect of rF10 on the phosphorylation of Btk in the cellular context. Again, Btk proteins and reprobodies were co-expressed in HEK293 cells and phosphorylation on Y551 assessed using immunoblots (Fig. 27B). In the presence of rF10, lower levels of Btk pY551 were observed than when equal amounts of rNB were expressed. Phosphorylation of the KD alone was unaltered in the presence of reprobodies, indicating selective SH2 domain-dependent inhibition of Btk autophosphorylation by rF10 (Fig. 27C). This inhibitory effect, particularly in the SH2-KD construct, was corroborated as we observed a significant decrease in total pY phosphorylation in the same experimental setting (Fig. 27D-E). This data collectively showed that targeting the Btk SH2 with a reprobod body binder at the proposed SH2-kinase interface selectively inhibits Btk activity.

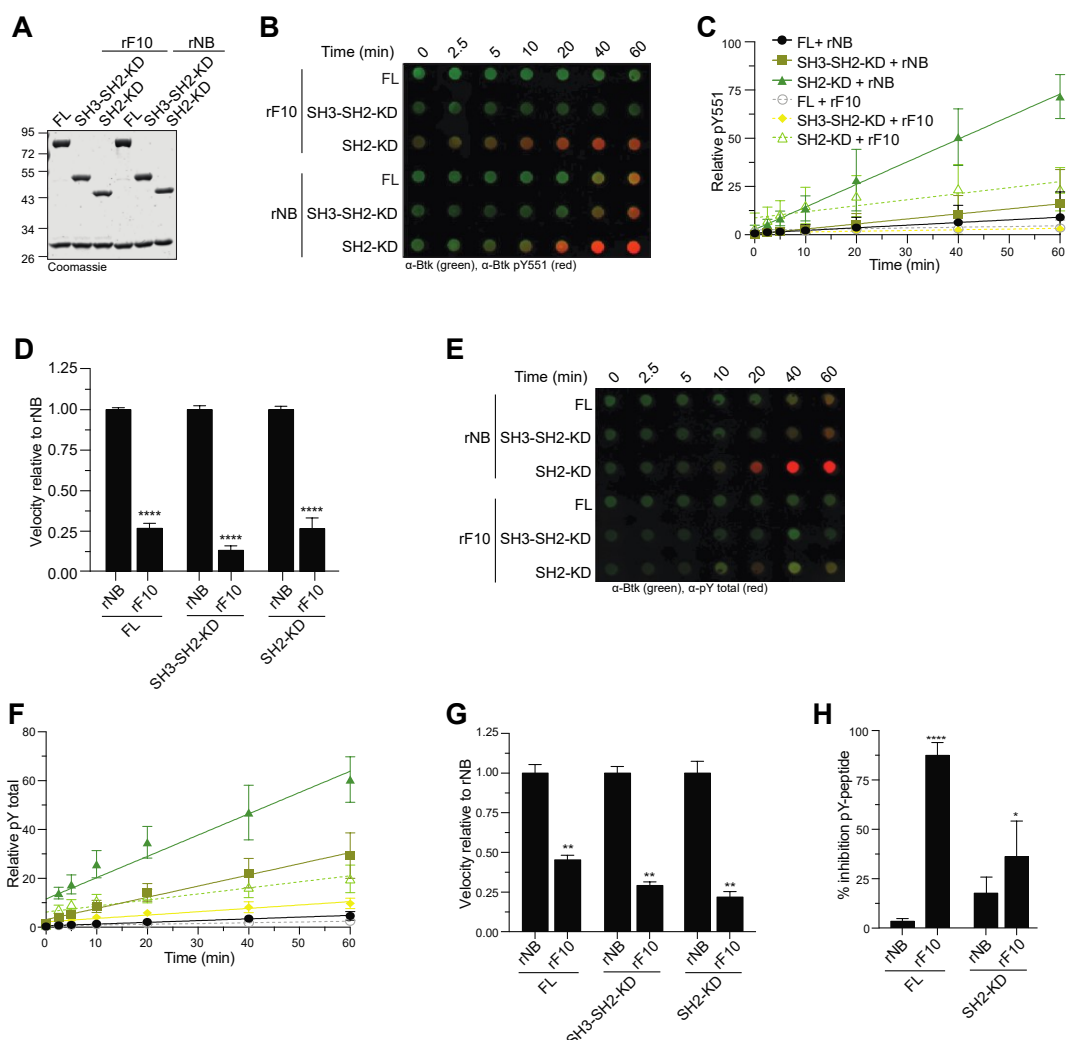


Figure 26 – rF10 reepody inhibits Btk activation *in vitro*.

A: Representative SDS-PAGE analysis of recombinant Btk proteins mixed with rF10 and rNB control reepodies and used for *in vitro* autophosphorylation assays.

B: Autophosphorylation *in vitro* of Btk performed in the presence of rF10 (dashed lines) or rNB (continuous lines). The levels of pY551 (red channel) and total Btk (green channel) were assessed using immunoblotting in a dot blot apparatus.

C: Quantitative analysis of Btk autophosphorylation kinetics. The ratio of pY551 and total Btk protein is plotted over time. Means \pm SD of three independent experiments are shown. The slopes (relative velocities) of linear fits were calculated.

D: Relative velocities of autophosphorylation for each Btk construct and relative to control reepody are shown. Data show the mean \pm SD of three independent experiments. P-values relative to each control rNB reepody were calculated using an unpaired t-test.

E-G: Autophosphorylation assay used to assess the total pY phosphorylation levels.

H: Kinase assay against a PLC γ 2 peptide in the presence of reepodies. Reported inhibition (% inhibition of phosphorylated peptide) from two independent experiments done in duplicates (n=4). P-values were calculated relative to each rNB control using an unpaired t-test.

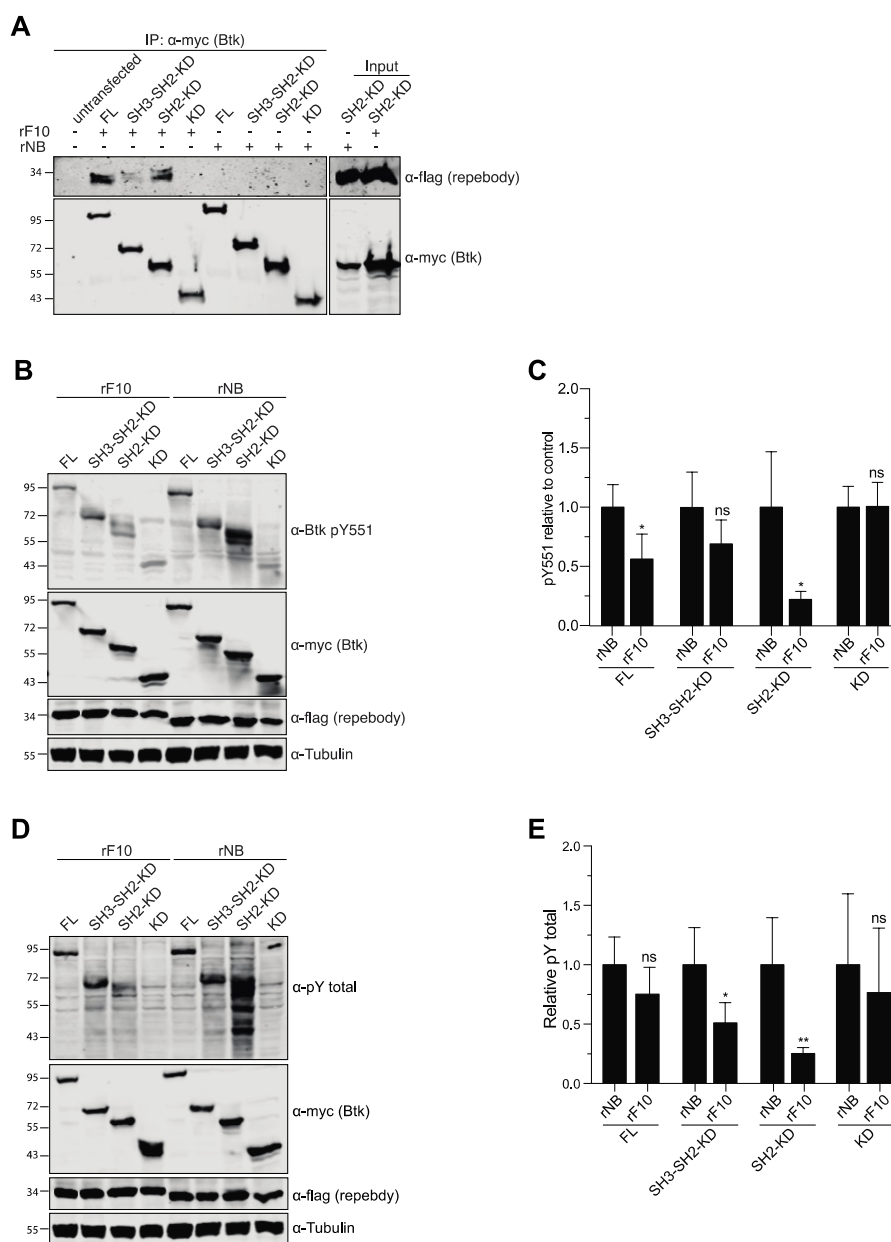


Figure 27 – rF10 repebody inhibits Btk phosphorylation in the cellular context.

A: HEK293 cells were transiently co-transfected with indicated Btk constructs and repebodies, and lysates were subjected to immunoprecipitation using anti-Myc coated beads. A representative sample of lysate for each repebody was loaded as expression control.

B: Immunoblot analysis of lysates from HEK293 cells transiently co-transfected with indicated Btk constructs and repebodies used to assess Btk pY551 phosphorylation.

C: Quantification of pY551 and normalized to total Btk (Myc-Btk) expression level and relative to control repebody. Data shown are the mean \pm SD of three biological replicates, and P-values were calculated against each control rNB repebody using unpaired *t*-test.

D and E: Effect of rF10 in the total pY phosphorylation of Btk in HEK293 cells.

3.2.5 Targeting the Btk SH2-KD interface decreases the viability and inhibits signaling of lymphoma cells

A common approach to treat different B-cell malignancies is the targeted inhibition of Btk using small-molecule inhibitors. As the rF10 showed a significant decrease in Btk activation, we hypothesized whether targeting the SH2-KD interface is sufficient to inhibit Btk activity in neoplastic B-cells. We selected a set of DLBCL cell lines that express WT Btk and are sensitive to ibrutinib (Fig. 28A) and transduced them with an expression cassette to inducibly express rF10 or the rNB upon addition of doxycycline. Induction of rF10 expression in HBL-1 cells decreases about 10-fold the cumulative cell number of HBL-1 cells as compared to rNB, all uninduced conditions or parental cells (Fig. 28B), as well as a more modest decrease in cell number in TMD8 cells (Fig. 28C). The strongest inhibitory effect seen in HBL-1 cells was accompanied by a dramatic increase in apoptosis measured by Annexin V staining and was comparable to the treatment of parental cells with ibrutinib (Fig. 28D).

Targeting of BCR signaling using small-molecule inhibitors can be assessed via phosphorylation of Btk and downstream targets such as PLC γ 2. In order to verify the effect of allosteric Btk inhibition in malignant B-cells, reprobodies were expressed and phosphorylated and total level of BCR signaling proteins assessed by immunoblot. rF10 expression promotes decreased Btk pY551 phosphorylation in HBL-1 cells, which could not be increased by BCR stimulation using anti-human IgM (Fig. 29A and B). Interestingly, an increase in Btk and PLC γ 2 protein (Fig. 29C) levels was observed upon rF10 expression, which may suggest a compensatory mechanism to counteract the activity of rF10 on Btk inhibition. The rF10 effects on BCR signaling were also consistent in DOHH2 cells, where it resulted in decreased Btk pY551, even upon BCR stimulation, decreased PLC γ 2 phosphorylation on Y1217, one of the two main Btk phosphorylation sites, as well as strongly decreased in Erk activation (Fig. 29D). Despite the strong inhibition of the BCR signaling pathways by rF10, we did not observe growth inhibition of DOHH2 cells when targeting the SH2-KD interface using the rF10 (data not shown).

These findings demonstrate that allosteric targeting of the Btk SH2-KD alone is sufficient to inhibit Btk activity in malignant B-cells, which triggers a decrease in cell proliferation due to apoptosis depending on the cellular context, accompanied by a substantial decrease Btk phosphorylation and BCR signaling.

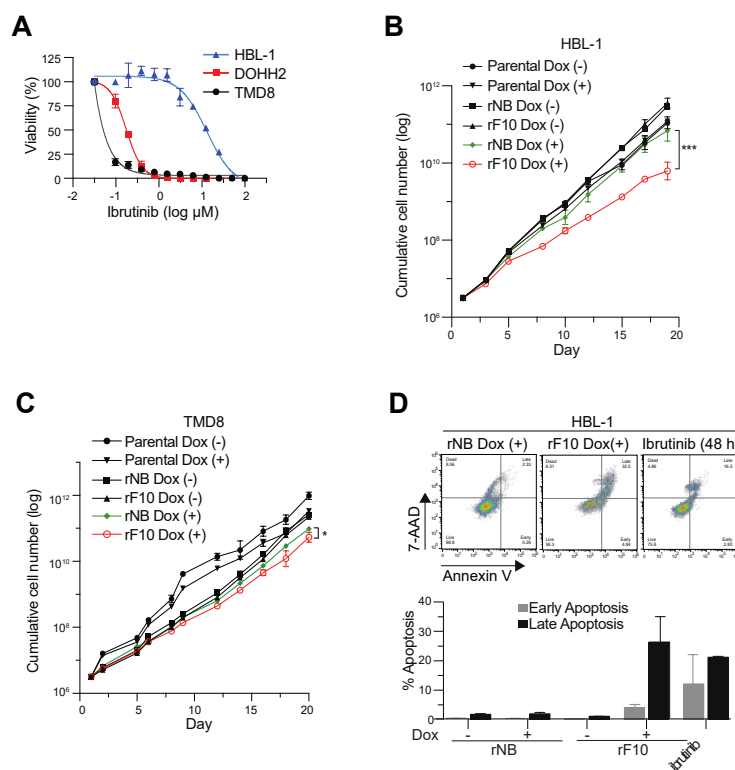


Figure 28 – Allosteric inhibition of Btk decreases DLBCL cell proliferation.

A: Dose-response for ibrutinib in human DLBCL cell lines. Data are the mean \pm SD of a representative experiment (n=3).

B and C: Cumulative cell numbers of upon expression of repebodies.

D: Apoptosis staining of HBL-1 expressing repebodies for 7 days. A representative FACS staining is shown. The quantification of early (7AAD-/Annexin V+) and late (7AAD+/Annexin V+) apoptotic cells obtained from two independent experiments. HBL-1 parental cells treated with 10 μ M of ibrutinib for 48 hours were used as positive control.

The combination of multiple drugs hitting the same targets can have a beneficial effect in cancer treatment and is particularly exemplified by ATP-site and myristate-binding site inhibitors targeting Bcr-Abl. As the allosteric inhibition of the Btk SH2-KD interface triggers a sustained, although mild response in inhibiting DLBCL cell lines, we also verified whether the combination of rF10 with ATP-site ibrutinib promote stronger cell inhibition. In the HBL-1 cell line, a consistent decrease in cell viability upon rF10 expression was observed, and the addition of ibrutinib did not compete with this effect as the IC₅₀ of combinations was not affected after 3 nor 5 days of treatment (Fig. 30A and B). The annexin V staining with combined rF10 expression and ibrutinib treatment suggested a further increase in apoptosis, as compared to the single treatments alone (Fig. 30C). These results indicate that allosteric inhibition of Btk represents a second targeting mechanism and suggests that combinations with ATP-competitive drugs could be beneficial.

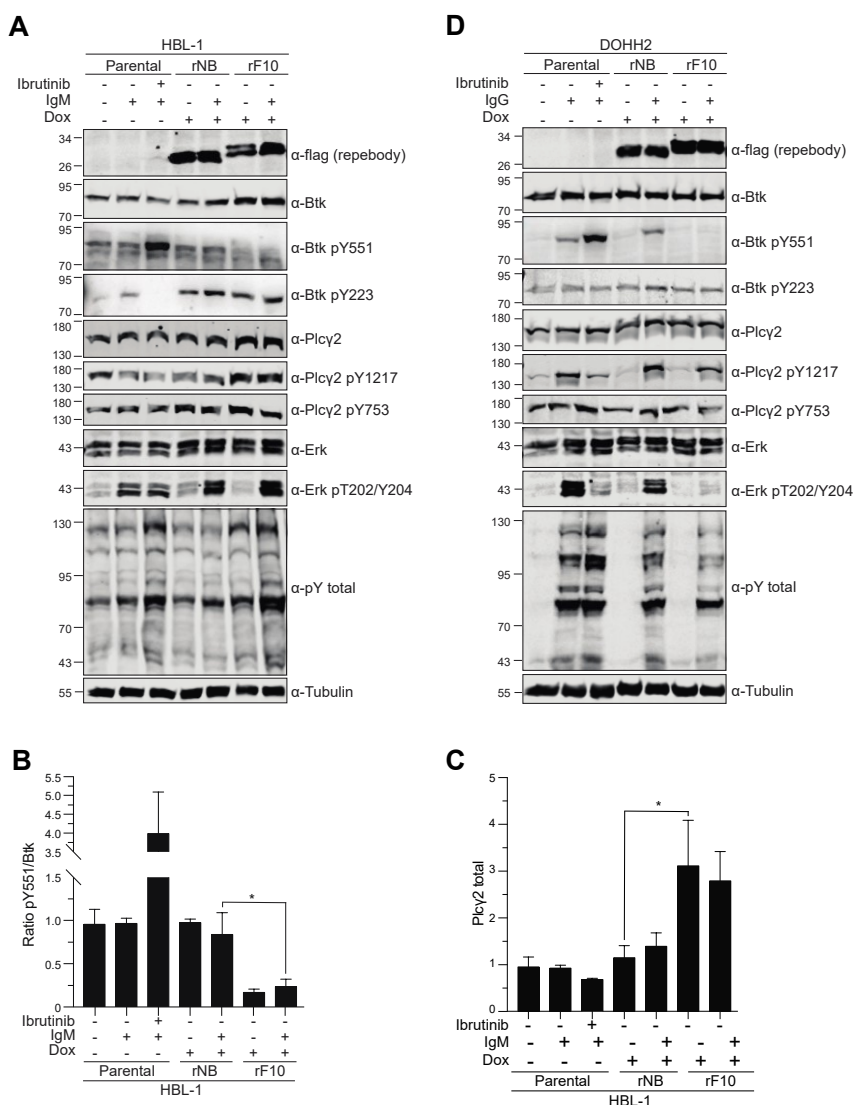


Figure 29 – Allosteric inhibition of Btk in DLBCL cells.

A: Expression of repebodies (flag-tagged) was induced for 48 hours in HBL-1 cells, and BCR signaling stimulated with anti-human IgM or mock-treated for 2 minutes before cell lysis. Ibrutinib treatment (100 nM) was performed for 15 minutes prior to anti-IgM stimulation. Immunoblot analysis of whole-cell lysates with the indicated antibodies is shown. Tubulin was used as loading control.

B and C: Quantification of Btk pY551 and total PLCγ2 proteins from immunoblot shown in (A) and normalized to total Btk expression and tubulin, respectively. Data shown are the mean \pm SD from two biological replicates ($n=3$), and P-values were calculated using an unpaired *t*-test.

D: DOHH2 cells expressing the repebodies and immunoblot performed as described above.

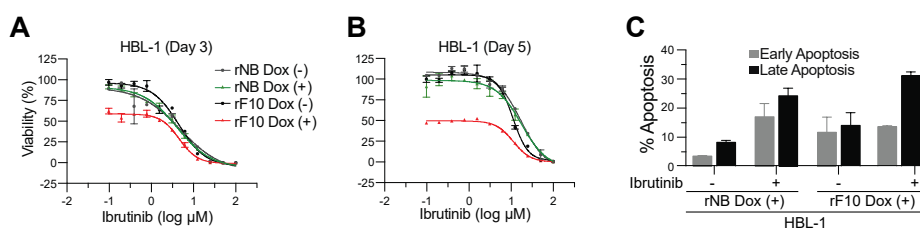


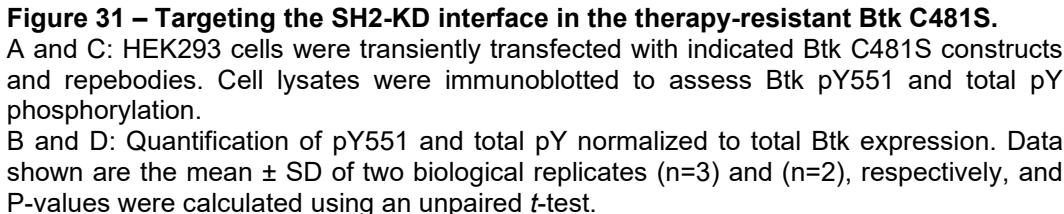
Figure 30 – Combination of rF10 and ibrutinib in HBL-1 cells.

A and B: HBL-1 cells expressing rF10 or control rNB repebodies for 3 and 5 days were combined to different concentrations of ibrutinib and cell viability accessed using Cell Titer Glo reagent.

C: HBL-1 inducibly expressing rF10 or rNB control for 5 days in combination with ibrutinib (10 μ M for 48 hours) were stained with 7AAD and Annexin V to analyze apoptosis by FACS. The quantification of early (7AAD-/Annexin V+) and late (7AAD+/Annexin V+) apoptotic cells were obtained from two replicates (n=2).

3.2.6 Therapy-resistant Btk is targeted and inhibited by rF10

Resistance to ATP-competitive inhibitors is a common drawback seen in several kinases relevant to cancer. Patients heavily treated with ibrutinib have shown the development of C481S/T mutation within the ATP-site that decreases the affinity to irreversible Btk inhibitors. There is no alternative approved drug able to target these resistant variants. As the rF10 targets the allosteric SH2-KD interaction far from the ATP-site, we next tested if it would be also active against Btk C481S mutant proteins. Co-expression of different Btk C481S constructs with repebodies in HEK293 cells revealed that the rF10 inhibits Btk phosphorylation at Y551, particularly in the SH2-KD protein (Fig. 31A and B). A decrease in total pY phosphorylation was also observed for the SH2-KD to a similar extent than of WT SH2-KD (Fig. 31C and D). To our knowledge, this is the first report of an alternative mechanism able to inhibit WT and drug-resistant Btk by solely targeting an allosteric site.



4 DISCUSSION

4.1 Allosteric activation of Btk

Integration of distinct structural and biochemical approaches has provided important insights into the multiple allosteric interactions that retain Btk in its autoinhibited conformation⁸. In contrast, little was known about the interdomain rearrangements coordinating Btk activation. Previous studies on other Tec kinase members, in particular Itk, reported an increase in kinase activity in the presence of its PIDs, including the SH2 domain^{89,185}. In contrast to Src kinases that are autoinhibited by the assembling of non-catalytic domains, in Btk the catalytic core is largely inactive compared to the full-length protein¹⁷⁸ which is only partially explained by specific structural elements of its catalytic unit (e.g. I432 and W395 residues)^{92,166,173}.

Our finding that addition of the SH2 domain substantially increases Btk phosphorylation at Y551 (3-fold), as well as multiple other phosphorylation sites throughout the SH2, SH2-KD linker, and KD, suggests the existence of an unexpected allosteric interaction between the Btk SH2 and KD required to activate Btk's catalytic activity. While the role of phosphorylation on Y551 in the activation loop is well documented and absolutely required for Btk catalytic activity¹⁸⁶⁻¹⁸⁸, the importance of the multiple other Btk phosphorylation sites remains unclear. The phosphorylated residues detected by our MS analysis of the activated SH2-KD protein include the Y345 within the SH2-KD linker, a residue that does not affect Btk activation when mutated in cells or *in vivo*⁹².

The molecular and structural approaches applied in our study provide together the first mechanistic overview of the active Btk SH2-KD unit and reveal an interface between the SH2 and the top of the KD. A particular arrangement of several hydrophobic residues from the N- and C-lobes assembling the regulatory and catalytic spines are required to switch on the catalytic mechanism in most kinases. Importantly, the direct interaction between the SH2 and the N-lobe is consistent with studies reporting that coordination of the W395 side chain capping the regulatory spine is essential to promote catalytic activity^{92,173}. It provides

a rational explanation for the lack of catalytic activity seen by us and others in the isolated Btk KD^{144,178}.

Strikingly, residues involved in the Btk SH2-kinase interface are identical in most other Tec members but are not conserved in the Abl and Fes kinase families, while residues critical for the Abl SH2-kinase interaction are not conserved in Tec kinases (Fig. 32). This further supports the notion that allosteric SH2-kinase interfaces in different kinases families appear to be diverse in terms of location, charge, hydrophobicity, size, and, consequently, dynamics. The Btk SH2-KD interaction seems fairly flexible and precluded Btk crystallization, in contrast to the respective Fes and Abl SH2-KD constructs^{16,17} as well as Csk, where both SH2 and SH3 domains contact the N-lobe¹⁷⁹. Additional multi-domain structures including the SH2-kinase linker will potentially capture the preferential position of the SH2 towards the KD and further corroborate the model of SH2-mediated activation of Tec kinase members.

Our data also provides the first structural insights into the molecular mechanism-of-action of a subset of SH2 mutations observed in XLA patients. These SH2 mutations particularly located in the region predicted to interact with the N-lobe in the active Btk may favor a more compact and distorted conformation. Noteworthy, the SH2 region interacting with the N-lobe in the active conformation is different from the region facing the C-lobe in the autoinhibited Btk, which is maintained by a salt-bridge between the pY-binding site and D659¹⁶⁷ and mimics the pY-tail latch of Src kinases⁸. Other XLA mutations on different regions of the SH2 domain, including K296E which does not disturb catalytic activity *in vitro*, may impact Btk function by a distinct mechanism that includes binding to SH2 interactors and PLCG2-dependent calcium response independent of Btk phosphorylation. Reconstitution of mutants into DT40 chicken lymphoma B-cells, which are deficient for Btk and PLCG2-dependent calcium response¹⁸⁹, provides an example of a cellular system that could be exploited to further investigate the effect of XLA mutation in cell signaling.

Together, this study adds a critical step to the molecular shifts required for Btk activation in cells, where the disassembling of the autoinhibited Btk by PIP₃ binding to PH and dimer formation in the plasma membrane is followed by allosteric interaction of the SH2 domain on top of KD to trigger Btk activation (Fig. 33). It remains to be investigated whether this PH-dependent dimerization could also promote trans-autophosphorylation on other residues as assumed to be the case for Y551 in the current activation model for Btk⁸. Whereas in cells the Lck-dependent Btk phosphorylation on Y551 seems to precede Y223

autophosphorylation¹⁸⁶, our *in vitro* kinetics revealed rapid increase phosphorylation on Y223 followed by Y551. Our data agrees with a previous model where autophosphorylation on Y223 may contribute to full activation of the kinase to further transphosphorylate other Btk molecules on Y551¹⁴⁵.

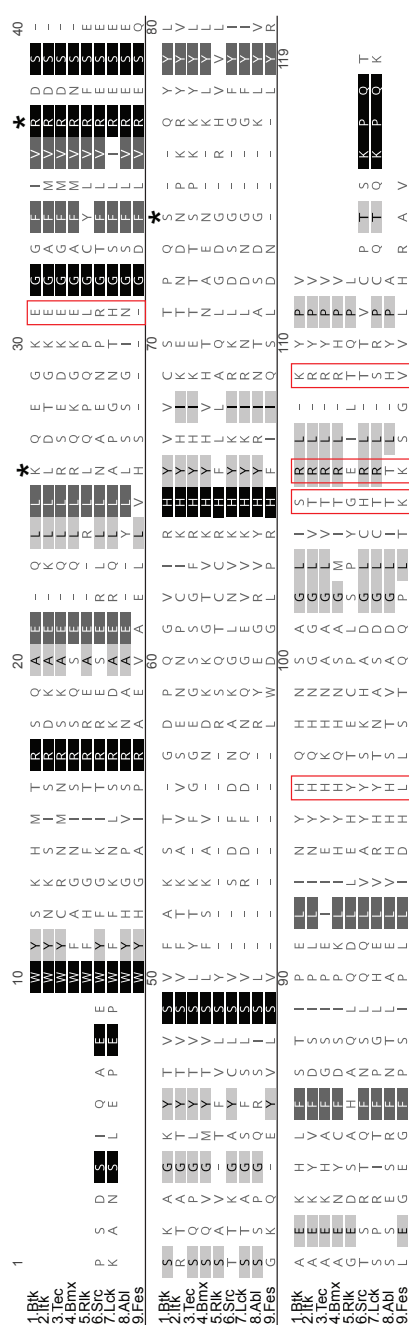


Figure 32 – Sequence alignment of SH2 domains from human Btk and related kinases.

Black squares represent residues highly conserved and grey squares show residues relatively conserved.

Red boxes are residues mutated in XLA patients and located in the predicted SH2-KD interface.

Black asterisk symbol (*) indicates other residues mutated in XLA patients.

4.2 Allosteric inhibition of Btk

Targetable allosteric regulatory sites have been identified for a few kinases and include the myristoyl binding pocket and SH2-kinase interface in Bcr-Abl, as well as the PIF pocket in different AGC kinases^{14,21,27,190}. Here we identified and validated the SH2-KD interface as a unique site for allosteric Btk inhibition using an engineered repebody protein (Fig. 33). To our knowledge, this is the first alternative targeting strategy for WT and ibrutinib-resistant Btk variants. The three FDA-approved Btk inhibitors, ibrutinib, acalabrutinib, and zanubrutinib are highly susceptible to resistance development by mutations of C481 to which these inhibitors covalently bind. Therefore, the therapeutic exploitation of the Btk SH2-KD interface for patients with TKI-resistant B-cell malignancies is highly attractive. Unlike other Btk mutations on the Btk KD (C481S, T474A, and L528W) that trigger resistance to ibrutinib¹⁹¹, identification of the ibrutinib-resistant T316A variant located in the SH2 from patients with tumor relapse demonstrates that additional therapy-insensitive mutations are likely to develop¹⁹². Alternatively, the PIP₃-dependent dimerization of the PH domain, which is required for membrane-associated activation of Btk, was proposed to be an allosteric site although not yet explored for targeted inhibition^{144,163}.

SH2 domains are conserved, abundant domains in proteomes, and hence difficult to target using small molecules. Small engineered protein binders, in particular monobodies and repebodies, have emerged as powerful tools to target SH2 domains of a variety of kinases and phosphatases and encourage the development of alternative SH2 inhibitors^{33,34,193}. In addition, recent advances in cytoplasmic delivery strategies of protein binders, its combination with targeted protein degradation and feasibility PROTAC-based Btk degradation demonstrate progress towards therapeutic applicability¹⁹⁴. The combined targeting of different sites on the same Btk molecule to limit resistance development is likely to follow the paradigm of the allosteric Bcr-Abl myristoyl pocket inhibitor asciminib, which abrogates drug resistance when combined with ATP-competitive Bcr-Abl inhibitors³⁰.

The DLBCL cell lines employed in our study demonstrated good expression levels of repebodies and were selected from a larger panel of Btk-dependent cell lines initially transduced (data not shown). Although good quality antibodies are commercially available, phosphorylated Btk comprises only a limited fraction ($\leq 5\%$) from the total cellular pool of Btk molecules in the BCR-activated B-cells. We observed a similar issue for certain Btk

cell lines (e.g. TMD8) even after performing BCR stimulation in order to increase phosphorylation events and facilitate the readout of the immunoblot analysis.

It is important to note that targeting the Btk SH2-KD interface leads to particularly strong effects in DLBCL cell lines harboring CD79B mutations (Y196F in HBL-1 and Y196H in TMD8 cells) that trigger chronic activation of BCR, and are therefore heavily dependent on Btk signaling to support cell growth. Our observation that anti-IgM stimulation in these cells results did not increase total pY phosphorylation (Fig. 29A and data not shown) agrees with the fact that BCR is already activated in these cell lines, and consequently supports the decrease in cell proliferation seen upon Btk allosteric targeting. Consistently, DOHH2 cells containing CD79 WT do not depend on the chronic BCR signaling and thus respond to BCR stimulation with anti-IgG (Fig. 29D) – this corroborates the lack of effect in cell growth upon treatment with the rF10 repebody alone (data not shown). However, Btk allosteric targeting clearly blocked BCR signaling and decreased the MAPK component Erk in stimulated DOHH2 cells. Noteworthy, the treatment of cells with ibrutinib led to increased Y551 consistent with the fact that the activation loop Y551 is fully exposed when ibrutinib is binding to the kinase¹⁶⁰. These findings indicate that patients with tumors functionally dependent on BCR signaling might benefit from this allosteric Btk targeting approaches⁵⁰.

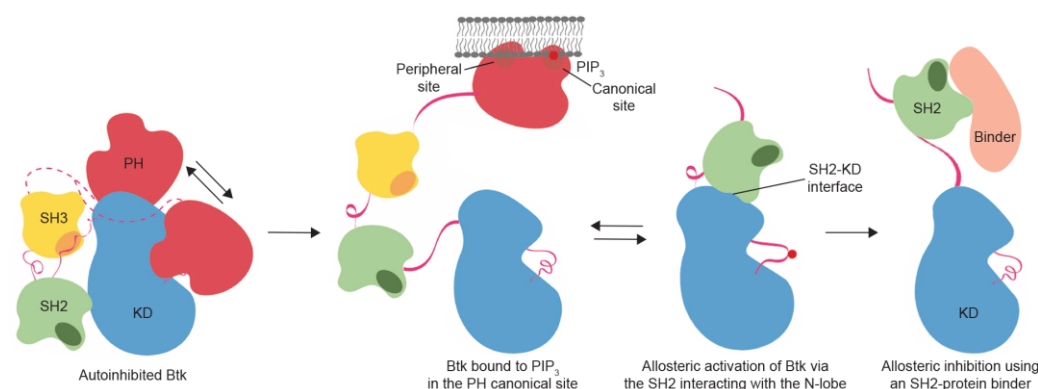


Figure 33 – Proposed model for the allosteric activation and inhibition of Btk via its SH2 domain.

Engagement of the PH domain with PIP₃ or other inositol molecules (e.g. IP₆) opens up the autoinhibited conformation of Btk to induce homodimerization via its peripheral site (omitted in this scheme). Release of intramolecular constraints promotes interaction of the SH2 domain with the N-lobe of the kinase to induce kinase activation accompanied by phosphorylation of its activation loop and potentially other sites. Abrogation of the Btk SH2-KD interaction using an SH2 binder triggers kinase inhibition and decrease Btk-dependent signaling.

Although we have focused our study on the effect of Btk allosteric inhibition in B-cell malignancies, this could also impact Btk function in the context of autoimmune diseases like rheumatoid arthritis. Here, allosteric inhibition of Btk in FcR signaling in basophils and mast cells could provide potential therapeutic benefits as seen using non-approved ATP-site Btk inhibitors (e.g. RN486)¹⁵³. Moreover, the absence of obvious off-target activity seen for certain allosteric inhibitors, particularly asciminib, demonstrates that a small-molecule allosteric inhibitor can potentially reach great specificity and benefit even at the long-term treatment of chronic conditions with minimum adverse effects. It remains to be investigated whether the SH2-KD interface has an impact on Btk contribution for regulating alternative pathways.

Our study adds novel structural insights into the complex regulation of Tec kinases, where the SH2 domain plays a critical role in the kinase activation which is independent of its canonical function. Disruption of the SH2-KD interface hampers Btk activation and provides a molecular mechanism that explains a subset of pathogenic XLA mutations. Finally, the exploration of the SH2-KD interface as a targetable allosteric site, even in therapy-resistant Btk variants, provides a completely novel way to target Btk and potentially other Tec kinases. These findings support and encourage the rational development of allosteric inhibitors targeting Btk with the potential to benefit not only patients with B-cell malignancies but also other disease contexts where Btk plays an essential role.

5 MATERIAL AND METHODS

5.1 Cell lines and culture conditions

HEK293 and HEK293T cells were cultured in DMEM (Gibco) supplemented with 10% fetal calf serum (Gibco) and 1% penicillin/streptomycin (Bioconcept). Human DLBCL cell lines DOHH2, HBL-1 and TMD8 (expressing full-length WT Btk protein) were kindly provided by M. Thome-Miazza (University of Lausanne), cultured in RPMI-1640 media (Gibco) supplemented with 1 mM L-glutamine (Gibco), 10% fetal calf serum (Gibco) and 1% penicillin/streptomycin (Bioconcept). All cell lines were cultured at 37°C under 5% CO₂.

5.2 Protein expression and purification

Btk SH2 domains were cloned into the pETM30 plasmid with an N-terminal 6xHis-GST tag with tobacco etch virus (TEV) cleavage site, and expressed in *E.coli* BL21(DE3). Repebodies were cloned into the pET21a plasmid (Millipore) with a C-terminal 6xHis tag, and expressed in *E.coli* Origami (DE3). Expression of recombinant proteins was performed overnight at 18°C in LB medium after induction with 0.5 mM IPTG at an optical density of ~0.8. For protein purification, bacteria were harvested in purification buffer (50 mM Tris pH 7.5, 500 mM NaCl, 1 mM DTT, 5% glycerol, 10 mM imidazole) containing DNase, homogenized using an Avestin Emulsiflex C3 homogenizer, followed by lysate clarification through centrifugation. Proteins were first purified by gravity flow Ni-NTA agarose (Qiagen, 30210) followed by tag cleavage with recombinant TEV protease in dialysis buffer (25 mM Tris pH 7.5, 300 mM NaCl, 1 mM DTT, 5% glycerol). Finally, samples were subjected to size exclusion chromatography (SEC) on a Superdex 75 16/60 column equilibrated with dialysis buffer, and peak fractions pooled and analyzed by SDS-PAGE.

For insect cell expression, sequences were cloned into a pFast-Bac-Dual plasmid (ThermoFisher). To obtain unphosphorylated Btk, Flag-tagged Yersinia protein tyrosine

phosphatase (YopH) was simultaneously expressed from the same vector. Baculoviruses were prepared following the instructions from Bac-to-Bac Baculovirus Expression System (ThermoFisher) protocol. Briefly, pFast-Bac Dual plasmids were transfected to *E.coli* DH10B followed by bacmids purification

(PureLink, Invitrogen) and transfection in Sf9 cells using the transfection reagent FuGene HD (Promega, E2311). Supernatants containing the baculoviruses were used to produce recombinant proteins in Sf9 cells at density 1.5×10^6 cells mL⁻¹ in SF-900 SFM (10902-096, Thermo) cultured at 28°C and 80% air humidity. After 3 days, cells were and resuspended in purification buffer containing 1mM PMSF, protease cocktail inhibitor (Roche) and Benzonase (Millipore), and lysed by sonication. Cleared lysates were purified and tags removed as described above. All purified proteins could be stored at -80°C without loss of activity. Absence of YopH phosphatase activity was reassured by a phosphatase activity assay using colorimetric PNPP substrate (Thermo) and immunoblotting.

5.3 Mass spectrometry

For confirmation of protein identity and phosphorylation status, recombinant proteins were analyzed on a Xevo G2-S QTOF mass spectrometer (Waters) operated in positive ionization using the ZSpray™ dual-orthogonal multimode ESI/APCI/ESCI source. Data were processed using MassLynx™ 4.1 software and MaxEnt1 application for deconvolution.

5.4 Multi-angle light scattering analysis (SEC-MALS)

Multi-angle light scattering was used to probe for oligomerization states. All measurements were performed at room temperature using a Dawn Heleos multi-angle light scattering detector (Wyatt Technologies) coupled to an SEC column. 80 µL (0.5 mg mL⁻¹) of purified recombinant protein was injected into a Superdex 75 HR10/30 column (GE Healthcare) in buffer containing 25 mM Tris-HCl pH 7.5, 150 mM NaCl, 1 mM TCEP, and eluted at a flow rate of 0.5 mL min⁻¹. Absolute molecular weight and homogeneity were determined using ASTRA version 5.3 (Wyatt Technologies).

5.5 Site-directed mutagenesis

All point mutations were introduced using the Quikchange II Site-Directed Mutagenesis Kit (Agilent) using primers described in Table 7. Sequence alignments were generated using Geneious (Biomatters).

Table 7 – Oligonucleotides used for site-directed mutagenesis.

Mutation	Primer sequence 5' to 3' (forward and reverse)
Btk K296E	For: GCTGAGCAACTGCTAGAGCAAGAGGGGAAAG Rev: CTTTCCCCTCTTGCTCTAGCAGTTGCTCAGC
Btk Y223F	For: GTGGCCCTTTTCGATTACATGCCAATG Rev: CATTGGCATGTAATCGAAAAGGGCCAC
Btk E301K	For: GCAAGAGGGGAAAAAGGGAGGTTTCATTGTC Rev: GACAATGAAACCTCCCTTTTCCCCTCTTGC
Btk R307G	For: GGTTTCATTGTCTGGCGACTCCAGCAAAGC Rev: GCTTTGCTGGAGTCGCCGACAATGAAACC
Btk K311E	For: CAGAGACTCCAGCGAGGCTGGCAAATATACAG Rev: CTGTATATTTGCCAGCCTCGCTGGAGTCTCTG
Btk Q341A	For: GTTGTGTGTTCCACACCTGCGAGCCAGTATTACCTGGC Rev: GCCAGGTAATACTGGCTCGCAGGTGTGGAACACACAAC
Btk H364D	For: CATTAACTACCATCAGGACAACCTCTGCAGGACTC Rev: GAGTCCTGCAGAGTTGTCCTGATGGTAGTTAATG
Btk S371P	For: CTGCAGGACTCATACCCAGGCTCAAATATCCAG Rev: CTGGATATTTGAGCCTGGGTATGAGTCCTGCAG
Btk R372G	For: CTCTGCAGGACTCATATCCGGCCTCAAATATCCAG Rev: CTGGATATTTGAGGCCGGATATGAGTCCTGCAGAG
Btk K374N	For: CTCTGCAGGACTCATATCCAGGCTCAACTATCCAG Rev: CTGGATAGTTGAGCCTGGATATGAGTCCTGCAGAG
Btk K400E	For: AGGTCAGGTCCTCTGGATCAATTTCCCATGATCCGT Rev: ACGGATCATGGGAAATTGATCCAGAGGACCTGACCT
Btk T403K	For: CCCCAGCTCCTTCAAGAACTTCAGGTCCTTTGGATCAA Rev: TTGATCCAAAGGACCTGAAGTTCTTGAAGGAGCTGGGG
Btk L405E	For: CAGTCCCCAGCTCCTTCTCGAAGGTCAGGTCCTTTG Rev: CAAAGGACCTGACCTTCGAGAAGGAGCTGGGGACTG
Btk I429E	For: GCCTTCTTTGATCATCTTCTCGGCCACGTCGTACTGGCC Rev: GGCCAGTACGACGTGGCCGAGAAGATGATCAAAGAAGGC
Btk C481S	For: GGTAGTTCAGGAGGCTGCCATTGGCCATGTA Rev: TACATGGCCAATGGCAGCCTCCTGAACTACC
Btk D521N	For: GTTCCTTCACCGAAACCTGGCAGCTCG Rev: CGAGCTGCCAGGTTTCGGTGAAGGAAC
Btk Y551F	For: GGATGATGAATTCACAAGCTCAGTAG Rev: CTAAGTACTGAGCTTGTGAATTCATCATCC

5.6 Circular dichroism (CD)

Far-UV spectra (190-300 nm) of recombinant Btk SH2 WT and mutants were carried out in buffer containing 10 mM Na-phosphate buffer pH 7.2 and 100 mM NaF using a 0.1 cm quartz cell and CD Spectrometer Chirascan V100 (AppliedPhotophysics). Data was acquired at a step size of 1 nm and a bandwidth of 1 nm. 3 scan records for each protein were subtracted from the background (buffer only) and averaged to generate the data reported in units of mean molar ellipticity per residue. Melting curve analysis was

performed by measuring proteins at the wavelength corresponding to the peak for the predominantly β -sheet SH2 domain (218 nm) in a temperature range from 20 to 94°C, ramp-rate 1°C per minute.

5.7 Kinase autophosphorylation assay

1 μ M of recombinant Btk proteins were incubated in Tris 25 mM pH 7.5, 150 mM NaCl, 5% glycerol, 1 mM ATP, 20 mM $MgCl_2$, 1 mM DTT. For inhibition of autophosphorylation, 2 μ M of reprobodies were pre-incubated with 1 μ M of Btk proteins for 15 minutes before starting the reaction upon the addition of 1mM ATP. Reactions were carried out at room temperature and stopped at desired time points by adding 2X Laemmli buffer to each tube, followed by boiling 5 minutes at 95°C. Samples were immunoblotted onto a nitrocellulose membrane using a Dot-Blot apparatus (Bio-Rad).

5.8 HEK293 transfection

Btk constructs were expressed in HEK293 cells using pCS2-gateway plasmid containing an N-terminal 6xMyc tag, while reprobodies were cloned into pcDNA3.1 vector and contained a C-terminal Flag tag. Transient transfections with respective plasmids were performed using Polyfect transfection reagent (Qiagen). 48 hours after transfection, cells were harvested, lysed and samples further processed for immunoblotting.

5.9 Cell lysis and immunoblotting

Cells were lysed in IP buffer (50 mM Tris-HCl pH 7.5, 150 mM NaCl, 1% NP-40, 5mM EDTA, 5mM EGTA, 25 mM NaF, 1mM orthovanadate, 1mM PMSF, 10 mg mL⁻¹ TPCK and protease cocktail inhibitor from Roche), and cleared by centrifugation at 14,000 rpm for 10 minutes at 4°C. Total protein concentration was measured using a Bradford assay (Bio-Rad). All immunoblotting analysis was performed using 100 μ g of total protein.

5.10 Antibodies

A list of primary and secondary antibodies used is available in Table 8. Western blot quantification of fluorescent secondary antibodies was done using the Li-Cor Odyssey system. ECL prime detection reagent (RPN2232, GE Healthcare) was used to detect HRP-conjugated antibodies using the C-digit Blot scanner (Li-Cor). Western blot normalization was done using total protein signal or indicated loading control.

Table 8 – List of antibodies.

Antibody	Provider	Identifier
Mouse monoclonal anti-Total pY (clone 4G10)	Millipore	Cat# 05-321; RRID: AB_309678
Mouse monoclonal anti-Btk (D6T2C)	Cell Signaling	Cat# 56044; RRID: AB_2799503
Rabbit polyclonal anti-Btk	Thermo Scientific	Cat# PA5-27392; RRID: AB_2544868
Mouse monoclonal anti-Btk (pY551)/Itk (pY511) Clone 24a	BD Biosciences	Cat# 558034; RRID: AB_2067823
Rabbit polyclonal anti-Btk (pY223)	Cell Signaling	Cat# 5082; RRID: AB_10561017
Rabbit polyclonal anti-p44/42 MAPK (Erk1/2)	Cell Signaling	Cat# 9102; RRID: AB_330744
Mouse monoclonal anti-phospho-p44/42 (Erk1/2) (Thr202/Tyr204) (E10)	Cell Signaling	Cat# 9106; RRID: AB_331768
Rabbit polyclonal anti-PLC γ 2	Cell Signaling	Cat# 3872; RRID: AB_2299586
Rabbit polyclonal anti-PLC γ 2 (Tyr1217)	Cell Signaling	Cat# 3871; RRID: AB_2299548
Mouse monoclonal anti-Flag	Sigma	Cat# F3165; RRID: AB_259529
Mouse monoclonal anti-penta-his	Qiagen	Cat# 34660; RRID: AB_2619735
Rabbit polyclonal anti-PLC γ 2 (Tyr753) [EPR5914-3]	Abcam	Cat# ab133455; RRID: AB_2163712
Mouse monoclonal anti-Tubulin	Sigma	Cat# T9026; RRID: AB_477593
Mouse monoclonal anti-Myc-tag Myc.A7 DyLight800	Thermo Scientific	Cat# MA1-21316-D800; RRID: AB_2536996
Goat polyclonal anti-mouse IgG IRDye 800CW	LiCor	Cat# 926-32210; RRID: AB_621842
Donkey polyclonal anti-Rabbit IgG (H+L) IRDye800	Rockland	Cat# 611-732-127; RRID: AB_220158
Goat polyclonal anti-Mouse IgG (H+L) Peroxidase AffiniPure	Jackson ImmunoResearch	Cat# 115-035-003; RRID: AB_10015289
Goat polyclonal anti-Rabbit IgG (H+L) Peroxidase AffiniPure	Jackson ImmunoResearch	Cat# 111-035-003; RRID: AB_2313567

5.11 Immunoprecipitation

Immunoprecipitation from HEK293 cell lysates was done using 1 mg of total protein adjusted to 1 mL volume with IP buffer. Anti-c-Myc Agarose Affinity Gel (Thermo, A7470) was added to the lysates and incubated for 3 hours on a rotating wheel at 4°C. Beads were

subsequently washed three times with IP buffer and finally boiled in Laemmli buffer for 5 minutes at 95°C before subjected to immunoblotting.

5.12 B-cell transduction and BCR stimulation

Repebodies containing a C-terminal flag tag were cloned into the doxycycline-inducible (Tet-ON) lentiviral vector pcW57.1 (Addgene) and co-transfected with envelope and packaging plasmids (pMD2G and pCMVR8.74 respectively, a kind gift from the Trono Lab, EPFL) into HEK293T cells using the CalPhos Mammalian Transfection kit (Clontech). Lentiviruses were concentrated by ultracentrifugation at 30,000xg for 2 hours at 16°C, and added to lymphoma cell lines, followed by a single spinoculation step at 300xg for 60 minutes at room temperature. On the next day, cell media was replaced and cells selected using 2 µg mL⁻¹ puromycin. Repebodies were induced by the addition of 2 µg mL⁻¹ of doxycycline. For BCR stimulation, cells at density 5x10⁶ cells mL⁻¹ were incubated at 37°C with 20 µg mL⁻¹ anti-human IgM/G F(ab')₂ from goat (Jackson ImmunoResearch, 109-006-129 and 109-006-098) in RPMI-1640 media without calf serum. Cells were then harvested, immediately lysed and samples further processed for immunoblotting.

5.13 Cell viability assays

DLBCL cell lines were treated for 48 hours with ibrutinib (concentration range 50 nM to 100 µM) and viability assessed using Cell Titer Glow (Promega). Luminescence was measured in a SpectraMax M5 plate reader (Molecular Devices). Cellular IC₅₀ was obtained by non-linear regression curve fit analysis. DMSO (50 µM) and doxorubicin (10 µM) were used as negative and positive controls, respectively. To assess the effects of repebodies on the viability of DLBCL, transduced cells were treated with 2 µg mL⁻¹ of doxycycline to induce expression of repebodies, and cell number verified using a Casy Cell Counter (OLS Omni Life Science). Cell density was maintained at 5x10⁵ cells mL⁻¹ and regularly diluted when cell density reached 3x10⁶ cells mL⁻¹. Parental (non-transduced) and non-induced cells were used as control.

5.14 Apoptosis staining

For the apoptosis staining, transduced cells were seeded in 6-well cell culture plates, treated with $2\text{ }\mu\text{g mL}^{-1}$ of doxycycline and/or ibrutinib, and stained for the apoptosis marker Annexin V. Briefly, cells were washed twice with PBS and resuspended in Annexin V binding buffer containing Cy5-Annexin V (BD) and 7AAD (BD) using instructions from the supplier. Cells were gently dissociated and filtered through a $35\text{ }\mu\text{m}$ nylon mesh before data acquisition in a Gallios flow cytometer (BD). A minimum of 10,000 gated events was collected for each sample and data was analyzed using the FlowJo (v10.6) software.

5.15 Development of repebodies

Selection and affinity maturation of human Btk SH2-specific repebody (rF10) were performed through phage display and a modular evolution approach as previously described³².

5.16 Molecular dynamics (MD) simulations

System preparation: Btk SH2-KD structural model used for our MD simulations was built starting from the X-ray structures of the apo-KD of Btk (PDB 1K2P) and SH2 domain (PDB 6HTF). Briefly, the SH2 domain was initially positioned at $\sim 60\text{ }\text{\AA}$ on the top of KD. The linker sequence was manually added using Maestro (Schrödinger Release 2016-1: Maestro, Schrödinger) and refined through scaled MD simulation. The protein was immersed in a water box neutralized by adding an appropriate number of Cl⁻ ions. After minimization, the protein underwent three simulations steps of 500 ps each to gradually reach the target temperature of 300 K. To enhance the sampling of the linker sequence, we performed a 70 ns long scaled MD simulations. To obtain the optimal configuration of the linker sequence, we performed a cluster analysis on the last 70 ns long trajectory. The centroid of the most populated cluster was then employed as a starting point for the next MD simulations. Both the MD simulations and cluster analysis were performed by using BiKi LifeSciences suite¹⁹⁵.

Scaled MD simulations: We run multiple replicas Scaled MD simulations¹⁸⁰ to enhance the sampling of Btk kinase and speed up the binding events between SH2 and KD. As a starting point, we employed the refined structure of the Btk SH2-KD-linker model. The equilibrated system was submitted to 40 replicates ~100 ns long scaled MD simulations. Here, restraints were not applied because the high scaling factor enabled adequate sampling without affecting the overall folding of the system. BiKi LifeSciences suite¹⁹⁵ was used for Scaled MD simulations, using similar settings as described above.

Data Analysis: The collected 4 μ s-long scaled MD trajectories resulted in a total of 400,000 frames. From this large ensemble, we extracted the unique and non-redundant Btk SH2-KD configurations, using a clustering procedure implemented in BiKi¹⁹⁵. The resulting 760 structures were submitted to another cluster analysis to probe the preferred 3D structural organization of SH2 domain with respect to KD. Also, we run a CRY SOL analysis¹⁹⁶ to compute the χ^2 value for each structure, in order to select the SH2-KD complexes with the best fitting with the experimental SAXS curves.

5.17 Small-angle X-ray scattering (SAXS)

SAXS data were collected at the BM29 beamline (ESRF Grenoble, France). All proteins were measured in buffer containing 25mM Tris pH 7.5, 300 mM NaCl, 1 mM TCEP, and 5% glycerol. A robotic sample changer measured in the batch mode, while in-line SEC-SAXS was performed using a Superdex S200 Increase 10/300 column (GE Healthcare) with a flow rate of 0.7 mL min⁻¹ at room temperature. Acquired data were averaged and subtracted from an appropriate solvent-blank to produce the final curve using the ATSAS Suite, EMBL¹⁹⁷, and CHROMIXS¹⁹⁸. Initial data pre-processing and reduction were performed using an automatic pipeline. Final scattering curves were analyzed using PRIMUS for evaluation of molecular dimensions (R_g) and maximum particle dimension (D_{max}) using GNOM¹⁹⁹. Moreover, the Porod volume was computed using the Porod invariant²⁰⁰, and the molecular mass estimated using SAXS MoW 2.0²⁰¹, Bayesian inference approach²⁰², and Volume-of-correlation. *Ab initio* models were computed with DAMMIF²⁰³. SREFLEX¹⁹⁸ was employed to improve the agreement of flexible multidomain models to the experimental data. Finally, the flexibility of multidomain complexes was assessed with Ensemble Optimization Method 2.0¹⁸⁴. Fitting of models to experimental data was assessed using CRY SOL¹⁹⁶ molecular and superimpositions performed with the

SASpy²⁰⁴. Data collection and structure determination statistics are described in Tables 4 and 6.

5.18 Crystallization, data collection, and structure determination

Recombinant Btk SH2 and rF10 proteins were mixed at 1:1 ratio and the complex purified with a Superdex 75 column 16/600 (GE Healthcare) in buffer containing 25 mM Tris pH 7.5, 300 mM NaCl, 1 mM TCEP. The purified complex was concentrated to ~25 mg mL⁻¹ and crystallized at 18°C using the hanging-drop vapor-diffusion method by mixing 1:1 with a solution containing 1 M Tris pH 8.5, 300 mM sodium fluoride, 300 mM sodium bromide, 300 mM sodium iodide, 25% MPD; 25% PEG 1000; 25% PEG 3350. 20% glycerol was used as a cryoprotectant. X-ray diffraction data was collected at the SLS Beamline X06DA in the Swiss Lightsource (SLS, Villigen, Switzerland) at a wavelength of 1 Å and temperature of 100 K. Data collection and structure determination statistics are described in Supplementary Table 3. Diffraction data was processed and scaled with the XDS package. The structure was solved by molecular replacement employing models derived from a previously reported rebody (PDB 5B4P) and Btk SH2 (PDB 2GE9) excluding loop regions. Molecular replacement, manual model building, B-factor refinement, solvent addition, energy-minimization, and refinement of structures were conducted iteratively using Phaser and Coot (Phenix version 1.13). Molecular graphics were generated using PyMOL (DeLano Scientific). Data collection and structure determination statistics are described in Table 5.

5.19 Isothermal titration calorimetry (ITC)

Proteins were extensively dialyzed in buffer containing 20 mM Hepes pH 7.5 and 150 mM NaCl, briefly degassed, and concentration determined by measuring UV absorbance at 280 nm. ITC measurements were performed on a MicroCal PEAQ-ITC (Malvern) instrument. The rebody (100 µM) was titrated into SH2 domains (10 µM) at room temperature in 16 steps with 0.49 µL for the first and 2.49 µL for the other steps. Thermodynamic parameters were obtained using the MicroCal software.

5.20 Fluorescent polarization (FP) binding assays

Btk SH2 WT and mutants were incubated at several concentrations with 1 μ M of FITC-labeled ADNDpYIIPLPD peptide in Tris 40 mM pH 8, 150 mM NaCl and 1 mM DTT. Competitive FP assay was performed using 25 μ M of Btk SH2 and 1 μ M of peptide incubated with rebody in a range of 200 μ M - 20 nM. FP signal was measured using a SpectraMax M5 plate reader (Molecular Devices) with excitation at 485 nm and emission at 530 nm in a 96 well black-plate (Greiner, 784-900).

5.21 *In vitro* kinase assay

2 μ M of rebodyes were pre-incubated with 1 μ M of recombinant Btk proteins in buffer Tris 25 mM pH 7.5, 150 mM NaCl, 5% glycerol, 20 mM MgCl₂, 1 mM DTT in the presence of 50 μ M ATP, 7 μ Ci γ -³²P-ATP, and PLC γ 2 peptide (biotin-ERDINSLYDVSRAmide). Peptide concentrations ranged from 100 μ M to 3.125 μ M. Reactions were carried out on a final volume of 20 μ L at room temperature for 20 minutes and terminated using 10 μ L 7.5 M guanidinihydrochlorid. Samples were spotted onto a SAM2 Biotin Capture membrane (Promega) and further treated according to the instructions of the manufacturer.

5.22 Mapping of Btk autophosphorylation sites

Sample preparation: Recombinant autophosphorylated Btk SH2-KD was separated by SDS-PAGE and stained with Coomassie. Bands of interest were excised, in-gel digested in reduced in 10 mM DTE, 50 mM AB, and then alkylated in 55 mM iodoacetamide, 50 mM AB. After a washing step, gel extracts were digested with MS Grade Trypsin over-night. Resulting peptides were finally extracted using a high organic containing solvent and dried by vacuum centrifugation before LC-MS2 measurements or phosphopeptides enrichment.

Next, 90% of the extracted peptide was used for phosphopeptides enrichment step while the remaining 10% was used for sample identification. Titanium dioxide affinity principle was used for enrichment using home-made titania tips. Dried samples were resuspended 0.75% TFA, 60% acetonitrile, 300 mg ml⁻¹ lactic acid, loaded on tips, and eluted in 0.5%

ammonium hydroxide and 5% piperidine. Samples were acidified and dried down prior to LC-MS2 measurements.

MS analysis: For the MS detection of phosphopeptides, dried samples were resuspended in 0.1% TFA and separated by C18 Reverse Phase nano UPLC using a Dionex Ultimate 3000 RSLC system (Thermo Fischer) connected to an Orbitrap Elite Mass Spectrometer (Thermo Fischer). Samples were first trapped on a home-made capillary C18 pre-column and then separated on a C18 capillary column (Nikkyo Technos Co; Magic AQ C18; 3 μ m - 100 Å; 15 cm x 75 μ m ID). Data-dependent mode was used for MS acquisitions where the 20 most intense parent ions were selected for subsequent fragmentation by CID. A potential phosphopeptides m/z inclusion list was also generated and used to maximize detection chances.

5.23 Quantification and statistical analysis

All data reported were analyzed using Prism 7 (GraphPad) using software-defined fitting models and unpaired *t*-test statistical tests. Calculated P-values are indicated as non-significant (ns), $p \leq 0.05$ (*), $p \leq 0.01$ (**), $p \leq 0.001$ (***) and $p \leq 0.0001$ (****).

5.24 Data availability

The X-ray structure of the rF10-SH2 complex was deposited at Protein Data Bank (PDB entry 6HTF). Full SAXS curves and analyzed data for WT Btk proteins were deposited at SASBDB (entries SASDF53, SASDF63, SASDF73, and SASDF83). Data can be accessed using the following hyperlinks:

www.rcsb.org/structure/6HTF

www.sasbdb.org/data/SASDF53/

www.sasbdb.org/data/SASDF63/

www.sasbdb.org/data/SASDF73/

www.sasbdb.org/data/SASDF83/

6 REFERENCES

1. Olsen, J. V. *et al.* Global, *In Vivo*, and Site-Specific Phosphorylation Dynamics in Signaling Networks. *Cell* **127**, 635–648 (2006).
2. Robinson, D. R., Wu, Y.-M. & Lin, S.-F. The protein tyrosine kinase family of the human genome. *Oncogene* **19**, 5548–5557 (2000).
3. Beenstock, J., Mooshayef, N. & Engelberg, D. How Do Protein Kinases Take a Selfie (Autophosphorylate)? *Trends Biochem. Sci.* **41**, 938–953 (2016).
4. Knighton, D. R. *et al.* Crystal structure of the catalytic subunit of cyclic adenosine monophosphate-dependent protein kinase. *Science* **253**, 407–414 (1991).
5. Huse, M. & Kuriyan, J. The conformational plasticity of protein kinases. *Cell* **109**, 275–282 (2002).
6. Endicott, J. A., Noble, M. E. M. & Johnson, L. N. The structural basis for control of eukaryotic protein kinases. *Annu. Rev. Biochem.* **81**, 587–613 (2012).
7. Schindler, T. *et al.* Structural Mechanism for STI-571 Inhibition of Abelson Tyrosine Kinase. *Science* **289**, 1938–1942 (2000).
8. Shah, N. H., Amacher, J. F., Nocka, L. M. & Kuriyan, J. The Src module: an ancient scaffold in the evolution of cytoplasmic tyrosine kinases. *Crit. Rev. Biochem. Mol. Biol.* **53**, 535–563 (2018).
- *This is an Open Access article distributed under the terms of the Creative Commons CC BY license. Figures were reproduced following the copyright directives from the journal found in the following page:
www.tandfonline.com/doi/abs/10.1080/10409238.2018.1495173?tab=permissions&scroll=top
9. Pawson, T., Raina, M. & Nash, P. Interaction domains: from simple binding events to complex cellular behavior. *FEBS Lett.* **513**, 2–10 (2002).
10. Filippakopoulos, P., Müller, S. & Knapp, S. SH2 domains: modulators of nonreceptor tyrosine kinase activity. *Curr. Opin. Struct. Biol.* **19**, 643–649 (2009).
11. Saksela, K. & Permi, P. SH3 domain ligand binding: What's the consensus and where's the specificity? *FEBS Lett.* **586**, 2609–2614 (2012).
12. Superti-Furga, G., Fumagalli, S., Koegl, M., Courtneidge, S. A. & Draetta, G. Csk inhibition of c-Src activity requires both the SH2 and SH3 domains of Src. *EMBO J.* **12**, 2625–2634 (1993).

13. Xu, W., Doshi, A., Lei, M., Eck, M. J. & Harrison, S. C. Crystal structures of c-Src reveal features of its autoinhibitory mechanism. *Mol. Cell* **3**, 629–638 (1999).
14. Hantschel, O. *et al.* A myristoyl/phosphotyrosine switch regulates c-Abl. *Cell* **112**, 845–857 (2003).
15. Nagar, B. *et al.* Structural basis for the autoinhibition of c-Abl tyrosine kinase. *Cell* **112**, 859–871 (2003).
16. Filippakopoulos, P. *et al.* Structural coupling of SH2-kinase domains links Fes and Abl substrate recognition and kinase activation. *Cell* **134**, 793–803 (2008).
17. Lorenz, S., Deng, P., Hantschel, O., Superti-Furga, G. & Kuriyan, J. Crystal structure of an SH2-kinase construct of c-Abl and effect of the SH2 domain on kinase activity. *Biochem. J.* **468**, 283–291 (2015).
18. Nagar, B. *et al.* Organization of the SH3-SH2 unit in active and inactive forms of the c-Abl tyrosine kinase. *Mol. Cell* **21**, 787–798 (2006).
19. Lamontanara, A. J., Georgeon, S., Tria, G., Svergun, D. I. & Hantschel, O. The SH2 domain of Abl kinases regulates kinase autophosphorylation by controlling activation loop accessibility. *Nat Commun* **5**, 5470 (2014).
20. Sherbenou, D. W. *et al.* BCR-ABL SH3-SH2 domain mutations in chronic myeloid leukemia patients on imatinib. *Blood* **116**, 3278–3285 (2010).
21. Grebien, F. *et al.* Targeting the SH2-kinase interface in Bcr-Abl inhibits leukemogenesis. *Cell* **147**, 306–319 (2011).
22. Li, Y. H. *et al.* The Human Kinome Targeted by FDA Approved Multi-Target Drugs and Combination Products: A Comparative Study from the Drug-Target Interaction Network Perspective. *PLoS ONE* **11**, e0165737 (2016).
23. Hantschel, O., Grebien, F. & Superti-Furga, G. The growing arsenal of ATP-competitive and allosteric inhibitors of BCR-ABL. *Cancer Res.* **72**, 4890–4895 (2012).
24. Druker, B. J. *et al.* Activity of a specific inhibitor of the BCR-ABL tyrosine kinase in the blast crisis of chronic myeloid leukemia and acute lymphoblastic leukemia with the Philadelphia chromosome. *N. Engl. J. Med.* **344**, 1038–1042 (2001).
25. Hochhaus, A. *et al.* Molecular and chromosomal mechanisms of resistance to imatinib (STI571) therapy. *Leukemia* **16**, 2190–2196 (2002).
26. Giles, F. J. *et al.* Nilotinib in imatinib-resistant or imatinib-intolerant patients with chronic myeloid leukemia in chronic phase: 48-month follow-up results of a phase II study. *Leukemia* **27**, 107–112 (2013).
27. Wylie, A. A. *et al.* The allosteric inhibitor ABL001 enables dual targeting of BCR–ABL1. *Nature* **543**, 733–737 (2017).
28. Qiu, X. & Che, Y. Faculty of 1000 evaluation for The allosteric inhibitor ABL001 enables dual targeting of BCR-ABL1. *Nature* **543**, 733–737 (2017).
29. Zhang, J. *et al.* Targeting Bcr–Abl by combining allosteric with ATP-binding-site inhibitors. *Nature* **463**, 501–506 (2010).

30. Eide, C. A. *et al.* Combining the Allosteric Inhibitor Asciminib with Ponatinib Suppresses Emergence of and Restores Efficacy against Highly Resistant BCR-ABL1 Mutants. *Cancer Cell* **36**, 431–443.e5 (2019).
31. Koide, A., Bailey, C. W., Huang, X. & Koide, S. The fibronectin type III domain as a scaffold for novel binding proteins. *J. Mol. Biol.* **284**, 1141–1151 (1998).
32. Lee, S.-C. *et al.* Design of a binding scaffold based on variable lymphocyte receptors of jawless vertebrates by module engineering. *Proc. Natl. Acad. Sci. U.S.A.* **109**, 3299–3304 (2012).
33. Wojcik, J. *et al.* Allosteric Inhibition of Bcr-Abl Kinase by High Affinity Monobody Inhibitors Directed to the Src Homology 2 (SH2)-Kinase Interface. *J. Biol. Chem.* **291**, 8836–8847 (2016).
34. Kükenshöner, T. *et al.* Selective Targeting of SH2 Domain-Phosphotyrosine Interactions of Src Family Tyrosine Kinases with Monobodies. *J. Mol. Biol.* **429**, 1364–1380 (2017).
35. Spencer-Smith, R. *et al.* Inhibition of RAS function through targeting an allosteric regulatory site. *Nat. Chem. Biol.* **13**, 62–68 (2017).
36. Gupta, A. *et al.* Facile target validation in an animal model with intracellularly expressed monobodies. *Nat. Chem. Biol.* **14**, 895–900 (2018).
37. Yun, M. *et al.* A High-Affinity Repebody for Molecular Imaging of EGFR-Expressing Malignant Tumors. *Theranostics* **7**, 2620–2633 (2017).
38. Roth, D. B. V(D)J Recombination: Mechanism, Errors, and Fidelity. *Microbiol Spectr* **2**, (2014).
39. Eisen, H. N. Affinity enhancement of antibodies: how low-affinity antibodies produced early in immune responses are followed by high-affinity antibodies later and in memory B-cell responses. *Cancer Immunol Res* **2**, 381–392 (2014).
40. Rickert, R. C. New insights into pre-BCR and BCR signalling with relevance to B-cell malignancies. *Nat Rev Immunol* **13**, 578–591 (2013).
41. Yeoh, E.-J. *et al.* Classification, subtype discovery, and prediction of outcome in pediatric acute lymphoblastic leukemia by gene expression profiling. *Cancer Cell* **1**, 133–143 (2002).
42. Smith, A. *et al.* Lymphoma incidence, survival and prevalence 2004-2014: sub-type analyses from the UK's Haematological Malignancy Research Network. *Br. J. Cancer* **112**, 1575–1584 (2015).
43. Treanor, B. B-cell receptor: from resting state to activate. *Immunology* **136**, 21–27 (2012).
44. Yang, J. & Reth, M. in *B-cell Receptor Signaling* **393**, 27–43 (Springer, Cham, 2015).
45. Kim, Y. J., Sekiya, F., Poulin, B., Bae, Y. S. & Rhee, S. G. Mechanism of B-cell receptor-induced phosphorylation and activation of phospholipase C-gamma2. *Mol. Cell. Biol.* **24**, 9986–9999 (2004).
46. Wen, Y. *et al.* The regulators of BCR signaling during B-cell activation. *Blood Science* **1**, 119 (2019).

47. Kraus, M., Alimzhanov, M. B., Rajewsky, N. & Rajewsky, K. Survival of resting mature B lymphocytes depends on BCR signaling via the Igalpha/beta heterodimer. *Cell* **117**, 787–800 (2004).
48. Burger, J. A. & Chiorazzi, N. B-cell receptor signaling in chronic lymphocytic leukemia. *Trends Immunol.* **34**, 592–601 (2013).
49. Ngo, V. N. *et al.* A loss-of-function RNA interference screen for molecular targets in cancer. *Nature* **441**, 106–110 (2006).
50. Davis, R. E. *et al.* Chronic active B-cell-receptor signalling in diffuse large B-cell lymphoma. *Nature* **463**, 88–92 (2010).
51. Kraan, W. *et al.* High prevalence of oncogenic MYD88 and CD79B mutations in diffuse large B-cell lymphomas presenting at immune-privileged sites. *Blood Cancer J* **3**, e139–e139 (2013).
52. Schmitz, R. *et al.* Genetics and Pathogenesis of Diffuse Large B-Cell Lymphoma. *New England Journal of Medicine* **378**, 1396–1407 (2018).
53. Thompson, A. A. *et al.* Aberrations of the B-cell receptor B29 (CD79b) gene in chronic lymphocytic leukemia. *Blood* **90**, 1387–1394 (1997).
54. Contri, A. *et al.* Chronic lymphocytic leukemia B-cells contain anomalous Lyn tyrosine kinase, a putative contribution to defective apoptosis. *J. Clin. Invest.* **115**, 369–378 (2005).
55. Gobessi, S. *et al.* Inhibition of constitutive and BCR-induced Syk activation downregulates Mcl-1 and induces apoptosis in chronic lymphocytic leukemia B-cells. *Leukemia* **23**, 686–697 (2009).
56. Muzio, M. *et al.* Constitutive activation of distinct BCR-signaling pathways in a subset of CLL patients: a molecular signature of anergy. *Blood* **112**, 188–195 (2008).
57. Hewamana, S. *et al.* The NF-kappaB subunit Rel A is associated with *in vitro* survival and clinical disease progression in chronic lymphocytic leukemia and represents a promising therapeutic target. *Blood* **111**, 4681–4689 (2008).
58. Refaeli, Y. *et al.* The B-cell antigen receptor and overexpression of MYC can cooperate in the genesis of B-cell lymphomas. *PLoS Biol.* **6**, e152 (2008).
59. García-Muñoz, R., Galiacho, V. R. & Llorente, L. Immunological aspects in chronic lymphocytic leukemia (CLL) development. *Ann. Hematol.* **91**, 981–996 (2012).
60. Xu, Y., Harder, K. W., Huntington, N. D., Hibbs, M. L. & Tarlinton, D. M. Lyn tyrosine kinase: accentuating the positive and the negative. *Immunity* **22**, 9–18 (2005).
61. Tomita, N. *et al.* Standard R-CHOP therapy in follicular lymphoma and diffuse large B-cell lymphoma. *J Clin Exp Hematop* **53**, 121–125 (2013).
62. Liu, D. & Mamorska-Dyga, A. Syk inhibitors in clinical development for hematological malignancies. *J Hematol Oncol* **10**, 145–7 (2017).
63. Curran, E. & Smith, S. M. Phosphoinositide 3-kinase inhibitors in lymphoma. *Curr Opin Oncol* **26**, 469–475 (2014).
64. Seymour, J. F. *et al.* Venetoclax-Rituximab in Relapsed or Refractory Chronic Lymphocytic Leukemia. *N. Engl. J. Med.* **378**, 1107–1120 (2018).

65. Richardson, P. G. *et al.* A phase 2 study of bortezomib in relapsed, refractory myeloma. *N. Engl. J. Med.* **348**, 2609–2617 (2003).
66. Hajek, R. *et al.* A Phase 2 Study of Ibrutinib in Combination with Bortezomib and Dexamethasone in Patients with Relapsed/Refractory Multiple Myeloma. *Eur. J. Haematol.* *ejh*.13377 (2019). doi:10.1111/ejh.13377
67. Mohanty, R. *et al.* CAR T cell therapy: A new era for cancer treatment (Review). *Oncol. Rep.* **42**, 2183–2195 (2019).
68. Neelapu, S. S. *et al.* Axicabtagene Ciloleucel CAR T-Cell Therapy in Refractory Large B-Cell Lymphoma. *N. Engl. J. Med.* **377**, 2531–2544 (2017).
69. Maude, S. L., Teachey, D. T., Porter, D. L. & Grupp, S. A. CD19-targeted chimeric antigen receptor T-cell therapy for acute lymphoblastic leukemia. *Blood* **125**, 4017–4023 (2015).
70. Shah, N. N. & Fry, T. J. Mechanisms of resistance to CAR T cell therapy. *Nat Rev Clin Oncol* **16**, 372–385 (2019).
71. Liu, E. *et al.* Use of CAR-Transduced Natural Killer Cells in CD19-Positive Lymphoid Tumors. *N. Engl. J. Med.* **382**, 545–553 (2020).
72. Wardemann, H. *et al.* Predominant autoantibody production by early human B-cell precursors. *Science* **301**, 1374–1377 (2003).
73. Samuels, J., Ng, Y.-S., Coupillaud, C., Paget, D. & Meffre, E. Impaired early B-cell tolerance in patients with rheumatoid arthritis. *J. Exp. Med.* **201**, 1659–1667 (2005).
74. Yurasov, S. *et al.* Defective B-cell tolerance checkpoints in systemic lupus erythematosus. *J. Exp. Med.* **201**, 703–711 (2005).
75. McInnes, I. B. & Schett, G. The pathogenesis of rheumatoid arthritis. *N. Engl. J. Med.* **365**, 2205–2219 (2011).
76. Song, Y. W. & Kang, E. H. Autoantibodies in rheumatoid arthritis: rheumatoid factors and anticitrullinated protein antibodies. *QJM* **103**, 139–146 (2010).
77. Cohen, M. D. & Keystone, E. Rituximab for Rheumatoid Arthritis. *Rheumatol Ther* **2**, 99–111 (2015).
78. Cheung, T. T. & McInnes, I. B. Future therapeutic targets in rheumatoid arthritis? *Semin Immunopathol* **39**, 487–500 (2017).
79. Ferrari, S. *et al.* Mutations of the Igbeta gene cause agammaglobulinemia in man. *J. Exp. Med.* **204**, 2047–2051 (2007).
80. ORCHS, H. D. X-linked agammaglobulinemia. A clinical and molecular analysis. *Medicine* **75**, 287–299 (1996).
81. Vetrie, D. *et al.* The gene involved in X-linked agammaglobulinaemia is a member of the src family of protein-tyrosine kinases. *Nature* **361**, 226–233 (1993).
82. Väliäho, J., Smith, C. I. E. & Vihinen, M. BTKbase: the mutation database for X-linked agammaglobulinemia. *Hum. Mutat.* **27**, 1209–1217 (2006).
83. Fukuda, M., Kojima, T., Kabayama, H. & Mikoshiba, K. Mutation of the pleckstrin homology domain of Bruton's tyrosine kinase in immunodeficiency

- impaired inositol 1,3,4,5-tetrakisphosphate binding capacity. *J. Biol. Chem.* **271**, 30303–30306 (1996).
84. Hyvönen, M. & Saraste, M. Structure of the PH domain and Btk motif from Bruton's tyrosine kinase: molecular explanations for X-linked agammaglobulinaemia. *EMBO J.* **16**, 3396–3404 (1997).
85. Zhu, Q. *et al.* Deletion within the Src homology domain 3 of Bruton's tyrosine kinase resulting in X-linked agammaglobulinemia (XLA). *J. Exp. Med.* **180**, 461–470 (1994).
86. Mattsson, P. T. *et al.* Six X-Linked Agammaglobulinemia-Causing Missense Mutations in the Src Homology 2 Domain of Bruton's Tyrosine Kinase: Phosphotyrosine-Binding and Circular Dichroism Analysis. *The Journal of Immunology* **164**, 4170–4177 (2000).
87. Fluckiger, A. C. *et al.* Btk/Tec kinases regulate sustained increases in intracellular Ca²⁺ following B-cell receptor activation. *EMBO J.* **17**, 1973–1985 (1998).
88. Pérez de Diego, R. *et al.* Naturally occurring Bruton's tyrosine kinase mutations have no dominant negative effect in an X-linked agammaglobulinaemia cellular model. *Clin. Exp. Immunol.* **152**, 33–38 (2008).
89. Joseph, R. E., Severin, A., Min, L., Fulton, D. B. & Andreotti, A. H. SH2-dependent autophosphorylation within the Tec family kinase Itk. *J. Mol. Biol.* **391**, 164–177 (2009).
90. Mao, C., Zhou, M. & Uckun, F. M. Crystal structure of Bruton's tyrosine kinase domain suggests a novel pathway for activation and provides insights into the molecular basis of X-linked agammaglobulinemia. *J. Biol. Chem.* **276**, 41435–41443 (2001).
91. Väliäho, J., Faisal, I., Ortutay, C., Smith, C. I. E. & Vihinen, M. Characterization of all possible single-nucleotide change caused amino acid substitutions in the kinase domain of Bruton tyrosine kinase. *Hum. Mutat.* **36**, 638–647 (2015).
92. Guo, S., Wahl, M. I. & Witte, O. N. Mutational analysis of the SH2-kinase linker region of Bruton's tyrosine kinase defines alternative modes of regulation for cytoplasmic tyrosine kinase families. *Int. Immunol.* **18**, 79–87 (2006).
93. Middendorp, S., Dingjan, G. M., Maas, A., Dahlenborg, K. & Hendriks, R. W. Function of Bruton's tyrosine kinase during B-cell development is partially independent of its catalytic activity. *The Journal of Immunology* **171**, 5988–5996 (2003).
94. Karube, K. *et al.* Integrating genomic alterations in diffuse large B-cell lymphoma identifies new relevant pathways and potential therapeutic targets. *Leukemia* **32**, 675–684 (2018).
95. Young, R. M. *et al.* Crispr-Cas9 genetic screens uncover a b-cell receptor-MYD88 superpathway in diffuse large B-cell lymphoma. *Hematol Oncol* **35**, 25–25 (2017).
96. Phelan, J. D. *et al.* A multiprotein supercomplex controlling oncogenic signalling in lymphoma. *Nature* **560**, 387–391 (2018).

-
97. Aoki, Y., Isselbacher, K. J. & Pillai, S. Bruton tyrosine kinase is tyrosine phosphorylated and activated in pre-B lymphocytes and receptor-ligated B-cells. *Proc. Natl. Acad. Sci. U.S.A.* **91**, 10606–10609 (1994).
 98. de Weers, M. *et al.* B-cell antigen receptor stimulation activates the human Bruton's tyrosine kinase, which is deficient in X-linked agammaglobulinemia. *J. Biol. Chem.* **269**, 23857–23860 (1994).
 99. Di Paolo, J. A. *et al.* Specific Btk inhibition suppresses B-cell- and myeloid cell-mediated arthritis. *Nat. Chem. Biol.* **7**, 41–50 (2011).
 100. Crofford, L. J., Nyhoff, L. E., Sheehan, J. H. & Kendall, P. L. The role of Bruton's tyrosine kinase in autoimmunity and implications for therapy. *Expert Review of Clinical Immunology* **12**, 763–773 (2016).
 101. Molina-Cerrillo, J., Alonso-Gordoa, T., Gajate, P. & Grande, E. Bruton's tyrosine kinase (BTK) as a promising target in solid tumors. *Cancer Treatment Reviews* **58**, 41–50 (2017).
 102. Mahajan, S. *et al.* Rational design and synthesis of a novel anti-leukemic agent targeting Bruton's tyrosine kinase (BTK), LFM-A13 [alpha-cyano-beta-hydroxy-beta-methyl-N-(2, 5-dibromophenyl)propenamide]. *J. Biol. Chem.* **274**, 9587–9599 (1999).
 103. Akker, E. V. D. *et al.* The Btk inhibitor LFM-A13 is a potent inhibitor of Jak2 kinase activity. *Biological Chemistry* **385**, 409–413
 104. Hantschel, O. *et al.* The Btk tyrosine kinase is a major target of the Bcr-Abl inhibitor dasatinib. *Proc. Natl. Acad. Sci. U.S.A.* **104**, 13283–13288 (2007).
 105. Liu, Q. *et al.* Developing irreversible inhibitors of the protein kinase cysteinome. *Chem. Biol.* **20**, 146–159 (2013).
 106. Copland, M. *et al.* Dasatinib (BMS-354825) targets an earlier progenitor population than imatinib in primary CML but does not eliminate the quiescent fraction. *Blood* **107**, 4532–4539 (2006).
 107. Honigberg, L. A. *et al.* The Bruton tyrosine kinase inhibitor PCI-32765 blocks B-cell activation and is efficacious in models of autoimmune disease and B-cell malignancy. *Proc. Natl. Acad. Sci. U.S.A.* **107**, 13075–13080 (2010).
 108. Wu, J., Zhang, M. & Liu, D. Acalabrutinib (ACP-196): a selective second-generation BTK inhibitor. *J Hematol Oncol* **9**, 21–4 (2016).
 109. Guo, Y. *et al.* Discovery of Zanubrutinib (BGB-3111), a Novel, Potent, and Selective Covalent Inhibitor of Bruton's Tyrosine Kinase. *J. Med. Chem.* **62**, 7923–7940 (2019).
 110. Kozaki, R., Yoshizawa, T., Yasuhiro, T., Res, J. M. C.2012. Development of a Bruton's tyrosine kinase (Btk) inhibitor–ONO-WG-307, a potential treatment for B-cell malignancies. *oncodesign.com*
 111. Crawford, J. J. *et al.* Discovery of GDC-0853: A Potent, Selective, and Noncovalent Bruton's Tyrosine Kinase Inhibitor in Early Clinical Development. *J. Med. Chem.* **61**, 2227–2245 (2018).
 112. Binnerts, M. E. *et al.* Abstract C186: SNS-062 is a potent noncovalent BTK inhibitor with comparable activity against wild type BTK and BTK with an acquired resistance mutation. *Mol. Cancer Ther.* **14**, C186–C186 (2015).

-
113. Reiff, S. D. *et al.* The BTK Inhibitor ARQ 531 Targets Ibrutinib-Resistant CLL and Richter Transformation. *Cancer Discov* **8**, 1300–1315 (2018).
 114. Brandhuber, B. *et al.* LOXO-305, A Next Generation Reversible BTK Inhibitor, for Overcoming Acquired Resistance to Irreversible BTK Inhibitors. *Clin Lymphoma Myeloma Leuk* **18**, S216 (2018).
 115. Hendriks, R. W., Yuvaraj, S. & Kil, L. P. Targeting Bruton's tyrosine kinase in B-cell malignancies. *Nat. Rev. Cancer* **14**, 219–232 (2014).
 116. Barr, P. M. *et al.* Sustained efficacy and detailed clinical follow-up of first-line ibrutinib treatment in older patients with chronic lymphocytic leukemia: extended phase 3 results from RESONATE-2. *Haematologica* **103**, 1502–1510 (2018).
 117. Byrd, J. C. *et al.* Ibrutinib versus ofatumumab in previously treated chronic lymphoid leukemia. *N. Engl. J. Med.* **371**, 213–223 (2014).
 118. O'Brien, S. *et al.* Ibrutinib for patients with relapsed or refractory chronic lymphocytic leukaemia with 17p deletion (RESONATE-17): a phase 2, open-label, multicentre study. *Lancet Oncol.* **17**, 1409–1418 (2016).
 119. Thompson, P. A. *et al.* Atrial fibrillation in CLL patients treated with ibrutinib. An international retrospective study. *Br. J. Haematol.* **175**, 462–466 (2016).
 120. Brown, J. R. *et al.* Characterization of atrial fibrillation adverse events reported in ibrutinib randomized controlled registration trials. *Haematologica* **102**, 1796–1805 (2017).
 121. Baptiste, F. *et al.* High incidence of atrial fibrillation in patients treated with ibrutinib. *Open Heart* **6**, e001049 (2019).
 122. Gao, W. *et al.* Selective antitumor activity of ibrutinib in EGFR-mutant non-small cell lung cancer cells. *J. Natl. Cancer Inst.* **106**, 13075 (2014).
 123. Yang, G. *et al.* HCK is a survival determinant transactivated by mutated MYD88, and a direct target of ibrutinib. *Blood* **127**, 3237–3252 (2016).
 124. Senis, Y. A., Mazharian, A. & Mori, J. Src family kinases: at the forefront of platelet activation. *Blood* **124**, 2013–2024 (2014).
 125. Lee, R. H., Piatt, R., Conley, P. B. & Bergmeier, W. Effects of ibrutinib treatment on murine platelet function during inflammation and in primary hemostasis. *Haematologica* **102**, e89–e92 (2017).
 126. Bye, A. P. *et al.* Ibrutinib Inhibits Platelet Integrin $\alpha\text{IIb}\beta 3$ Outside-In Signaling and Thrombus Stability But Not Adhesion to Collagen. *Arterioscler. Thromb. Vasc. Biol.* **35**, 2326–2335 (2015).
 127. McMullen, J. R. *et al.* Ibrutinib increases the risk of atrial fibrillation, potentially through inhibition of cardiac PI3K-Akt signaling. *Blood* **124**, 3829–3830 (2014).
 128. Barf, T. *et al.* Acalabrutinib (ACP-196): A Covalent Bruton Tyrosine Kinase Inhibitor with a Differentiated Selectivity and *In Vivo* Potency Profile. *J. Pharmacol. Exp. Ther.* **363**, 240–252 (2017).
 129. Patel, V. *et al.* Comparison of Acalabrutinib, A Selective Bruton Tyrosine Kinase Inhibitor, with Ibrutinib in Chronic Lymphocytic Leukemia Cells. *Clin. Cancer Res.* **23**, 3734–3743 (2017).

-
130. Byrd, J. C. *et al.* Acalabrutinib (ACP-196) in Relapsed Chronic Lymphocytic Leukemia. *N. Engl. J. Med.* **374**, 323–332 (2016).
 131. Wang, M. *et al.* Acalabrutinib in relapsed or refractory mantle cell lymphoma (ACE-LY-004): a single-arm, multicentre, phase 2 trial. *Lancet* **391**, 659–667 (2018).
 132. Li, N. *et al.* Abstract 2597: BGB-3111 is a novel and highly selective Bruton's tyrosine kinase (BTK) inhibitor. *Cancer Res.* **75**, 2597–2597 (2015).
 133. Syed, Y. Y. Zanubrutinib: First Approval. *Drugs* **80**, 91–97 (2020).
 134. Tam, C. S. *et al.* Phase 1 study of the selective BTK inhibitor zanubrutinib in B-cell malignancies and safety and efficacy evaluation in CLL. *Blood* **134**, 851–859 (2019).
 135. Wu, H. *et al.* Irreversible inhibition of BTK kinase by a novel highly selective inhibitor CHMFL-BTK-11 suppresses inflammatory response in rheumatoid arthritis model. *Sci Rep* **7**, 466 (2017).
 136. Chang, B. Y. *et al.* The Bruton tyrosine kinase inhibitor PCI-32765 ameliorates autoimmune arthritis by inhibition of multiple effector cells. *Arthritis Res Ther* **13**, 1–15 (2011).
 137. Woyach, J. A. *et al.* Resistance mechanisms for the Bruton's tyrosine kinase inhibitor ibrutinib. *N. Engl. J. Med.* **370**, 2286–2294 (2014).
 138. Woyach, J. A. How I manage ibrutinib-refractory chronic lymphocytic leukemia. *Blood* **129**, 1270–1274 (2017).
 139. Cheng, S. *et al.* Functional characterization of BTK(C481S) mutation that confers ibrutinib resistance: exploration of alternative kinase inhibitors. *Leukemia* **29**, 895–900 (2015).
 140. Neuman, L. L. *et al.* First-in-Human Phase 1a Study of the Safety, Pharmacokinetics, and Pharmacodynamics of the Noncovalent Bruton Tyrosine Kinase (BTK) Inhibitor SNS-062 in Healthy Subjects. *Blood* **128**, 2032–2032 (2016).
 141. Mohamed, A. J. *et al.* Bruton's tyrosine kinase (Btk): function, regulation, and transformation with special emphasis on the PH domain. *Immunol. Rev.* **228**, 58–73 (2009).
 142. Rawlings, D. J. *et al.* Activation of BTK by a phosphorylation mechanism initiated by SRC family kinases. *Science* **271**, 822–825 (1996).
 143. Baba, Y. *et al.* BLNK mediates Syk-dependent Btk activation. *Proc. Natl. Acad. Sci. U.S.A.* **98**, 2582–2586 (2001).
 144. Wang, Q. *et al.* Autoinhibition of Bruton's tyrosine kinase (Btk) and activation by soluble inositol hexakisphosphate. *Elife* **4**, 1948 (2015).
 145. Park, H. *et al.* Regulation of Btk function by a major autophosphorylation site within the SH3 domain. *Immunity* **4**, 515–525 (1996).
 146. Wilcox, H. M. & Berg, L. J. Itk Phosphorylation Sites Are Required for Functional Activity in Primary T Cells. *J. Biol. Chem.* **278**, 37112–37121 (2003).
 147. Morrogh, L. M., Hinshelwood, S., Costello, P., Cory, G. O. & Kinnon, C. The SH3 domain of Bruton's tyrosine kinase displays altered ligand binding

- properties when auto-phosphorylated *in vitro*. *Eur. J. Immunol.* **29**, 2269–2279 (1999).
148. Nore, B. F. *et al.* Identification of phosphorylation sites within the SH3 domains of Tec family tyrosine kinases. *Biochimica et Biophysica Acta (BBA) - Proteins and Proteomics* **1645**, 123–132 (2003).
149. Kang, S. W. PKC β modulates antigen receptor signaling via regulation of Btk membrane localization. *EMBO J.* **20**, 5692–5702 (2001).
150. Fu, C., Turck, C. W., Kurosaki, T. & Chan, A. C. BLNK: a central linker protein in B-cell activation. *Immunity* **9**, 93–103 (1998).
151. Rodriguez, R. *et al.* Tyrosine residues in phospholipase C γ 2 essential for the enzyme function in B-cell signaling. *J. Biol. Chem.* **276**, 47982–47992 (2001).
152. Humphries, L. A. *et al.* Tec kinases mediate sustained calcium influx via site-specific tyrosine phosphorylation of the phospholipase C γ Src homology 2–Src homology 3 linker. *J. Biol. Chem.* **279**, 37651–37661 (2004).
153. Pal Singh, S., Dammeijer, F. & Hendriks, R. W. Role of Bruton's tyrosine kinase in B-cells and malignancies. *Mol. Cancer* **17**, 57 (2018).
154. Baraldi, E. *et al.* Structure of the PH domain from Bruton's tyrosine kinase in complex with inositol 1,3,4,5-tetrakisphosphate. *Structure* **7**, 449–460 (1999).
155. Murayama, K. *et al.* Crystal structure of the Bruton's tyrosine kinase PH domain with phosphatidylinositol. *Biochemical and Biophysical Research Communications* **377**, 23–28 (2008).
156. Henrik Hansson *et al.* Solution Structure of the SH3 Domain from Bruton's Tyrosine Kinase†,‡. *Biochemistry* **37**, 2912–2924 (1998).
157. Tzeng, S.-R., Lou, Y.-C., Pai, M.-T., Jain, M. L. & Cheng, J.-W. Solution structure of the human BTK SH3 domain complexed with a proline-rich peptide from p120cbl. *J. Biomol. NMR* **16**, 303–312 (2000).
158. Huang, K.-C., Cheng, H.-T., Pai, M.-T., Tzeng, S.-R. & Cheng, J.-W. Solution structure and phosphopeptide binding of the SH2 domain from the human Bruton's tyrosine kinase. *J. Biomol. NMR* **36**, 73–78 (2006).
159. Marcotte, D. J. *et al.* Structures of human Bruton's tyrosine kinase in active and inactive conformations suggest a mechanism of activation for TEC family kinases. *Protein Sci.* **19**, 429–439 (2010).
160. Bender, A. T. *et al.* Ability of Bruton's Tyrosine Kinase Inhibitors to Sequester Y551 and Prevent Phosphorylation Determines Potency for Inhibition of Fc Receptor but not B-Cell Receptor Signaling. *Mol. Pharmacol.* **91**, 208–219 (2017).
161. Várnai, P., Rother, K. I. & Balla, T. Phosphatidylinositol 3-kinase-dependent membrane association of the Bruton's tyrosine kinase pleckstrin homology domain visualized in single living cells. *J. Biol. Chem.* **274**, 10983–10989 (1999).
162. Li, T. *et al.* Activation of Bruton's tyrosine kinase (BTK) by a point mutation in its pleckstrin homology (PH) domain. *Immunity* **2**, 451–460 (1995).

-
163. Wang, Q., Pechersky, Y., Sagawa, S., Pan, A. C. & Shaw, D. E. Structural mechanism for Bruton's tyrosine kinase activation at the cell membrane. *Proc. Natl. Acad. Sci. U.S.A.* **116**, 9390–9399 (2019).
164. Hashimoto, S. *et al.* Identification of the SH2 domain binding protein of Bruton's tyrosine kinase as BLNK--functional significance of Btk-SH2 domain in B-cell antigen receptor-coupled calcium signaling. *Blood* **94**, 2357–2364 (1999).
165. Kuglstatter, A. *et al.* Insights into the conformational flexibility of Bruton's tyrosine kinase from multiple ligand complex structures. *Protein Sci.* **20**, 428–436 (2011).
166. Boyken, S. E. *et al.* A Conserved Isoleucine Maintains the Inactive State of Bruton's Tyrosine Kinase. *J. Mol. Biol.* **426**, 3656–3669 (2014).
167. Joseph, R. E., Wales, T. E., Fulton, D. B., Engen, J. R. & Andreotti, A. H. Achieving a Graded Immune Response: BTK Adopts a Range of Active/Inactive Conformations Dictated by Multiple Interdomain Contacts. *Structure* (2017). doi:10.1016/j.str.2017.07.014
168. Amatya, N. *et al.* Lipid-targeting pleckstrin homology domain turns its autoinhibitory face toward the TEC kinases. *PNAS* **116**, 21539–21544 (2019).
169. Márquez, J. A. *et al.* Conformation of full-length Bruton tyrosine kinase (Btk) from synchrotron X-ray solution scattering. *EMBO J.* **22**, 4616–4624 (2003).
170. Hawkins, J. & Marcy, A. Characterization of Itk tyrosine kinase: contribution of noncatalytic domains to enzymatic activity. *Protein Expr. Purif.* **22**, 211–219 (2001).
171. Joseph, R. E., Min, L. & Andreotti, A. H. The linker between SH2 and kinase domains positively regulates catalysis of the Tec family kinases. *Biochemistry* **46**, 5455–5462 (2007).
172. Joseph, R. E. & Andreotti, A. H. Controlling the activity of the Tec kinase Itk by mutation of the phenylalanine gatekeeper residue. *Biochemistry* **50**, 221–229 (2011).
173. Chopra, N. *et al.* Dynamic Allostery Mediated by a Conserved Tryptophan in the Tec Family Kinases. *PLoS Comput Biol* **12**, e1004826 (2016).
174. Chung, J. K. *et al.* Switch-like activation of Bruton's tyrosine kinase by membrane-mediated dimerization. *Proc. Natl. Acad. Sci. U.S.A.* **116**, 10798–10803 (2019).
175. Luckow, V. A., Lee, S. C., Barry, G. F. & Olins, P. O. Efficient generation of infectious recombinant baculoviruses by site-specific transposon-mediated insertion of foreign genes into a baculovirus genome propagated in *Escherichia coli*. *J. Virol.* **67**, 4566–4579 (1993).
176. Ciccarone, V. C., Polayes, D. A. & Luckow, V. A. Generation of Recombinant Baculovirus DNA in *E.coli* Using a Baculovirus Shuttle Vector. *Methods Mol. Med.* **13**, 213–235 (1998).
177. Bliska, J. B., Guan, K. L., Dixon, J. E. & Falkow, S. Tyrosine phosphate hydrolysis of host proteins by an essential *Yersinia* virulence determinant. *PNAS* **88**, 1187–1191 (1991).

-
178. Lin, L. *et al.* Activation loop phosphorylation modulates Bruton's tyrosine kinase (Btk) kinase domain activity. *Biochemistry* **48**, 2021–2032 (2009).
179. Ogawa, A. *et al.* Structure of the carboxyl-terminal Src kinase, Csk. *J. Biol. Chem.* **277**, 14351–14354 (2002).
180. Mollica, L. *et al.* Kinetics of protein-ligand unbinding via smoothed potential molecular dynamics simulations. *Sci Rep* **5**, 1–12 (2015).
181. Mertens, H. D. T. & Svergun, D. I. Structural characterization of proteins and complexes using small-angle X-ray solution scattering. *J. Struct. Biol.* **172**, 128–141 (2010).
182. Bernadó, P. & Blackledge, M. Structural biology: Proteins in dynamic equilibrium. *Nature* **468**, 1046–1048 (2010).
183. Bernadó, P., Mylonas, E., Petoukhov, M. V., Blackledge, M. & Svergun, D. I. Structural characterization of flexible proteins using small-angle X-ray scattering. *J. Am. Chem. Soc.* **129**, 5656–5664 (2007).
184. Tria, G., Mertens, H. D. T., Kachala, M. & Svergun, D. I. Advanced ensemble modelling of flexible macromolecules using X-ray solution scattering. *IUCrJ* **2**, 207–217 (2015).
185. Raji E Joseph, Lie Min, Ruo Xu, Eli D Musselman, A.Amy H Andreotti. A Remote Substrate Docking Mechanism for the Tec Family Tyrosine Kinases†. *Biochemistry* **46**, 5595–5603 (2007).
186. Wahl, M. I. *et al.* Phosphorylation of two regulatory tyrosine residues in the activation of Bruton's tyrosine kinase via alternative receptors. *PNAS* **94**, 11526–11533 (1997).
187. Kurosaki, T. & Kurosaki, M. Transphosphorylation of Bruton's tyrosine kinase on tyrosine 551 is critical for B-cell antigen receptor function. *J. Biol. Chem.* **272**, 15595–15598 (1997).
188. Dinh, M. *et al.* Activation mechanism and steady state kinetics of Bruton's tyrosine kinase. *J. Biol. Chem.* **282**, 8768–8776 (2007).
189. Tomlinson, M. G. *et al.* A conditional form of Bruton's tyrosine kinase is sufficient to activate multiple downstream signaling pathways via PLC Gamma 2 in B-cells. *BMC Immunol.* **2**, 4 (2001).
190. Leroux, A. E., Schulze, J. O. & Biondi, R. M. AGC kinases, mechanisms of regulation and innovative drug development. *Seminars in Cancer Biology* **48**, 1–17 (2018).
191. Maddocks, K. J. *et al.* Etiology of Ibrutinib Therapy Discontinuation and Outcomes in Patients With Chronic Lymphocytic Leukemia. *JAMA Oncol* **1**, 80–87 (2015).
192. Sharma, S. *et al.* Identification of a structurally novel BTK mutation that drives ibrutinib resistance in CLL. *Oncotarget* **7**, 68833–68841 (2016).
193. Sha, F. *et al.* Dissection of the BCR-ABL signaling network using highly specific monoclonal antibody inhibitors to the SHP2 SH2 domains. *Proc. Natl. Acad. Sci. U.S.A.* **110**, 14924–14929 (2013).

-
194. Schmit, N. E., Neopane, K. & Hantschel, O. Targeted Protein Degradation through Cytosolic Delivery of Monobody Binders Using Bacterial Toxins. *ACS Chem. Biol.* **14**, 916–924 (2019).
195. Decherchi, S., Bottegoni, G., Spitaleri, A., Rocchia, W. & Cavalli, A. BiKi Life Sciences: A New Suite for Molecular Dynamics and Related Methods in Drug Discovery. *Journal of Chemical Information and Modeling* **58**, 219–224 (2018).
196. Svergun, D., Barberato, C., Koch, M. H. J.IUCr. CRY SOL – a Program to Evaluate X-ray Solution Scattering of Biological Macromolecules from Atomic Coordinates. *Journal of Applied Crystallography* **28**, 768–773 (1995).
197. Franke, D. *et al.* ATSAS 2.8: a comprehensive data analysis suite for small-angle scattering from macromolecular solutions. *Journal of Applied Crystallography* **50**, 1212–1225 (2017).
198. Panjkovich, A. & Svergun, D. I. Deciphering conformational transitions of proteins by small angle X-ray scattering and normal mode analysis. *Phys Chem Chem Phys* **18**, 5707–5719 (2016).
199. Konarev, P. V. *et al.* PRIMUS: a Windows PC-based system for small-angle scattering data analysis. *Journal of Applied Crystallography* **36**, 1277–1282 (2003).
200. Porod, G. Die Röntgenkleinwinkelstreuung von dichtgepackten kolloiden Systemen. II. Teil. *Kolloid-Zeitschrift* **125**, 108–122 (1952).
201. Fischer, H. *et al.* Determination of the molecular weight of proteins in solution from a single small-angle X-ray scattering measurement on a relative scale. *Journal of Applied Crystallography* **43**, 101–109 (2010).
202. Hajizadeh, N. R., Franke, D., Jeffries, C. M. & Svergun, D. I. Consensus Bayesian assessment of protein molecular mass from solution X-ray scattering data. *Sci Rep* **8**, 1–13 (2018).
203. Franke, D., Svergun, D. I.IUCr. DAMMIF, a program for rapid ab-initio shape determination in small-angle scattering. *Journal of Applied Crystallography* **42**, 342–346 (2009).
204. Panjkovich, A., Bioinformatics, D. S.2016. SASpy: a PyMOL plugin for manipulation and refinement of hybrid models against small angle X-ray scattering data. *academic.oup.com*

7 CURRICULUM VITAE



Daniel DUARTE

Route Cantonale 97, St. Sulpice, Switzerland
dpduarte@me.com
+41 78 685 08 91
www.linkedin.com/in/danielpduarte/
30 years old, Brazilian, Swiss B permit

Cancer research scientist with a strong medical background and in-depth knowledge of the drug development process and clinical trials. Excellent communication skills acquired over 8 years of experience in private and public entities.

Therapeutic areas: Oncohematology and Immunology.

Core experience

Swiss Institute for Experimental Cancer Research (ISREC), Doctoral Assistant	2016-2020
Uniscience Corporation, Brazil, Scientific Advisor/ Field Application Specialist	2015-2016
Netherlands Cancer Institute – AVL Hospital, Amsterdam, Graduate Fellow	2012-2013

Additional research experience

Swiss Federal Institute of Technology Lausanne (EPFL), Teaching Assistant	2017-2019
Biomedicum Helsinki, Finland, Research Assistant	2013-2014
University of California Davis, USA, Research Associate	2011
Santa Catarina State University, Brazil, Laboratory Assistant	2008-2010
Brazilian Synchrotron National Laboratory - LNLS, Brazil, Intern	2010

Education

Swiss Federal Institute of Technology Lausanne (EPFL), Ph.D. in Molecular Life Sciences	2020
University of Helsinki, Finland, M.Sc. in Translational Medicine	2014
University of Amsterdam, The Netherlands, M.Sc. in Oncology (visiting scholar)	2013
Santa Catarina State University, Brazil, Doctor of Veterinary Medicine (D.V.M.)	2007-2012

Certifications

ICH E6 (R2) Good Clinical Practice – Certification from The Global Health Network	2020
Prince 2 on Project Management – Certification from Axelos	2020
Biosafety levels 2 and 3 (BSL2-3) – Certification from EPFL	2016
Animal Experimentation (Functions AB, 2010/63/EU) – University of Helsinki	2014

Languages

English (C2), Portuguese (mother tongue), French (B2, ongoing), Spanish (B1)

Expertise

Research skills:

- Technical writing and document translation in 3 languages, scientific literature.
- Hands-on experience in cellular and molecular biology, cloning, genetics, immunology, flow cytometry, gene editing (CRISPR), DNA sequencing, library preparation for NGS, microbiology, retro/lentiviral vectors, protein expression and purification (HPCL), biochemical and immunoassays structural biology, high-throughput screen of small-molecules, and *in vivo* experiments.

Other skills:

- Project management, data analysis and visualization, sound teaching experience.
- Effective communicator of scientific and clinical data to different audiences.
- Solid IT skills including Office and Adobe software, GraphPad, and bioinformatics.

Volunteer work

Association SOS Eau Giteranyi – Switzerland	2019-present
Student Representative , TRANSMED Steering Committee – Finland	Elected in 2013
Association Amigo do Carroceiro – Brazil	2008-2010

Selected awards and scholarships

- | | |
|---|-----------|
| • Best poster award, Hercules School of Biomolecular Structure and Dynamics, France | 2008 |
| • Master's project grant (13 months) from the University of Helsinki | 2013-2014 |
| • Highly competitive (nationwide) fellowship to pursue training at NKI-AVL, Netherlands | 2012 |
| • Merit scholarship for an exchange at the University of California, USA | 2011 |
| • Two-year scholarship from the Science National Council, Brazil | 2009-2010 |

Selected publications

- Duarte DP, et al. **Btk SH2-kinase interface is critical for allosteric kinase activation and its targeting inhibits B-cell neoplasms**. *Nat. Comm.* 11, 2319 (2020)
- Duarte DP, et al. **Molecular characterization of *Trypanosoma evansi* mevalonate kinase**. *Front. Cell. Infect. Microbiol.* 10 (8:223) (2018)
- de Graaf EL, et al. **Signal transduction reaction monitoring deciphers site-specific PI3K-mTOR/MAPK pathway dynamics**. *J. Proteome Res.* 14(7): 2906-14 (2015)
- Duarte DP; Kaplon, J and Peeper, DS. **Inhibition of pyruvate dehydrogenase kinase 1 (PDK1) in melanoma**. Internal report NKI-AVL Hospital (2013)
- Duarte, DP; et al. **Development of an immunoassay for the differential diagnosis of trypanosomosis of veterinary interest: A preliminary proteomic survey of *Trypanosoma evansi* trypomastigotes using LC/MS/MS approach for differential diagnostics**. Poster at the Brazilian Conference of Animal Health (2011)
- Over 24 abstracts/presentations in scientific conferences.

8 ANNEX

Duarte, D.P. *et al.* **Btk SH2-kinase interface is critical for allosteric kinase activation and its targeting inhibits B-cell neoplasms.** *Nat. Commun.* 11, 2319 (2020).

PMID: 32385234

DOI: doi.org/10.1038/s41467-020-16128-5

This article was submitted on 02 January 2020 and published online on 08 May 2020 at Nature Communications. This Annex includes the main article and supplementary material. The full version and source data file can be found at the publisher's website.

Copyright disclaimer: Nature Communications articles are published open access under a CC BY license (Creative Commons Attribution 4.0 International License) which allows full re-use of open access materials to reproduce, copy, distribute, transmit, and adapt this content including for commercial purposes, provided they attribute the contribution in the manner specified by the author or licensor. Under Creative Commons, authors retain copyright in their articles.

ARTICLE



<https://doi.org/10.1038/s41467-020-16128-5>

OPEN

Btk SH2-kinase interface is critical for allosteric kinase activation and its targeting inhibits B-cell neoplasms

Daniel P. Duarte¹, Allan J. Lamontanara¹, Giuseppina La Sala^{2,3}, Sukyo Jeong⁴, Yoo-Kyoung Sohn⁴, Alejandro Panjkovich⁵, Sandrine Georgeon¹, Tim Kükenshöner¹, Maria J. Marcaida³, Florence Pojer⁶, Marco De Vivo², Dmitri Svergun⁵, Hak-Sung Kim⁴, Matteo Dal Peraro³ & Oliver Hantschel^{1,7}✉

Bruton's tyrosine kinase (Btk) is critical for B-cell maturation and activation. Btk loss-of-function mutations cause human X-linked agammaglobulinemia (XLA). In contrast, Btk signaling sustains growth of several B-cell neoplasms which may be treated with tyrosine kinase inhibitors (TKIs). Here, we uncovered the structural mechanism by which certain XLA mutations in the SH2 domain strongly perturb Btk activation. Using a combination of molecular dynamics (MD) simulations and small-angle X-ray scattering (SAXS), we discovered an allosteric interface between the SH2 and kinase domain required for Btk activation and to which multiple XLA mutations map. As allosteric interactions provide unique targeting opportunities, we developed an engineered repebody protein binding to the SH2 domain and able to disrupt the SH2-kinase interaction. The repebody prevents activation of wild-type and TKI-resistant Btk, inhibiting Btk-dependent signaling and proliferation of malignant B-cells. Therefore, the SH2-kinase interface is critical for Btk activation and a targetable site for allosteric inhibition.

¹Swiss Institute for Experimental Cancer Research (ISREC), School of Life Sciences, École polytechnique fédérale de Lausanne (EPFL), 1015 Lausanne, Switzerland. ²Laboratory of Molecular Modeling and Drug Discovery, Istituto Italiano di Tecnologia, Via Morego 30, 16163 Genoa, Italy. ³Institute of Bioengineering, École polytechnique fédérale de Lausanne (EPFL), 1015 Lausanne, Switzerland. ⁴Department of Biological Sciences, Korea Advanced Institute of Science and Technology (KAIST), Daejeon, Korea. ⁵European Molecular Biology Laboratory (EMBL), Hamburg Unit, 22607 Hamburg, Germany. ⁶Protein Crystallography Core Facility, School of Life Sciences, École polytechnique fédérale de Lausanne (EPFL), 1015 Lausanne, Switzerland. ⁷Institute of Physiological Chemistry, Faculty of Medicine, Philipps-University of Marburg, 35032 Marburg, Germany. ✉email: oliver.hantschel@uni-marburg.de

Protein kinases are major drug targets as most cancers carry driver mutations in kinases or are functionally addicted to certain kinase signaling pathways. To date, 55 ATP-competitive kinase inhibitors have been approved for the treatment of multiple solid and hematological tumors^{1,2}. A major setback in targeted kinase inhibitor therapy is the development of drug resistance, commonly due to point mutations in the targeted kinase, but also by various other mechanisms³. An attractive alternative is the targeting of allosteric sites, other than the ATP binding pocket, critical for the regulation of kinase activity or substrate recruitment. Targetable allosteric regulatory sites have been identified for a few kinases and include the myristoyl binding pocket and SH2-kinase interface in BCR-ABL, as well as the PIF pocket in different AGC kinases^{4–7}. As allosteric regulatory pockets are unique to a single kinase or a small class of kinases, one should be able to inhibit oncogenic signaling more selectively. Furthermore, combined or sequential use of allosteric and ATP-competitive inhibitors is a very attractive strategy for cancer treatment, which may diminish or even abolish the outgrowth of resistant clones^{5,8}.

Bruton's tyrosine kinase (Btk) is a central kinase in B-cell receptor (BCR) signaling that is expressed in the B-cell lineage and in myeloid cells. Loss-of-function mutations in Btk are found in humans with X-linked agammaglobulinemia (XLA). These patients are severely immunocompromised due to the impaired development of B-cells⁹. In contrast, elegant functional genomics work has demonstrated that Btk signaling is critical for the survival of the activated B-cell-like (ABC) subtype of diffuse large B-cell lymphoma (DLBCL) and several other B-cell cancers^{10,11}. Inhibition of Btk using the FDA-approved BCR-ABL inhibitor dasatinib, which has Btk as one of its major off-targets, provided proof-of-concept evidence for Btk targeting and supported the parallel development of more selective Btk inhibitors^{10–12}. Among those, the first-in-class Btk inhibitor ibrutinib¹³, which was approved in 2013, has shown remarkable clinical activity in chronic lymphocytic leukemia (CLL), mantle cell lymphoma (MCL), Waldenström's macroglobulinemia and graft-versus-host disease. The more selective drugs acalabrutinib¹⁴ and zanubrutinib¹⁵ were approved in 2017 and 2019, respectively, as second-line treatments for MCL. However, patients treated with Btk TKIs may acquire resistance caused by Btk mutations of Cys-481 required for covalent binding or, more rarely, by mutations in PLCγ2, downstream of Btk¹⁶. Therefore, allosteric mechanisms that regulate Btk activity are particularly attractive as additional drug targets to cope with drug resistance in Btk-dependent B-cell malignancies.

Btk and its paralogues Tec, Itk, Bmx and Txk share a conserved SH3-SH2-kinase domain unit with the Src and Abl kinase family of cytoplasmic tyrosine kinases^{17,18}. Structural and biochemical data showed that intramolecular interactions of the SH3 and SH2 domains with the kinase domain N- and C-lobe, respectively, result in a compact autoinhibited conformation of Btk analogous to Src and Abl kinases^{18,19}. In addition, the N-terminal PH-TH domain module of Btk contributes to stabilizing Btk's autoinhibited conformation^{19,20}. Through inositol phosphate binding to a peripheral site on the PH domain, Btk activation is triggered via dimerization and subsequent trans-autophosphorylation of the kinase domain¹⁹. Btk activity is positively regulated by two major phosphorylation events. Tyr-551 in the activation loop can be phosphorylated by upstream Src kinases or trans-autophosphorylated by another Btk molecule. Tyr-223, located in the SH3 domain, is the main Btk autophosphorylation site and thought to be autophosphorylated after Tyr-551 phosphorylation²¹. Although an early small-angle X-ray scattering (SAXS) reconstruction suggested a linear and elongated conformation of active Btk²²,

there is little insight on the structural mechanisms and precise molecular events that govern Btk activation.

Here we show that, based on the analysis of XLA mutations in the SH2 domain, Btk activation critically depends on the formation of an allosteric interface between its SH2 and the N-lobe of kinase domain, which we mapped using a combination of enhanced sampling molecular dynamics (MD) simulations and SAXS. Development of a high-affinity engineered protein antagonist to the Btk SH2 domain targeting its interface with the kinase domain prevents Btk activation in cells, inhibits proliferation and Btk-dependent signaling in malignant B-cells. Therefore, we demonstrate the Btk SH2 domain as alternative allosteric site for therapeutic inhibition of Btk and its most common drug-resistant mutant.

Results

A set of XLA mutations in the SH2 domain impair Btk kinase activation. Sequencing data indicate that approximately 20% of missense mutations in XLA patients are located within the Btk SH2 domain, but how these mutations result in Btk loss-of-function is poorly understood²³. While several mutations were shown to decrease protein stability and/or impair canonical phosphotyrosine (pY) peptide binding to the SH2 domain²⁴, we were intrigued by a mutational hotspot of surface-exposed residues located on the opposite side of the pY-binding pocket and thus unlikely to be involved in pY-peptide binding (Fig. 1a). We first assessed the effects of five representative XLA mutations in this area (K296E, H364D, S371P, R372G, and K374N) and one control XLA mutation (R307G) in the pY binding pocket, on Btk SH2 domain folding, stability, and pY-binding by producing the purified recombinant proteins (Fig. 1b, Supplementary Fig. 1a, b). Far-UV circular dichroism (CD) spectra and thermal shift analysis demonstrated that the XLA mutations did not significantly change Btk SH2 domain folding and only mildly decreased melting temperature compared to the wild-type protein (Fig. 1c and Supplementary Fig. 1c). We next determined the effect of the selected XLA mutations on pY-binding in a fluorescence-polarization (FP) binding assay with a labeled pY-peptide. All XLA mutants bound the pY-peptide with similar affinities as the wild-type Btk SH2 domain, whereas the R307G control mutation in the pY binding pocket strongly impaired binding (Fig. 1d). Thus, the selected XLA mutations do not act by perturbing folding, stability or pY-binding of the Btk SH2 domain.

To determine whether these SH2 mutations affect Btk kinase activity in cells, they were introduced in a Btk SH2-kinase domain (SH2-KD) construct and expressed in HEK293 cells. Expression of wild-type SH2-KD resulted in robust activation loop phosphorylation (pY551; Fig. 1e, f). In contrast, all tested XLA mutations strongly decreased phosphorylation at Y551 (Fig. 1e, f). To test the effect of these mutations on phosphorylation of Y223 within the Btk SH3 domain, which is the most commonly used readout for Btk activity, we introduced them into the larger Btk construct spanning the SH3, SH2 and kinase domains (SH3-SH2-KD). The deleterious effect of an even larger set of XLA mutations in the Btk SH2 domain (Supplementary Fig. 1d) could be corroborated in the SH3-SH2-KD construct with strong impairment of both pY551 and pY223 (Supplementary Fig. 1e, f). Importantly, introduction of a control non-XLA mutation (K311E) on the opposite side of the SH2 domain did not affect pY551 and pY223 (Supplementary Fig. 1e, f). As expected, when the XLA mutants were introduced in the full-length (autoinhibited) protein, no significant effect on pY551 was observed (Supplementary Fig. 1g).

The intriguing observation that certain XLA mutations do not impact on canonical Btk SH2 domain function suggests the

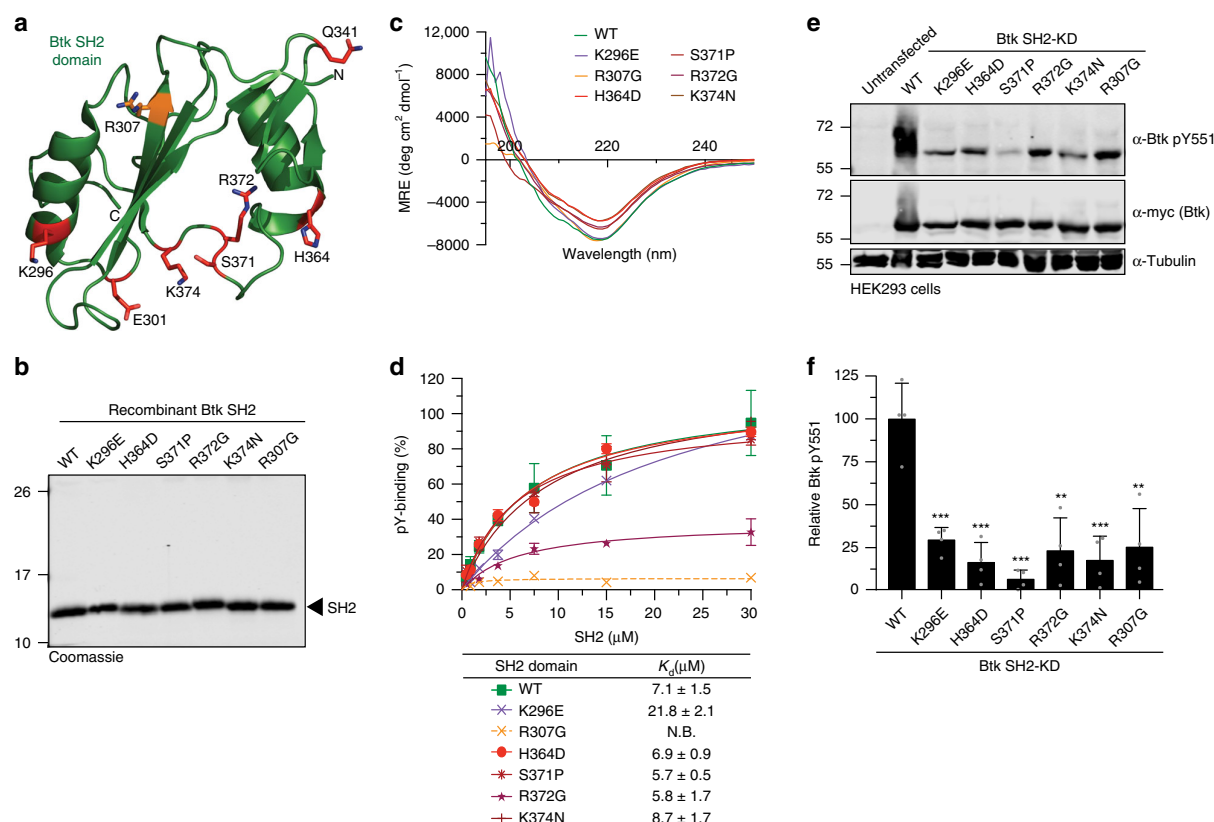


Fig. 1 Mutations in Btk SH2 domain abrogates pY551 phosphorylation. **a** Mapping of a subset of XLA-patient mutations (red sticks) onto the human Btk SH2 domain structure (PDB 2GE9). The residue R307 (orange sticks) is part of the pY-binding motif (FIVRD). Here and in all subsequent figures, the residue numbering refers to full-length human Btk. **b** Representative SDS-PAGE analysis of recombinant wild-type and mutant Btk SH2 domains purified from *E. coli*. **c** Averaged far-UV circular dichroism (CD) spectra of recombinant wild-type and XLA mutant Btk SH2 domains. Mean residue ellipticity (MRE) for each protein was calculated from three independent measurements. **d** Binding of a fluorescently labeled pY-peptide to recombinant Btk SH2 domains. Indicated K_d values were obtained from the fitting to a 1:1 binding model. Data are mean ± SD of two technical replicates. Non-binding (N.B.). **e** HEK293 cells were transiently transfected with a construct containing an N-terminal 6xMyc-tagged human Btk SH2-KD wild-type or mutants. Immunoblotting of cell lysates was performed to assess Btk pY551 phosphorylation. **f** Quantification of pY551 immunoblot shown in **e** and normalized to total Btk (Myc) expression. Data are mean ± SD of three biological replicates (n = 4) and P-values were calculated using an unpaired t-test. **P ≤ 0.01 and ***P ≤ 0.001. Source data are provided as a Source Data file.

presence of a yet unidentified mechanism on how the Btk SH2 domain participates in kinase activation.

SH2 domain is critical for Btk kinase activation. As the phenotype of the above-described XLA mutations on Btk kinase activation resembles the phenotype of structure-guided targeted mutations in SH2-kinase domain intramolecular interfaces in the Abl and Fes kinases^{6,25}, we hypothesized Btk kinase activation by an analogous allosteric mechanism. To address this, we recombinantly expressed sequential domain deletion constructs (Fig. 2a) in the presence of YopH phosphatase using baculovirus-infected Sf9 cells to obtain unphosphorylated proteins. All proteins were purified to homogeneity (Fig. 2b). Mass spectrometry and immunoblotting analysis confirmed their identity and absence of phosphorylation (Supplementary Fig. 2a, b). These recombinant Btk proteins were incubated with Mg²⁺/ATP and in vitro autophosphorylation on Y551 was monitored over time (Fig. 2c). A kinase-dead Btk SH2-KD protein (D521N) was included as negative control. The SH2-KD construct showed a strong increase in autophosphorylation kinetics compared to the kinase domain alone (KD) and the SH2-KD D521N control (Fig. 2d, e). In agreement with the crystal structure of mouse Btk

SH3-SH2-KD, we observed lower pY551 autophosphorylation than with the SH2-KD construct, but still significantly higher than for the Btk KD, as the presence of the SH3 domain likely induced a more closed autoinhibited conformation of Btk, similar to Abl and Src kinases¹⁹ (Fig. 2d, e). The observed lower in vitro autophosphorylation for full-length Btk (Fig. 2d, e) is in line with a recent molecular model of full-length Btk in solution, where the PH-TH domain docks onto the KD to further stabilize its autoinhibition²⁰. Furthermore, strong total pY phosphorylation of SH2-KD was corroborated in this assay (Supplementary Fig. 2c–e) and corresponds to multiple autophosphorylation sites that we mapped using mass spectrometry (MS, Supplementary Table 1). Using this assay, we could also show that phosphorylation on Y223 preceded Y551 phosphorylation in vitro, which agrees with a previous model where autophosphorylation on Y223 may contribute to full activation of the kinase to further transphosphorylate other Btk molecules on Y551²¹ (Supplementary Fig. 2f).

The strong activating effect of the Btk SH2 domain on autophosphorylation in vitro could be corroborated when expressing these constructs in HEK293 cells. Here, the presence of SH2 domain strongly increased Btk autophosphorylation,

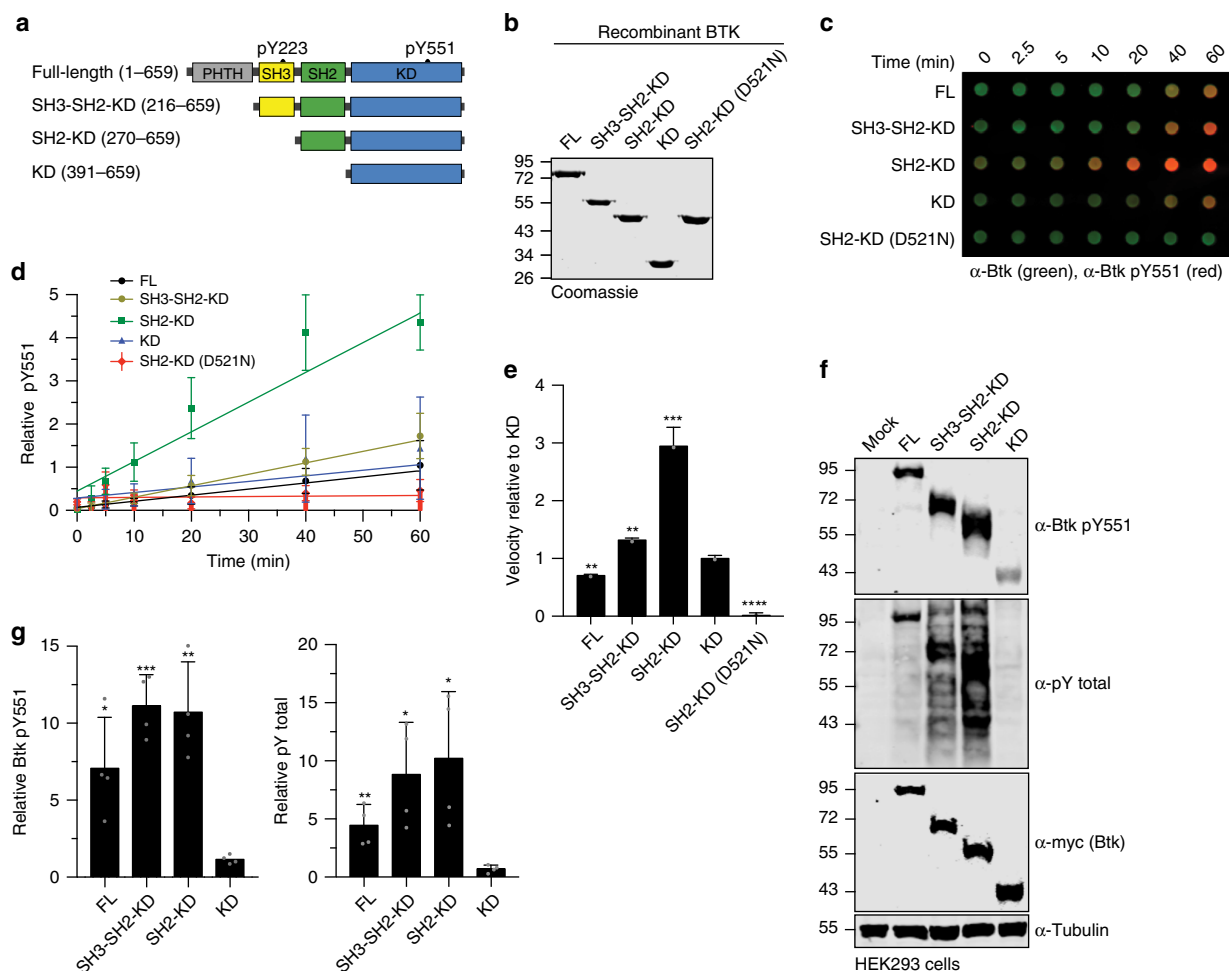


Fig. 2 Btk SH2 domain is critical for kinase activation. **a** Schematic representation of Btk constructs used in this study. Construct/domain boundaries and location of the key activating tyrosine phosphorylation sites (pY223 and pY551) are indicated. **b** Representative SDS-PAGE analysis of recombinant untagged Btk proteins purified from Sf9 cells. **c** In vitro autophosphorylation assay performed with recombinant Btk proteins at room temperature. The levels of pY551 (red channel) and total Btk (green channel) were assessed using immunoblotting in a dot blot apparatus. **d** Btk autophosphorylation kinetics shown in **c** normalized to total Btk signal and the calculated slopes of linear fits (relative velocities). Data are mean \pm SD of at three independent experiments ($n = 3$). **e** Relative velocities of Btk autophosphorylation relative to KD. Data are mean \pm SD of three independent experiments ($n = 3$) and P -values were calculated using an unpaired t -test. **f** HEK293 cells were transiently transfected with the indicated Btk constructs containing an N-terminal 6xMyc tag and kinase activation assessed by immunoblotting of cell lysates. **g** Quantification of pY551 and total pY shown in **f** normalized to total Btk (Myc) expression and relative to the KD. Data are mean \pm SD of three biological replicates ($n = 4$) and P -values were calculated using an unpaired t -test. $^*P \leq 0.05$, $^{**}P \leq 0.01$, $^{***}P \leq 0.001$ and $^{****}P \leq 0.0001$. Source data are provided as a Source Data file.

when compared to KD alone, which shows very low pY551 levels (Fig. 2f, g). Noteworthy, the SH3-SH2-KD construct showed even higher activation when expressed in cells (Fig. 2f, g), which could be due to binding of cellular SH3-SH2 ligands that destabilize the autoinhibited conformation of SH3-SH2-KD. This data indicated that the presence of the Btk SH2 domain is critical for the activation of Btk in vitro and in cells.

Btk SH2-KD adopts an elongated conformation to trigger kinase activation. We next turned our focus to investigate the structural basis for SH2-dependent allosteric activation of Btk. In contrast to the Fes, Abl and Csk kinases, where SH2-KD units resembling active conformations could be crystallized and had revealed diverse intramolecular interfaces with the N-lobe of the kinase domain, we and others have failed to crystallize active Btk. To provide molecular models of the Btk SH2-KD unit, we used

enhanced sampling molecular dynamics (MD) simulations to probe for the interaction of the Btk SH2 domain with the KD. We ran multiple replicas of scaled MD simulations for a total of $\sim 4 \mu\text{s}$ long trajectories with the Btk SH2-KD unit, including the native SH2-kinase domain linker. Scaled MD is an enhanced sampling MD simulation scheme that allows the sampling of μs -ms time-scale events, such as domain-domain binding²⁶. This time frame is prohibitive using classical approaches, such as equilibrium MD simulations. Using this approach, we could sample the binding of SH2 to KD in $\sim 100 \text{ ns}$ of simulated time, thus collecting multiple binding events and associated statistics.

Our MD data demonstrated that the SH2 may interact with the KD at different positions, notably at the back, top, and front of the N-lobe (Supplementary Fig. 3a). The most representative clusters were located in the back of the KD, followed by a more elongated conformation with the SH2 placed on top of the N-lobe

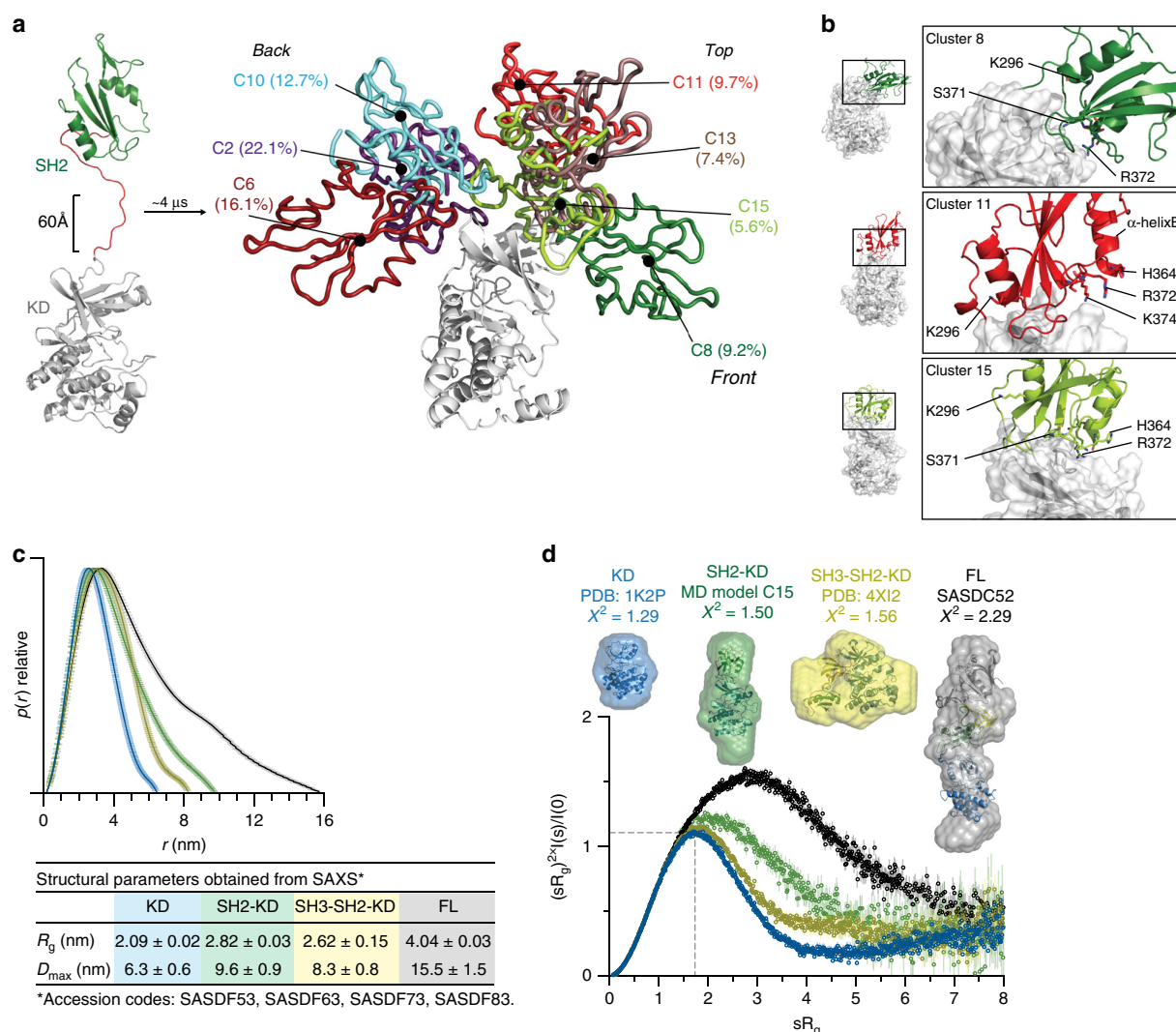


Fig. 3 SH2 domain interacts with the N-lobe of the KD in the active Btk. **a** Scaled MD simulations were performed using a model including the Btk SH2 and KD crystal structures (PDB 6HTF and 1K2P, respectively). The most populated clusters of the SH2 positions (several colors) relative to the KD (white) are shown. The percentages indicate the population of the cluster with respect to the entire simulation time. **b** Detailed view of the SH2-KD interface of clusters 8, 11 and 15. SH2 residues mutated in XLA are indicated as sticks. **c** Comparative maximal particle dimension (D_{max}) of recombinant Btk proteins and summary of structural parameters (R_g and $D_{max} \pm$ error) obtained from SAXS. See Supplementary Table 2 for details. **d** Dimensionless Kratky plot of recombinant Btk proteins. The gray dashed line represents the theoretical peak assuming an ideal Guinier region for a globular particle. Ab initio envelope reconstructions obtained from SAXS (surface representation) superimposed on the crystal structures for Btk KD and SH3-SH2-KD (PDB 1K2P and 4X12, respectively) are shown on top. For the SH2-KD protein, the structure of an elongated MD model with the best agreement with the experimental SAXS data is shown (model C15 shown in **a** and **b**). FL protein shows an extended conformation as observed in a previous SAXS reconstruction (SASDC52). Source data are provided as a Source Data file.

(Fig. 3a). Strikingly, the elongated models suggest that several of the SH2 residues mutated in XLA participate in the interaction interface with the N-lobe of the KD (Fig. 3b).

In order to provide an unbiased and independent experimental validation of the MD model, we performed an extensive analysis of multiple recombinant Btk proteins with small-angle X-ray scattering (SAXS). This method allows to directly reconstruct low-resolution particle shapes ab initio and also to study conformational dynamics of multidomain proteins and complexes in solution. From the SAXS data, the SH2-KD construct adopts a more elongated conformation with increased particle dimension (D_{max}) in comparison to the KD and SH3-SH2-KD proteins (Fig. 3c and Supplementary Fig. 3b). The extended

conformation of the SH2-KD protein is independent of kinase activity, as also seen with a kinase-inactive mutant (D521N; Supplementary Table 2). In addition to the increased particle dimension, the normalized Kratky plot suggests that SH2-KD is flexible compared to the globular KD and SH3-SH2-KD proteins (Fig. 3d, bottom). Ab initio shape reconstructions from SAXS corroborate the available KD and (closed autoinhibited) SH3-SH2-KD crystal structures (PDB 1K2P and 4X12, respectively, Fig. 3d, top). Importantly, the ab initio envelopes of SH2-KD can be superimposed very well with the elongated MD models (e.g., C15, $\chi^2 = 1.50$) in which the SH2 domain is interacting with the N-lobe of the KD (Fig. 3d). The full-length protein has been previously reported to adopt an equilibrium of conformations

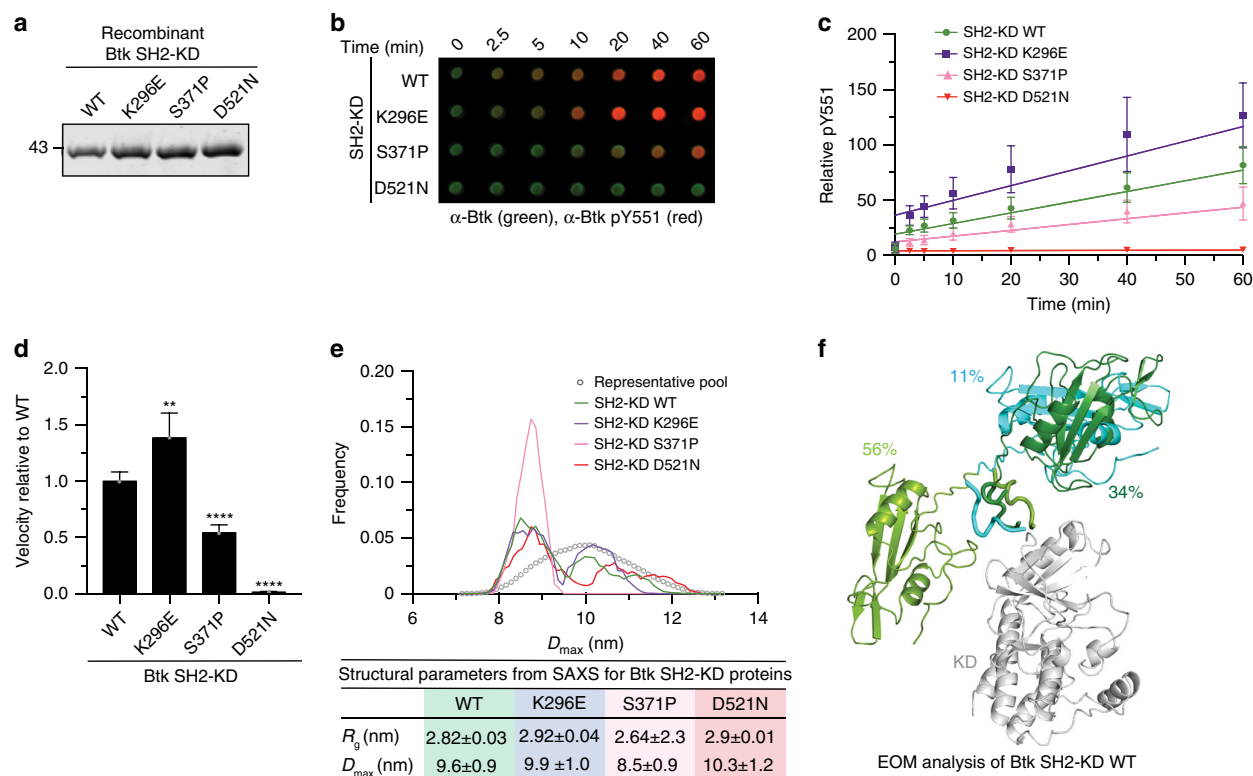


Fig. 4 Mutation on the Btk SH2-KD interface perturbs its active conformation and decrease kinase activation. **a** Representative SDS-PAGE analysis of recombinant untagged SH2-KD proteins purified from Sf9 cells. **b** In vitro autophosphorylation assay performed with recombinant Btk proteins at room temperature. The levels of pY551 (red channel) and total Btk (green channel) were assessed using immunoblotting in a dot blot apparatus. **c** Btk autophosphorylation kinetics shown in **b** normalized to total Btk signal and the calculated slopes of linear fits (relative velocities). Data shown are the mean ± SD of two independent experiments ($n = 6$). **d** Relative velocities of Btk autophosphorylation relative to wild-type. Data are mean ± SD of two independent experiments ($n = 6$) and P -values were calculated using an unpaired t -test. $^{**}P \leq 0.01$ and $^{****}P \leq 0.0001$. **e** Flexibility analysis of SH2-KD based on ensemble of optimization method (EOM) using the experimental SAXS data from recombinant Btk wild-type and mutant proteins. Data from a representative experiment shows the maximal particle dimension (D_{max}) of selected conformers for each protein (lines) from a representative pool of theoretical conformations (dotted line). The table summarizes the obtained structural parameters (R_g and D_{max} ± error). See Supplementary Table 2 for details. **f** Cartoon representation of the ensemble of SH2-KD conformations selected by EOM analysis (**e**, green line). The percentages represent the contribution of each conformer to a SAXS profile in good agreement with the experimental curve. The KD is represented in white and SH2 conformers are colored. SH2-linker distance estimated by the algorithm is represented as ribbon. Source data are provided as a Source Data file.

with a predominant compact and autoinhibited state in solution²⁰, whereas our SAXS data from the full-length protein is compatible with its extended conformation and agrees with a previous report²². Overall, independent use of MD and SAXS supports an extended model for the Btk SH2-KD, where the SH2 is placed on top and interacts predominantly with the N-lobe of the KD. In line with this model and the data on XLA mutations in the SH2 domain, point mutations in the N-lobe that were structurally predicted to disrupt the allosteric SH2-KD interface impair Btk activation (Supplementary Fig. 3c–e). Interestingly, the L405E mutation in the N-lobe resulted in a strong over-activation of SH2-KD. This gain-of-function phenotype is compatible with an additional salt bridge with positively charged residues in the SH2 domain that may cause a stabilization of the SH2-KD interface (Supplementary Fig. 3f).

To further probe the validity of this model, we took advantage of XLA mutations at different positions on the SH2 surface. Based on our SH2-KD model, S371 is part of the interface with the KD N-lobe, while K296 is solvent-exposed and does not participate in this interdomain interaction (model C15, Fig. 3b). When introduced into Btk SH2-KD and recombinantly purified to homogeneity (Supplementary Fig. 3g, h), the S371P protein

showed decreased in vitro autophosphorylation kinetic on Y551 compared to the wild-type protein (Fig. 4a–d). Interestingly, the K296E mutant protein showed a mild increase in Y551 autophosphorylation compared to wild-type, as the mutation may disfavor a more inactive conformation of the SH2-KD protein (Fig. 4a–d). Total pY phosphorylation of the S371P protein was also impaired and further supports the lower autophosphorylation capacity observed for this construct (Supplementary Fig. 3i–k).

To provide additional insights on how these mutations affect SH2-KD conformation, we assessed protein flexibility using SAXS data combined with the ensemble optimization method (EOM²⁷). EOM generates a large number of conformations (>10,000) using the KD and SH2 domain structures taking the native linker into account, calculates theoretical SAXS curves for all models, and selects a mixture of conformers that fits the experimental SAXS data. First, SAXS data from the mutants indicated that the S371P protein is somewhat more compact than wild-type, K296E and D521N proteins (Supplementary Fig. 3l, m, Supplementary Table 2). EOM analysis revealed that SH2-KD wild-type is rather flexible with few different conformers co-existing in solution, but indicating extended conformations with the SH2 placed on top of

the kinase (Fig. 4e, f). Analysis of the kinase-dead D521N and K296E SH2-KD proteins indicate similar flexibility as for the wild-type protein and also similar overall molecular dimensions (R_g and D_{max}). In contrast, the S371P mutant protein showed a shift towards more compact conformation, with a decrease in R_g and D_{max} compared to the wild-type and mutations not affecting the interdomain interface (Fig. 4e). The compact conformation adopted by the SH2-KD S371P is consistent with the decreased phosphorylation observed in the autophosphorylation assay (Fig. 4d). Noteworthy, EOM analysis performed for the SH3-SH2-KD and full-length wild-type proteins is consistent with the models showing, respectively, a compact and a mixture of compact and elongated conformations in solution (Supplementary Fig. 3n). Summarizing, we provide a model for Btk activation via allosteric interaction of the SH2 domain predominantly placed on top of KD. Although the SH2-KD interaction seems less sturdy as in Abl and Fes, a molecular model for the interface of SH2 interacting with the KD can be deduced from our data.

Development of a protein binder targeting the BTK SH2 domain. In order to demonstrate the importance of the proposed allosteric interaction of the Btk SH2 domain with the kinase domain in regulating Btk activity, we developed a repebody binder. Repebodies are engineered non-antibody scaffold proteins composed of leucine-rich repeat (LRR) modules that can be engineered to bind targets with high specificity. A human Btk SH2 domain-targeting repebody, termed rF10, was generated using phage display selection and affinity maturation²⁸ (Supplementary Fig. 4a). rF10 and a non-binding control repebody (rNB) were readily purified from *E. coli* (Fig. 5a). The affinity of rF10 to the Btk SH2 domain is ~15 nM with a binding stoichiometry of 1:1 (Fig. 5b). In contrast, rF10 showed no binding to the SH2 domains from its close relatives, the tyrosine kinases Abl and Lck, demonstrating a >500-fold selectivity for the Btk SH2 domain (Fig. 5b). Consistent with a high-affinity interaction, a stable 1:1 rF10-SH2 complex could be recovered by size-exclusion chromatography either in complex with the Btk SH2 domain alone (Fig. 5c, d) or the full-length Btk protein (Supplementary Fig. 4b, c).

As other engineered SH2 binders, in particular monobodies^{29–31}, predominantly target the pY peptide binding site, we first tested whether the rF10 repebody interferes with pY-peptide binding using an FP binding assay. Even in the presence of a 20-fold molar excess of rF10, no competition with pY-peptide binding was observed (Fig. 5e), indicating that rF10 has a different binding epitope on the SH2 domain. The observed increased FP signal with increasing rF10 concentrations is consistent with the formation of a ternary complex (SH2-pY-peptide-rF10; Fig. 5e).

We next solved the crystal structure of the Btk SH2-rF10 complex at 1.9 Å resolution (Fig. 5f, Supplementary Table 3, PDB 6HTF), which is the first crystal structure of the isolated human Btk SH2 domain. The overall SH2 domain conformation is very similar to the previously published NMR structure of human Btk SH2 domain³² (PDB 2GE9), indicating that rF10 binding does not result in major conformational changes^{31,33}. Consistent with the ITC and pY binding assays, the rF10-SH2 crystal structure indicates that rF10 binds to SH2 domain in a 1:1 interaction and the interaction does not involve the pY-binding groove. rF10 binds to multiple residues from the SH2 domain BC loop (K322, S323, G325 and P327) and the C-terminus of the α -helix B (S366 and K374), and it buries a surface area of 2274 Å² (Fig. 5f). To further corroborate the rF10 interaction site, a recombinant SH2 containing the XLA mutation K374N in the interface between the SH2-rF10 showed a ~9-fold decreased affinity (Fig. 5g) compared to the wild-type SH2 domain.

Superimposition of the Btk SH2-rF10 structure with a representative SH2-KD structure (MD model C15) revealed dramatic steric clashes of the KD and rF10 (Fig. 5h, Supplementary Movie 1). The coincidental strong overlap of the rF10 binding epitope with the proposed Btk SH2-kinase interface led us to hypothesize that rF10 may abrogate the SH2-KD interaction and thereby act as an allosteric Btk antagonist. To probe this hypothesis, we first performed SAXS analysis of rF10 alone and in complex with several Btk constructs (Supplementary Fig. 4d, e, Supplementary Table 4). In line with our hypothesis, SAXS-based reconstructions of rF10-Btk complexes suggests that the conformation of SH2-KD is altered and the interdomain interface is disrupted (Supplementary Fig. 4f). This observation encouraged us to further investigate the functional effects of the rF10 repebody on Btk activity and signaling in vitro and in cells.

Targeting the SH2-KD interface with rF10 inhibits Btk kinase.

As rF10 was confirmed to bind the Btk SH2 domain, we first measured the binding affinity of rF10 to recombinant SH2-KD, SH3-SH2-KD and full-length Btk. rF10 was found to bind all three proteins with similar low nanomolar affinities (Supplementary Fig. 5a). We next performed in vitro autophosphorylation assays using different recombinant Btk constructs in the presence of a 2-fold molar excess of rF10 or rNB control (Fig. 6a, b). rF10 showed a strong inhibitory effect on pY551 autophosphorylation of all tested Btk constructs containing the SH2 domain (full-length, SH3-SH2-KD and SH2-KD; Fig. 6c, d). Interestingly, even though the constructs SH3-SH2-KD and full-length Btk adopt an autoinhibited conformation with low autophosphorylation activity (Fig. 2c–e), rF10 strongly decreased their remaining activity (Fig. 6c, d). Consistent with this data also total pY phosphorylation of Btk was decreased in the presence of rF10 (Supplementary Fig. 5b–e).

To test the ability of rF10 to act as an allosteric Btk inhibitor in cells, we first tested whether rF10 interacted with different Btk constructs in mammalian cells. Pull-down assays showed interactions of rF10, but not of the rNB control repebody, with all Btk constructs containing the SH2 domain, but not with the Btk KD alone (Fig. 6e). In the presence of rF10, lower levels of Btk pY551 and total pY were observed than when equal amounts of rNB were expressed. Phosphorylation of the KD alone was unaltered in the presence of repebodies, indicating selective SH2 domain-dependent inhibition of Btk autophosphorylation by rF10 (Fig. 6f, g and Supplementary Fig. 5f, g). To determine the effect of allosteric inhibition of Btk by rF10 on kinase activity, we performed in vitro kinase assays with a substrate peptide encompassing Tyr-753 of PLC γ 2, a canonical Btk substrate. In the presence of rF10, but not rNB, kinase activity of full-length Btk was strongly inhibited (Supplementary Fig. 5h).

This data collectively showed that targeting the Btk SH2 with a repebody binder at the proposed SH2-kinase interface selectively inhibits Btk activity.

rF10 decreases viability and inhibits Btk signaling of lymphoma cells. Finally, we investigated whether targeting the SH2-KD interface is sufficient to inhibit Btk activity in neoplastic B-cells. We selected DLBCL cell lines that express wild-type Btk and are sensitive to ibrutinib (Supplementary Fig. 6a) and transduced them to inducibly express rF10 or the rNB. Upon induction of rF10 expression by doxycycline in HBL-1 cells, we observed a more than 10-fold reduction in cumulative cell numbers as compared to rNB, all uninduced conditions or parental cells (Fig. 7a). This was accompanied by a dramatic increase in apoptosis, comparable to the treatment of parental cells with

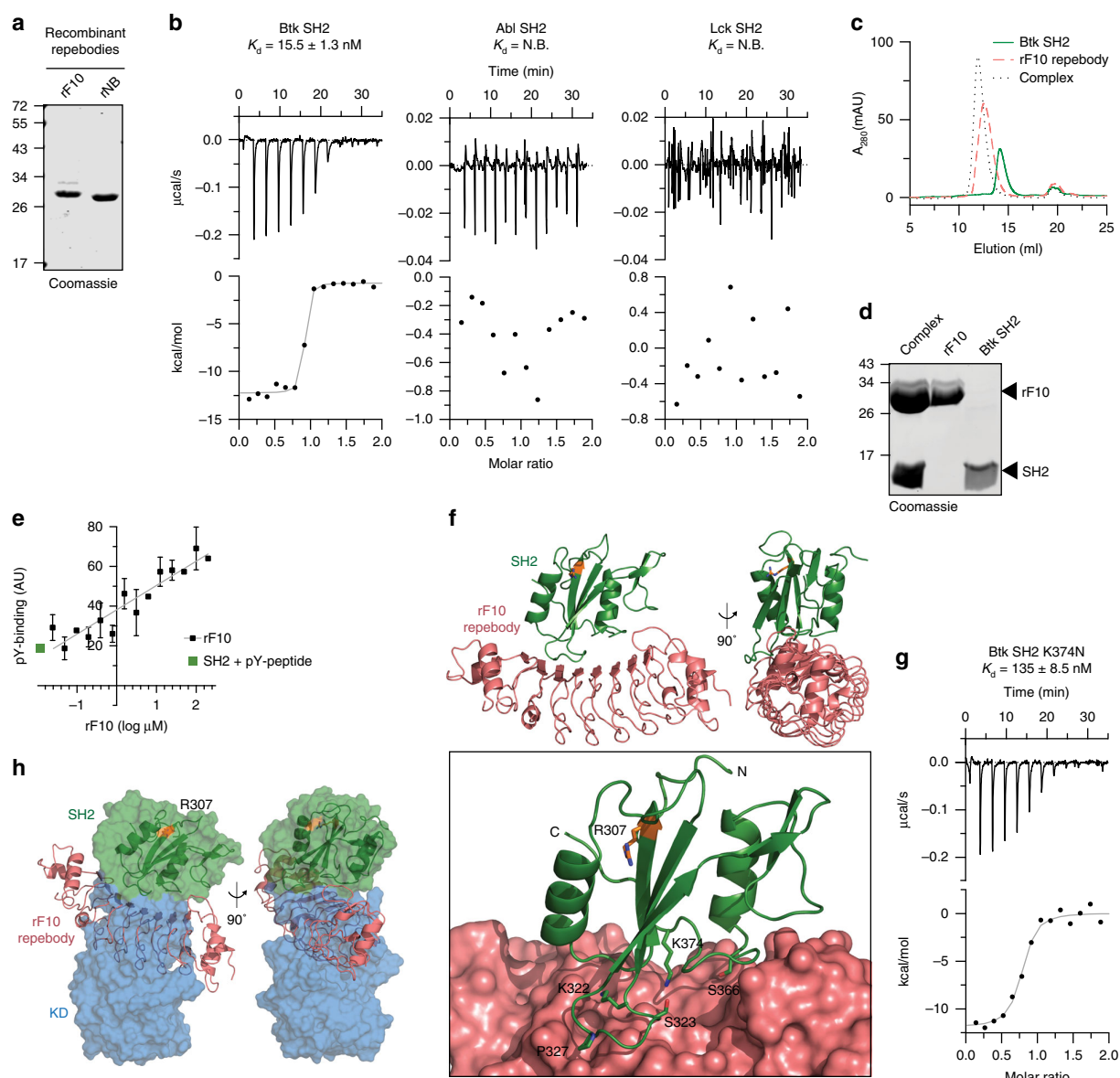


Fig. 5 Development of a high-affinity protein binder to the human Btk SH2 domain. **a** Representative SDS-PAGE analysis of recombinant repebodies rF10 and rNB purified from *E. coli*. **b** Representative ITC measurement of rF10 repebody to the SH2 domains of Btk, Abl and Lck kinases. The top panel shows the raw signal and the bottom panel shows the integrated calorimetric data of the area of each peak. The continuous line shows the best fit to the experimental data assuming a 1:1 binding model. Reported K_d value for Btk was calculated from three independent measurements. N.B. signifies non-binding. **c** Size-exclusion chromatogram (SEC) analysis of Btk SH2 and rF10 alone, and the SH2-rF10 complex formed by pre-incubation of SH2 and rF10 prior to column injection. **d** Peaks isolated from the SEC analysis shown in **c** resolved by SDS-PAGE and stained with Coomassie. **e** Binding-competition assay using fluorescently labeled pY-peptide to recombinant Btk SH2 domain in the presence of various concentrations of rF10 repebody. Data are mean \pm SD from three technical replicates. **f** Cartoon representation of the crystal structure of human Btk SH2 (green) in complex with rF10 repebody (salmon), PDB 6HTF. Structural statistics are reported in Supplementary Table 3. The bottom panel shows the rF10 in surface representation, residue R307 (orange) indicates the position of the pY-binding site, and side chains of SH2 residues interacting with rF10 are shown as green sticks. **g** ITC measurement of rF10 repebody to Btk SH2 K374N performed as in **b**. The K_d value was calculated from two independent measurements. **h** Superimposition of the active Btk SH2-KD model (surface representation, SH2 in green and KD in blue) with the rF10-SH2 structure (cartoon representation, SH2 in green and rF10 in salmon). Source data are provided as a Source Data file.

ibrutinib (Fig. 7b). Also in TMD8 cells, a decrease of the cumulative cell numbers were observed (Supplementary Fig. 6b). Cells in which the SH2-kinase interface is targeted with rF10 remain sensitive to ibrutinib (Supplementary Fig. 6c). Combined rF10 expression and ibrutinib treatment further increased apoptosis, as compared to the single perturbations (Supplementary Fig. 6d).

These results indicated that allosteric inhibition of Btk represents a second targeting mechanism and that combinations with ATP-competitive drugs might be beneficial.

rF10 expression promotes decreased Btk pY551 phosphorylation in HBL-1 cells, which could not be recovered by BCR stimulation using anti-human IgM (Fig. 7c, d). Interestingly, an

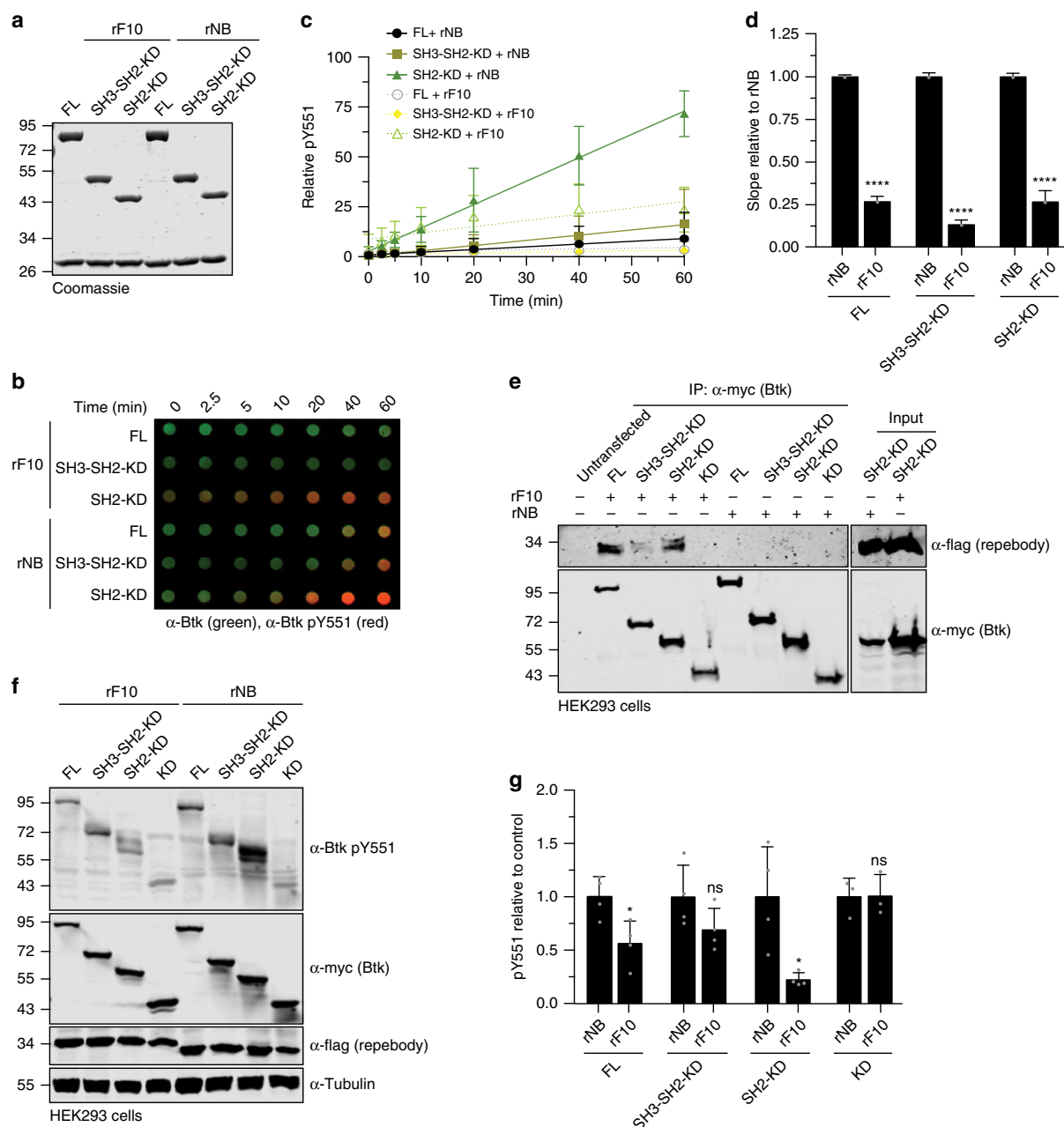


Fig. 6 rF10 reebody inhibits Btk activation in vitro and in cells. **a** Representative SDS-PAGE analysis of in vitro autophosphorylation assay containing recombinant Btk proteins mixed with rF10 or non-binding (rNB) control reebodies. **b** In vitro autophosphorylation assay performed with recombinant Btk protein with 2-fold excess of rF10 or rNB at room temperature. The levels of pY551 (red channel) and total Btk (green channel) were assessed using immunoblotting in a dot blot apparatus. **c** Btk autophosphorylation kinetics in the presence of rF10 (dashed lines) or rNB (continuous lines) reebodies shown in **b** normalized to total Btk signal and the calculated slopes of linear fits (relative velocities). Data are mean ± SD of three independent experiments ($n = 6$). **d** Relative velocities of Btk autophosphorylation relative to control reebody. Data are mean ± SD of three independent experiments ($n = 3$) and P -values relative to rNB were calculated using an unpaired t -test. **** $P \leq 0.0001$. **e** HEK293 cells were transiently co-transfected with indicated Btk constructs and reebodies, and cell lysates subjected to immunoprecipitation using anti-Myc coated beads. A representative sample of cell lysate for each reebody is shown as expression control. **f** Immunoblot analysis of cell lysates from HEK293 cells transiently co-transfected with indicated Btk constructs and reebodies used to assess Btk pY551 phosphorylation. **g** Quantification of pY551 shown in **f** normalized to total Btk (Myc) expression and relative to rNB control. Data are mean ± SD of three biological replicates ($n = 4$) and P -values were calculated using an unpaired t -test. * $P \leq 0.05$, **** $P \leq 0.0001$, and non-significant (ns). Source data are provided as a Source Data file.

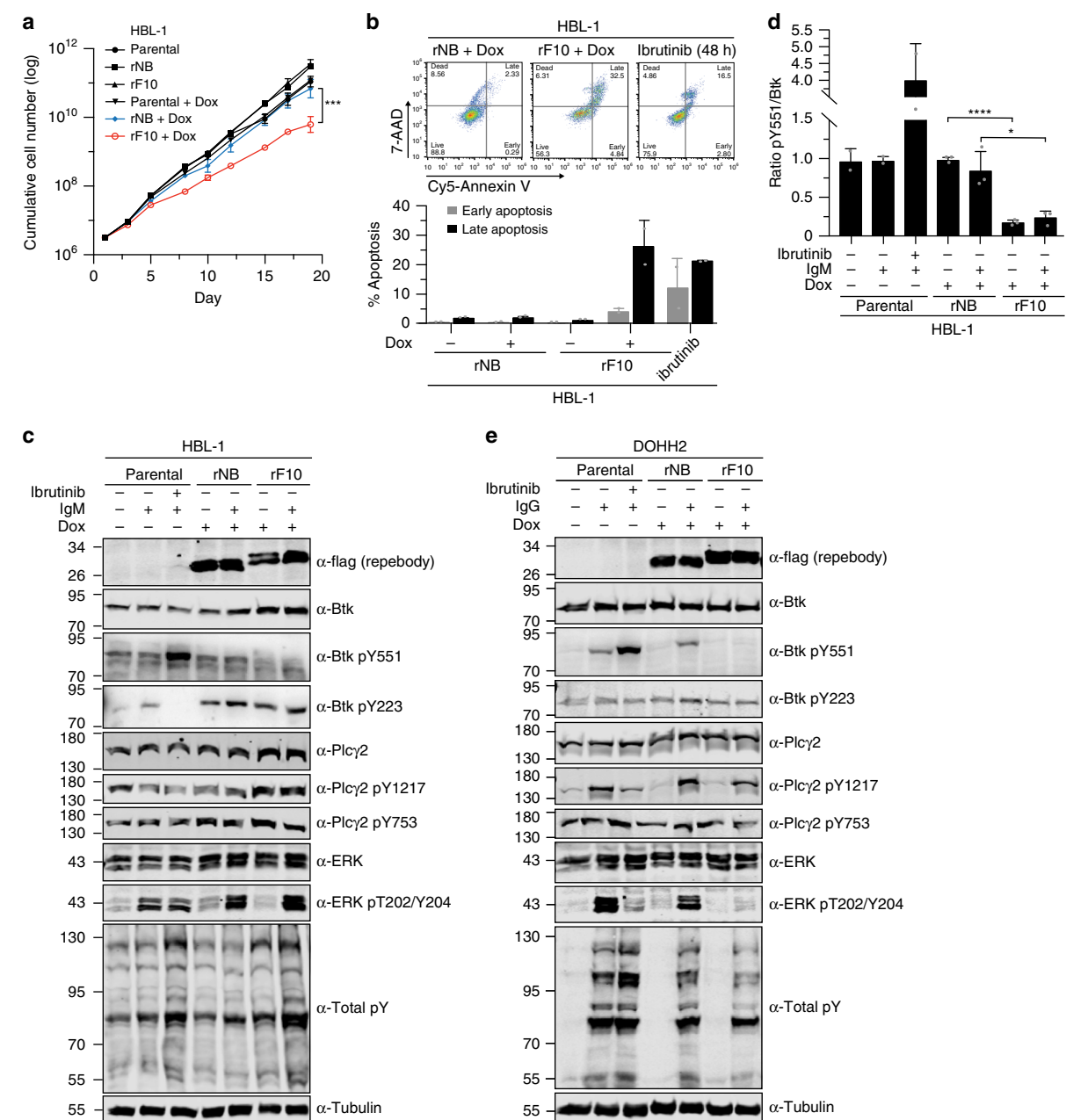


Fig. 7 Targeting the Btk SH2-KD interface decreases the viability of B-cell lymphoma cells and inhibits BCR signaling. **a** Cumulative cell number of HBL-1 cells lentivirally transduced with a doxycycline-inducible system for expression of rF10 or rNB control repebodies ($n = 4$). Parental cells are non-transduced cells. **b** Apoptosis analysis of transduced HBL-1 expressing the repebodies for 7 days. A representative gating of FACS staining is shown on top. The quantification of early (7AAD-/Annexin V+) and late (7AAD+/Annexin V+) apoptotic cells was obtained from two independent experiments ($n = 2$). Parental HBL-1 cells treated with 10 μ M of ibrutinib for 48 h were used as positive control. **c** Immunoblot analysis from transduced HBL-1 cells expressing the repebodies (Flag-tagged) for 48 h. BCR signaling was stimulated with anti-human IgM or mock-treated for 2 min before cell lysis. Ibrutinib treatment (100 nM) was performed for 15 min prior to anti-IgM stimulation. Tubulin was used as loading control. **d** Quantification of Btk pY551 shown in **c** and normalized to total Btk expression. Data are mean \pm SD from two biological replicates ($n = 3$) and P -values were calculated using an unpaired t -test. * $P \leq 0.05$. **e** Immunoblotting from transduced DOHH2 cells expressing the repebodies as performed in **c**. Source data are provided as a Source Data file.

increase in Btk and PLC γ 2 protein levels was observed upon rF10 expression, which may suggest a compensatory mechanism to counteract the activity of rF10 on Btk inhibition (Fig. 7c and Supplementary Fig. 6e). The rF10 effects on BCR signaling were also consistent in DOHH2 cells. Here, rF10 expression resulted in decreased Btk pY551, even upon BCR stimulation, decreased

PLC γ 2 phosphorylation on Y1217, one of the two main Btk phosphorylation sites, as well as strongly decreased in Erk activation (Fig. 7e).

We next tested whether targeting the SH2-KD interface offers an alternative approach to target TKI-resistant Btk. Importantly, rF10 was able to decrease pY551 (Fig. 8a, b) and total pY

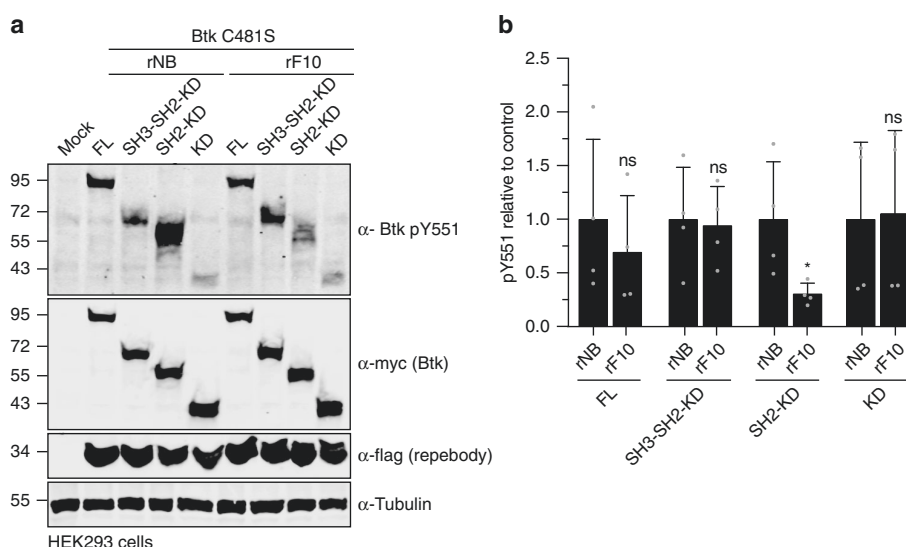


Fig. 8 Targeting the Btk SH2-KD interface decreases activation of therapy-resistant Btk with mutation on C481. **a** Immunoblot analysis of cell lysates from HEK293 cells transiently co-transfected with indicated Btk C481S constructs and rebodyies used to assess Btk pY551 phosphorylation.

b Quantification of pY551 shown in **a** normalized to total Btk (Myc) expression and relative to rNB control. Data are mean \pm SD of two biological replicates ($n = 3$) and P -values were calculated using an unpaired t -test. $^*P \leq 0.05$. Source data are provided as a Source Data file.

(Supplementary Fig. 7a, b) of Btk C481S SH2-KD expressed in HEK293 cells and to a similar extent than of wild-type SH2-KD.

To our knowledge, this is the first report of an alternative mechanism able to inhibit wild-type and drug-resistant Btk by targeting an allosteric site. Together, we demonstrated that the SH2-KD interface is critical for Btk kinase activation and a targetable site to improve therapies of Btk-driven malignancies.

Discussion

While recent studies provided considerable insight on how Btk is autoinhibited, little is known about the interdomain rearrangements coordinating Btk activation¹⁸. Here, we demonstrated that an unsuspected allosteric interaction between the Btk SH2 and KD is critical for kinase activation thereby explaining the loss-of-function phenotype of a subset of XLA mutations in the SH2 domain. Furthermore, we identified and validated the SH2-KD interface as a unique site for allosteric Btk inhibition using an engineered rebody protein. To our knowledge, this is the first alternative targeting strategy for ibrutinib-resistant Btk variants. The three FDA-approved Btk inhibitors, ibrutinib, acalabrutinib and zanubrutinib are highly susceptible to resistance development by mutations of C481 to which these inhibitors covalently bind. Therefore, the therapeutic exploitation of the Btk SH2-KD interface for patients with TKI-resistant B-cell malignancies is highly attractive.

SH2 domains are conserved, abundant domains in proteomes, and hence difficult to target using small molecules. Small engineered protein binders, in particular monobodies, have emerged as powerful tools to target SH2 domains of a variety of kinases and phosphatases and encourage the development of alternative SH2 inhibitors^{30,31,33}. In particular, recent advances in cytoplasmic delivery strategies of protein binders, its combination with targeted protein degradation and feasibility PROTAC-based Btk degradation demonstrate progress towards therapeutic applicability^{34,35}. The combined targeting of different sites on the same Btk molecule to limit resistance development is likely to follow the paradigm of the allosteric Bcr-Abl myristoyl pocket inhibitor asciminib, which abrogates drug resistance when combined with ATP-competitive Bcr-Abl inhibitors³⁶. In addition to

the SH2-kinase interaction, inhibition of dimerization of the PH-TH domain, which is required for membrane-associated activation of Btk, was proposed for allosteric targeting although not yet explored¹⁹.

It is important to note that targeting the Btk SH2-KD interface leads to particularly strong effects in DLBCL cell lines harboring CD79B ITAM mutations (Y196F in HBL-1 and Y196H in TMD8 cells) that trigger chronic activation of BCR, and are therefore heavily dependent on Btk signaling to support cell growth. This may indicate that patients with this genotype might benefit strongly from allosteric targeting approaches of Btk¹⁰. Besides B-cell malignancies, Btk is an emerging target in autoimmune diseases, e.g. rheumatoid arthritis. Here, allosteric inhibition of Btk in Fc receptor (FcRs) signaling in basophils and mast cells could provide potential therapeutic benefits³⁷.

Previous studies on other Tec kinase members, in particular Itk, reported an increase in kinase activity in the presence of protein-interacting domains, including the SH2 domain^{38,39}. This early mechanistically unexplained observation may hint towards conservation of the allosteric SH2-kinase interface in all Tec kinases. Strikingly, residues involved in the Btk SH2-kinase interface are identical in most other Tec members, but are not conserved in the Abl and Fes kinase families and residues critical for the Abl SH2-kinase interaction are not conserved in Tec kinases^{6,25} (Supplementary Fig. 7c). This further supports the notion that allosteric SH2-kinase interfaces in different kinase families appear to be diverse in terms of location, charge, hydrophobicity, size, and, importantly, dynamics. The Btk SH2-KD interaction seems highly dynamic, which precluded crystallization, in contrast to the respective Fes and Abl SH2-KD constructs^{25,40}, as well as Csk, where both SH2 and SH3 domains contact the N-lobe⁴¹.

Our data also provides a first structural insight on the molecular mechanism-of-action of several SH2 mutations in XLA. Those may disturb Btk activity by shifting the SH2-KD conformation towards a more compact and thus less active kinase compared to a native elongated conformation. Additional multi-domain structures including the SH2-kinase linker will potentially capture the preferential position of the SH2 towards the KD,

and further corroborate the model of SH2-mediated activation of Tec kinase members.

Our study adds important structural insights into the complex regulation of Tec kinases, where the SH2 domain plays a critical role in kinase activation, which is independent of its canonical function. Disruption of the SH2-KD interface hampers Btk activation and provides a molecular mechanism that explains a subset of pathogenic XLA mutations. Finally, the exploration of the SH2-KD interface as a targetable allosteric site, even in therapy-resistant Btk variants, provides an attractive approach to target Btk and potentially other Tec kinases.

Methods

Cell lines and culture conditions. HEK293 (ATCC, CRL-1573) and HEK293T (ATCC, CRL-3216) cells were cultured in DMEM (Gibco) supplemented with 10% fetal calf serum (Gibco) and 1% penicillin/streptomycin (Bioconcept). Human DLBCL cell lines DOHH2, HBL-1 and TMD8 (expressing full-length wild-type Btk protein) were kindly provided by M. Thome-Miazza (University of Lausanne), cultured in RPMI-1640 media (Gibco) supplemented with 1 mM L-glutamine (Gibco), 10% fetal calf serum (Gibco) and 1% penicillin/streptomycin (Bioconcept). All cell lines were cultured at 37 °C under 5% CO₂.

Protein expression and purification. Btk SH2 domains were cloned into the pETM30 plasmid with an N-terminal 6xHis-GST tag with tobacco etch virus (TEV) cleavage site, and expressed in *E. coli* BL21(DE3). Reprobodies were cloned into the pET21a plasmid (Millipore) with a C-terminal 6xHis-tag, and expressed in *E. coli* Origami (DE3). Expression of recombinant proteins was performed overnight at 18 °C in LB medium after induction with 0.5 mM IPTG at an optical density of ~0.8. For protein purification, bacteria were harvested in purification buffer (50 mM Tris pH 7.5, 500 mM NaCl, 1 mM DTT, 5% glycerol, 10 mM imidazole) containing DNase, homogenized using an Avestin Emulsiflex C3 homogenizer, followed by lysate clarification through centrifugation. Proteins were first purified by gravity flow Ni-NTA agarose (Qiagen, 30210) followed by tag cleavage with recombinant TEV protease in dialysis in buffer (25 mM Tris pH 7.5, 300 mM NaCl, 1 mM DTT, 5% glycerol). Finally, samples were subjected to size exclusion chromatography (SEC) on a Superdex 75 16/60 column equilibrated with dialysis buffer, and peak fractions pooled and analyzed by SDS-PAGE.

For insect cell expression, sequences were cloned into a pFast-Bac-Dual plasmid (ThermoFisher). To obtain unphosphorylated Btk, Flag-tagged Yersinia protein tyrosine phosphatase (YopH) was simultaneously expressed from the same vector. Baculoviruses were prepared following the instructions from Bac-to-Bac Baculovirus Expression System (ThermoFisher) protocol. Briefly, pFast-Bac Dual plasmids were transfected to *E. coli* DH10B followed by bacmids purification (PureLink, Invitrogen) and transfection in Sf9 cells using the transfection reagent FuGene HD (Promega, E2311). Supernatant containing the baculoviruses were used to produce recombinant proteins in Sf9 cells at density 1.5×10^6 cells mL⁻¹ in SF-900 SFM (10902-096, Thermo) cultured at 28 °C and 80% air humidity. After 3 days, cells were and resuspended in purification buffer containing 1 mM PMSF, protease cocktail inhibitor (Roche) and Benzonase (Millipore), and lysed by sonication. Cleared lysates were purified and tags removed as described above. All purified proteins could be stored at -80 °C without loss of activity. Absence of YopH phosphatase activity was reassured by a phosphatase activity assay using colorimetric PNPP substrate (Thermo) and immunoblotting.

Site-directed mutagenesis. All point mutations were introduced using the Quikchange II Site-Directed Mutagenesis Kit (Agilent) using primers described in Supplementary Table 5. Sequence alignments were generated using Geneious (Biomatters).

Kinase autophosphorylation assay. 1 μ M of recombinant Btk proteins were incubated in Tris 25 mM pH 7.5, 150 mM NaCl, 5% glycerol, 1 mM ATP, 20 mM MgCl₂, 1 mM DTT. For inhibition of autophosphorylation, 2 μ M of reprobodies were pre-incubated with 1 μ M of Btk proteins for 15 minutes before starting the reaction upon the addition of 1 mM ATP. Reactions were carried out at room temperature and stopped at desired time points by adding 2X Laemmli buffer to each tube, followed by boiling 5 minutes at 95 °C. Samples were immunoblotted onto a nitrocellulose membrane using a Dot-Blot apparatus (Bio-Rad).

HEK293 transfection. Btk constructs were expressed in HEK293 cells using pCS2-gateway plasmid containing an N-terminal 6xMyc tag, while reprobodies were cloned into pcDNA3.1 vector and contained a C-terminal Flag tag. Transient transfections with respective plasmids were performed using Polyfect transfection reagent (Qiagen). 48 h after transfection, cells were harvested, lysed and samples further processed for immunoblotting.

Cell lysis and immunoblotting. Cells were lysed in IP buffer (50 mM Tris-HCl pH 7.5, 150 mM NaCl, 1% NP-40, 5 mM EDTA, 5 mM EGTA, 25 mM NaF, 1 mM orthovanadate, 1 mM PMSF, 10 mg mL⁻¹ TPCK and protease cocktail inhibitor from Roche), and cleared by centrifugation at 14,000 rpm for 10 minutes at 4 °C. Total protein concentration was measured using Bradford assay (Bio-Rad). All immunoblotting analysis was performed using 100 μ g of total protein. Original uncropped immunoblots are provided in the Source Data file.

Antibodies. Anti-Total pY (clone 4G10), 1:1000, Millipore # 05-321; anti-Btk (D6T2C), 1:1000, Cell Signaling # 56044; anti-Btk, 1:1000, Thermo Scientific # PA5-27392; anti-Btk (pY551)/Itk (pY511) Clone 24a, 1:1000, BD Biosciences # 558034; anti-Btk (pY223), 1:1000, Cell Signaling #5082; anti-p44/42 MAPK (Erk1/2), 1:1000, Cell Signaling #9102; anti-phospho-p44/42 MAPK (Erk1/2) (Thr202/Tyr204) (E10), 1:1000, Cell Signaling #9106; anti-PLC γ 2, dilution 1:1000, Cell Signaling, #3872; anti-PLC γ 2 (Tyr1217), 1:1000, Cell Signaling #3871; anti-Flag, 1:5000, Sigma # F3165; anti-Penta-his, 1:5000, Qiagen #34660; anti-PLC γ 2 (Tyr753) [EPR5914-3], 1:1000, Abcam #ab133455; anti-Tubulin, 1:2000, Sigma #T9026; anti-Myc-tag Myc.A7 DyLight800, 1:10,000, Thermo Scientific #MA1-21316-D800; anti-mouse IgG IRDye 800CW, 1:10,000, LiCor #926-32210; anti-Rabbit IgG (H+L) IRDye800, 1:10,000, Rockland #611-732-127; anti-Mouse IgG (H+L) Peroxidase AffiniPure, 1:10,000, Jackson ImmunoResearch #115-035-003; anti-Rabbit IgG (H+L) Peroxidase AffiniPure, 1:10,000, Jackson ImmunoResearch #111-035-003. The full information on primary and secondary antibodies that were used for the reported experiments is available in the Reporting Summary.

Western blot quantification. Quantification using of fluorescent secondary antibodies was done using the Li-Cor Odyssey system. ECL prime detection reagent (RPN2232, GE Healthcare) was used to detect HRP-conjugated antibodies using the C-digit Blot scanner (Li-Cor). Western blot normalization was done using total protein signal or loading control (tubulin).

Immunoprecipitation. Immunoprecipitation from HEK293 cell lysates was done using 1 mg of total protein adjusted to 1 mL volume with IP buffer. Anti-c-Myc Agarose Affinity Gel (Thermo, A7470) was added to the cell lysates and incubated for 3 h on a rotating wheel at 4 °C. Beads were subsequently washed three times with IP buffer and finally boiled in Laemmli buffer for 5 min at 95 °C before subjected to immunoblotting.

Mass spectrometry. For confirmation of protein identity and phosphorylation status, recombinant proteins were analyzed on a Xevo G2-S QTOF mass spectrometer (Waters) operated in positive ionization using the ZSpray dual-orthogonal multimode ESI/APCI/ESCI source. Data were processed using MassLynx 4.1 software and MaxEnt1 application for deconvolution.

B-cell transduction and BCR stimulation. Reprobodies containing a C-terminal Flag tag were cloned into the doxycycline-inducible (Tet-ON) lentiviral vector pcW57.1 (Addgene) and co-transfected with envelope and packaging plasmids (pMD2G and pCMVRS.74 respectively, a kind gift from the Trono Lab, EPFL) into HEK293T cells using the CalPhos Mammalian Transfection kit (Clontech). Lentiviruses were concentrated by ultracentrifugation at 30,000g for 2 h at 16 °C, and added to lymphoma cell lines, followed by a single spinoculation step at 300g for 60 min at room temperature. On the next day, cell media was replaced and cells selected using 2 μ g mL⁻¹ puromycin. Reprobodies were induced by the addition of 2 μ g mL⁻¹ of doxycycline. For BCR stimulation, cells at density 5×10^6 cells mL⁻¹ were incubated at 37 °C with 20 μ g mL⁻¹ anti-human IgM/G F(ab')₂ from goat (Jackson ImmunoResearch, 109-006-129 and 109-006-098) in RPMI-1640 media without calf serum. Cells were then harvested, immediately lysed and samples further processed for immunoblotting.

Cell viability assays. DLBCL cell lines were treated for 48 h with ibrutinib (concentration range 50 nM to 100 μ M) and viability assessed using Cell Titer Glow (Promega). Luminescence was measured in a SpectraMax M5 plate reader (Molecular Devices). DMSO (50 μ M) and doxorubicin (10 μ M) were used as negative and positive controls, respectively. To assess the effects of reprobodies on the viability of DLBCL, transduced cells were treated with 2 μ g mL⁻¹ of doxycycline to induce expression of reprobodies, and cell number verified using a Casy Cell Counter (OLS Omni Life Science). Cell density was maintained at 5×10^5 cells mL⁻¹ and regularly diluted when cell density reached 3×10^6 cells mL⁻¹. Parental (non-transduced) and non-induced cells were used as control.

Flow cytometry. Transduced cells were seeded in 6-well cell culture plates, treated with 2 μ g mL⁻¹ of doxycycline and/or ibrutinib, and stained for the apoptosis marker Annexin V. Briefly, treated cells were washed twice with PBS and resuspended in Annexin V binding buffer containing Cy5-Annexin V (BD, 559934) and 7AAD (BD, 559927) using instructions from the supplier. Cells were gently dissociated and filtered through a 35 μ m nylon mesh before data acquisition in a Gallios flow cytometer (BD). A minimum of 10,000 gated events were collected for each sample and data was analyzed using the FlowJo (v10.6) software.

Molecular dynamics (MD) simulations. System preparation: The Btk SH2-KD structural model used for our MD simulations was built starting from the X-ray structures of the apo-KD of Btk (PDB: 1K2P) and SH2 domain (PDB: 6HTF). The SH2 domain was initially positioned on the top of KD at ~60 Å from it (the distance is measured considering the center of mass of SH2 and N-lobe of KD). The linker sequence was manually added by means of Maestro (Schrödinger Release 2016-1: Maestro, Schrödinger, LLC, New York, 2016) obtaining an extended configuration (Fig. 3a) and subsequently refined through a scaled MD simulation run. Firstly, the protein was parameterized by using the Amber 14SB force field⁴² and immersed in a TIP3P⁴³ water box having 12 Å of buffer between the protein and the three edges of the box. The protein was then neutralized by adding an appropriate number of Cl⁻ ions. After minimization, the protein underwent to three NVT simulations steps of 500 ps each to gradually reach the target temperature of 300 K (first step from 0 to 100 K, second step from 100 K to 200 K and last step from 200 K to 300 K). Here, a restraints of 1000 kJ mol⁻¹ nm⁻² was applied to backbone and the velocity-rescaling thermostat⁴⁴ was used. Then, 1 ns of NPT simulation was performed maintaining the restraints and employing the Parrinello-Rahman barostat⁴⁵ to reach the target pressure of 1 bar. Finally, to enhance the sampling of the linker sequence, we performed a 70 ns long Scaled MD simulations²⁶, using a $\lambda = 0.8$, and releasing the restraints for the linker sequence. Electrostatics were treated with the cutoff method for short-range interactions and with the Particle Mesh Ewald method⁴⁶ for the long-range ones ($r_{\text{list}} = 1.1$ nm, cutoff distance = 1.1 nm, VdW distance = 1.1 nm, PME order = 4). To obtain the optimal configuration of the linker sequence, we performed a cluster analysis on the last 70 ns long trajectory. The centroid of the most populated cluster was then employed as starting point for the next MD simulations. Both the MD simulations and cluster analysis were performed by using BiKi LifeSciences suite⁴⁷.

Scaled MD simulations: We run multiple replicas Scaled MD simulations²⁶ to enhance the sampling of Btk kinase and speed up the binding events between SH2 and KD. As starting point, we employed the refined structure of the Btk SH2-KD-linker model (see system preparation section). The equilibrated system was submitted to 40 replicates ~100 ns long Scaled MD simulations using a $\lambda = 0.9$. Here, restraints were not applied because the high scaling factor enabled adequate sampling without affecting the overall folding of the system. BiKi LifeSciences suite⁴⁷ was used for Scaled MD simulations, using the same settings as in the system preparation section.

Data Analysis: The final aim of our MD studies is to collect all possible Btk SH2-KD bound configurations and to determine which is the most likely bound configuration(s) using both SAXS and mutational studies data. The collected 4 μ s-long scaled MD trajectories resulted in a total of 400,000 frames. From this large ensemble, we extracted the unique and non-redundant Btk SH2-KD configurations, using a clustering procedure implemented in BiKi⁴⁷. The resulting 760 structures were submitted to another cluster analysis to probe the preferred 3D structural organization of SH2 domain with respect of KD. Also, we run a CRYSOLO analysis⁴⁸ to compute the χ^2 value for each structure, in order to select the SH2-KD complexes with the best fitting with the experimental SAXS curves.

Development of reprobodies. Selection and affinity maturation of human Btk SH2-specific reprobody (rF10) were performed through phage display and a modular evolution approach as previously described²⁸.

Small-angle X-ray scattering (SAXS). SAXS data were collected at the BM29 beamline (ESRF Grenoble, France). All proteins were measured in buffer containing 25 mM Tris pH 7.5, 300 mM NaCl, 1 mM TCEP and 5% glycerol. A robotic sample changer carried out the measurement in the batch mode, while in-line SEC-SAXS was performed using a Superdex S200 Increase 10/300 column (GE Healthcare) with a flow rate of 0.7 mL min⁻¹ at room temperature. Acquired data were averaged and subtracted from an appropriate solvent-blank to produce the final curve using the ATSAS Suite, EMBL⁴⁹ and CHROMIXS⁵⁰. Initial data pre-processing and reduction were performed using an automatic pipeline. Final scattering curves were analyzed using PRIMUS for evaluation of molecular dimensions (R_g)⁵¹ and maximum particle dimension (D_{max}) using GNOM⁵². Moreover, the Porod volume was computed using the Porod invariant⁵³, and the molecular mass estimated using SAXSMoW 2.0⁵⁴, Bayesian inference approach⁵⁵ and Volume-of-correlation⁵⁶. Ab initio models were computed with DAMMIF⁵⁷. SREFLEX⁵⁰ was employed to improve the agreement of flexible multidomain models to the experimental data. Finally, the flexibility of multidomain complexes was assessed with Ensemble Optimization Method 2.0²⁷. Fitting of models to experimental data was assessed using CRYSOLO⁴⁸ molecular and superimpositions performed with the SASpy⁵⁸. Data collection and structure determination statistics are described in Supplementary Tables 2 and 4.

Structure determination. Recombinant Btk SH2 and rF10 proteins were mixed at 1:1 ratio and the complex purified with a Superdex 75 column 16/600 (GE Healthcare) in buffer containing 25 mM Tris pH 7.5, 300 mM NaCl, 1 mM TCEP. The purified complex was concentrated to ~25 mg mL⁻¹ and crystallized at 18 °C using the hanging-drop vapor-diffusion method by mixing 1:1 with a solution containing 1 M Tris pH 8.5, 300 mM sodium fluoride, 300 mM sodium bromide, 300 mM sodium iodide, 25% MPD; 25% PEG 1000; 25% PEG 3350. 20% glycerol

was used as a cryoprotectant. X-ray diffraction data was collected at the SLS Beamline X06DA in the Swiss Lightsource (SLS, Villigen, Switzerland) at a wavelength of 1 Å and temperature of 100 K. Data collection and structure determination statistics are described in Supplementary Table 3. Diffraction data was processed and scaled with the XDS package. The structure was solved by molecular replacement employing models derived from a previously reported reprobody (PDB 5B4P) and Btk SH2 (PDB 2GE9) excluding loop regions. Molecular replacement, manual model building, B-factor refinement, solvent addition, energy-minimization and refinement of structures were conducted iteratively using Phaser and Coot (Phenix version 1.13). Molecular graphics were generated using PyMOL (DeLano Scientific).

Isothermal titration calorimetry (ITC). Proteins were extensively dialyzed in buffer containing 20 mM Hepes pH 7.5 and 150 mM NaCl, briefly degassed, and concentration determined by measuring UV absorbance at 280 nm. ITC measurements were performed on a MicroCal PEQ-ITC (Malvern) instrument. The reprobody (100 μ M) was titrated into SH2 domains (10 μ M) at room temperature in 16 steps with 0.49 μ L for the first and 2.49 μ L for the other steps. Thermodynamic parameters were obtained using the MicroCal software.

Fluorescent Polarization (FP) binding assays. Btk SH2 WT and mutants were incubated at several concentrations with 1 μ M of FITC-labeled peptide (ADNDpYIIPDP) in Tris 40 mM pH 8, 150 mM NaCl and 1 mM DTT. Competitive FP assay was performed using 25 μ M of Btk SH2 and 1 μ M of peptide incubated with reprobody in a range of 200 μ M–20 nM. FP signal was measured using a SpectraMax M5 plate reader (Molecular Devices) with excitation at 485 nm and emission at 530 nm in a 96 well black-plate (Greiner).

Multi-angle light scattering analysis (SEC-MALS). Multi-angle light scattering was used to probe for oligomerization states. All measurements were performed at room temperature using a Dawn Heleos multi-angle light scattering detector (Wyatt Technologies) coupled to an SEC column. 80 μ L (0.5 mg mL⁻¹) of purified recombinant protein was injected into a Superdex 75 HR10/30 column (GE Healthcare) in buffer containing 25 mM Tris-HCl pH 7.5, 150 mM NaCl, 1 mM TCEP, and eluted at a flow rate of 0.5 mL min⁻¹. Absolute molecular weight and homogeneity were determined using ASTRA version 5.3 (Wyatt Technologies).

Circular dichroism (CD). Far-UV spectra (190–300 nm) of recombinant Btk SH2 WT and mutants were carried out in buffer containing 10 mM Na-phosphate buffer pH 7.2 and 100 mM NaF using a 0.1 cm quartz cell and CD Spectrometer Chirascan V100 (AppliedPhotophysics). Data was acquired at a step size of 1 nm and bandwidth of 1 nm. 3 scan records for each protein were subtracted from the background (buffer only) and averaged to generate the data reported in units of mean molar ellipticity per residue. Melting curve analysis was performed by measuring proteins at the wavelength corresponding to the peak for the predominantly β -sheet SH2 domain (218 nm) in a temperature range from 20 to 94 °C, ramp-rate 1 °C per minute.

In vitro Kinase assay. 2 μ M of reprobodies were pre-incubated with 1 μ M of recombinant Btk proteins in buffer Tris 25 mM pH 7.5, 150 mM NaCl, 5% glycerol, 20 mM MgCl₂, 1 mM DTT in the presence of 50 μ M ATP, 7 μ Ci γ -³²P-ATP, and PLC γ 2 peptide carrying an N-terminal biotin (biotin-ERDINSLYDYSR-amide). Peptide concentrations ranged from 100 μ M to 30 μ M. Reactions were carried out on a final volume of 20 μ L at room temperature for 20 min and terminated using 10 μ L 7.5 M guanidiniumhydrochloride. Samples were spotted onto a SAM2 Biotin Capture membrane (Promega) and further treated according to the instructions of the manufacturer.

Mapping of Btk autophosphorylation sites. Sample preparation: Recombinant autophosphorylated Btk SH2-KD was separated by SDS-PAGE and stained with Coomassie. Bands of interest were excised, in-gel digested in reduced in 10 mM DTE, 50 mM AB, and then alkylated in 55 mM iodoacetamide, 50 mM AB. After a washing step, gel extracts were digested with MS Grade Trypsin over-night. Resulting peptides were finally extracted using a high organic containing solvent and dried by vacuum centrifugation prior to LC-MS2 measurements or phosphopeptides enrichment.

Next, 90% of the extracted peptide was used for phosphopeptides enrichment step while the remaining 10% was used for sample identification. Titanium dioxide affinity principle was used for enrichment using home-made titania tips (based on Thingholm and Larsen 2009). Dried samples were resuspended 0.75% TFA, 60% acetonitrile, 300 mg mL⁻¹ lactic acid, loaded on tips, and eluted in 0.5% ammonium hydroxide and 5% piperidine. Samples were acidified and dried down prior to LC-MS2 measurements.

MS analysis: For the MS detection of phosphopeptides, dried samples were resuspended in 0.1% TFA and separated by C18 Reverse Phase nano UPLC using a Dionex Ultimate 3000 RSLC system (Thermo Fischer) connected to an Orbitrap Elite Mass Spectrometer (Thermo Fischer). Samples were first trapped on a home-made capillary C18 pre-column and then separated on a C18 capillary column

(Nikkyo Technos Co; Magic AQ C18; 3 μm - 100 \AA ; 15 cm \times 75 μm ID). Data-dependent mode was used for MS acquisitions were the 20 most intense parent ions were selected for subsequent fragmentation by CID. A potential phosphopeptides m/z inclusion list was also generated and used to maximize detection chances.

Quantification and statistical analysis. All data reported were analyzed using Prism 7 (GraphPad) using software-defined fitting models and unpaired t -test statistical test. Calculated P -values are indicated as non-significant (ns), $P \leq 0.05$ (*), $P \leq 0.01$ (**), $P \leq 0.001$ (***) and $P \leq 0.0001$ (****).

Reporting Summary. Further information on research design is available in the Nature Research Reporting Summary linked to this article.

Data availability

The data that support the findings of this study are available from the corresponding author upon reasonable request. The X-ray structure of the rF10-SH2 complex was deposited at Protein Data Bank, PDB 6HTF [<https://www.rcsb.org/structure/6HTF>]. Full SAXS curves and analyzed data for wild-type Btk proteins were deposited at SASBDB [<https://www.sasbdb.org/data>] with accession numbers SASDF53, SASDF63, SASDF73, and SASDF83.

Received: 2 January 2020; Accepted: 15 April 2020;

Published online: 08 May 2020

References

- Druker, B. J. et al. Efficacy and safety of a specific inhibitor of the BCR-ABL tyrosine kinase in chronic myeloid leukemia. *N. Engl. J. Med.* **344**, 1031–1037 (2001).
- Hantschel, O. Unexpected off-targets and paradoxical pathway activation by kinase inhibitors. *ACS Chem. Biol.* **10**, 234–245 (2015).
- Konieczkowski, D. J., Johannessen, C. M. & Garraway, L. A. A convergence-based framework for cancer drug resistance. *Cancer Cell* **33**, 801–815 (2018).
- Hantschel, O. et al. A myristoyl/phosphotyrosine switch regulates c-Abl. *Cell* **112**, 845–857 (2003).
- Wylie, A. A. et al. The allosteric inhibitor ABL001 enables dual targeting of BCR-ABL1. *Nature* **543**, 733–737 (2017).
- Grebien, F. et al. Targeting the SH2-kinase interface in Bcr-Abl inhibits leukemogenesis. *Cell* **147**, 306–319 (2011).
- Leroux, A. E., Schulze, J. O. & Biondi, R. M. AGC kinases, mechanisms of regulation and innovative drug development. *Semin. Cancer Biol.* **48**, 1–17 (2018).
- Fang, Z., Grutter, C. & Rauh, D. Strategies for the selective regulation of kinases with allosteric modulators: exploiting exclusive structural features. *ACS Chem. Biol.* **8**, 58–70 (2013).
- Vihinen, M., Mattsson, P. T. & Smith, C. I. Bruton tyrosine kinase (BTK) in X-linked agammaglobulinemia (XLA). *Front. Biosci.* **5**, D917–D928 (2000).
- Davis, R. E. et al. Chronic active B-cell-receptor signalling in diffuse large B-cell lymphoma. *Nature* **463**, 88–92 (2010).
- Young, R. M. & Staudt, L. M. Targeting pathological B cell receptor signalling in lymphoid malignancies. *Nat. Rev. Drug Discov.* **12**, 229–243 (2013).
- Hantschel, O. et al. The Btk tyrosine kinase is a major target of the Bcr-Abl inhibitor dasatinib. *Proc. Natl. Acad. Sci. USA* **104**, 13283–13288 (2007).
- Pan, Z. et al. Discovery of selective irreversible inhibitors for Bruton's tyrosine kinase. *ChemMedChem* **2**, 58–61 (2007).
- Byrd, J. C. et al. Acalabrutinib (ACP-196) in relapsed chronic lymphocytic. *Leuk. N. Engl. J. Med.* **374**, 323–332 (2016).
- Guo, Y. et al. Discovery of Zanubrutinib (BGB-3111), a novel, potent, and selective covalent inhibitor of Bruton's tyrosine kinase. *J. Med. Chem.* **62**, 7923–7940 (2019).
- Quinquenel, A. et al. Prevalence of BTK and PLCG2 mutations in a real-life CLL cohort still on ibrutinib after 3 years: a FILO group study. *Blood* **134**, 641–644 (2019).
- Hantschel, O. & Superti-Furga, G. Regulation of the c-Abl and Bcr-Abl Tyrosine Kinases. *Nat. Rev. Mol. Cell Biol.* **5**, 33–44 (2004).
- Shah, N. H., Amacher, J. F., Nock, L. M. & Kuriyan, J. The Src module: an ancient scaffold in the evolution of cytoplasmic tyrosine kinases. *Crit. Rev. Biochem. Mol. Biol.* **53**, 535–563 (2018).
- Wang, Q. et al. Autoinhibition of Bruton's tyrosine kinase (Btk) and activation by soluble inositol hexakisphosphate. *Elife* **4**, e06074 (2015).
- Joseph, R. E., Wales, T. E., Fulton, D. B., Engen, J. R. & Andreotti, A. H. Achieving a graded immune response: BTK adopts a range of active/inactive conformations dictated by multiple interdomain contacts. *Structure* **25**, 1481–1494 e4 (2017).
- Park, H. et al. Regulation of Btk function by a major autophosphorylation site within the SH3 domain. *Immunity* **4**, 515–525 (1996).
- Marquez, J. A. et al. Conformation of full-length Bruton tyrosine kinase (Btk) from synchrotron X-ray solution scattering. *EMBO J.* **22**, 4616–4624 (2003).
- Valiaho, J., Smith, C. I. & Vihinen, M. BTKbase: the mutation database for X-linked agammaglobulinemia. *Hum. Mutat.* **27**, 1209–1217 (2006).
- Mattsson, P. T. et al. Six X-linked agammaglobulinemia-causing missense mutations in the Src homology 2 domain of Bruton's tyrosine kinase: phosphotyrosine-binding and circular dichroism analysis. *J. Immunol.* **164**, 4170–4177 (2000).
- Filippakopoulos, P. et al. Structural coupling of SH2-kinase domains links Fes and Abl substrate recognition and kinase activation. *Cell* **134**, 793–803 (2008).
- Mollica, L. et al. Kinetics of protein-ligand unbinding via smoothed potential molecular dynamics simulations. *Sci. Rep.* **5**, 11539 (2015).
- Tria, G., Kachala, M. & Svergun, D. I. Advanced ensemble optimization method EOM 2.0. In *Proceedings of the 15th International Small-Angle Scattering Conference (SAS2012)* (eds. McGilivray, D. J., Trehwella, J., Gilbert, E. P. & Hanley, T. L.) (Sydney, 2013).
- Lee, S. C. et al. Design of a binding scaffold based on variable lymphocyte receptors of jawless vertebrates by module engineering. *Proc. Natl. Acad. Sci. USA* **109**, 3299–3304 (2012).
- Wojcik, J. et al. A potent and highly specific FN3 monoclonal antibody inhibitor of the Abl SH2 domain. *Nat. Struct. Mol. Biol.* **17**, 519–527 (2010).
- Sha, F. et al. Dissection of the BCR-ABL signaling network using highly specific monoclonal antibodies to the SHP2 SH2 domains. *Proc. Natl. Acad. Sci. USA* **110**, 14924–14929 (2013).
- Kukenshoner, T. et al. Selective targeting of SH2 domain-phosphotyrosine interactions of Src family tyrosine kinases with monoclonal antibodies. *J. Mol. Biol.* **429**, 1364–1380 (2017).
- Huang, K. C., Cheng, H. T., Pai, M. T., Tzeng, S. R. & Cheng, J. W. Solution structure and phosphopeptide binding of the SH2 domain from the human Bruton's tyrosine kinase. *J. Biomol. NMR* **36**, 73–78 (2006).
- Wojcik, J. et al. Allosteric inhibition of Bcr-Abl kinase by high affinity monoclonal antibodies directed to the Src homology 2 (SH2)-kinase interface. *J. Biol. Chem.* **291**, 8836–8847 (2016).
- Schmit, N. E., Neopane, K. & Hantschel, O. Targeted protein degradation through cytosolic delivery of monoclonal binders using bacterial toxins. *ACS Chem. Biol.* **14**, 916–924 (2019).
- Dobrovolsky, D. et al. Bruton tyrosine kinase degradation as a therapeutic strategy for cancer. *Blood* **133**, 952–961 (2019).
- Eide, C. A. et al. Combining the allosteric inhibitor asciminib with ponatinib suppresses emergence of and restores efficacy against highly resistant BCR-ABL1 mutants. *Cancer Cell* **36**, 431–443 e5 (2019).
- Pal Singh, S., Dammeijer, F. & Hendriks, R. W. Role of Bruton's tyrosine kinase in B cells and malignancies. *Mol. Cancer* **17**, 57 (2018).
- Joseph, R. E., Min, L., Xu, R., Musselman, E. D. & Andreotti, A. H. A remote substrate docking mechanism for the tec family tyrosine kinases. *Biochemistry* **46**, 5595–5603 (2007).
- Joseph, R. E., Severin, A., Min, L., Fulton, D. B. & Andreotti, A. H. SH2-dependent autophosphorylation within the Tec family kinase Itk. *J. Mol. Biol.* **391**, 164–177 (2009).
- Lorenz, S., Deng, P., Hantschel, O., Superti-Furga, G. & Kuriyan, J. Crystal structure of an SH2-kinase construct of c-Abl and effect of the SH2 domain on kinase activity. *Biochem. J.* **468**, 283–291 (2015).
- Ogawa, A. et al. Structure of the carboxyl-terminal Src kinase, Csk. *J. Biol. Chem.* **277**, 14351–14354 (2002).
- Maier, J. A. et al. ff14SB: improving the accuracy of protein side chain and backbone parameters from ff99SB. *J. Chem. theory Comput.* **11**, 3696–3713 (2015).
- Jorgensen, W. L. & Madura, J. D. Quantum and statistical studies of liquids 25. Solvation and conformation of methanol in water. *J. Am. Chem. Soc.* **105**, 1407–1413 (1983).
- Bussi, G., Donadio, D. & Parrinello, M. Canonical sampling through velocity rescaling. *J. Chem. Phys.* **126**, 014101 (2007).
- Parrinello, M. & Rahman, A. Polymorphic transitions in single-crystals - a new molecular-dynamics method. *J. Appl. Phys.* **52**, 7182–7190 (1981).
- Darden, T., York, D. & Pedersen, L. Particle mesh Ewald - an N-Log(N) method for Ewald sums in large systems. *J. Chem. Phys.* **98**, 10089–10092 (1993).
- Decherchi, S., Bottegoni, G., Spitaleri, A., Rocchia, W. & Cavalli, A. BiKi life sciences: a new suite for molecular dynamics and related methods in drug discovery. *J. Chem. Inf. Model* **58**, 219–224 (2018).

48. Svergun, D., Barberato, C. & Koch, M. H. J. CRYSOLO - a program to evaluate x-ray solution scattering of biological macromolecules from atomic coordinates. *J. Appl. Crystallogr.* **28**, 768–773 (1995).
49. Franke, D. et al. ATSAS 2.8: a comprehensive data analysis suite for small-angle scattering from macromolecular solutions. *J. Appl. Crystallogr.* **50**, 1212–1225 (2017).
50. Panjkovich, A. & Svergun, D. I. Deciphering conformational transitions of proteins by small angle X-ray scattering and normal mode analysis. *Phys. Chem. Chem. Phys.* **18**, 5707–5719 (2016).
51. Konarev, P. V., Volkov, V. V., Sokolova, A. V., Koch, M. H. J. & Svergun, D. I. PRIMUS: a Windows PC-based system for small-angle scattering data analysis. *J. Appl. Crystallogr.* **36**, 1277–1282 (2003).
52. Svergun, D. I. Determination of the regularization parameter in indirect-transform methods using perceptual criteria. *J. Appl. Crystallogr.* **25**, 495–503 (1992).
53. Porod, G. Die Röntgenkleinwinkelstreuung Von Dichtgepackten Kolloiden Systemen. *Kolloid Z.* **125**, 108–122 (1952).
54. Fischer, H., Neto, M. D., Napolitano, H. B., Polikarpov, I. & Craievich, A. F. Determination of the molecular weight of proteins in solution from a single small-angle X-ray scattering measurement on a relative scale. *J. Appl. Crystallogr.* **43**, 101–109 (2010).
55. Hajizadeh, N. R., Franke, D., Jeffries, C. M. & Svergun, D. I. Consensus Bayesian assessment of protein molecular mass from solution X-ray scattering data. *Sci. Rep.* **8**, 7204 (2018).
56. Rambo, R. P. & Tainer, J. A. Accurate assessment of mass, models and resolution by small-angle scattering. *Nature* **496**, 477–481 (2013).
57. Franke, D. & Svergun, D. I. DAMMIF, a program for rapid ab-initio shape determination in small-angle scattering. *J. Appl. Crystallogr.* **42**, 342–346 (2009).
58. Panjkovich, A. & Svergun, D. I. SASpy: a PyMOL plugin for manipulation and refinement of hybrid models against small angle X-ray scattering data. *Bioinformatics* **32**, 2062–2064 (2016).

Acknowledgements

This work was supported by grants from the Swiss Cancer League (grant KLS-3595-02-2015) and the Global Research Laboratory (GRL) Program (Korea National Research Foundation). We thank M. Tully (ESRF Grenoble) for support during SAXS measurements, M. Thome-Miazza for cell lines, A. Reynaud for help with crystallization, L. Menin and D. Ortiz for MS analysis and J. Kuriyan for some Btk expression constructs. We acknowledge the Paul Scherrer Institute (Villigen) for provision of synchrotron radiation beamtime and local contacts for their support during crystal diffraction. We thank all members of the Hantschel lab for continuous support and discussions.

Author contributions

D.D. conducted and analyzed most experiments. A.L. contributed to study design and experiments. G.L.S. performed the molecular dynamics simulations under M.D.P. and M.D.V. supervision. S.J., Y.-K. S. and H.-S.K. developed the rebody. M.J.M. contributed to the SAXS data acquisition. A.P. and D.S. provided assistance for the SAXS analysis. S.G. provided technical assistance and vital tools for all experiments. F.P. performed crystallography data acquisition and support to solve the structure. T.K. assisted with the ITC measurements. D.D. and O.H. designed and coordinated the study, planned the experiments, interpreted the data and wrote the manuscript.

Competing interests

The authors declare no competing interests.

Additional information

Supplementary information is available for this paper at <https://doi.org/10.1038/s41467-020-16128-5>.

Correspondence and requests for materials should be addressed to O.H.

Peer review information *Nature Communications* thanks Edvard Smith, and the other, anonymous, reviewer(s) for their contribution to the peer review of this work. Peer reviewer reports are available.

Reprints and permission information is available at <http://www.nature.com/reprints>

Publisher's note Springer Nature remains neutral with regard to jurisdictional claims in published maps and institutional affiliations.



Open Access This article is licensed under a Creative Commons Attribution 4.0 International License, which permits use, sharing, adaptation, distribution and reproduction in any medium or format, as long as you give appropriate credit to the original author(s) and the source, provide a link to the Creative Commons license, and indicate if changes were made. The images or other third party material in this article are included in the article's Creative Commons license, unless indicated otherwise in a credit line to the material. If material is not included in the article's Creative Commons license and your intended use is not permitted by statutory regulation or exceeds the permitted use, you will need to obtain permission directly from the copyright holder. To view a copy of this license, visit <http://creativecommons.org/licenses/by/4.0/>.

© The Author(s) 2020

SUPPLEMENTARY INFORMATION

Btk SH2-kinase interface is critical for allosteric kinase activation and its targeting inhibits B-cell neoplasms

Duarte et al.

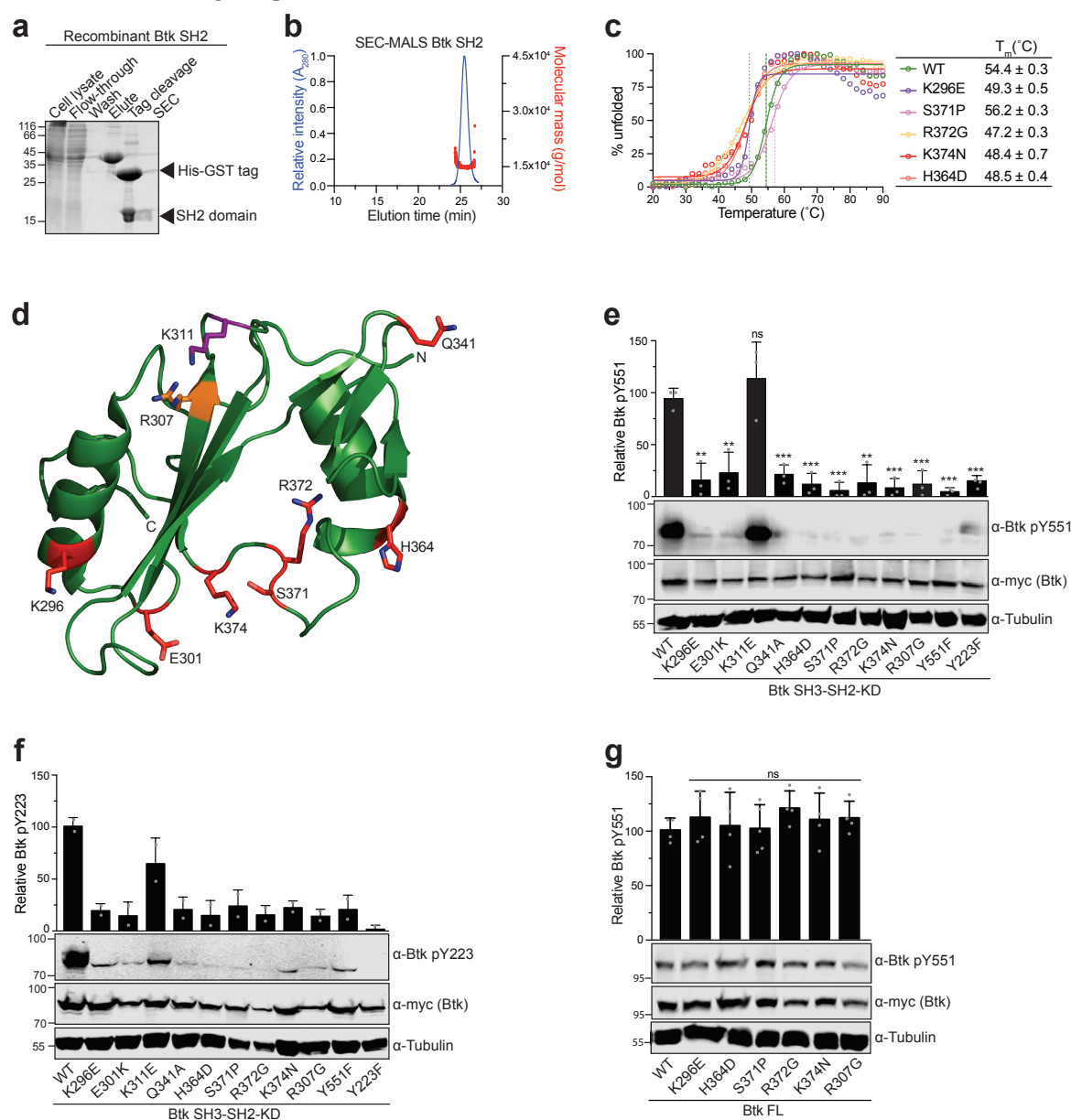
Contents

Supplementary Figures 1-7

Supplementary Tables 1-5

SUPPLEMENTARY FIGURES 1-7

Supplementary Figure 1



Supplementary Figure 1, related to Figure 1. Effect of XLA mutations *in vitro* and in HEK cells.

(a) Representative SDS-PAGE analysis of purification steps for recombinant Btk SH2 wild-type from *E. coli*. TEV cleavage was used to removal of 6xHis-GST tag used for purification. All Btk SH2 mutants were purified using an identical protocol.

(b) Representative SEC-MALS analysis of purified Btk SH2 domain wild-type (monomer = 13.2 kDa). All proteins were analyzed by SEC-MALS and found in the homogenous state in solution (data not shown).

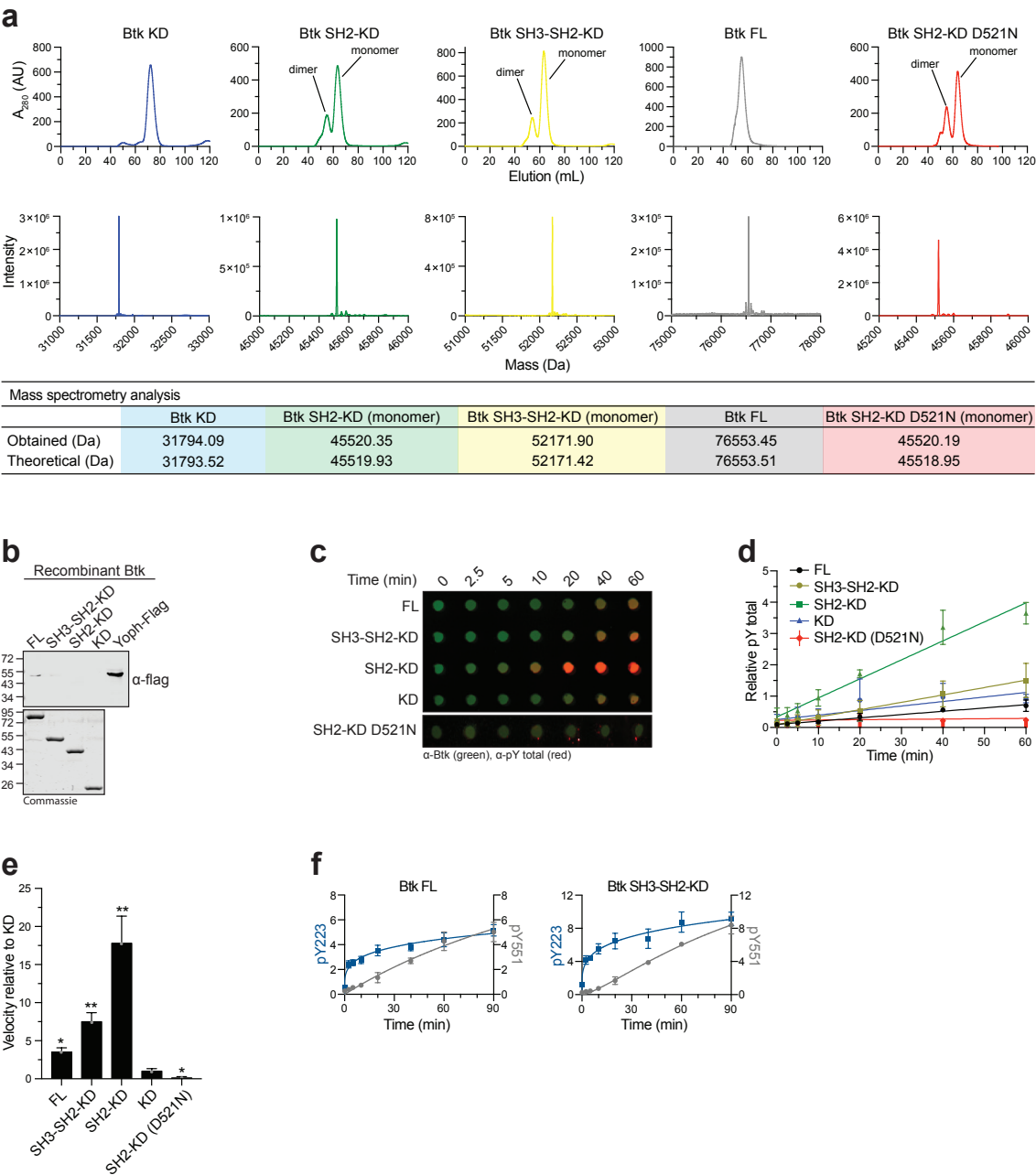
(c) Thermal shift assay (TSA) of recombinant Btk SH2 domains. Melting temperature (T_m) for wild-type Btk was calculated from two independent measurements.

(d) Mapping of a subset of XLA-patient mutations (red sticks) onto the human Btk SH2 structure (PDB 2GE9). The residue R307 (orange sticks) is part of the pY-binding motif (FIVRD). The residue K311 is a non-XLA control mutation facing the opposite surface of the SH2 domain. N- and C-terminal are indicated as N and C, respectively.

(e,f,g) HEK293 cells were transiently transfected with indicated Btk constructs containing an N-terminal 6xMyc tag. Immunoblotting of total cell lysates was performed to assess Btk phosphorylation on sites Y551 and pY223, and relative phosphorylation normalized to total Btk (Myc-Btk) expression. Tubulin was used as loading control. Data shown in (e) and (g) are the mean ± SD of three biological replicates ($n=3$), while data shown in (f) is the mean ± SD of two technical replicates ($n=2$). P-values were calculated against the wild-type (WT) using an unpaired *t*-test. ** $P \leq 0.01$, *** $P \leq 0.001$, and non-significant (ns).

Source data are provided as a Source Data file.

Supplementary Figure 2



Supplementary Figure 2, related to Figure 2. Purification of recombinant Btk and autophosphorylation *in vitro*.

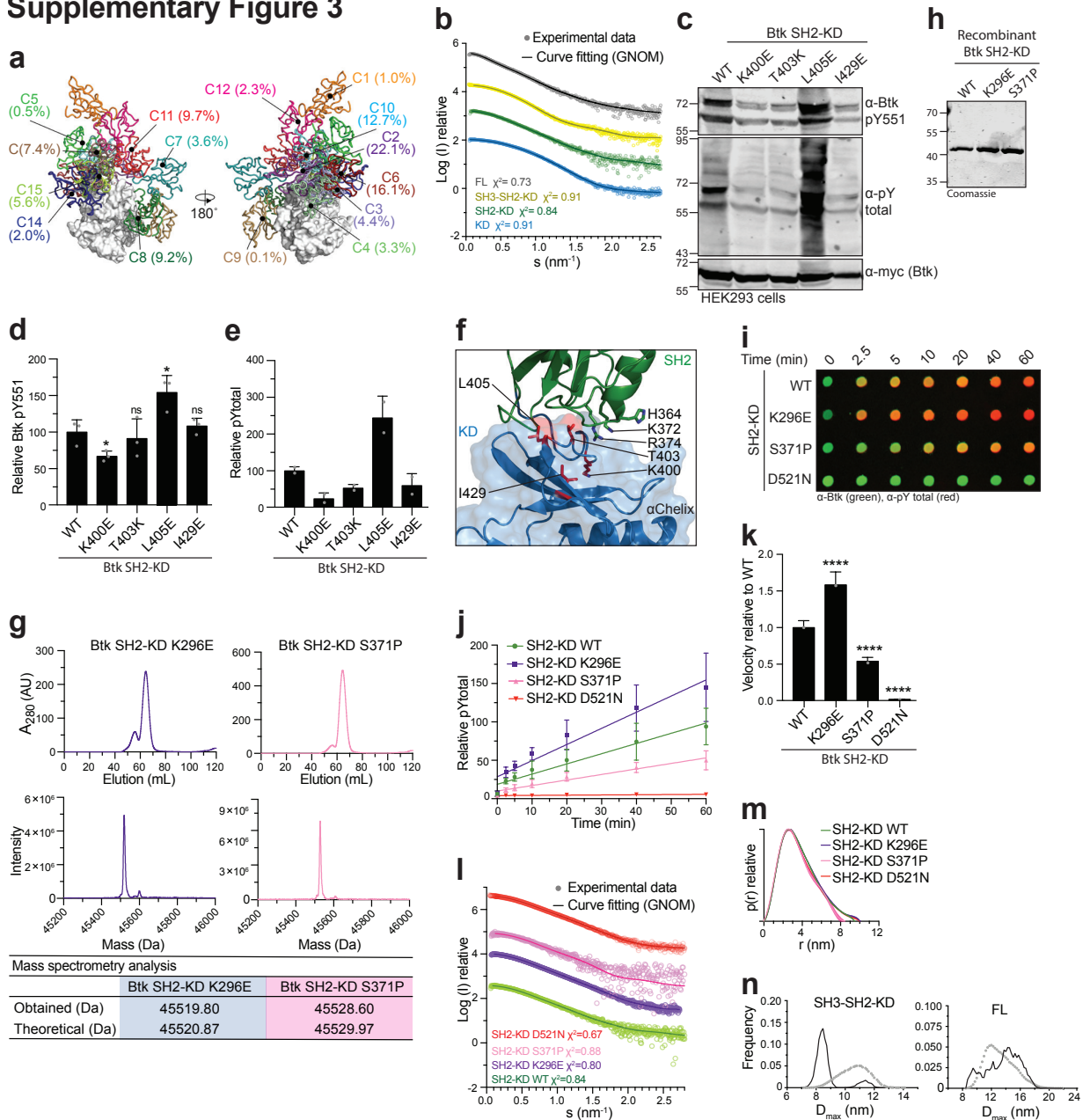
(a) SEC of recombinant Btk expressed and purified from Sf9 cells (top). Only monomeric peaks were used for the described assays. All samples were subjected to MS analysis for confirmation of protein identity and unphosphorylated state (> 95% for all samples, bottom). The table summarizes the theoretical and obtained molecular weight for the indicated proteins.

(b) Representative immunoblot to confirm the absence of recombinant Yoph-flag phosphatase from proteins purified in Sf9 cells (top) and corresponding SDS-PAGE of recombinant untagged Btk proteins (bottom).

(c,d,e) Btk autophosphorylation *in vitro* assay performed as described in methods. The levels of total phosphotyrosine and total Btk were assessed using immunoblot in a dot-blot apparatus, relative autophosphorylation kinetics plotted overtime and normalized to total Btk protein, and relative autophosphorylation velocities calculated from the linear fitting. Data are the mean \pm SD of two independent experiments (n=3). P-values relative to Btk KD were calculated using unpaired *t*-test. *P \leq 0.05 and **P \leq 0.01.

(f) Autophosphorylation kinetics of Y223/Y551 *in vitro* assessed as described above. Data shown are the mean \pm SD of two independent experiments done in duplicates (n=2). Source data are provided as a Source Data file.

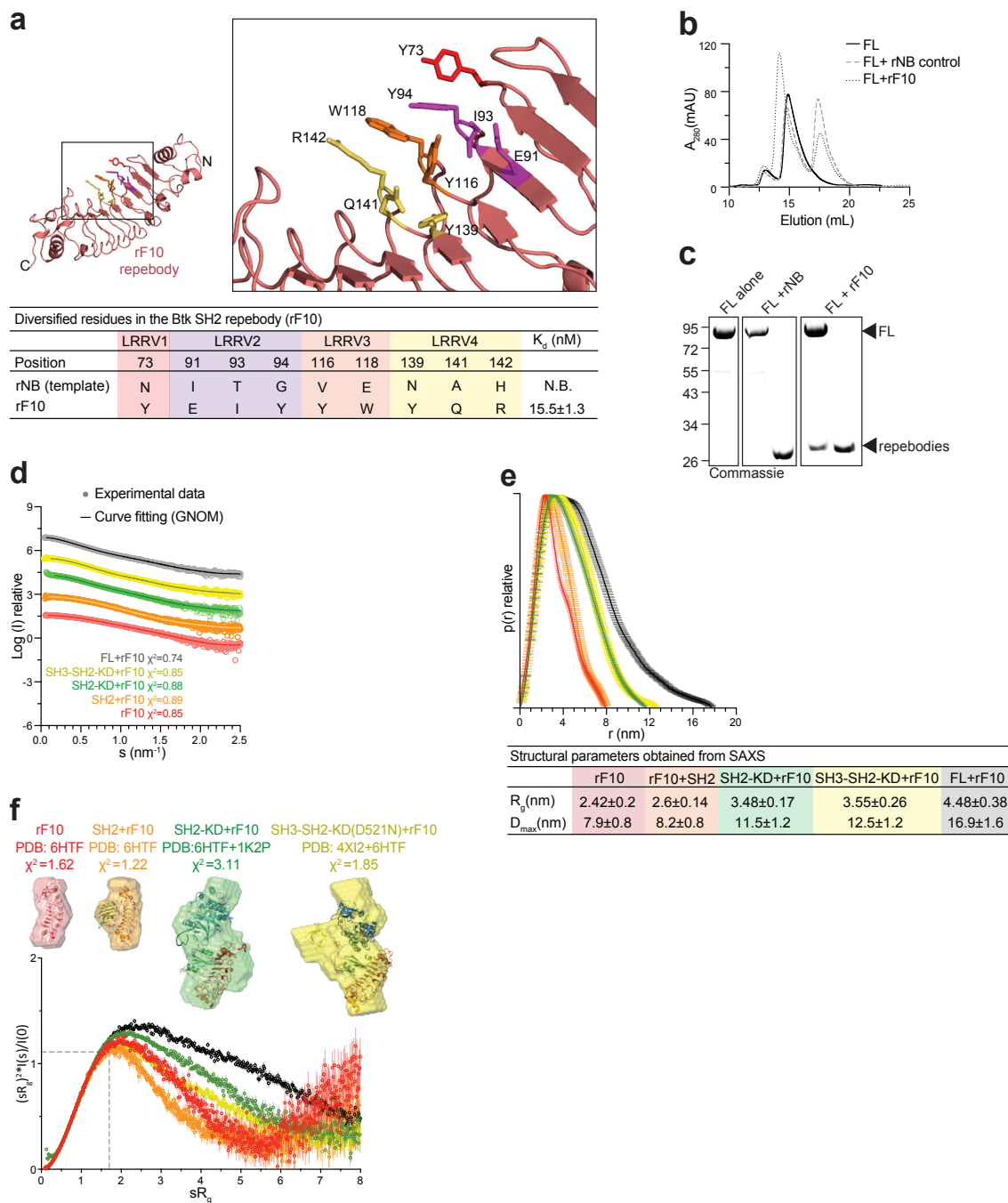
Supplementary Figure 3



Supplementary Figure 3, related to Figure 3 and 4. MD and SAXS analysis of Btk wild-type and mutants.

(a) MD simulation for the SH2-KD complex. Obtained clusters of the SH2 positions (several colors) relative to the KD (white).
 (b) Experimental SAXS data of recombinant wild-type Btk proteins. The indicated χ^2 represents the GNOM fitting (line) against the experimental data (dots) for each construct. See Supplementary Table 2 for details. Raw data is available at SASDB.
 (c,d,e) HEK293 cells were transiently transfected with indicated Btk constructs containing an N-terminal 6xmyc tag. Immunoblotting of total cell lysates was performed to assess Btk phosphorylation on Y551 and pY total, and relative phosphorylation normalized to total Btk (Myc-Btk) expression. Tubulin was used as loading control. Data shown in (d) and (e) are the mean \pm SD of three ($n=3$) and two technical ($n=2$) replicates, respectively. P-values relative to Btk WT were calculated using an unpaired t -test.
 (f) Residues mutated are shown as red sticks in a representative Btk SH2-KD structure obtained in the MD simulation (C15).
 (g) SEC of recombinant mutant Btk purified from Sf9 cells. All samples were subjected to MS analysis for confirmation of protein identity and unphosphorylated state (>95% for all samples, bottom).
 (h) Representative SDS-PAGE analysis of recombinant untagged Btk SH2-KD mutant proteins purified from Sf9 cells.
 (i,j,k) *In vitro* autophosphorylation of Btk SH2-KD mutants performed as described in methods. The levels of total phosphotyrosine and total Btk were assessed using immunoblot in a dot-blot apparatus, relative autophosphorylation kinetics plotted overtime and normalized to total Btk protein, and relative autophosphorylation velocities obtained from linear fit. Data are the mean \pm SD of two independent experiments ($n=6$). P-values relative to Btk wild-type (WT) were calculated using unpaired t -test. * $P \leq 0.05$, ** $P \leq 0.01$, *** $P \leq 0.001$, **** $P \leq 0.0001$, and non-significant (ns).
 (l,m) Experimental SEC-SAXS data and D_{\max} of mutant Btk proteins as indicated in (b). See Supplementary Table 2 for details.
 (n) Flexibility analysis (EOM 2.0) of Btk WT showing the D_{\max} of selected conformers (lines) from a representative pool of theoretical conformations (dot line).
 Source data are provided as a Source Data file.

Supplementary Figure 4



Supplementary Figure 4, related to Figure 5. rF10 repebody development and SAXS analysis of Btk-rF10 complexes.

(a) The rF10 repebody (cartoon representation, salmon) was developed by randomizing variable sites within leucine-rich repeats (LRRV) using phage display and modular evolution approach. The residues from the LRRV1 (red), LRRV2 (magenta), LRRV3 (orange) and LRRV4 (yellow) mediating the binding to Btk SH2 domain are indicated as sticks. The table shows the amino acid sequence and binding affinity to the human Btk SH2 domain. Non-binding (N.B.).

(b) Size-exclusion chromatogram (SEC) analysis of full-length Btk alone and mixed with rF10 or rNB control. The FL+rF10 forms a stable 1:1 complex which shifts to the left.

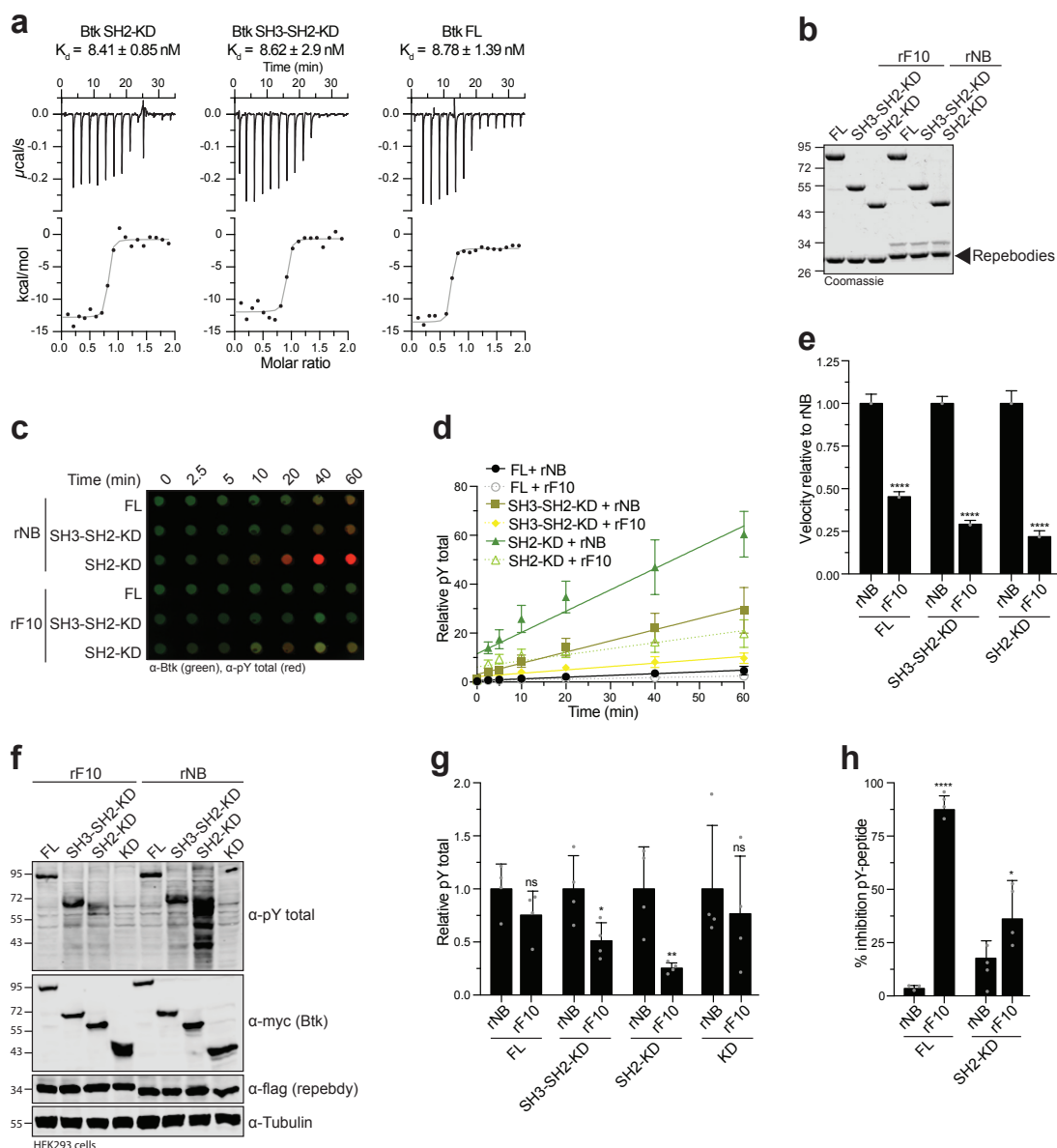
(c) Peaks isolated from the SEC analysis shown in (b) resolved by SDS-PAGE and stained with Coomassie.

(d,e) Experimental SEC-SAXS data and D_{max} for rF10 alone and rF10-Btk complexes. The indicated χ^2 represents the GNOM fitting (line) against the experimental data (dots) for each respective sample. The table summarizes the particle dimensions (R_g and D_{max}) and the \pm error for the indicated constructs. See Supplementary Table 4 for details.

(f) Dimensionless Kratky plot of rF10 alone and rF10-Btk complexes. *Ab initio* reconstructions obtained from SAXS (surface representation) were superimposed to the indicated crystal/MD structures. For the rF10-SH2-KD and rF10-SH3-SH2-KD complexes, rigid body modeling using SASREF was applied to obtain the final models displayed.

Source data are provided as a Source Data file.

Supplementary Figure 5



Supplementary Figure 5, related to Figure 6. Functional characterization of the rF10 repebody.

(a) ITC measurement of rF10 repebody to different Btk constructs containing the SH2 domain (SH2-KD, SH3-SH2-KD and FL proteins). Top panels show the raw signal from a representative measurement, and bottom panels show the integrated calorimetric data of the area of each peak. The continuous line indicates the best fit to the experimental data assuming a 1:1 binding model. The K_D (\pm SD) value was calculated from two independent measurements.

(b) Representative SDS-PAGE analysis of recombinant Btk proteins mixed with rF10 and rNB control repebodies and used for autophosphorylation inhibition *in vitro*.

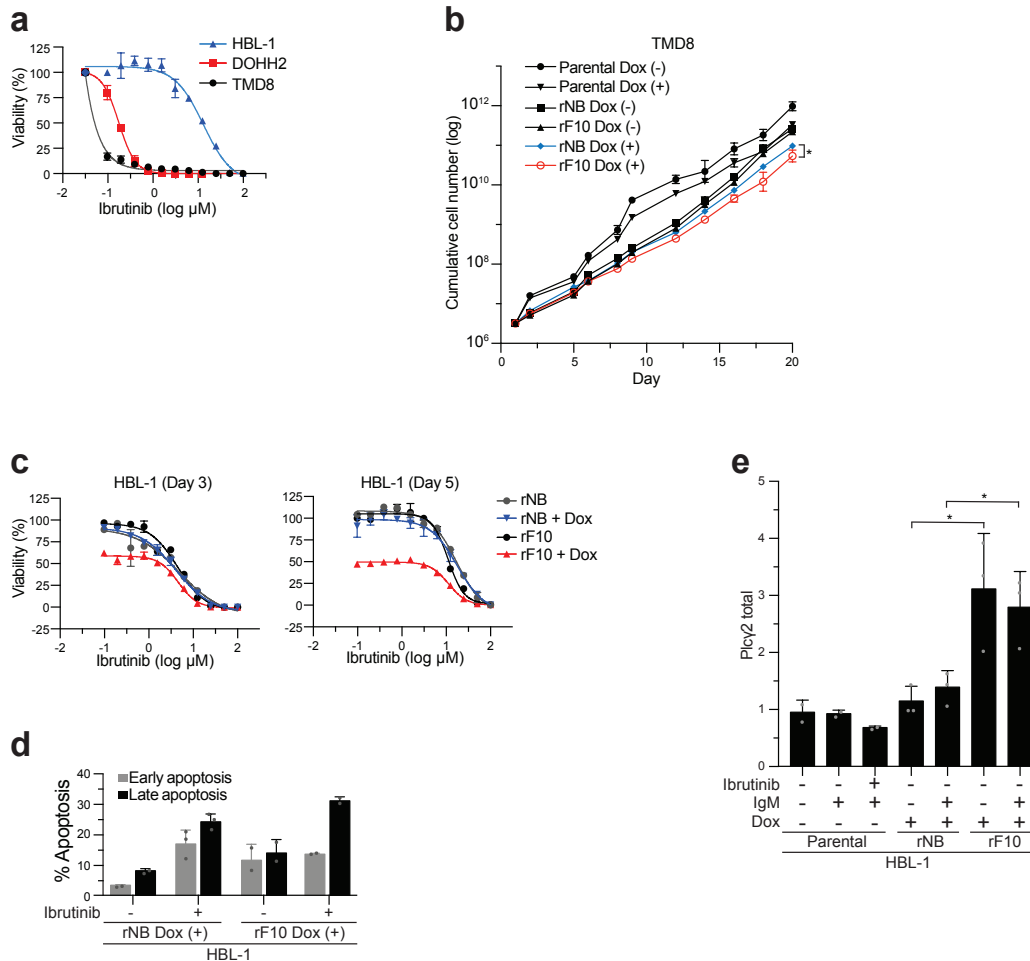
(c,d,e) *In vitro* autophosphorylation assay for Btk proteins in the presence of indicated repebodies was performed as described in methods. The levels of total phosphotyrosine and total Btk were assessed using immunoblot in a dot-blot apparatus. Relative autophosphorylation kinetics in the presence of rF10 (dashed lines) or rNB (continuous lines) repebodies plotted overtime and normalized to total Btk protein, and relative autophosphorylation velocities relative to each control repebody. Data are the mean \pm SD of three independent experiments (n=4). P-values relative to each control rNB repebody were calculated using an unpaired *t*-test.

(f,g) HEK293 cells were transiently co-transfected with indicated Btk constructs and repebodies. Immunoblot was used to assess total phosphotyrosine phosphorylation. Quantification of total phosphotyrosine normalized to total Btk (Myc-Btk) expression level and relative to control repebody. Data shown are the mean \pm SD of three biological replicates (n=4), and P-values were calculated relative to each rNB control using an unpaired *t*-test.

(h) Btk kinase activity against a PLCγ2 peptide (ERDINS₇₅₃YDVSR) in the presence of rF10 or control repebody. Reported inhibition (% of inhibition of peptide phosphorylation) from two independent experiments done in duplicates (n=4). P-values were calculated relative to each rNB control using an unpaired *t*-test. **P* ≤ 0.05, ***P* ≤ 0.01, ****P* ≤ 0.001 and non-significant (ns).

Source data are provided as a Source Data file.

Supplementary Figure 6



Supplementary Figure 6, related to Figure 7. Effect of rF10 in DLBCL cell lines.

(a) Dose-response for ibrutinib in human DLBCL cell lines. Data points represent the mean \pm SD of a representative experiment done in duplicate ($n=2$). Cellular IC₅₀ was obtained by non-linear regression curve fit analysis.

(b) TMD8 cell line was transduced with a doxycycline-inducible system for expression of reprobodies, and cumulative cell number monitored upon treatment with $2 \mu\text{g mL}^{-1}$ of doxycycline ($n=3$). Parental cells are non-transduced cells.

(c) Viability of HBL-1 cells inducibly expressing rF10 and rNB control (+Dox) or non induced (-Dox) in the presence of ibrutinib was measured after 3 and 5 days using Cell Titer-Glo reagent. Data points represent the mean \pm SD of a representative experiment done in duplicate ($n=2$). Cellular IC₅₀ was obtained by non-linear regression curve fit analysis.

(d) HBL-1 inducibly expressing rF10 or rNB control for 5 days in combination with ibrutinib ($10 \mu\text{M}$ for 48 hours) were stained with 7AAD and Annexin V to analyze apoptosis by FACS. The quantification of early (7AAD-/Annexin V+) and late (7AAD+/Annexin V+) apoptotic cells were obtained from two replicates ($n=2$).

(e) Quantification of total PLC γ 2 level from HBL-1 inducibly expressing reprobodies (flag-tagged) for 48 hours. BCR stimulation and ibrutinib treatment were performed as described in methods. Data shown are the mean \pm SD from two biological replicates ($n=3$), and P-values were calculated using unpaired *t*-test. * $P \leq 0.05$ ($n=3$).

Source data are provided as a Source Data file.

a

Btk C481S

	rNB				rF10			
	mock	FL	SH3-SH2-KD	SH2-KD	FL	SH3-SH2-KD	SH2-KD	

95
72
55
43

α-pY total

95
72
55
43

α-myc (Btk)

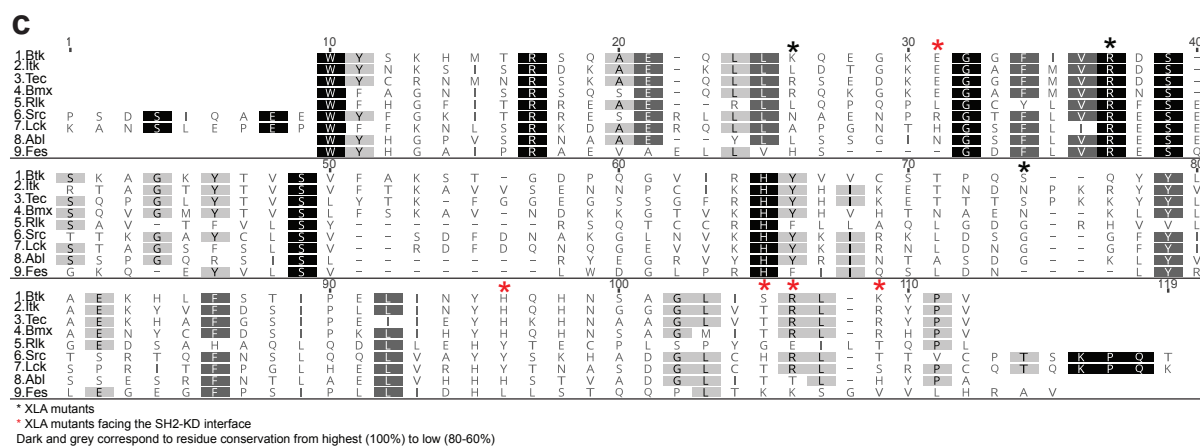
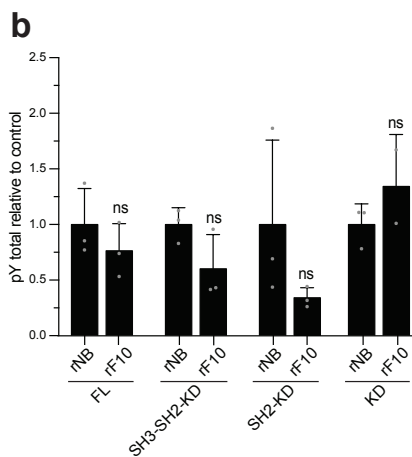
34

α-flag (repebody)

55

α-Tubulin

HEK293 cells



Supplementary Figure 7, related to Figure 8 and Discussion. Targeting the Btk SH2-KD interface decreases activation of therapy-resistant Btk with mutation on C481.

(a,b) HEK293 cells were transiently co-transfected with indicated Btk-C481S constructs and repebodies. Immunoblot was used to assess total phosphotyrosine phosphorylation. Quantification of total phosphotyrosine normalized to total Btk (myc-Btk) expression level and relative to control repebody. Data shown are the mean \pm SD of two biological replicates (n=3). (c) Sequence alignment of SH2 domains from human Btk and related kinases. Black squares represent residues highly conserved and grey squares show residues relatively conserved. Black asterisk symbol (*) indicates residues mutated in XLA patients, while red asterisks are residues mutated in XLA patients and located in the predicted SH2-KD interface. Source data are provided as a Source Data file.

SUPPLEMENTARY TABLES 1-5

Supplementary Table 1. *In vitro* autophosphorylation sites on the Btk SH2-KD protein.

Site	Peptide sequence	Location	Peptide count
Y279	SDSIEM $\underline{\text{Y}}$ EWYSK	SH2	56
Y282	SDSIEM $\underline{\text{Y}}$ EWYSK	SH2	56
Y315	AGK $\underline{\text{Y}}$ TVSVFAK	SH2	60
Y334	STGDPQG $\underline{\text{V}}$ IRHYVVCSTPQSQ $\underline{\text{Y}}$ YLAEK	SH2	46
Y344	STGDPQG $\underline{\text{V}}$ IRHYVVCSTPQSQ $\underline{\text{Y}}$ YLAEK	SH2	46
Y345	STGDPQG $\underline{\text{V}}$ IRHYVVCSTPQSQ $\underline{\text{Y}}$ YLAEK	SH2	46
Y361	HLFSTIPELIN $\underline{\text{Y}}$ HQHNSAGLISRLK	SH2	4
Y375	$\underline{\text{Y}}$ PVSQQNK	SH2-KD linker	3
Y392	NAPSTAGLG $\underline{\text{Y}}$ GSWEIDPK	SH2-KD linker	10
Y425	WRGQ $\underline{\text{Y}}$ DVAIK	KD	10
Y461	LVQL $\underline{\text{Y}}$ GVCTK	KD	2
Y511	DVCEAME $\underline{\text{Y}}$ LESK	KD	4
Y545	VSDFGLSR $\underline{\text{Y}}$ VLDD $\underline{\text{E}}$ YTSSVGSK	KD	37
Y551	VSDFGLSR $\underline{\text{Y}}$ VLDD $\underline{\text{E}}$ YTSSVGSK	KD	37
Y571	FPVRWSPPEVL $\underline{\text{M}}$ YSK	KD	15
Y627	V $\underline{\text{Y}}$ TIMYSCWHEK	KD	6
Y631	VYTIM $\underline{\text{Y}}$ SCWHEK	KD	6
Total peptide count			444

Supplementary Table 2. SAXS parameters of human Btk wild-type and mutants.

Data collection parameters							
Instrument	MD29 beamline, ESRF Grenoble - France						
Wavelength (Å)	0.9919						
q-range (nm ⁻¹)	0.03563 - 5						
Exposure time (sec)	5 (10 frames x 0.5 sec)						
Temperature (K)	290						
Samples	KD	SH2-KD	SH3-SH2-KD	Full-length	SH2-KD K296E	SH2-KD S371P	SH2-KD D521N
Measurement mode	batch	SEC-SAXS	batch	batch	SEC-SAXS	SEC-SAXS	batch
Concentration range (mg.ml ⁻¹)	0.9 – 4.2	100µ at 20.4	0.9 – 9.2	0.4 – 5.5	100µl at 30	100µl at 10.8	0.6 – 1.9
SASDB identifier	SASDF53	SASDF63	SASDF73	SASDF83	N/A	N/A	N/A
Structural parameters							
R _g (nm) from Guinier	2.09 ± 0.02	2.832 ± 0.3	2.62 ± 0.15	4.04 ± 0.03	2.92 ± -0.04	2.64 ± 0.23	2.83 ± 0.07
I(0)* (cm ⁻¹) from Guinier	24.86 ± 0.036	85.5 ± 0.12	44.28 ± 0.056	60.24 ± 0.16	171.59 ± 0.15	8.66 ± 0.075	20.71 ± 0.044
R _g (nm) from P(r)	2.096 ± 0.0003	2.88 ± 0.0005	2.62 ± 0.0006	4.34 ± 0.0014	2.95 ± 0.0003	2.70 ± 0.03	2.9 ± 0.05
D _{max} (nm)	6.75 ± 0.67	9.6 ± 0.95	8.3 ± 0.83	15.5 ± 1.2	10 ± 1.0	8.5 ± 0.86	10.3 ± 1.2
Porod volume (nm ³)	52.4	65.9	72.44	114.07	66.47	62.53	60.82
Dry volume calculated from sequence (nm ³)**	38.468	55.077	63.126	92.784	55.059	55.89	55.076
Molecular mass determination (kDa)							
From Porod volume (V _p /~1.6)	24.9	47.6	40.9	76.1	48.5	39.1	42.7
From SAXS MoW2***	28.9	49.7	35.7	65.2	50.9	44.6	46.4
Bayesian inference	28.9	46.6	41.9	67.1	46.6	42.8	40.2
From I(0) using V _c invariant	28.2	43.5	43.4	65.6	43.7	40.2	42.7
Calculated from sequence****	31.8	45.5	52.2	76.5	45.5	45.5	45.5
Number of residues	274	396	452	664	396	396	396
Software list							
Primary data reduction	Automated pipeline at beamline						
Data processing	PRIMUS (ATSAS v.2.8.0)						
Ab initio analysis	DAMMIN and GASBOR						
Fitting	CRY SOL						
Model refinement	SREFLEX						
Flexibility analysis	EOM 2.0						
Model superimpositions	SASpy plugin for Pymol						
3D graphics images	Pymol (v.1.8.2.1)						

*I(0) values shown in SEC-SAXS measurements vary depending on protein concentration at the analyzed peak, and are therefore not normalized to protein concentration. The structural parameters analyzed are independent of this value (i.e., R_g, D_{max}, volumes).

**<http://biotools.nubic.northwestern.edu/proteincalc.html>

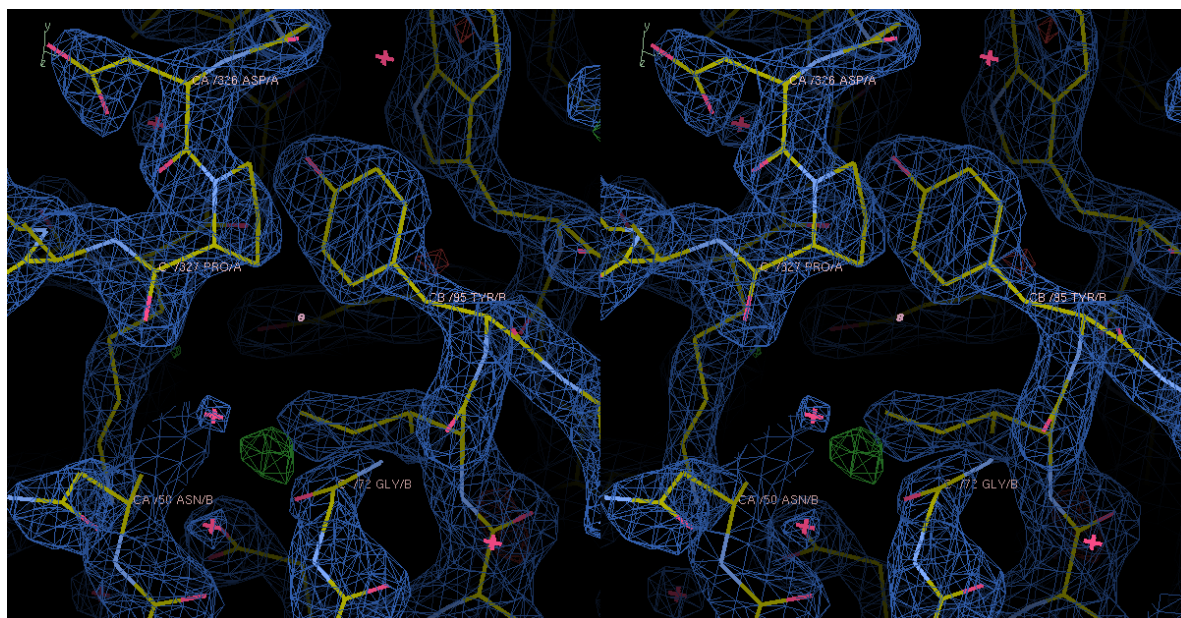
***SAXS MoW2

****<http://web.expasy.org/>

Supplementary Table 3. X-ray data.

Crystal structure	6HTF (rF10-SH2)
Data collection	
Space group	P 21 21 2
Cell dimensions	
<i>a</i> , <i>b</i> , <i>c</i> (Å)	145.53, 32.95, 80.63
α , β , γ (°)	90, 90, 90
Resolution (Å)	50 (2.1) *
<i>R</i> _{meas}	10.2 (81.1)
<i>I</i> / σ <i>I</i>	12.99 (1.95)
Completeness (%)	93.93 (84.43)
Redundancy	3.89 (3.90)
Refinement	
Resolution (Å)	2.1
No. reflections	22064
<i>R</i> _{work} / <i>R</i> _{free}	0.213 / 0.252
No. atoms	3041
Protein	2915
Ligand/ion	0
Water	126
Protein residues	362
B-factors	
Protein	40.75
Ligand/ion	N/A
Water	36.85
R.m.s. deviations	
Bond lengths (Å)	0.023
Bond angles (°)	1.44
Ramachandran analysis	
Favored regions	95.53%
Allowed regions	4.47%
Outliers	0

*Values in parentheses are for the highest-resolution shell.



Supplementary Table 4. SAXS parameters of Btk-rF10 complexes.

Data collection parameters					
Instrument	MD29 beamline, ESRF Grenoble - France				
Wavelength (Å)	0.9919				
q-range (nm ⁻¹)	0.03563 - 5				
Exposure time (sec)	5 (10 frames x 0.5 sec)				
Temperature (K)	290				
Samples	rF10	SH2-rF10	SH2-KD-rF10	SH3-SH2-KD-rF10	Full-length-rF10
Measurement mode	SEC-SAXS	batch	SEC-SAXS	batch	batch
Concentration range (mg.ml ⁻¹)	100 µl at 14	0.6 – 2.7	100µl at 20	0.4 – 3.6	0.4 – 2.9
SASBDB identifier	N/A	N/A	N/A	N/A	N/A
Structural parameters					
R _g (nm) from Guinier	2.42 ± 0.2	2.6 ± 0.3	3.46 ± 0.12	3.55 ± 0.26	4.48 ± 0.38
I(0)* (cm ⁻¹) from Guinier	37.12 ± 0.06	35.7 ± 0.18	87.82 ± 0.24	61.09 ± 0.19	79.46 ± 0.23
R _g (nm) from P(r)	2.47 ± 0.006	2.6 ± 0.01	3.52 ± 0.007	3.6 ± 0.01	4.69 ± 0.02
D _{max} (nm)	7.9 ± 0.8	8.2 ± 0.8	11.5 ± 1.2	12.5 ± 1.2	16.9 ± 1.7
Porod volume (nm ³)	50.85	67.4	100.6	116.46	156.04
Dry volume calculated from sequence (nm ³)**	37.581	53.569	92.638	100.685	130.345
Molecular mass determination (kDa)					
From Porod volume (V _p /~1.6)	24.8	37.9	70.4	81.2	100.8
From SAXS MoW2***	27.1	41.9	79.5	86.2	116.2
Bayesian inference	28.2	37.7	67.1	74.3	94.2
From I(0) using V _c invariant	27.6	39.3	63.5	74.6	89.4
Calculated from sequence****	31.1	44.3	76.6	83.2	107.7
Number of residues	274	391	670	726	938
Software list					
Primary data reduction	Automated pipeline at beamline				
Data processing	PRIMUS (ATSAS v.2.8.0)				
Ab initio analysis	DAMMIN and GASBOR				
Fitting	CRY SOL				
Model refinement	SREFLEX				
Flexibility analysis	EOM 2.0				
Model superimpositions	SASpy plugin for Pymol				
3D graphics images	Pymol (v.1.8.2.1)				

*I(0) values shown in SEC-SAXS measurements vary depending on protein concentration at the analyzed peak, and are therefore not normalized to protein concentration. The structural parameters analyzed are independent of this value (i.e., R_g, D_{max}, volumes).

**<http://biotools.nubic.northwestern.edu/proteincalc.html>

***SAXS MoW2

****<http://web.expasy.org/>

Supplementary Table 5. Oligonucleotides used for site-directed mutagenesis.

Primer name	Sequence 5' to 3' (forward and reverse)
Btk K296E	For: GCTGAGCAACTGCTAGAGCAAGAGGGGAAAAG Rev: CTTTCCCCTCTTGCTCTAGCAGTTGCTCAGC
Btk Y223F	For: GTGGCCCTTTTCGATTACATGCCAATG Rev: CATTGGCATGTAATCGAAAAGGGCCAC
Btk E301K	For: GCAAGAGGGGAAAAAGGGAGGTTTCATTGTC Rev: GACAATGAAACCTCCCTTTTCCCCTCTTGC
Btk R307G	For: GGTTTCATTGTCGGCGACTCCAGCAAAGC Rev: GCTTTGCTGGAGTCGCCGACAATGAAACC
Btk K311E	For: CAGAGACTCCAGCGAGGCTGGCAAATATACAG Rev: CTGTATATTTGCCAGCCTCGCTGGAGTCTCTG
Btk Q341A	For: GTTGTGTGTTCCACACCTGCGAGCCAGTATTACCTGGC Rev: GCCAGGTAATACTGGCTCGCAGGTGTGGAACACACAAC
Btk H364D	For: CATTAACTACCATCAGGACAACTCTGCAGGACTC Rev: GAGTCCTGCAGAGTTGCTCTGATGGTAGTTAATG
Btk S371P	For: CTGCAGGACTCATACCCAGGCTCAAATATCCAG Rev: CTGGATATTTGAGCCTGGGTATGAGTCCTGCAG
Btk R372G	For: CTCTGCAGGACTCATATCCGGCCTCAAATATCCAG Rev: CTGGATATTTGAGGCCGGATATGAGTCCTGCAGAG
Btk K374N	For: CTCTGCAGGACTCATATCCAGGCTCAACTATCCAG Rev: CTGGATAGTTGAGCCTGGATATGAGTCCTGCAGAG
Btk K400E	For: AGGTCAGGTCCTCTGGATCAATTTCCCATGATCCGT Rev: ACGGATCATGGGAAATTGATCCAGAGGACCTGACCT
Btk T403K	For: CCCCAGCTCCTTCAAGAACTTCAGGTCCTTTGGATCAA Rev: TTGATCCAAAGGACCTGAAGTTCTTGAAGGAGCTGGGG
Btk L405E	For: CAGTCCCCAGCTCCTTCTCGAAGGTCAGGTCCTTTG Rev: CAAAGGACCTGACCTTCGAGAAGGAGCTGGGGACTG
Btk I429E	For: GCCTTCTTTGATCATCTTCTCGGCCACGTCGTA CTGGCC Rev: GGCCAGTACGACGTGGCCGAGAAGATGATCAAAGAAGGC
Btk C481S	For: GG TAGTTCAGGAGGCTGCCATTGGCCATGTA Rev: TACATGGCCAATGGCAGCCTCCTGA ACTACC
Btk D521N	For: GTTCCTTCACCGAAACCTGGCAGCTCG Rev: CGAGCTGCCAGGTTTCGGTGAAGGAAC
Btk Y551F	For: GGATGATGAATTCACAAGCTCAGTAG Rev: CTACTGAGCTTGTGAATTCATCATCC